AEROSOL INDIRECT EFFECTS ON CLOUDS AND GLOBAL CLIMATE

by

Yang Chen

A dissertation submitted in partial fulfillment
of the requirements for the degree of
Doctor of Philosophy
(Atmospheric and Space Sciences)
in The University of Michigan
2006

Doctoral Committee:

    Professor Joyce E. Penner, Chair
    Associate Professor Nilton O. Renno
    Assistant Professor Christopher J. Poulsen
    Research Scientist Natalia G. Andronova

ACKNOWLEDGEMENTS

The first person I would like to thank is my academic advisor, Professor Joyce Penner. During my Ph.D studies in the University of Michigan, she kept an eye on the progress of my work and always was available when I needed her advises. Her enthusiasm and integral view on research have made a deep impression on me. Her guidance and encouragement would be beneficial to my whole life.

I am also grateful for Dr. Xiaohong Liu, who gave me a lot of very useful ideas and suggestions, helping me completing this work.

I had the pleasure to have worked with many elite scientists and students in our group. John, Sandy, Michael, Akinori, Natalia, Sophia, Yan, Christiane, Huan, Minghuai, Luis, Roy, Li, I thank you all for having shared many experiences and thoughts with me throughout the last years.

Finally, special thanks to my parents. I will remember everything you did for me.

TABLE OF CONTENTS

LIST OF FIGURES

Figure

xiv

LIST OF TABLES

CHAPTER I

Introduction

1.1 Global climate system

1.1.1 Energy balance in the atmosphere

Energy from the sun drives the weather and climate on the earth. The energy is stored and transferred in different parts of the earth system. These parts are called 'spheres'. The earth system includes the atmosphere, the lithosphere, the hydrosphere, the biosphere, and the cryosphere. These spheres are closely connected with moisture, momentum, and energy exchanging between them. The weather and the climate on the earth are affected by the change of elements in these spheres.

The main body in this research is the atmosphere, in which most of the weather and climate phenomena take place. According to the Intergovernmental Panel on Climate Change (IPCC), the climate is defined as:

"Climate in a narrow sense is usually defined as the 'average weather', or more rigorously, as the statistical description in terms of the mean and variability of relevant quantities over a period of time ranging from months to thousands or millions of years. The classical period is 30 years, as defined by the World Meteorological Organization (WMO). These quantities are most often surface variables such as temperature, precipitation, and wind. Climate in a wider sense is the state, including

a statistical description, of the climate system."
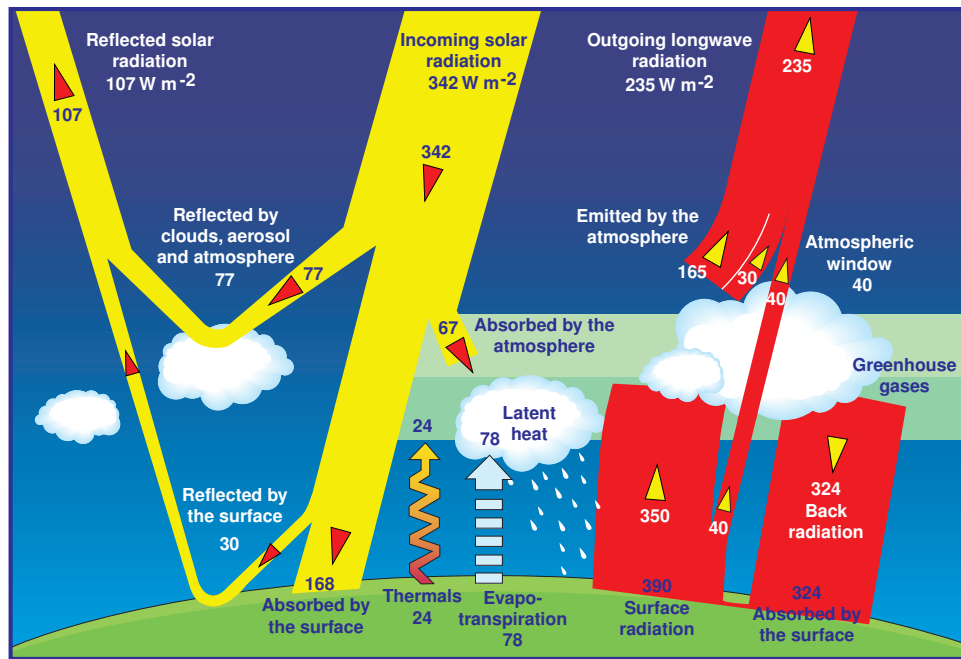
Figure 1.1: The earth's radiation and energy balance (*Kiehl and Trenberth*, 1997).

The earth, as a whole, emits the same amount of radiation as it absorbs, though with different wavelength. Figure 1.1 gives a schematic description on the earth's annual global mean energy balance, with an emphasis on the atmosphere. The average solar radiation received at the top of the atmosphere is about $342\,\mathrm{Wm^{-2}}$ (*Kiehl and Trenberth*, 1997). Part of this radiation ($\sim 107\,\mathrm{Wm^{-2}}$) is directly reflected back to the space by the atmospheric molecules, by the aerosols and clouds in the atmosphere, and by the earth surface. The rest of the energy is absorbed by the atmosphere (~ 67 $\mathrm{Wm^{-2}}$) and the surface ($\sim 168\,\mathrm{Wm^{-2}}$). Besides absorbing, the atmosphere (including clouds) and the surface also emit radiations with longer wave length to keep a radiative balance. The amount of solar radiation emitted by the surface is larger than the absorbed solar radiation, so there are other interchanges of energy between the atmosphere and the surface, which includes the latent heat and the sensible heat.

For human beings living mainly on the surface of the earth, the radiative balance between the surface and lower atmosphere is particularly important.

Radiant energy, arranged in order of its wavelengths, is called the spectrum of radiation. Since the temperature of the sun is much higher than that of the earth, the spectrum of solar radiation and terrestrial radiation are much different. Figure 1.2 shows the solar and terrestrial emission spectra. The temperature of photosphere, where most of the solar radiation received from the earth is emitted, is about 6000 K. The wavelength for the maximum of solar radiation is 480 nm. We should note that the solar radiation at some particular wavelengths is absorbed by different gases in the atmosphere, so not all the radiation reaches the surface. On contrast, the mean temperature of the earth surface is only about 283 K. Therefore most of the terrestrial radiation has much longer wavelengths in the spectrum (centered at ~ 10 μm). So the solar radiation is often called shortwave radiation (SW) while the terrestrial radiation is called longwave radiation (LW).
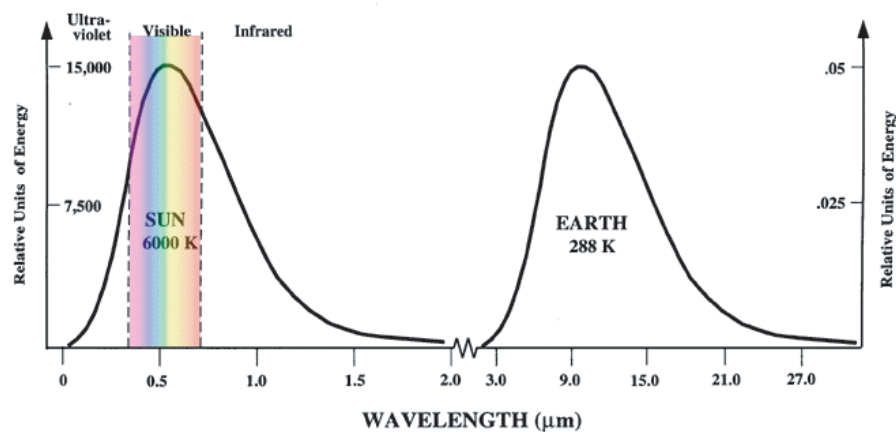
Figure 1.2: Comparison of the emission spectra of the sun and the earth. Note the huge disparity in the amount of energy emitted by the sun (left-hand scale) and the earth (right-hand scale). Source: PAOS Weather Lab in Colorado University (http://wxpaos09.colorado.edu).

Although on average, the total input and output of radiation to and from the earth are essentially in balance, they are not in balance at every part of the earth. The solar radiance reaching the surface depends, in part, on the solar zenith angle, the absorbing gas concentrations, the aerosol concentration, size distribution and chemical composition, the cloud amount and optical thickness, and the surface albedo. The LW radiative flux emitted by the earth mainly depends on the surface temperature, the amount of green house gases, the clouds and their properties. Generally speaking, low latitude areas receive more energy from the sun and the net effect here is 'warming', while the net effect at high latitudes is 'cooling'. This uneven distribution of the energy drives the latitudinal transfer of energy and the so-called 'general circulation'.

1.1.2 Climate change and climate forcing

Climate change is a statistically significant variation in either the mean state of the climate or in its variability, persisting for an extended period. Climate change can be due to a natural variability over temporal and spatial scales. For example, the Sun's output of energy varies by small amounts over the 11 year cycle associated with sunspots, and this may affect the climate in the atmosphere periodically. However, since the mid-18$^{\text{th}}$ century, human activities have caused more changes in the global climate than natural changes have. The main way humans alter global climate is by interferencing with the natural flows of energy through changes in atmospheric composition, not by the actual generation of heat in energy use (*Karl and Trenberth*, 2003). A main concern is the continuing increase of the green house gases (GHG) such as carbon dioxide (CO_2) in the atmosphere due to the fossil fuel burning, biomass burning and other human activities. This rising GHG in the atmosphere

traps more LW radiation within the atmosphere which is then radiated downward and increases the radiation absorbed by the surface of the earth, thereby increasing the surface temperature and causing the global warming. Because of its negative impact on human communities and on ecosystems, global warming is the most important environmental problem the world faces (*Houghton*, 2005). Most GHGs have long lifetimes in the atmosphere, so this effect has been clearly recorded by instrumental observations. Figure 1.3 shows the change of global average temperature and CO_2 concentrations since the year 1860.
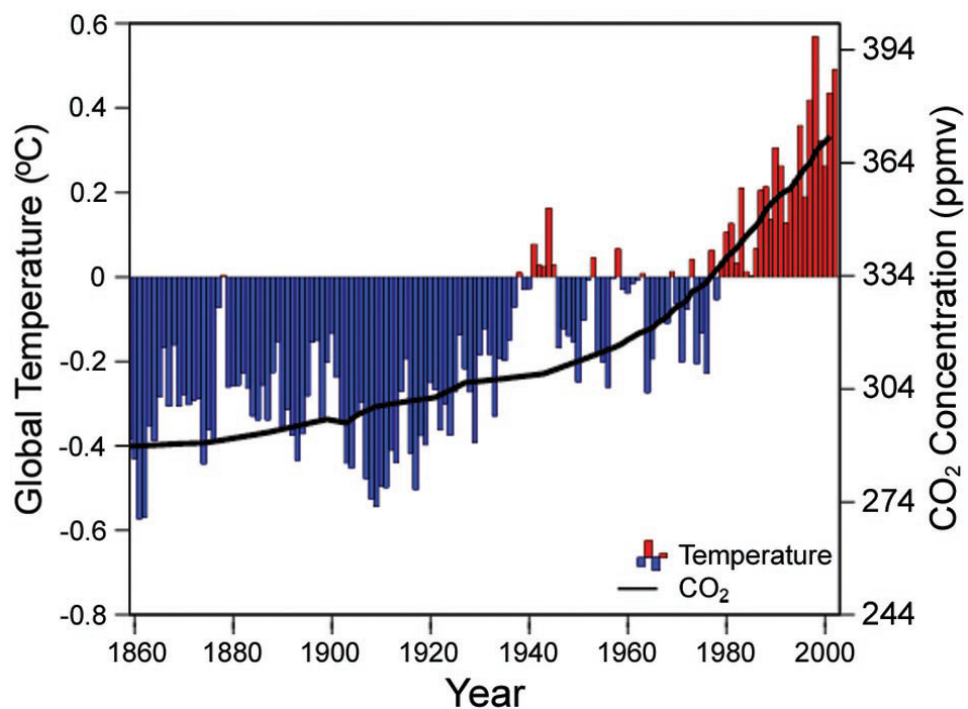
Figure 1.3: Combined land, air and sea surface temperature since 1860. The global mean CO_2 concentrations during the same period are also shown. Source: Climate Research Unit, University of East Anglia, UK.

Radiative forcing is a change imposed on the earth's energy balance that has the potential to alter global temperature. This change includes the increase of carbon dioxide in the atmosphere, volcanic eruptions of gas and debris, and so on. Radiative forcing is measured in watts per square meter (Wm^{-2}). Climate response is the

meteorological result of these forcings, such as global mean temperature change, rainfall changes, polar ice change, or sea level changes. One of the responses we care most is the global mean surface temperature change (ΔT), which results from the adjustment of the climate system to external forcings (ΔF). The relationship between ΔT and ΔF is denoted by a parameter called the climate sensitivity (λ). The effects due to different changes in the climate system can be compared through the concept of radiative forcing.

The change of many elements causes a radiative forcing of the climate. A summary on the simulated radiative forcing for the period from 1750 to 2000 and their uncertainties is shown in Figure 1.4. The GHGs have the largest radiative forcing, and the estimation of this forcing has a quite high degree of accuracy. The radiative forcing due to aerosols could be of a similar magnitude as the GHG forcing. But the uncertainty related to the aerosol forcing, particularly the indirect forcing, is very large.

1.2 Aerosol effects on climate

1.2.1 Aerosol presence in the atmosphere

Aerosols are liquid or solid particles suspended in the atmosphere. Aerosol particles arise from natural sources, such as windborne dust, sea spray, volcano emissions, and from anthropogenic activities, such as fuel combustion, biomass burning, construction, etc.

Aerosols can enter the atmosphere through direct emissions. These types of aerosol are called 'primary aerosols'. Other aerosols form in the atmosphere by gas-to-particle conversion, and they are called 'secondary aerosols'. This gas-to-particle conversion is mainly due to the nucleation and condensation of low-volatility gases.
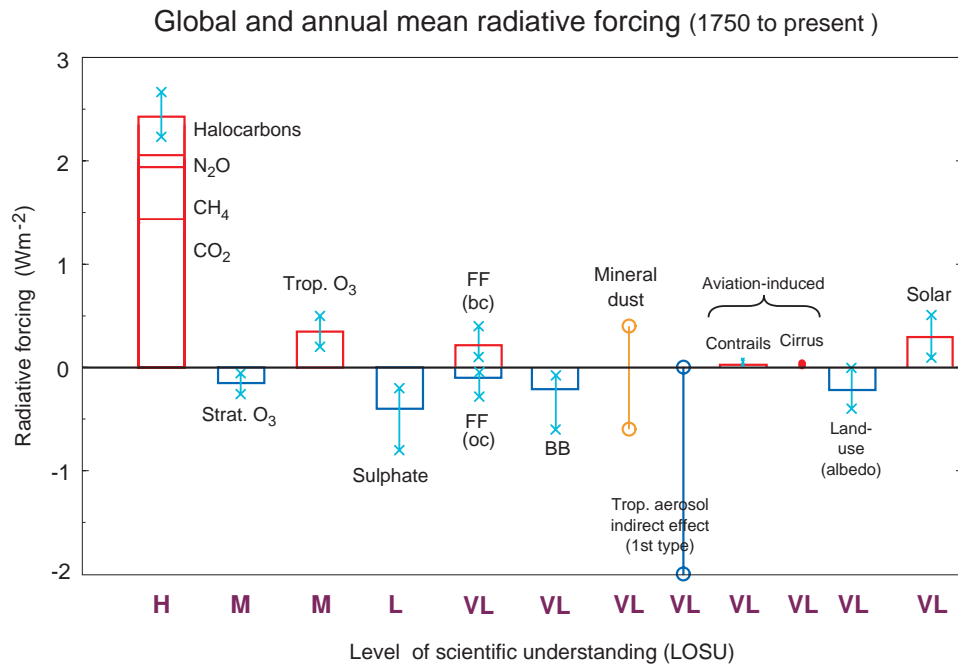
Figure 1.4: Global, annual mean radiative forcings due to a number of agents for the period from pre-industrial (1750) to 2000. The height of the rectangular bar denotes a best estimate value while its absence denotes no best estimate is possible because of large uncertainties. The vertical lines with 'x' or 'o' delimiters indicates estimates of the uncertainty ranges. A 'level of scientific understanding (LOSU)' index is accorded to each forcing, with H, M, L and VL denoting, high, medium, low and very low levels, respectively. This represents a judgment about the reliability of the forcing estimate involving factors such as the assumptions necessary to evaluate the forcing, the degree of knowledge of the mechanisms determining the forcing and the uncertainties surrounding the quantitative estimate of the forcing. The well-mixed greenhouse gases are grouped together into a single rectangular bar with the individual contributions shown. The second and third bars apply to stratospheric and tropospheric ozone. The next bars denote the direct effect of aerosols from fossil fuel (FF) burning-separated into black carbon (BC) and organic carbon (OC) components-and from biomass burning (BB). The sign of the effects due to mineral dust is itself an uncertainty. Only the first indirect aerosol effect is estimated, as little quantitative evidence exists regarding the second. All the forcings have distinct spatial and seasonal variations so that they cannot be added up and viewed a priori as providing offsets in terms of complete global climate impact. Source: *Houghton* (2005); *Ramaswamy et al.* (2001a).

8

Aerosols are removed from the atmosphere by dry deposition and wet deposition. Small particles can also be 'removed' by coagulation and aggregated to particles with larger sizes.
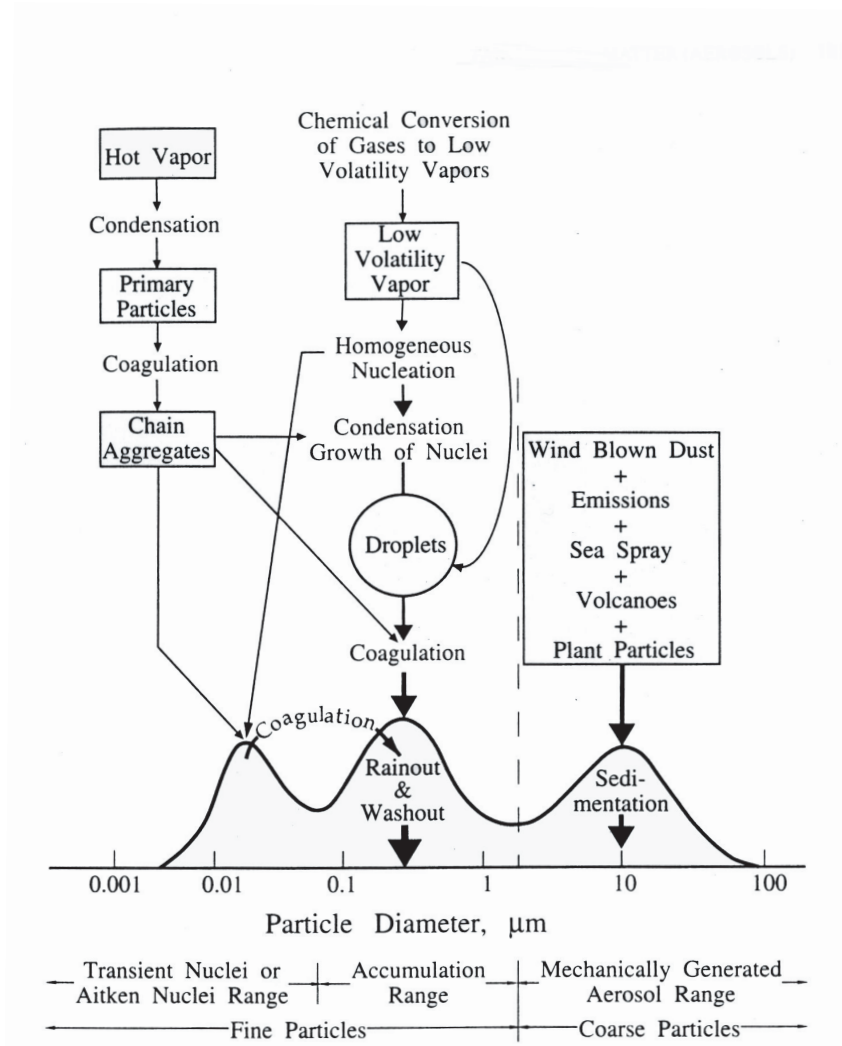
Figure 1.5: Idealized schematic of the distribution of particle surface area of an atmospheric aerosol (*Whitby and Cantrell*, 1976). Principal modes, sources, and particle formation and removal mechanisms are included.

Figure 1.5 shows a schematic of the surface area distribution of aerosol particles and their principal sources and sinks. Generally, the aerosols in the atmosphere can be divided into several 'modes' according to the size of the aerosols. A three mode division is often used: the nuclei mode (diameter < 0.1 μm), the accumulation mode

(0.1 μm < diameter < 2.5 μm), and the coarse mode (diameter > 2.5 μm). The sources and sinks for aerosols in different modes are different.

To consider this wide range in aerosol size spanning several orders, it is necessary to develop methods of mathematically characterizing aerosol size distributions. The number, surface area, and mass of aerosols for a size interval can be expressed numerically. For number size distributions, most aerosols are in the nuclei mode, while the peak in mass size distribution is usually in the coarse mode. The surface area distribution determines the aerosol direct scattering and absorption of solar radiance. The number distribution is important in determining how many aerosols can be activated as cloud droplets. Of the various mathematical functions, the log-normal distribution often provides a good fit and is regularly used in atmospheric applications. The log-normal distribution of a quantity is given by (*Seinfeld and Pandis*, 1997):

$$n_u\left(lnD_p\right) = \frac{du}{dlnD_p} = \frac{u}{(2\pi)^{\frac{1}{2}} ln\sigma_g} exp\left(-\frac{\left(lnD_p - ln\bar{D}_{pg}\right)^2}{2ln^2\sigma_g}\right) \qquad (1.1)$$

where u is the quantity of the distribution. It could be the total aerosol number concentration, the total surface area, or the total mass concentration. D_p is the diameter. $\bar{D}_{pg}$ is the mode diameter of the size distribution, and σ_g is the geometric standard deviation of the size distribution.

Unlike carbon dioxide, the distribution of the aerosols is highly variable both spatially and temporally. Total number concentrations of aerosols in urban polluted regions can be as high as 10^5 cm^{-3}, while in remote areas it is often as low as 10^2 cm^{-3}. The size distribution and chemical composition are also different in different regions. For example, the aerosols in marine areas are mainly composed of sodium chloride and the mean size is large. However in metropolitan area, sulfate and

nitrate aerosols often dominate, and most of the aerosols are in the nuclei mode
and the accumulation mode. Due to their variability, global measurements are not
available for most aerosol properties. This adds great complexity to study the effect
of aerosols on climate change.

1.2.2 Direct radiative effect

Aerosols can scatter and absorb solar and thermal infrared radiation directly,
thereby altering the radiative balance of the earth-atmosphere system. This is called
aerosol direct radiative effect. Many anthropogenic aerosol types contribute this
direct effect. Sulfate and nitrate aerosols, mainly formed from fossil fuel burning
and through chemical reactions in the atmosphere, can scatter the incoming solar
radiation effectively due to their small sizes. Carbonaceous aerosols from fossil fuel
and biomass combustion also increase the aerosol optical depth and the scattering of
SW radiation. One component in carbonaceous aerosols called Black Carbon (BC)(or
soot) can also absorb solar radiation, thereby changing the thermodynamics in the
atmosphere and warming or cooling the surface. Dust particles not only scatter
and absorb solar radiation, some of them also perturb terrestrial longwave radiation.
Modeling studies show that the range in the global mean aerosol direct forcing is
-0.1$\sim$-1.0 Wm^{-2} (*Penner et al.*, 2001a), which hints that the cumulative effect by
the aerosol particles is to cool the earth surface.

1.2.3 Aerosol-cloud interaction and aerosol indirect effect

Besides this direct effect, aerosols also alter the formation processes of warm, ice,
and mixed-phase clouds and their microphysical and radiative properties. Clouds are
a very important climate regulator. They not only reflect solar incident radiation,
causing cooling, but also trap outgoing LW radiation, causing warming. Because

clouds reflect of order 55 Wm^{-2}, a small change in the cloud amount can have a large impact on the climate (*Ramanathan et al.*, 1989). Aerosols increase the cloud droplet (N_d) and ice crystal number concentrations (N_i). They may also decrease the precipitation efficiency and prolong cloud lifetimes, thereby having a significant impact on the radiative balance and global climate. This effect is called aerosol indirect effect.

Twomey (1977) first suggested that an increase in atmospheric aerosols from anthropogenic emissions would lead to smaller cloud droplets because the same amount of cloud liquid water is distributed among more condensation nuclei. For the same liquid water content, a cloud with more numerous, but smaller drops, has a higher albedo than one with fewer, larger drops. This initialized the study on the aerosol indirect effect.

Two types of the aerosol indirect effects are mostly mentioned: the first aerosol indirect effect and second aerosol indirect effect. The former refers to the modulation of the cloud effective radius and cloud albedo by the aerosols acting as cloud condensation nuclei (CCN). Therefore it is also called the 'radius effect'. Since it was first suggested by Twomey, sometimes it is referred to as the 'Twomey effect'. A schematic plot of the 'Twomey effect' is shown in Figure 1.6. The second aerosol indirect effect refers to the change of cloud precipitation rate and lifetime by the aerosols, so it is often called the 'lifetime effect'. The cloud amount and the cloud liquid water content (LWC) may increase due to smaller precipitation rates and longer lifetimes. Most people attribute the discovery of this effect to Albrecht and it is sometimes called the 'Albrecht effect'.

Aerosols mainly affect low altitude warm clouds. However, some recent measurements showed human-induced particles, particularly BC, can change the nucleation
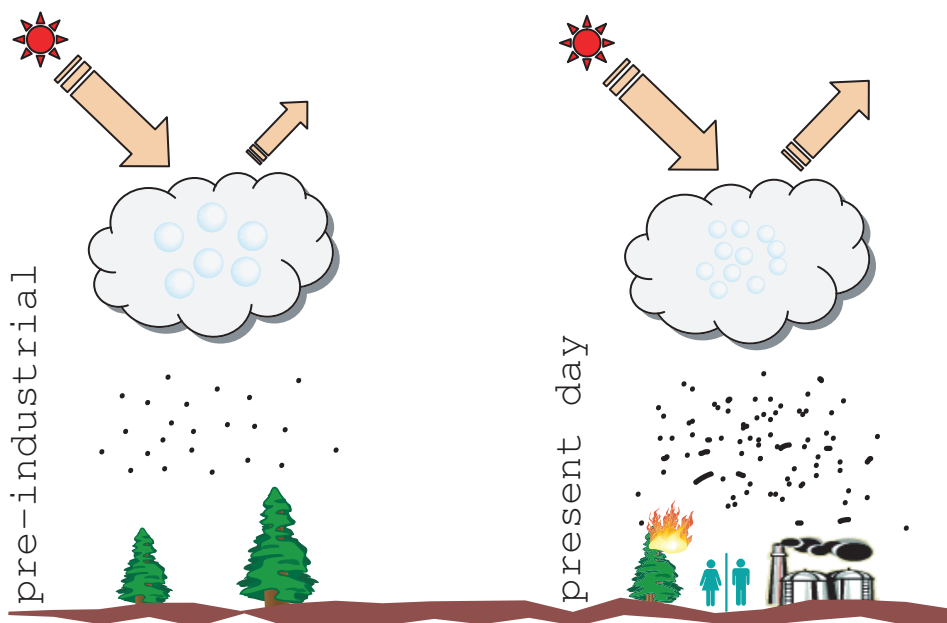
Figure 1.6: Schematic plot of first aerosol indirect effect. Left part shows the pre-industrial state. Right part shows that during present day, human activities modify the aerosol concentration, size distribution and chemical composition, thereby increasing the cloud droplet number concentration. The effective radius of cloud droplet decreases and the clouds scatter more solar radiation back to the space.

mechanism and the number concentration of high altitude cirrus clouds (*Ström and Ohlsson*, 1998; *Kristensson et al.*, 2000). This is a research field still at early stage, and not many measurements and model simulations have been done. There are still debates on the mechanisms and even on the sign of this effect (*DeMott et al.*, 1997).

Other than the above effects, absorbing aerosols such as BC, have a so-called 'semi-direct effect'. Due to their ability to absorb solar radiation, the presence of BC can heat the atmosphere and thus tend to reduce large-scale cloud cover (*Hansen et al.*, 1997). BC also can change the radiative properties of the clouds, as well as the albedo of snow and ice, when they are present in clouds, snow or ice. Sometimes these effects are also included in the study of the aerosol indirect effect.

As stated above, aerosols affect the clouds and climate through many mecha-

nisms. However, to study the aerosol-cloud-climate relationship is a very challenging task. First, aerosols usually have geographically localized sources and sinks, which vary on local to regional scales. The lifetime of aerosols is relatively short, thus also contributing to the temporal variability in the atmosphere. The aerosol size distribution can be very different in different regions due to their sources, and the representation of aerosol size distribution can affect the calculation of aerosol indirect radiative forcing (*Chen and Penner*, 2005). Therefore, although aerosols mainly act to cool the climate, the aerosol radiative effect cannot be considered simply as a long-term offset to the warming influence of greenhouse gases (*Houghton et al.*, 2001).

Second, the aerosol-cloud-climate system is a very complex system. As shown in Figure 1.7, aerosols and clouds are an important part of current General Circulation Models (GCM) used for estimating the climate change. Different mechanisms and phenomena are often entangled together. Therefore, the impacts of aerosols on clouds and climate are also complex. In addition, clouds and climate can cause positive or negative feedbacks on the aerosol particles. These make the aerosol-cloud interaction the most uncertain part in the climate simulations (See Figure 1.4).

1.2.4 Modeling study of aerosol indirect effects

Aerosol indirect effects are estimated from GCMs, single column models (SCMs), or radiative transfer models by conducting a present-day simulation and a pre-industrial simulation in which the anthropogenic emissions are set to zero. Usually, the difference in the top-of-the-atmosphere (TOA) flux (including SW and LW radiation) of the simulation is taken as the anthropogenic aerosol indirect effect.

For warm clouds, in order to calculate the first indirect forcing or the second
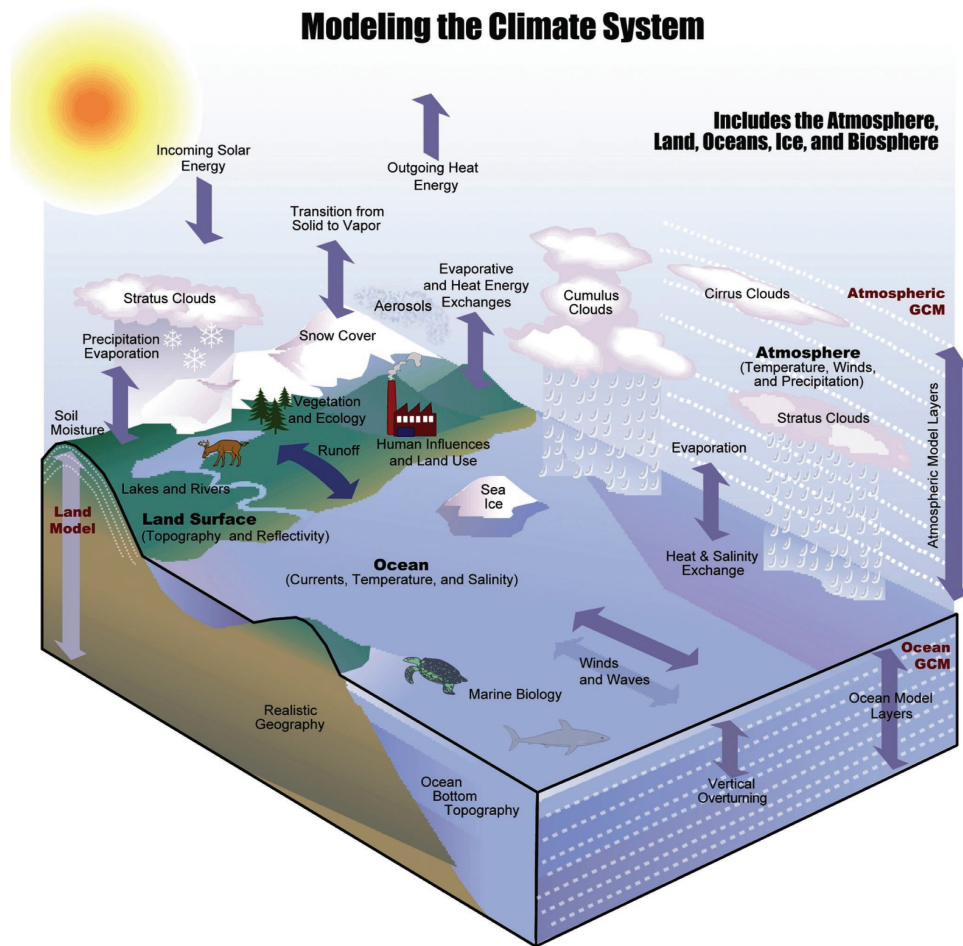
Figure 1.7: Components of the climate system and the interactions among them, including the human component (*Karl and Trenberth*, 2003).

indirect forcing, it is necessary to relate the cloud droplet number concentration to aerosol properties. However, a detailed numerically-resolved simulation of the cloud nucleation process is not possible in GCMs due to the high computational burden. Therefore a parameterization relating the clouds and aerosols is needed. One simple way is to directly relate the cloud droplet number concentration to the aerosol number concentration, or aerosol mass concentration, or other variables denoting the aerosol burden, based on the in-situ measurements.

Martin et al. (1994), *Jones et al.* (1994), *Menon et al.* (2002a,b), *Glantz and Noone* (2000) used observations to relate cloud droplet number concentration N_d to the aerosol number concentration for continental clouds, marine clouds, or both, respectively. The aerosol species included in the above studies included sulfate, sea salt and organic matter. *Boucher and Lohmann* (1995) summarized several sets of measurements and fit all the datasets to a single relationship between cloud drop number concentration and sulfate mass: $N_d = 10^{2.21+1.41log(mSO_4)}$.

However, empirical relationships such as that by *Boucher and Lohmann* (1995) do not give us any physical understanding of the cloud nucleation and growth process. So these formulas can not be used to help us understand the physical and chemical processes responsible for cloud nucleation. In addition, these relationships are derived from limited measurements at particular places and times. They may provide a relatively accurate estimation of the regional aerosol indirect effect during the time period of the measurements. However, these relationships can not be used to estimate the aerosol indirect effect at a global scale, or for a future scenario, since they are not able to treat the different aerosol types.

Physically-based parameterizations have been developed to solve these problems. In the derivation of this type of method, a concept called Cloud Condensation Nu-

clei (CCN) is sometimes used to describe the cloud-forming propensity of an aerosol population. CCN is the number of aerosol particles that can be activated (grow spontaneously) at a particular supersaturation. A classical CCN spectrum first described by Twomey can be described in the form of a power law (*Twomey*, 1977): $N_{CCN} = Cs^k_{\nu,w}$, in which C and k are constants. Initially this formula and the two parameters were derived based on chamber experiments. *Cohard et al.* (1998) suggested a more general description of the activation spectra in the following form $N_{CCN} = Cs^k_{\nu,w}F\left(\mu, \frac{k}{2}, \frac{k}{2} + 1; -\beta s^2_{\nu,w}\right)$, where $F(a, b, c; x)$ is the hypergeometric function and C, k, μ, β are adjustable parameters. This extended Twomey's parameterization to a more realistic activation spectra.

To use the above CCN spectra, a maximum supersaturation obtained in an uplifted parcel needs to be assumed. By assuming an aerosol size distribution, the maximum supersaturation can also be approximately estimated, and a simple form relating cloud droplet number concentration and aerosols can be derived. A lognormal size distribution for the aerosol particles is often used.

Ghan et al. (1993) proposed a cloud droplet parameterization: $\frac{N}{N_a} = \frac{1}{1+dN_a/w}$, where w is the updraft velocity and d is a coefficient dependent on aerosol properties. The derivation was based on Köhler theory and a lognormal aerosol size distribution, and growth between the time of activation and the time of maximum supersaturation was neglected. The coefficient d was calculated for different aerosol mode radii, different ammonium sulfate fraction in the aerosol, and a look-up table for d was constructed.

Chuang and Penner (1995), and *Chuang et al.* (1997) examined two different adding processes and two different mixing approaches for anthropogenic sulfate to pre-existing aerosols. They derived an explicit form of the coefficient d in Ghan's

formula for both continental aerosols and marine aerosols from the results of a microphysical model.

Abdul-Razzak et al. (1998) presented another general parameterization that combines the approaches of Twomey and *Ghan et al.* (1993). This parameterization related the fraction of aerosols activated to fundamental variables grouped into four dimensionless parameters.

Two methods for treating cloud nucleation by using the sectional representation of the aerosol size distribution have been published recently (*Abdul-Razzak and Ghan*, 2002; *Nenes and Seinfeld*, 2003). In both these two methods, the effective critical supersaturation of all sections is calculated based on the size and the chemical composition of the particles. And the maximum supersaturation of the parcel is parameterized based on a numerical solution of the algebraic equations representing the supersaturation change in an air parcel. These methods are suitable for any sectional representation of the aerosol size distribution, and can be applied to an arbitrary aerosol composition in each section.

However, up to now, only a few GCM modeling studies have used physically-based cloud nucleation parameterization methods. Studies by using the above two parameterization methods with sectional representations of the aerosol size distributions have not yet been reported. Most current estimations of the aerosol indirect forcing considered only one or two aerosol species, and assumed simple external or internal mixing states. The effects of highly soluble gases such as HNO_3 and semi-volatile organics in cloud nucleation processes have been studied experimentally or theoretically, but have not been added to GCM calculations of the aerosol indirect effect.

Modeling of the anthropogenic aerosol effect on cirrus clouds and climate is more

difficult. Aircrafts leave behind hot humid air and aerosol particles (mainly soot particles). These particles not only affect contrails, but also change the properties of the pre-existing cirrus clouds. However, there are several ice nucleation mechanisms, and their roles in forming clouds under different conditions are not very clear yet. Basically, ice nucleation may take place through either heterogeneous or homogeneous freezing, or through heterogeneous deposition. The mechanisms are not fully understood because not many measurements have been done at high altitudes where ice forms. There are also only a few general studies on aerosol effects on cirrus. No estimation of aerosol effects on global cirrus properties and climate has been made at present.

1.3 Purpose and outline of this study

1.3.1 Meaning and purpose

Figure 1.4 and the above discussion shows that there is large complexity and uncertainty in the study of aerosol indirect effect and the estimation of aerosol indirect forcing. However, accurately quantifying this effect is crucial to the projection of future climate change. If the aerosol indirect effect is very large, as some models predict, then the total forcing by aerosol and GHGs which have caused the 0.6 ℃ average temperature increase of the past 100 years must be small. So the climate sensitivity (which relates the forcing and the response) of the models is large if the models are confined to the previous record of temperature. As *Penner* (2004) pointed out, the future, then, might be more at the upper range of climate projections. But if aerosols do not have much impact on the clouds and do not cool the temperature much, then greenhouse gases may be only slightly masked by aerosol-induced cloud changes, and projections of future climate might follow the more benign path.

In this study, we will address these problems:

1. Is there any observational evidence showing that the aerosols can change the cloud radiative properties and the radiative balance of the earth? Can we separate other effects from the aerosol indirect effect?

2. What is the uncertainty in the estimation of the aerosol indirect effect? Which parameters contribute most to this uncertainty?

3. How do nitrate aerosols and nitric acid gas affect the cloud nucleation process? What is their influence on the aerosol indirect effect? Can we derive a parameterization considering this effect?

4. Have human beings induced aerosol affects on the cirrus clouds at high altitudes? What are the mechanisms behind the ice nucleation process? Can we give an estimation of the global forcing of this effect?

1.3.2   Outline

In Chapter II, we examine the effect of aerosols on cloud optical properties using measurements of aerosol and cloud properties at two North American sites that span polluted and clean conditions – a continental site in Oklahoma with high aerosol concentrations, and an Arctic site in Alaska with low aerosol concentrations. We determine the cloud optical depth by using a parameterization in which the shortwave downward surface radiation is required to fit the observation. We also use a cloud parcel model to simulate the cloud optical depth from observed aerosol properties due to the aerosol indirect effect. We then use a radiative transfer model to calculate the Top of the Atmosphere (TOA) outgoing shortwave fluxes at both sites. From the good agreement between the simulated aerosol indirect effect and observed surface

radiation, we conclude that the aerosol indirect effect has a significant influence on radiative fluxes. The possible reasons causing the uncertainty of the calculation are discussed and several sensitivity tests are made.

In Chapter III, we use 3-D meteorological fields together with a radiative transfer model to examine the spatially-resolved uncertainty in estimates of the first aerosol indirect forcing. In the reference case, we use the best estimates of the parameters and the processes in the calculation. Uncertainties in the indirect forcing associated with aerosol and aerosol precursor emissions, aerosol mass concentrations from different chemical transport models, aerosol size distributions, the cloud droplet parameterization, the representation of the in-cloud updraft velocity, the relationship between effective radius and volume mean radius, cloud liquid water content, cloud fraction, and the change in the cloud drop single scattering albedo due to the presence of black carbon are calculated by perturbing each of these parameters. The relative contributions of these parameters to the total uncertainty in estimating the indirect forcing are discussed. We also analyze the spatial distribution of this uncertainty and calculate the global mean value. This research is intended to provide a guide for future effects in learning the detailed mechanisms and reducing the uncertainty in the estimation of the aerosol indirect forcing.

Nitric acid gas and nitrate aerosols also affect the cloud nucleation process. In Chapter IV, we use a chemical transport model with different aerosol thermodynamic modules to estimate the nitrate distribution in the aerosol phase and in the gas phase. The effect of nitrate and nitric acid gas on cloud nucleation is studied. We also calculate the indirect forcing due to nitrate at several representative regions on the earth under typical cloud conditions. This forcing is compared to the indirect forcing of sulfate aerosols. The different effects of nitrate in the gas phase and in the

aerosol phase are examined and the uncertainty is analyzed. A substitution method is presented to account for the nitric acid gas effect, which can be used in a global simulation.

In Chapter V, we study the effect of human-induced aerosols on high altitude cirrus clouds. We use two recently developed ice nucleation parameterizations together with the aerosol concentrations from a chemical transport model to determine the global distribution of in-cloud ice crystal number concentration. Two meteorological fields are used and two different methods to represent the sub-grid scale variations of relative humidity are employed. The competition between homogeneous nucleation and heterogeneous is discussed. The results of ice crystal concentration and effective radius are compared to measured values. By using different emission scenarios, we employ a radiative transfer model to calculate the global forcing of aerosol effects on cirrus clouds. The top of atmosphere (TOA) longwave (LW), shortwave (SW), and net radiative forcings due to anthropogenic sulfate, anthropogenic soot from surface sources, and soot generated by aircraft are discussed. The change of cirrus cloud properties for different emission scenarios are investigated.

The final chapter gives a summary of the main conclusions of this study and future prospects for the study of aerosol indirect effects.

CHAPTER II

Observational evidence of a change in radiative forcing due to the aerosol indirect effect

2.1 Motivation

2.1.1 Evidence of aerosol indirect effect from observations

Aerosols serve as the cloud condensation nuclei (CCN). Therefore, the perturbation of aerosol concentration, size distribution and chemical composition due to human activities substantially modifies the microphysical and radiative properties of clouds, thereby modulating global radiative balance and surface temperature on the earth. Although the mechanisms that aerosol particles affect clouds and climate are complex and the amount of this effect remains very uncertain, analysis of observational data did show some evidence of this indirect effect. Starting from the so-called 'ship track study', these evaluations include in-situ measurements using flight-carry instruments and surface remote sensing instruments, and satellite measurements of the cloud and aerosol properties.

Early evidence for the impact of aerosols on clouds and climate was the satellite observation of the ship track signature in the marine clouds (*Coakley et al.*, 1987; *Radke et al.*, 1989). High reflectivity embedded in marine stratus clouds was found because the cloud albedo was increased due to the air pollution from ships. In-situ

observations improved the understanding of this first indirect effect by examining the difference of cloud droplet sizes between these ship tracks and adjacent clouds (*Radke et al.*, 1989). The exclusion of other explanations, such as the sea salt production in the wave of ships and the heat and moisture emission from ships (*Durkee et al.*, 2000; *Hobbs et al.*, 2000; *Noone et al.*, 2000), further supports the theory of aerosol modification on clouds.

Remote sensing instruments on satellites extended similar observations to other pollutant sources and to continental regions. *Kuang and Yung* (2000) found that the ultraviolet reflectance of coastal marine clouds measured from the Total Ozone Mapping Spectrometer (TOMS) is generally larger when affected by the continental pollution. The effect of smoke from biomass burning on cloud formation was also found by the measurement of Advanced Very High Resolution Radiometer (AVHRR) over the burning areas (*Kaufman and Fraser*, 1997). Satellite data also show a negative correlation between cloud albedo and cloud droplet effective radius (*Han et al.*, 1998), a negative correlation between cloud droplet effective radius and aerosol optical depth (*Wetzel and Stowe*, 1999), and a positive relationship between cloud albedo and aerosol number concentration (*Nakajima et al.*, 2001).

In-situ measurements do not cover as large an area as satellites, but they provide more precise measurements of the aerosol and cloud properties. These measurements also found linkages between cloud droplet effective radius and aerosol concentrations (*Yum et al.*, 1998), between cloud droplet number concentration and out-of-cloud aerosol particle number concentration (*Leaitch et al.*, 1996), and a contrast in the microphysics in polluted and clean clouds (*Twohy et al.*, 2001; *Liu et al.*, 2003). The cloud microphysics and aerosol properties are either measured directly by the instruments in the aircraft, or retrieved by using the surface remote sensing data.

Other than the above evidence of the aerosol effects on cloud effective radius and albedo, measurements also show that the cloud precipitation efficiency and lifetime are also affected by the perturbation of aerosols (*Rosenfeld and Woodley*, 2000). The measurements of aerosol effect on cirrus clouds, particularly that from aircraft soot particles, have also been reported recently (*Ström and Ohlsson*, 1998; *Kristensson et al.*, 2000). More observational evidence can be seen in the reviews given by *Schwartz and Slingo* (1996), *Haywood and Boucher* (2000), *Penner et al.* (2001b), *Menon* (2004), *Lohmann and Feichter* (2005).

2.1.2 Motivation of this study

The above measurements inspired the research on the aerosol indirect effect. They also provided more information for the numerical simulation study on global climate change. However, there are still limitations of the current observational evidence.

Since cloud albedo is not only determined by aerosol particles, but also affected by the microphysical, macrophysical and dynamical properties of the atmosphere and clouds, some previous observations may not fully and exclusively support the aerosol indirect effect. For instance, observations over the Atlantic Ocean (*Brenguier et al.*, 2000; *Schwartz et al.*, 2002) showed no clear difference in the cloud albedo between polluted clouds and clean clouds. This is because the effect due to smaller cloud droplet size in polluted clouds is offset by the effect due to drier atmosphere and thinner cloud thickness in those clouds. *Twohy et al.* (2001) also realized that mixing with dry air reduces droplet formation and makes the measurements of cloud droplets and condensation nuclei vary from one cloud to another. The large variability in cloud types, water content and updraft velocity complicates the problem. *Han et al.* (2002) pointed out the evaporation is easier for the small droplets and this would

give a cooling, suppressing the water source from the updrafts. Therefore, in the analysis of observations on the aerosol indirect effect, the effect due to cloud water content must be separated (*Brenguier et al.*, 2003).

Some observations shown above only linked aerosol number concentration and cloud droplet concentrations or effective radius, but they did not show the impact of these indirect effects on radiative fluxes. Other observations showed a clear difference of cloud radiative properties between polluted and clean regions, but the conclusion that this difference is mainly due to the difference in aerosol properties still lacks adequate support from the evidence. Satellite-based remote sensing instruments for measuring the aerosol indirect effect show large disparities in the magnitude of the effect, partly due to the different types of clouds measured by each instrument (*Rosenfeld and Feingold*, 2003). Therefore, as *Haywood and Boucher* (2000) pointed out, until now there are no convincing observations showing the entire chain of processes of the aerosol indirect effect from enhanced aerosol concentrations to enhanced cloud albedo on a scale large enough to influence significantly the earth's radiation budget.

Here in this chapter we provide observational evidence for a substantial alteration of radiative fluxes due to the indirect aerosol effect. Surface measurements of aerosol concentration and composition, as well as the surface radiative fluxes, are used to examine this effect. In our research, we differentiate the cause of different cloud albedo in polluted area and clean area due to the difference in aerosols and in liquid water path (LWP). We also show that the difference in aerosol properties does affect the TOA radiative flux.

2.2 Method and model description

2.2.1 Overview of this study

We examine the effect of aerosols on cloud optical properties using measurements of aerosol and cloud properties at two North American sites that span polluted and clean conditions – a continental site in Oklahoma with high aerosol concentrations, and an Arctic site in Alaska with low aerosol concentrations. We determine the cloud optical depth required to fit the observed shortwave downward surface radiation. We then use a cloud parcel model to simulate the cloud optical depth from observed aerosol properties due to the aerosol indirect effect. We also use a radiative transfer model to calculate the Top of the Atmosphere (TOA) outgoing shortwave fluxes in both sites. From the good agreement between the simulated aerosol indirect effect and observed surface radiation, we conclude that the aerosol indirect effect has a significant influence on radiative fluxes.

The Southern Great Plains (SGP) site is centered at $36°37'$ N, $97°30'$ W, in Oklahoma, and is a typical continental site with high aerosol number concentrations (500-600 cm^{-3} for particles with diameter between 0.1 and 10 μm, and $1{,}000$-$10{,}000$ cm^{-3} for total condensation nuclei (CN) concentration) and composition of mixed-continental origin. The North Slope of Alaska (NSA) site is located at $71°19'$ N, $156°37'$ W, in Barrow, Alaska, and is a typical Arctic site with low aerosol concentrations (CN concentration of 99 ± 120 cm^{-3} for this study) and composition determined partly by sea-salt particles. The geographical locations of these two sites are shown in Figure 2.1.

The Atmospheric Radiation Measurement (ARM) Program provides a unique opportunity to study the relationship between aerosol, cloud, and climate. ARM is a multi-laboratory, interagency program, which focuses on obtaining continuous

SGP   NSA

Figure 2.1: Geographical locations of two sites used in this study: Southern Great
Plains (SGP) and North Slope of Alaska (NSA). The SGP site is centered
at 36°37′ N, 97°30′ W, in Oklahoma. The NSA site is located at 71°19′
N, 156°37′ W, in Barrow, Alaska. SGP is a typical continental site with
high aerosol number concentrations, while NSA is a typical Arctic site
with low aerosol concentrations.

field measurements and providing data products that promote the advancement of
climate models. SGP and NSA are two of the main sites that represent a broad range
of weather conditions. In these sites, a comprehensive set of instruments is available
for measuring the atmospheric, aerosol, cloud, and radiative properties. A detail
description of the instruments and the method of these measurements is available in
the ARM website: http://www.arm.gov.

The time periods in this study were from 1 May to 30 September 2000 at the
ARM NSA site, and from November 1996 to November 1998 at the ARM SGP site.
During these two time periods the cloud temperatures at both sites are above -13
℃ for most of the time, so that clouds at both sites can be viewed mostly as liquid-
phase and liquid-dominant mixed-phase clouds. The aerosol indirect effects on cirrus
clouds and climate will be discussed in Chapter V.

2.2.2 Model description

Based on the measured aerosol properties, the cloud droplet number concentrations are calculated by using a size-resolved parcel model with detailed microphysics of nucleation. The model is a one-dimensional adiabatic model based on *Liu and Wang* (1996) and *Liu and Seidl* (1998). The closed air parcel, which includes dry air, water vapor and particles, is lifted with a constant updraft velocity (see Figure 2.2). Detailed growth of water vapor on aerosol particles, as well as the change of microphysics and thermodynamics, is recorded in this uplifting.
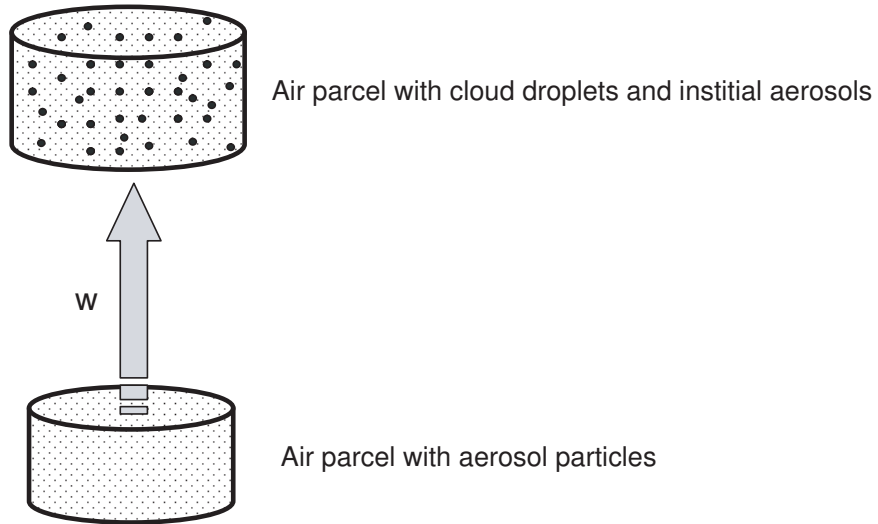
Figure 2.2: Schematic picture of the cloud nucleation parcel model. Some aerosols are activated to form cloud droplets in the updraft process due to the cooling and water condensation.

The growth of a cloud droplet radius r is given by:

$$r\frac{dr}{dt} = \frac{S - S_e}{\frac{\rho_w R'T}{D'_v e_s(T)} + \left(\frac{L}{R'T} - 1\right)\frac{L\rho_w S_e}{K'_a T}} \tag{2.1}$$

S is the ambient vapor saturation ratio, which is the vapor pressure divided by saturation vapor pressure over a plane water surface at the same temperature, $e_s(T)$. R' is the individual gas constant for water vapor. ρ_w is the density of liquid water.

T is the temperature. L is the latent heat of vaporation. D'_v and K'_a are modified vapor diffusivity and thermal conductivity considering the size effect (*Pruppacher and Klett*, 1997).

S_e is the equilibrium vapor saturation ratio, which depends on aerosol size and chemical composition. The formula for S_e is:

$$ln\left(S_e\right) = \frac{A}{r} - \frac{B}{\frac{r^3}{r_{ins}^3} - 1} \tag{2.2}$$

in which

$$A = \frac{2\sigma_w}{R'T\rho_w},$$

$$B = \frac{6n_s M_w}{\pi\rho_w}\frac{1}{8r_{ins}^3} = \frac{n_s M_w}{\frac{4}{3}\rho_w\pi r_{ins}^3},$$

$$n_s = \frac{4}{3}\pi r_0^3\rho_p\sum_k\left(\frac{m_k}{\sum_k m_k}\times\frac{\gamma_k}{M_k}\right),$$

and σ_w is the surface tension. M_w is molecular weight of water. r_{ins} is the radius of insoluble core. r_0 is the radius of dry particle. ρ_p is the density of aerosol particle. γ_k and M_k are number of ions and molar mass of electrolyte k. $\frac{m_k}{\sum_k m_k}$ gives the mass fraction of electrolyte k.

The first term in the right side of Equation 2.2 accounts for the so-called Kelvin effect, which is the increase of vapor pressure required for equilibrium due to the increase in the curvature associated with the decrease in r. The second term in the right side denotes the Raoult effect, or the solution effect, which reflects the decrease of equilibrium vapor saturation due to the presence of dissolved substances. Figure 2.3 gives an illustration of these effects. The solution effect dominates when the radius is small. These small droplets are in stable equilibrium with the vapor at relative humidity around 100%. When the ambient humidity surpasses the maximum S in the curve (called critical saturation S_{cr}), the particle can grow spontaneously to cloud droplet size, and we say that the condensation nuclei is 'activated'.
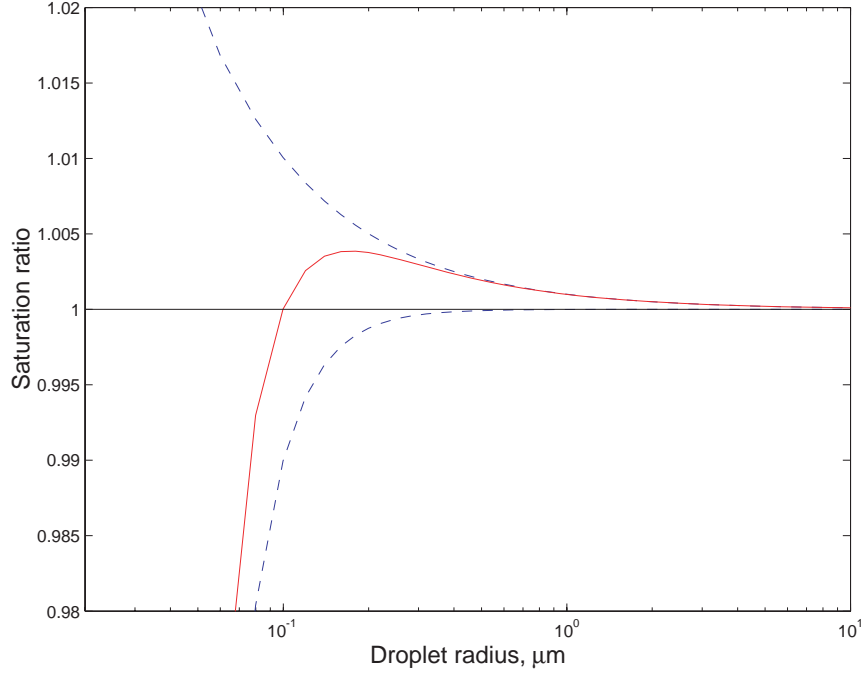
Figure 2.3: Equilibrium saturation ratio of a typical solution droplet. This Köhler curve is affected by the curvature effect and the solution effect. These two effects are shown in the plot as dashed lines. The solid line shows the results of the combination of these two effects.

In the lifting parcel, other prognostic parameters such as the water vapor mixing ratio, temperature, air pressure, and vapor saturation ratio are computed as follows.

Change of water vapor mixing ratio q_v and liquid water mixing ratio q_L:

$$\frac{dq_v}{dt} = -\frac{dq_L}{dt} = -\frac{4\pi\rho_w}{\rho_a} \int_0^\infty \left(r^2 n(r) \frac{dr}{dt} \right) dr \tag{2.3}$$

Change of temperature T:

$$\frac{dT}{dt} = -\frac{L}{c_p} \frac{dq_v}{dt} - \frac{g}{c_p} W \tag{2.4}$$

Change of air pressure P:

$$\frac{dP}{dt} = -\frac{(1 + q_v) P g W}{R_d + q_v R'} \tag{2.5}$$

Change of vapor saturation ratio S:

$$\frac{dS}{dt} = -S \left(\frac{L}{R'T^2} \frac{dT}{dt} + \frac{g}{R_d T} W \right) + \frac{S}{q_v} \frac{dq_v}{dt} \tag{2.6}$$

In the above equations, ρ_a is the density of the atmosphere. $n(r)$ is the number density of aerosols with radius r. c_p is the specific heat of the air at constant pressure. g is the acceleration of gravity. W is the updraft velocity of the air parcel.

The aerosol and cloud droplet considered in this parcel model are size-resolved, i.e., we grouped aerosol particles with similar dry size at the beginning of simulation. These groups form different size bins. The aerosol particles in each bin have the same chemical composition. In order to use the measured ion concentrations, in this model, the ions are distributed to electrolytes according to the water activity of their saturation solution. Once the electrolyte concentrations are obtained, the mean hygroscopicity and density of the droplet can be calculated. In the chemical part of this parcel model, the dilution of ion concentrations due to condensation growth of droplets, and the gas-liquid phase mass transfer. At each time step, PH values, mean hygroscopicity and density of dry sizes of particles within droplets are updated.

The radiative transfer modeling is based on LLNL Solar Radiative Transfer Model (SRTM) (*Grant et al.*, 1999). This model accepts trace gas mixing ratios, aerosol amounts and compositions, cloud types, properties and fractions from the external climate or chemistry model. It returns the SW radiative fluxes and heating rates back to the external model.

LLNL SRTM has layered structure vertically. A two-stream solution algorithm incorporating a layer adding technique is used to evaluate the shortwave fluxes at layer edges. Sources of diffuse radiation are calculated using the δ-Eddington algorithm described by *Joseph et al.* (1976).

The optical property driver (OPD) generates optical depths, single-scattering albedos, and asymmetry factors by taking physical information given by an external model. In this study, our major concern is the change of cloud optical properties

caused by the change of cloud droplet number concentration. This is obtained by relating the cloud droplet effective radius to the cloud droplet number concentration. A detailed calculation of cloud optical depth is shown in the following section.

2.2.3 The input data for simulation

As introduced above, we used a warm-cloud adiabatic parcel model to examine the effect of aerosols on cloud droplet number concentration. The parcel model requires that we specify the aerosol size distribution, total number concentration, chemical composition, and updraft velocity. Then, we estimated the cloud optical depth using the measured cloud properties (cloud geometric thickness and cloud liquid water path(LWP)). Cloud geometric thickness is the difference between the cloud top height and the cloud base height.
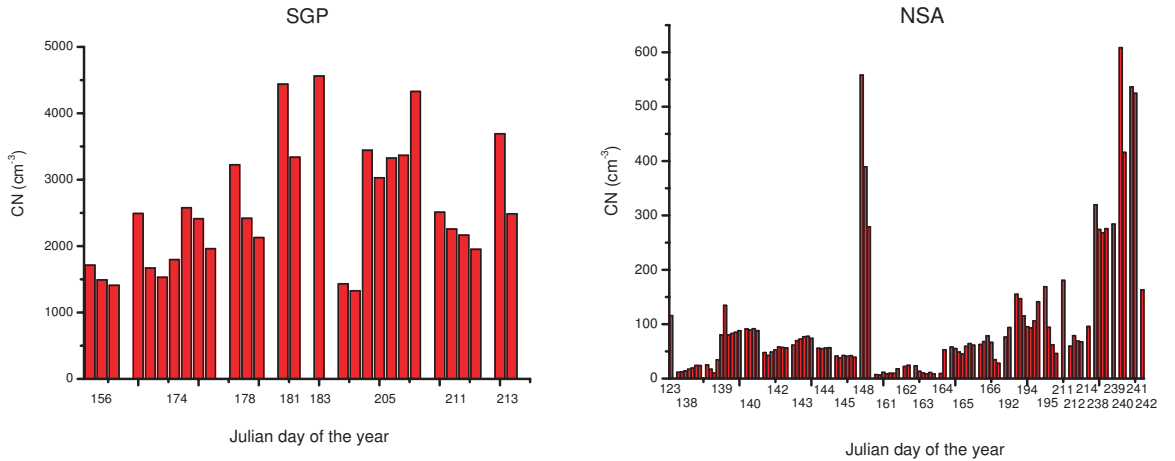
Figure 2.4: Aerosol number concentrations measured at the SGP and NSA site. Hourly mean concentrations of condensation nuclei (CN) are shown in group, according to their appearance in the Julian day of the year. The data are based on 1997 surface measurements at the SGP site and 2000 measurements at the NSA site.

The concentrations of aerosol particles at the surface are obtained from the Aerosol Observation System (AOS) (*Sheridan et al.*, 2001), which is conducted by NOAA Climate Monitoring and Diagnostics Laboratory (CMDL). The TSI (Model

3010) condensation nuclei counter (CNC) measures the total number concentration of condensation particles of diameter in the size range from 10 nm to 3 μm. The PMS (Model PCASP-X) Optical particle counter (OPC) measures the particle number concentration in 31 size channels from 0.1 to 10 μm diameter at SGP site. These data are available approximately daily at each site. Figure 2.4 shows a sample plot of daily mean data of aerosol concentrations at the SGP and NSA site.

No direct measurements of aerosol size distribution were available. However, typical continental and marine size distributions are available from a number of measurements (*Penner et al.*, 2001a). Moreover, for the SGP site, ARM provided measurements of the total aerosol concentration with diameter > 0.1 μm. So we developed a 2-mode lognormal size distribution that fitted both the total CN concentrations and the number concentration with diameter > 0.1 μm. We assumed that mode 1 had a mean diameter equal to 0.02 μm and a geometric standard deviation of 1.1, while mode 2 had a mean diameter of 0.08 μm and a geometric standard deviation of 1.75. For the NSA site, based on aerosol composition, we initially used either a typical marine size distribution (a single-mode lognormal size distribution with a mean diameter equal to 0.19 μm and a geometric standard deviation of 1.5) or a typical continental size distribution. Figure 2.5 shows the size distributions of the aerosol populations in the SGP and NSA site.

The aerosol ion compositions are measured by *Quinn et al.* (2002). The SGP site is a typical inland site in which the insoluble part is dominant. Ammonium sulfate is the main soluble substance. In the NSA site, sea salt fraction is as large as 30%. Nitrate is not an important component in both sites. The average measured aerosol chemical composition is shown in Table 2.1.

The cloud-top height is derived from Millimeter Wavelength Cloud Radar (MMCR)
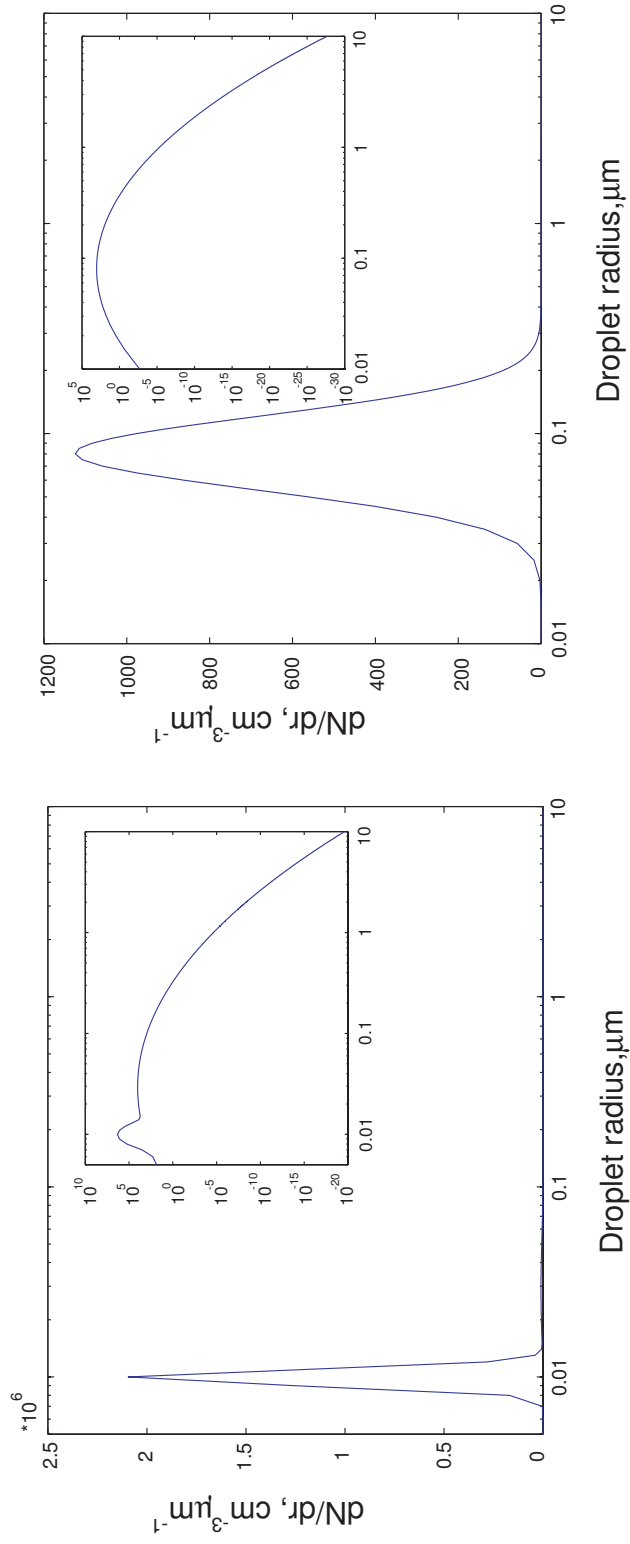
Figure 2.5: Aerosol size distribution used in this study. 2-mode lognormal size distribution is used for the SGP site. Mode 1 had a mean diameter of 0.02 μm and a geometric standard deviation of 1.1, while mode 2 had a mean diameter of 0.08 μm and a geometric standard deviation of 1.75. At the NSA site, a single-mode lognormal size distribution with a mean diameter of 0.19 μm and a geometric standard deviation of 1.5 is used. The inserted plots have logarithm y axis.

Table 2.1: The averaged concentrations and fractions of each ion at the SGP and NSA site are calculated based on measurements. In this table, concentrations of sodium ion and chlorine ion are added together to denote the total concentration of sodium chloride (sea salt). Concentrations of ammonium ion and sulfate ion are added together to denote the total concentration of ammonium sulfate. The undetermined fraction is assumed to be insoluble.

	SGP		NSA	
	ug/m^3	Percentage	ug/m^3	Percentage
NaCl	0.13	0.88	0.48	29.92
$(NH_4)_2SO_4$	4.36	29.10	0.54	33.28
Insoluble	9.79	65.26	0.51	31.63
NO_3^-	0.40	2.69	0.03	1.88
K^+	0.10	0.63	0.01	0.57
Mg^{2+}	0.03	0.17	0.02	1.49
Ca^{2+}	0.19	1.25	0.02	1.21

reflectivity profile, and the cloud-base height is derived from laser ceilometer measurements (*Dong and Mace*, 2003). Since the laser ceilometer is sensitive to the second moment of the particle distribution instead of the sixth moment like the MMCR, the ceilometer provides a more faithful estimate of cloud base. We averaged the available 5min data to 1hr mean data. Cloud geometric thickness is the difference between cloud-top and cloud-base height. At the NSA site, most clouds considered in this study have cloud base at 60~110 m, cloud top at 200~500 m, and cloud height from 100m to 500m. At SGP site, most clouds have cloud base at 90~1300 m, cloud top at 600~2300 m, and cloud height from 500m to 2100m. The cloud LWP is the vertical integral of cloud liquid water content. The value of LWP is derived from microwave radiometer brightness temperatures measured at 23.8 and 31.4 GHz using a statistical retrieval method (*Liljegren et al.*, 2001).

We estimated the vertical velocity for each time period based on the average updraft velocity and the turbulent kinetic energy (TKE) from the Model Output

Location Time Series (MOLTS) data provided by the National Centers for Environmental Prediction using $w = \overline{w} + c\sqrt{TKE}$, where $\overline{w}$ is the large scale updraft velocity and c=0.7 (*Lohmann et al.*, 1999a). In the later sensitivity test, we will show that the modeled cloud optical depth is not sensitive to updraft at the NSA site, and would be very similar at the SGP site had we used the maximum millimeter cloud radar Doppler values for the updraft velocity.

2.2.4 Selection of cloud events

In this study, we are mainly concerned with the low altitude stratiform clouds. Some cloud events may not be suitable for this study since they include ice crystals, or have too low solar zenith angle or too large cloud thickness. A data filter is needed for the cloud event selection and assuring the quality of calculation.

We established five criteria for choosing the cloud events under which cloud properties can be estimated using the retrieval method. These are: (1) only single-layer and overcast low-level stratus clouds are present as determined from cloud radar observations, (2) the cosine of solar zenith angle (θ_0) is larger than 0.2, (3) the range of solar transmission is between 0.1 and 0.7, (4) LWP is between 20 and 600 gm^{-2}, and (5) cloud top height is less than 3 km. These selection criteria favor liquid water shallow clouds and make it suitable for radiative transfer calculation. We identified approximately 300 hours of the stratus clouds (more than 3,600 samples at 5-min resolution) that satisfied these five criteria at the NSA site and 500 hours at the SGP site.

In addition to these criteria, for examining the effects of aerosols on clouds we also required that the atmosphere be well mixed below cloud base. The criterion of a well-mixed atmosphere below cloud base enables us to calculate the aerosol number

concentration at cloud base (N_a') by using the measured surface concentrations (N_a) assuming that the aerosol mixing ratio is constant with altitude: $N_a' = N_a \times \frac{P'}{P} \times \frac{T}{T'}$, where P and T are pressure and temperature at surface, while P' and T' are pressure and temperature at cloud base. This criterion was satisfied by requiring that the water vapor mixing ratio measured by the ARM rawinsonde sounding near the cloud base and that near the surface were within $\pm 15\%$. This is shown in Figure 2.6. Rawinsonde data are available for each day near local noon. These additional criteria reduced the number of cases for further analysis to 28 at the SGP site and 109 at the NSA site.
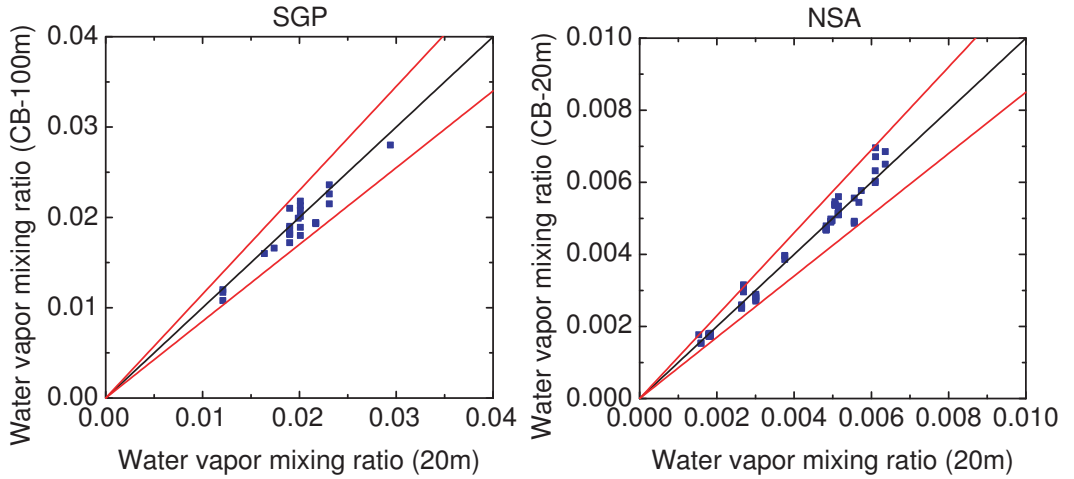
Figure 2.6: Well mixing from the surface to the cloud bases is shown by comparing the water vapor mixing ratio at surface and cloud base. The data of vapor mixing ratio are recorded by the radiosonde launched at a time close to each cloud event. The uncertainty of the radiosonde facility is larger at the initial launching and at the cloud base, so we used the data a little bit above surface and a little bit below the cloud base.

Figure 2.7 shows a typical temperature profile of a selected cloud event which was recorded by the instruments in the rawinsonde balloons. This cloud has a low altitude (50~230 m). The temperature of cloud top is about -2.5 ℃. The temperature in clouds decreases almost linearly.
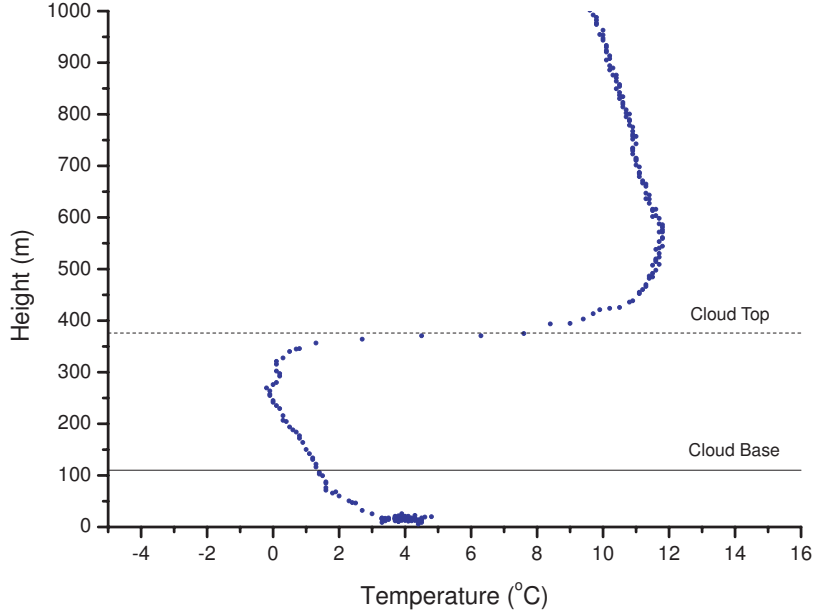
Figure 2.7: A vertical temperature profile recorded by the radiosonde for a selected case at the SGP site. The time period of this case is Aug 29th, 19:00-20:00 (local time). The launching time of the balloon is 22:40 at the same day. The cloud top and cloud base height shown in this plot are measured by millimeter wavelength cloud radar and ceilometer.

2.3 Relationship between cloud optical depth and cloud LWP

2.3.1 Calculation of cloud droplet number concentration

Detailed cloud parcel model and the data of aerosol properties were used to estimate the cloud droplet number concentration. As shown in Equation 2.6, the change of vapor saturation ratio S is a combination of two effects. The cooling in the updraft causes the decrease of saturation vapor pressure, thereby increasing the water vapor saturation ratio. On the other hand, the deposition of water vapor on droplets lowers the vapor concentration in the atmosphere, causing a decrease of S. At the start of the period of uplifting, the second effect is small since the total surface for deposition is small. So the value of S increases, and the speed of change depends on the updraft velocity. When S surpasses the equilibrium vapor saturation ratio S_e for the aerosols in certain size bins, these aerosols tend to grow. And as

S is larger than the critical saturation S_c, the droplets in those size bins can grow spontaneously. With more vapor deposition on the droplets, the size of particles increases, and the second effect becomes more and more important. Once the second effect becomes dominant, S reaches the maximum value(S_{max}) and starts decreasing from then on. A typical evolution of S_{max} in the uplifting is shown in Figure 2.8.
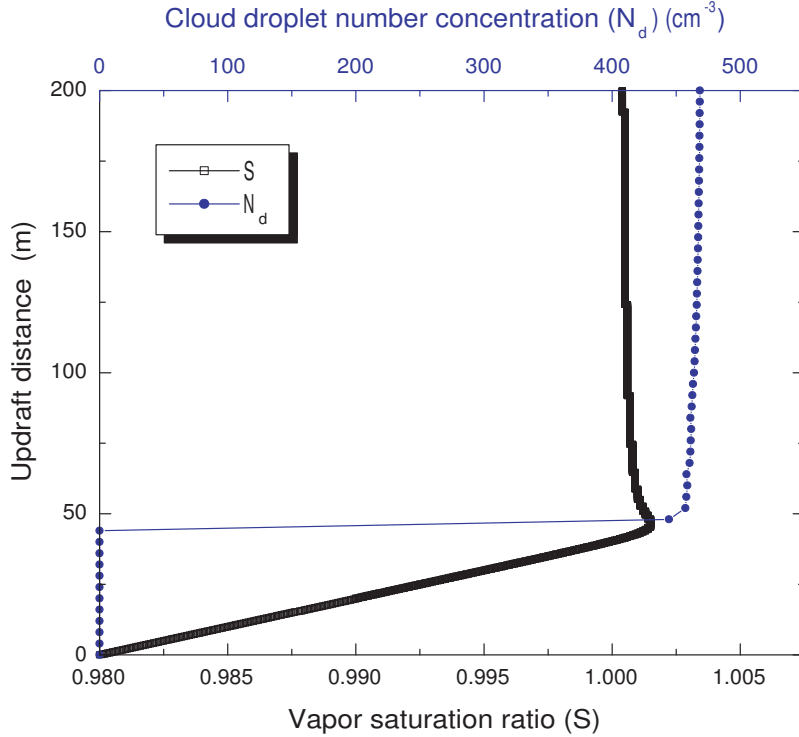
Figure 2.8: Evolution of saturation ratio in the uplifting air parcel is recorded in the nucleation model simulation. The aerosols are assumed to be pure ammonium sulfate and the number concentration is 1000 cm^{-3}. A lognormal distribution with mode radius 0.05 μm and standard deviation 1.9 is used for the aerosol population. Other simulation conditions are: T = 288 K, P = 900 mb, w = 40 cm/s. The number concentration of aerosols that are activated as cloud droplets is also shown in the plot.

The number of cloud droplets (N_d) is calculated by counting the number of particles in the size bins where the vapor saturation ratio S is larger than the critical saturation S_{cr}. Our simulation of S and N_d starts at t_{start} and ends at t_{end}, where $(t_{end} - t_{S_{max}}) = 2(t_{S_{max}} - t_{start})$. $t_{S_{max}}$ is the time when the maximum saturation

vapor is achieved. At t_{end}, the ambient saturation ratio and the calculated N_d are almost stable.

The CCN spectrum is the number of aerosol particles that are activated as a function of supersaturation ratio ($S_s = S - 1$). For the measured aerosol concentration and composition, we can vary the updraft velocity in the model and use this means of varying the supersaturation to determine the number of activated aerosols. A fit to the standard relationship for cloud condensation nuclei (CCN) as a function of supersaturation (S), CCN=cS_s^k, yields c=371±172 and k=0.39±0.11 for the SGP site, and k=0.31±0.31 for the NSA site (c was not computed for the NSA site because almost all aerosols are activated at this site). These values for k at SGP and NSA sites are very close to the values originally suggested for continental and marine air (*Twomey and Squires*, 1959).

2.3.2   Calculation of cloud optical depth

In this section, we will derive the formula for the cloud optical depth (τ_c) which can be calculated from N_d and cloud LWP.

The original form of cloud optical depth is (*Seinfeld and Pandis*, 1997)

$$\tau_c = \pi Q_{ext} N_d \int_0^H r_s^2 dh \qquad (2.7)$$

where Q_{ext} is the extinction coefficient, which is assumed to have a value of 2 since the size of the cloud droplets is generally much larger than the mean free path of the water vapor molecules. r_s is the surface mean radius.

Measurements have shown that the liquid water actually increases with the height above cloud base (*Martin et al.*, 1994). So in this calculation, the liquid water content is assumed to increase linearly from the cloud base: $LWC = C_w h$. C_w is a constant. Based on the integration formula $LWP = \int_0^H LWC dh$, C_w can be calculated by

$C_w = \frac{2LWP}{H^2}$, in which H is the cloud geometrical thickness.

The effective radius r_e is related to volume mean radius r_v based on measurements: $r_v^3 = kr_e^3$. Since according to definition, $r_e = r_v^3/r_s^2$, the surface mean radius can be transformed to the volume mean radius: $r_s^2 = k^{1/3}r_v^2$. So we can represent τ_c as a function of r_v:

$$\tau_c = \pi Q_{ext} N_d k^{1/3} \int_0^H r_v^2 dh \tag{2.8}$$

Based on the fact $LWC = \frac{4}{3}\rho_w N_d \pi r_v^3$ and the assumption $LWC = C_w h$, the volume mean radius can be represented as

$$r_v = \left(\frac{3C_w h}{4\rho_w N_d \pi}\right)^{1/3} \tag{2.9}$$

Substitute the r_v value in Equation 2.8 with this formula, we can easily find

$$\tau_c \approx (k\pi N_d)^{1/3} \left(\frac{C_w}{\rho_w}\right)^{2/3} H^{5/3} \tag{2.10}$$

Since $H = \sqrt{\frac{2LWP}{C_w}}$ we finally get

$$\tau_c \approx 1.765 \cdot (k\pi N_d)^{1/3} \rho_w^{-2/3} C_w^{-1/6} LWP^{5/6} \tag{2.11}$$

where ρ_w is the liquid water density. This is the equation we use to calculate cloud optical depth in this study.

Most studies in the literature use k=0.67 for continental air, and k=0.80 for marine air, based on the measurements given in *Martin et al.* (1994). However, k is a constant representing the shape of droplet spectrum, and is mainly related to the relative spectral dispersion (β). *Liu and Daum* (2002) summarized the dispersion of cloud droplet size distribution and the number concentration of cloud droplets. The increase in N_d may cause a broader size distribution because more small particles

are activated. Based on the data in *Liu and Daum* (2002), We fit a formula for k as a function of N_d:

$$k = \left[\left(5.0 \times 10^{-4} \times N_d\right) + 1.18\right]^{-3} \tag{2.12}$$

The original data and the fitting line are shown in Figure 2.9. The unit used for N_d is cm^{-3}.
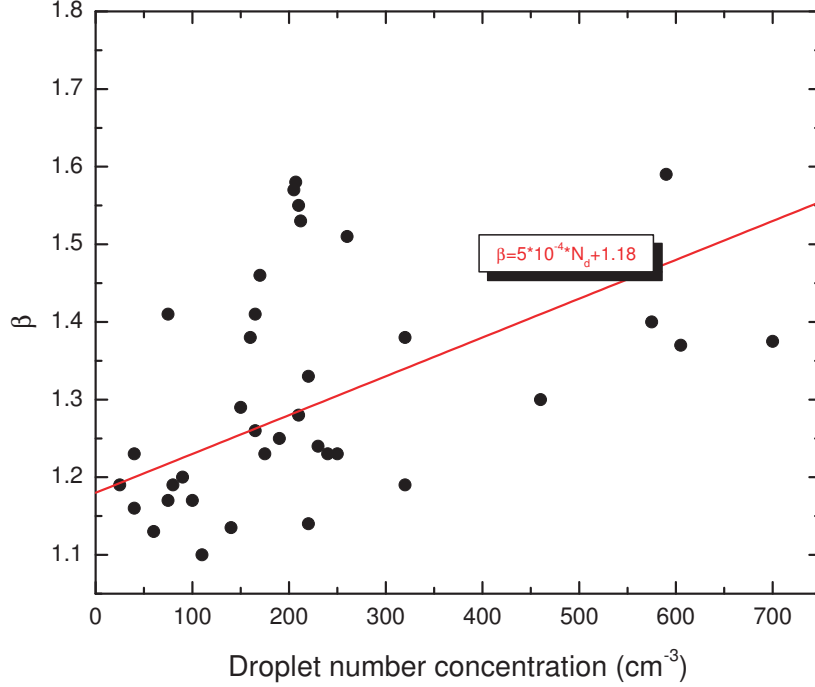
Figure 2.9: The fitting of dispersion coefficient as a function of droplet number concentration. Filled circles are the measured data given by *Liu and Daum* (2002). The solid line shows the regression. β is another form showing the relationship between effective radius and volume mean radius, and $\beta = k^{-1/3}$.

2.3.3 Comparison of cloud optical depth and LWP relationship

Dong et al. (1997) developed a parameterization method to derive cloud optical depth (τ_c) by requiring that a δ-2-stream radiative transfer model match the observed downward broadband shortwave flux by Eppley precision spectral pyranometer (PSP) at the surface, and validated its use by comparison with in situ aircraft data. The

measurement uncertainty of PSP is $\pm 6.0\%$, or 10 Wm^{-2} for global mean downwelling SW radiation (*Stoffel*, 2004). Figure 2.10 shows the relationship between the derived τ_c and the cloud LWP by using this method at both the SGP and NSA sites. In this figure, the LWP is derived from microwave radiometer brightness temperatures at 23.8 and 31.4 GHz using a statistical retrieval method. There is a significant difference in the slope of the relationship between cloud optical depth and LWP at these two sites. If this difference is really due to the difference in aerosol properties in the two sites, we can use the measured aerosol properties and detailed N_d simulation to reproduce these relationships. Below, we show that this difference can be explained by the indirect aerosol effect.

Figure 2.11 shows the $\tau_c \sim LWP$ calculated by using the parcel model. The line in each curve shows the relationship needed to match the observed surface shortwave broadband flux, which are the same as the red lines in Figure 2.10. The points shown by the grey dots at the NSA site have CN number concentration greater than 200 cm^{-3} and used the original single-mode size distribution. Because it is likely that higher CN number concentrations are indicative of the presence of a nucleation mode in the size distribution, we added a small lognormal mode (as used at the SGP site) to the single-mode distribution at the NSA site for these points (with the average ratio between the large and small modes that was found at the SGP site). The adjustment of size distribution to the 2-mode distribution improves the fit between the parcel model results for cloud optical depth and that required to fit the shortwave broadband flux.

Regression formula and statistical properties of the $\tau_c \sim LWP$ at both sites are calculated based on the simulated results. These data are shown in Table 2.2 together with the statistical data from *Dong et al.* (1997).
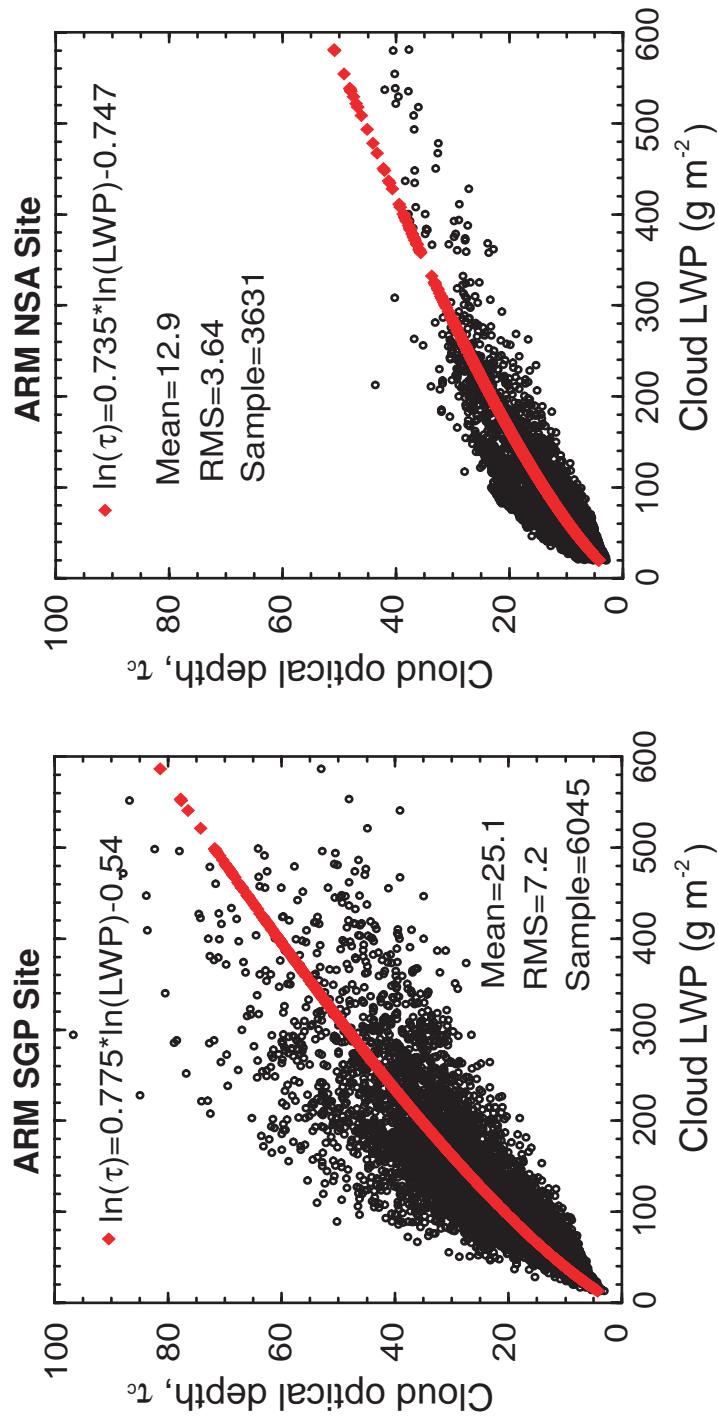
Figure 2.10: Cloud optical depth, as determined from the observed shortwave flux, plotted against LWP. The cloud optical depth was determined by requiring that a δ-2-stream radiative transfer model fit the observed ground level broadband shortwave radiative flux.
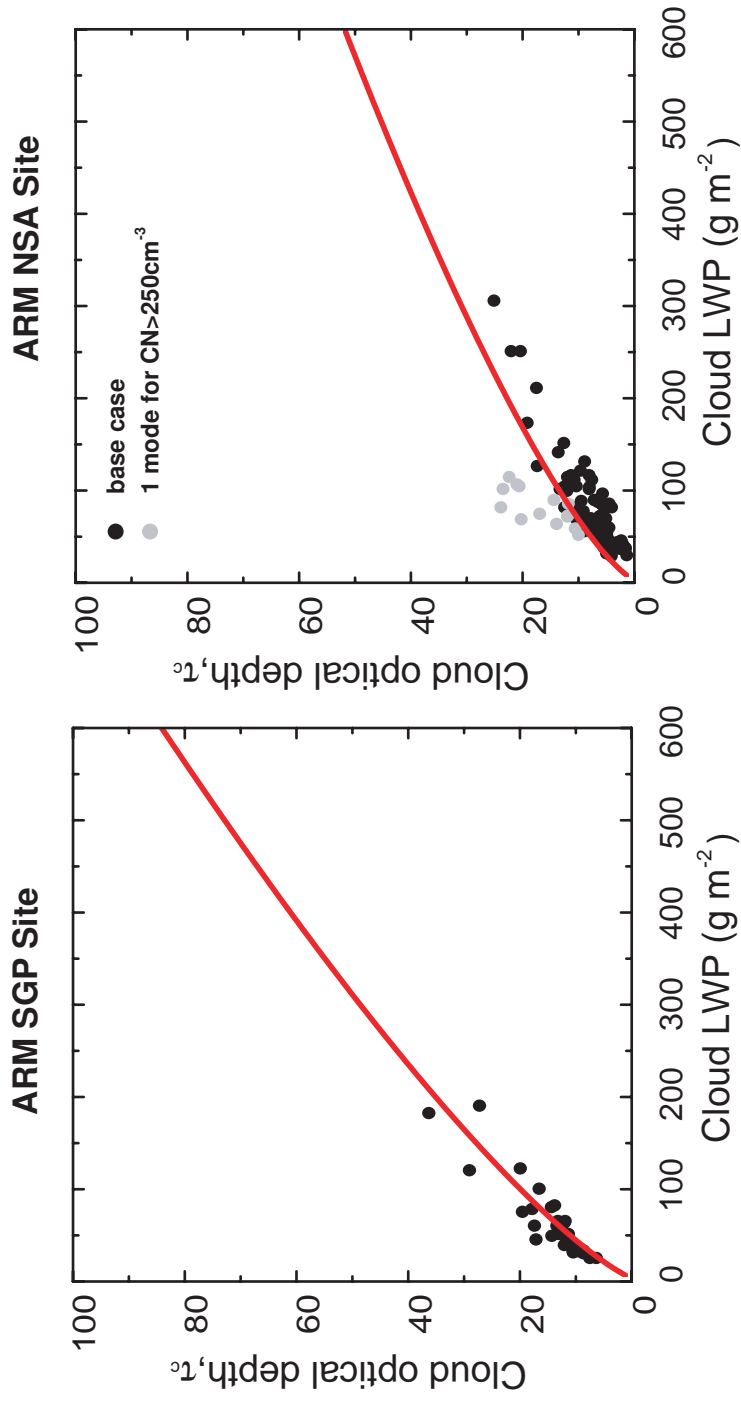
Figure 2.11: Cloud optical depth, as determined from the parcel model, plotted against LWP. Cloud optical depth was determined using the predicted droplet number concentrations from an adiabatic cloud parcel model and the measured aerosol concentrations and composition. In both Figure 2.10 and Figure 2.11, the cloud LWP was that determined from the microwave radiometer measurement.

Our study shows that the cloud optical depth required to fit the surface downward shortwave flux at both the SGP and NSA sites can be explained by the aerosol indirect cloud effect. Two different ways are used to derive the $\tau_c \sim LWP$ relationship, one from the retrieval method by assuring the radiative fluxes match the surface measurements, one from the physically-based numerical calculation by using the measured aerosol properties. The results from both methods show similar difference in the two sites representing different extent of pollution. The use of a parcel model to determine the cloud droplet number concentration enables us to separate the effect of the cloud LWP and cloud droplet number concentration on the cloud optical depth.

Table 2.2: Comparison of statistical properties derived from Figure 2.10 and Figure 2.11. The regression and statistics of c are calculated based on formula $ln(\tau_c) = aln(LWP) - b$.

	Mean cloud optical depth		Number of samples		Root mean square	
	SGP	NSA	SGP	NSA	SGP	NSA
A	25.1	12.9	6045	3631	7.2	3.64
B	18.4	7.4	28	109	5.3	4.1

A: τ_c is obtained by assuring the radiative transfer model fit the observed surface shortwave radiative flux.
B: τ_c is obtained from the parcel model simulation based on surface measurements of aerosols.

The large spread in the derived cloud optical depth from surface radiation measurements shown in Figure 2.11 can result from effects that are not taken into account in the parcel model: entrainment, drizzle formation, and ice formation and splintering. But could any of these processes contribute to a difference in the observed slope between the two sites?

Stratus clouds can entrain dry air though cloud top and propagate through the cloud layer. For example, *Lawson et al.* (2001) determined that only 9 of the 21

cloud slant profiles that were sampled during FIRE ACE were for 'adiabatic' clouds. More entrainment at the NSA site than at the SGP site could cause the slope of the relationship between cloud optical depth and cloud LWP to both decrease or to increase. For example, if we assume that entrainment decreases the LWC at the top of the cloud in the model simulations by 1/2 its adiabatic value (and entrainment is linear with height above an adiabatic cloud base), then the slope of the optical depth-LWP relationship increases from its value of 0.31 in the base case to 0.33 in the case of entrainment. If the LWC and the droplet numbers both decrease by 1/2 at cloud top then the slope is reduced to 0.29. In either case, the model-predicted relationship is still in good agreement with the measured relationship. Some of the scatter in the measured relationship shown in Figure 2.11 may be due to entrainment, but we think the difference between the NSA site and the SGP site can not be explained by more entrainment at one site compared to the other.

Mixed phase clouds were present about half the time in the FIRE ACE measurements reported by *Lawson et al.* (2001) and may also be important in some of the Arctic stratus clouds that we include in our study, but they probably do not affect the downward solar transmission and microwave radiometer-derived cloud LWP very much because compared to water drops large ice crystals lead to more forward scattering that compensates to some extent for the direct solar transmission loss attenuated by the ice particles (*Dong et al.*, 2001). If ice clouds form, they would need to form on an ice nucleus at these high temperatures (rather than forming through a homogeneous freezing mechanism), but the concentrations of ice nuclei are only of order 1 L^{-1} at -10 ℃ (and smaller at higher temperatures) using the *Meyers et al.* (1992) relationship and are even lower using the *Fletcher* (1962) curve. Because the CCN concentrations that we predict are much higher than this (about 55 cm^{-3} on

average with a range from 7 to 180 cm^{-3} at the NSA site), the modeled relationship between cloud optical depth and LWP would fall far below the measured red line in Figure 2.11 of the paper if we had used the Meyers method for predicting the ice concentration. On the other hand, if mechanisms such as the Hallet Mossop effect led to splintering of the ice particles with many more ice particles than drops, then the modeled cloud optical depth could be higher than the average measured relationship. But studies of ice splintering in Arctic clouds show that even when this occurs, the average numbers of ice particles are smaller than the average droplet numbers predicted here (*Rangno and Hobbs*, 2001). Ice particle production and splintering mechanisms no doubt contribute to some of the observed scatter in the relationship at the NSA site shown in Figure 2.11. However, neither the observed LWP nor the observed optical depth is very sensitive to the presence of ice particles (*Dong et al.*, 2001).

N$_d$ is calculated by a cloud nucleation parcel model and drizzle was not included in the model. Precipitation was measured at the surface at the SGP site and it was zero for the cases that we included in the model. The formation of drizzle at the NSA site is evident from the Doppler velocities shown in Figure 2.12. This would have led to larger average droplet sizes (and lower droplet number concentrations and cloud optical depths) than we predicted using the parcel model for a given LWP. So the slope of the $\tau_c \sim LWP$ relationship would have decreased compared to that shown in Figure 2.11. Because cloud optical depth is proportional to the droplet concentration to the 1/3 power, if drizzle had decreased the droplet number associated with the measured LWP by 1/2, the cloud optical depth would have decreased by a factor of 0.8. Presumably, the occurrence of drizzle might also explain some of the scatter in the observed points, though *Dong et al.* (1997) show that the retrieved optical depth

is not very sensitive to drizzle as long as drizzle is less than 25% of the total LWP. The downward measured Doppler velocities at cloud base at the NSA site shown in Figure 2.12 show that there is some drizzle, but they do not show the fraction of LWP associated with drizzle. The drizzle at this site is probably associated with ice particles which do not affect either the microwave radiometer-derived LWP (because ice particles have much smaller absorption coefficients than liquid water droplets (*Liu and Curry*, 1998; *Dong et al.*, 2001)) or the cloud optical depth retrieved from the surface pyronometer data (*Dong et al.*, 1997) as long as the LWP associated with the drizzle is less than 25% of the total LWP. If the drizzle at the NSA site was formed from warm cloud processes, and if it was significant enough to affect the measured cloud optical depth (i.e. if it explains more than 25% of the LWP) for a given LWP, then the warm cloud microphysics model (with drizzle included) could not match the observed cloud optical depth for a given LWP, because the predicted cloud optical depth for a given LWP with the warm microphysics model without drizzle is the maximum cloud optical depth that is possible to predict, given only warm cloud microphysics. Thus, it is unlikely that the measured cloud optical depth is significantly affected by warm rain drizzle.

2.4 Sensitivity tests

The uncertainties in the input data may also contribute to the spread in the plot of relationship between τ_c and LWP. Here we make some sensitivity tests to examine the effect of these uncertainties.

2.4.1 Updraft velocity

The in-situ measured vertical velocities vary from downdrafts to updrafts as large as 1 m^{-1} in clouds of the type we are modeling (*Lawson et al.*, 2001), but we do not

have in-situ velocities available for the time period of our study, so it is not possible to compare the velocities used in our study (which were derived from the MOLTS data) with in situ data. If we assume the MMCR Doppler velocity near cloud base is the same as the cloud updraft velocity and that this is the same as the updraft of the air parcels entering cloud base, we can compare the vertical velocities from the MOLTS model to the remotely sensed MMCR Doppler velocities. Figure 2.12 shows the hourly mean Doppler velocity for each case as well as the maximum values and the minimum values recorded in each hour together with the MOLTS velocity used in the adiabatic model for the cases used in our study. The hourly mean Doppler velocity (plotted as negative if the drops are moving downward) is often less than zero, indicating some drizzle especially at the NSA site. The maximum values of Doppler velocity are greater than zero at the SGP site, so we assumed these were not affected by downdrafts or drizzle and compared the relationship between the cloud optical depth and LWP using the maximum Doppler vertical velocity to that derived from the MOLTS model mean vertical velocity and TKE. It is nearly identical to our base case (see Figure 2.13). At the NSA site, the modeled relationship is not very sensitive to updraft velocity, because almost all of the particles activate and form drops at this site since CN concentrations are so low. For both sites, however, we may conclude that uncertainties in the vertical velocity at cloud base do not change the conclusion that the model-derived relationship is similar to the relationship derived from the surface radiation.

2.4.2 Cloud top height

The uncertainty of MMCR cloud top height at both the SGP and NSA sites is 45 meters. We did the simulation again with the cloud top from measurement
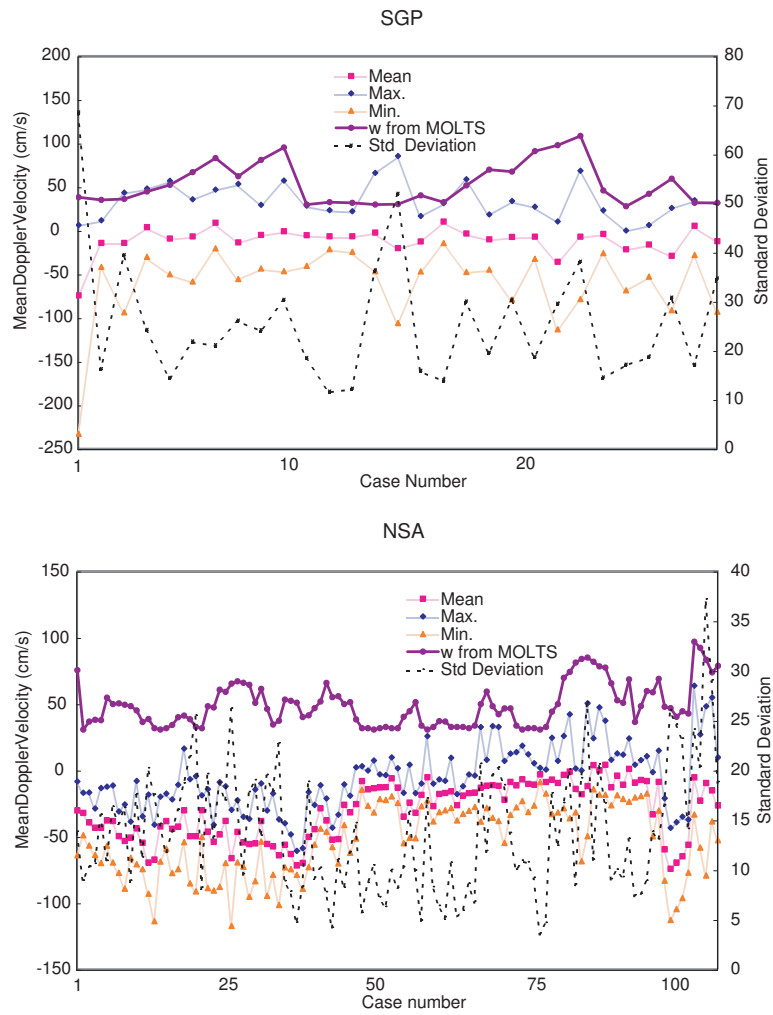
Figure 2.12: Vertical velocity used in the adiabatic model calculation (labeled MOLTS) and that from the hourly mean derived from the 5-minute millimeter Doppler radar measurements, and the maximum and minimum within each hour from the radar data. The standard deviation for the Doppler radar data over each hour is plotted on the right hand scale.
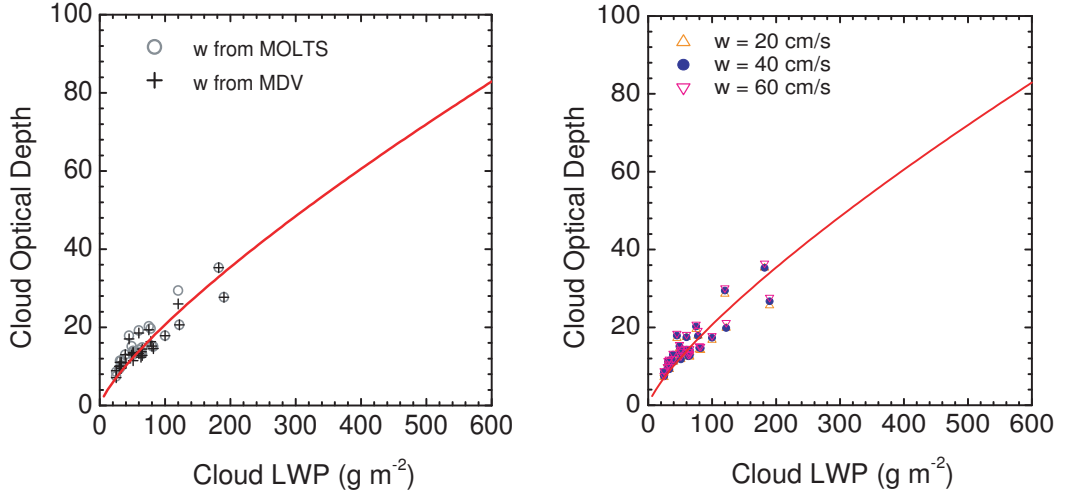
Figure 2.13: Calculated cloud optical depth versus cloud liquid water path using vertical velocity from the model MOLTS data and from the maximum MMCR Doppler velocity (MDV). The relationships by using fixed updraft velocity 20 cm/s, 40 cm/s, and 60 cm/s are also shown in the right. The cloud optical depth obtained at NSA site is not sensitive to the updraft velocity, so only results at SGP site are shown.

plus 45 meters and minus 45 meters. The results shown in Figure 2.14 show that this uncertainty does not significantly alter the modeled relationship between cloud optical depth and LWP.

2.4.3 Aerosol composition

In the base case simulation, we used an averaged aerosol composition based from measurements in all the cloud events. Here we use different aerosol composition for each event, which is used in the chemical transport model GRANTOUR. The results are shown in Figure 2.15. This change does modify the position of each individual point in the plot, but on the whole, the above conclusion still stands.

2.4.4 HNO$_3$ concentration

Typical concentrations of gas phase HNO$_3$ in continental and remote areas were used in the parcel model base case simulation (*Seinfeld and Pandis*, 1997). In this
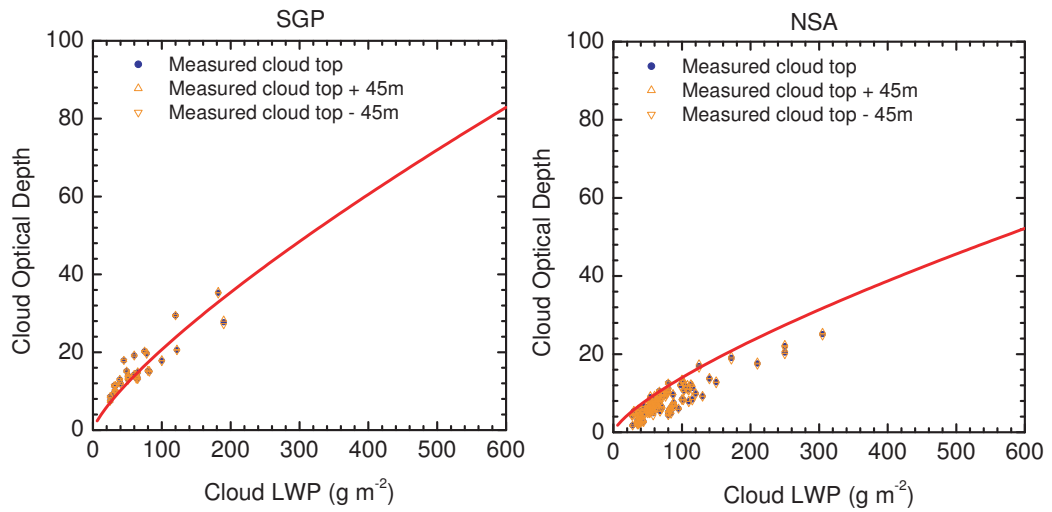
Figure 2.14: Modeled cloud optical depth versus cloud liquid water path determined by varying the cloud that was determined from cloud radar.
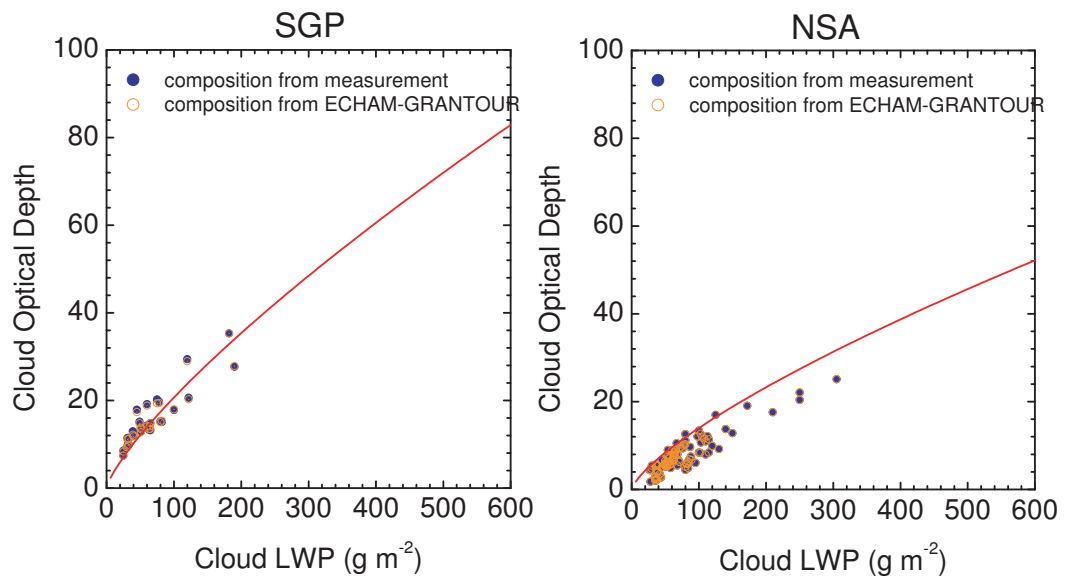
Figure 2.15: Modeled cloud optical depth versus cloud liquid water path determined by using aerosol chemical composition from the ECHAM-GRANTOUR running output.

sensitivity test, we changed the assumed HNO_3 concentration from 1.81 ppbv to 0.1 ppbv at the SGP site, and from 0.01 ppbv to 1.0 ppbv at the NSA site. The results at the SGP site (at the NSA site, almost all aerosol particles are activated even when the HNO_3 concentration is small, so the results are not shown in Figure 2.16) shown in Figure 2.16 suggest the gas phase HNO_3 could be a very important factor for the scattering in the τ_c~LWP relationship in Figure 2.11. However, the contrast between the NSA and SGP sites still exists and the main results do not change.
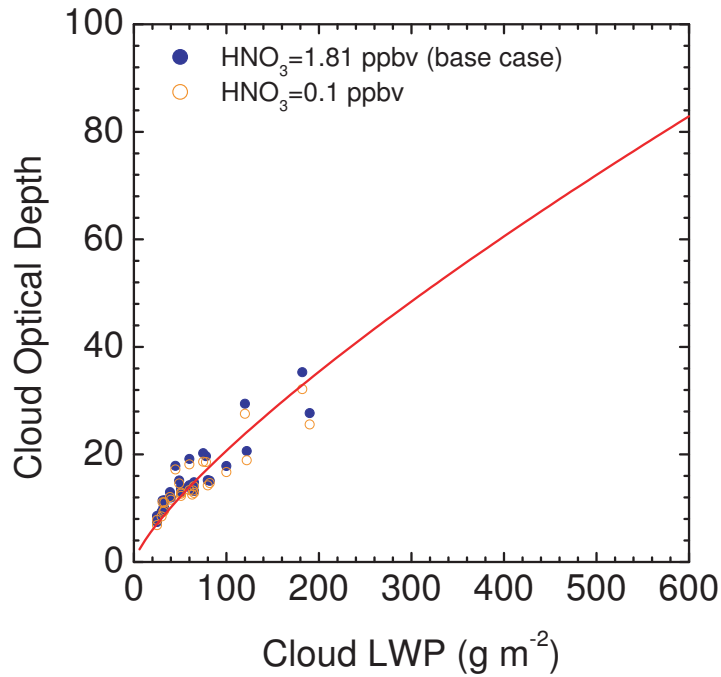
Figure 2.16: Modeled cloud optical depth versus cloud liquid water path determined by using different nitric acid gas concentration in the air parcel model simulation.

2.5   Effect of aerosol on radiative fluxes

2.5.1   TOA outgoing SW flux

The above study is based on the comparison of cloud optical depth from a parcel model and that from the surface radiative flux observation. A most important

demonstration of aerosol indirect effect is the modification of upward SW radiation flux at the top of the atmosphere (TOA). However, an examination of the TOA shortwave flux from the radiative transfer model applied to the two sites does not directly confirm the indirect effect, because the observed surface albedos at the NSA site for our cases (0.6±0.28) are significantly larger than those from the SGP site (0.2±0.02). However, the model can be used to estimate the outgoing flux difference if the clouds from the NSA site had the same average surface albedo and average zenith angle as those from the SGP site. The relationships between this TOA flux and cloud LWP are shown in Figure 2.17. Since the indirect effect is not a strong function of optical depth at very large optical depths, only points with $\tau_c < 25$ are shown.

The comparison of modeled TOA outgoing SW flux at the SGP and NSA site clearly demonstrates the indirect effect. The value of SW flux at LWP=0 is the clear sky TOA outgoing flux. The different rates of the regression line in SGP and NSA show that the different aerosols cause different TOA outgoing SW radiation, as seen in the satellites. In fact, this figure can be used to roughly estimate the quantity of the first aerosol indirect effect. For example, if the anthropogenic aerosol is 32% of the submicron mass (as calculated in the GRANTOUR aerosol model, *Penner et al.* (1994)) and aerosol size distribution is constant, one finds an average forcing for the cases measured at the SGP site (assuming constant LWP) of about 10.2 Wm^{-2}.

2.5.2 Transmittance of the clouds

By using the surface downward radiative fluxes at clear sky situation and cloudy sky situation, we can calculate the transmittance of the clouds based on the radiative transfer model simulations. The cloud transmittance is defined as the surface
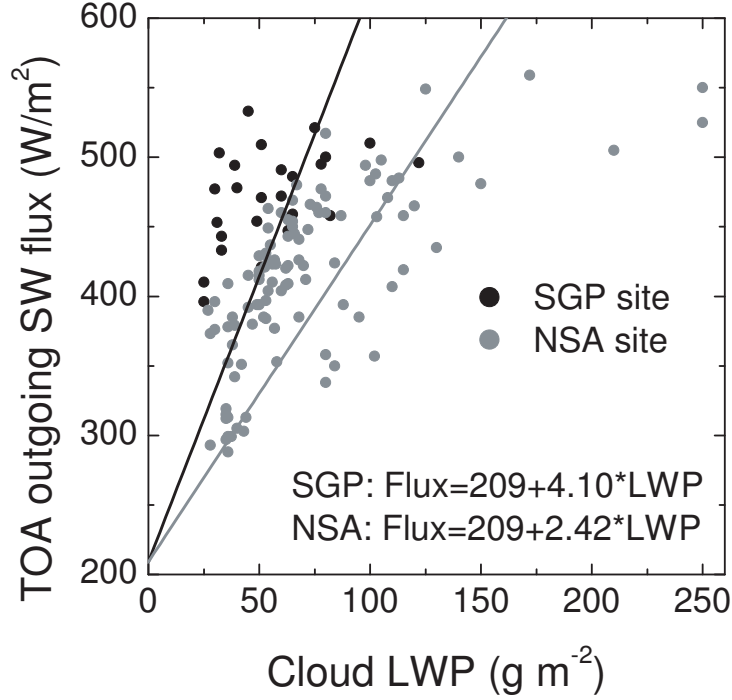
Figure 2.17: Modeled outgoing shortwave radiation at the SGP and NSA sites using the average albedo and zenith angle from the SGP site and the cloud properties from the adiabatic model. Only points with $\tau_c < 25$ are shown.

downward SW flux at cloud sky (CLDF) divided by that at clear sky (CLRF). This calculated transmittance has been compared to the observed values, which is shown in Figure 2.18. Despite the scatter, the good agreement between them confirms that our calculation of radiative transfer is reasonable.

2.6 Discussion and Conclusions

The ARM SGP site and the NSA site provide a unique opportunity to examine the effects of aerosols on cloud optical properties because the aerosol concentrations at each site span the range between polluted and clean conditions. Here, we examined whether the effect of aerosols on clouds can adequately explain the relationship between the liquid water path observed at each site and the cloud optical depth re-
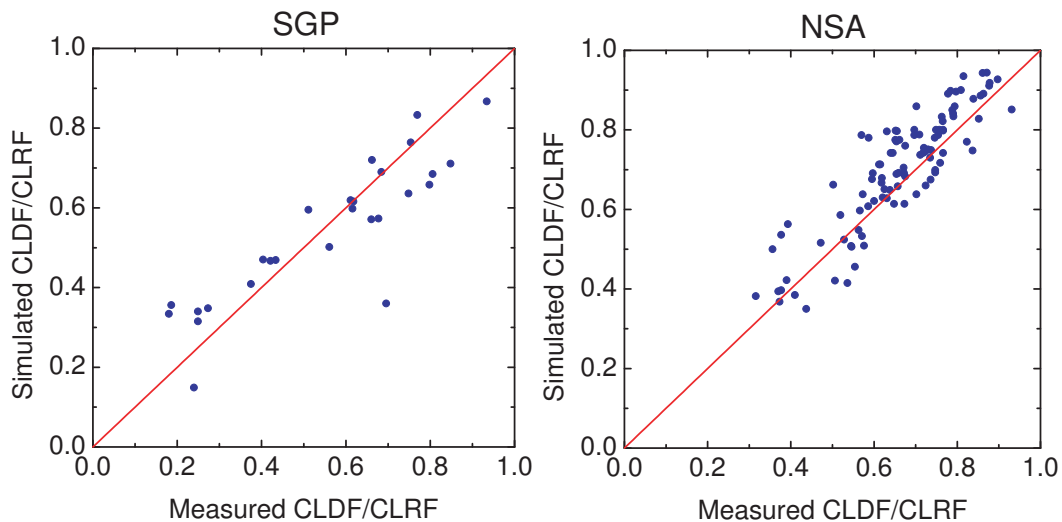
Figure 2.18: The transmittance of clouds calculated from simulation versus from measured surface fluxes.

quired to determine the observed surface flux. Aerosol number concentration at the SGP site was determined from the observed CN number concentration as well as the observed number concentration of particles with radii greater than 0.1 μm. Number concentration at the NSA site was determined from the observed CN concentration. Aerosol composition was taken from the observed composition at the SGP site and the predicted composition from a global aerosol model. Only the predicted composition was available from the NSA site. Cloud droplet number concentration was predicted from an adiabatic parcel model. The cloud optical properties at each site were determined from the predicted droplet number concentration together with the observed cloud liquid water path and the observed cloud base and cloud top.

Our analysis indicates that these sites provide important evidence corroborating the effect of aerosols on cloud optical properties and on shortwave fluxes at both the surface and the top of the atmosphere. We discussed possibilities that could bring the scatter in the model simulation, including the entrainment, the drizzle formation, and the ice formation and splintering. We also made sensitivity tests in

which different values of the updraft velocity, cloud top height, aerosol composition, HNO_3 concentration in the atmosphere are used. The good agreement between the cloud transmittance between the simulations and measurements lent further credence to our model simulations.

This research distinguishes the change of cloud optical depth and radiative fluxes due to the aerosols and due to the LWP. The evidence given in the simulations based on in-situ measurements indicates that the aerosol indirect effect needs to be considered in studies addressing issues of climate change in response to anthropogenic release of greenhouse gases.

Since the cloud droplet radii required to fit the ARM data are those predicted by the initial droplet concentration from the parcel model, these data only provide the first aerosol indirect effect, and do not support or reflect any large second aerosol indirect effect. In addition, this simulation omitted the coagulation of cloud particles and precipitation processes. To make more precise estimation of cloud droplet concentration and size, prognostic simulations of cloud droplets should be used in future studies.

CHAPTER III

Uncertainty analysis for estimates of the first aerosol indirect effect

3.1 Introduction

Although there has been a large amount of progress in the development of the study of aerosol effects on global climate, uncertainty in the estimation of the aerosol indirect forcing remains one of the highest in the climate studies today (*Ramaswamy et al.*, 2001b; *Lohmann and Feichter*, 2005). This is partly due to the high temporal and spatial inhomogeneity in aerosol concentrations and partly due to the complex relationship between the aerosol chemical and physical properties and cloud microphysics.

There are a number of estimates of the global aerosol indirect forcing in the literature (*Kiehl et al.*, 2000; *Lohmann et al.*, 2000; *Ghan et al.*, 2001; *Jones et al.*, 2001; *Iversen et al.*, 2001; *Rotstayn and Penner*, 2001; *Menon et al.*, 2002a; *Kristjansson*, 2002; *Chuang et al.*, 2002). Table 3.1 summarizes the global mean value of indirect forcing published in recent years. In most of these calculations, the prescribed or simulated aerosol field is related to cloud droplet number concentration through empirical or physically-based parameterizations. Many of these models also account for the influence of the change in cloud droplet effective radius on the autoconversion

rate. Although all of the calculations of first aerosol indirect forcing have a negative sign, their values can range from -0.5 to -1.85 Wm^{-2} as summarized in *Penner et al.* (2001a). This is much larger than the uncertainty in green house gas forcing, which is $2.2 \sim 2.7$ Wm^{-2} (*Ramaswamy et al.*, 2001b). An accurate estimation of aerosol effects on climate is important not only to research priorities, but also to constrain estimates of forcing that are consistent with observations of the historical temperature range (*Penner*, 2004).

The IPCC has stressed the importance of producing unbiased estimates of the uncertainty in aerosol indirect forcing, in order to give policy makers as well as research managers an understanding of the most important aspects of climate change that require refinement. However, not much has been done to quantify the uncertainty in the aerosol indirect forcing calculation. The reported range of uncertainty in the IPCC report (*Ramaswamy et al.*, 2001b) and the summary for policy makers (*Houghton et al.*, 2001) has mainly relied on uncertainties associated only with the range of results in literature, and are based on 'expert judgment'. *Penner et al.* (2001a) used a simple box-model and an empirical relationship between sulfate aerosol concentration and droplet concentrations (*Boucher and Lohmann*, 1995) to study the uncertainty in aerosol indirect forcing. Their analysis leads to an overall estimate for indirect forcing from fossil fuel-related aerosols of -1.4 Wm^{-2} with a 67% confidence interval of from 0 to -2.8 Wm^{-2}. However, this uncertainty analysis does not give any spatial information that might guide future research priorities or aircraft missions, nor does it establish separate uncertainty ranges for biomass aerosols and for fossil fuel aerosols.

There are several uncertainty studies in the climate change simulations, which can be used for reference in our study. *Murphy et al.* (2004) provided a systematic

Table 3.1: A summary of global mean aerosol indirect forcing (in Wm^{-2}) estimation in literature during recent years.

Year	Author	Forcing type	Forcing (Wm^{-2})	Species	Parameterization
2000	Kiehl et al.	1st	-0.40 ~ -1.78	Sulfate	Four empirical relations
2000	Lohmann et al.	1st	-1.1 ~-1.5	Sulfate, OC, BC	*Ghan et al. (1993)*
2001	Ghan et al.	1st and 2nd	-1.5 ~ -3.0	Sulfate	*Abdul-Razzak and Ghan (2000)*
2001	Hu et al.	1st	-1.2 ~-1.4	Sulfate	*Boucher and Lohmann (1995)*
2001	Iversen et al.	1st and 2nd	-1.5	Sulfate, BC	CCN lookup table with fixed S
2001	Jones et al.	1st and 2nd	-1.9	Sulfate	*Jones et al. (1994)*
		1st	-1.3		
		2nd	-0.5		
2001	Lohmann and Feichter	1st and 2nd	-1.4	Sulfate, BC	*Chuang and Penner (1995)*
2001	Rostayn and Penner	1st and 2nd	-2.57	Sulfate	*Boucher and Lohmann (1995)*
		1st	-1.46		
		2nd	-1.32		
2001	Williams et al.	1st and 2nd	-1.69	Sulfate	*Jones et al. (1994)*
		1st	-1.37		
		2nd	-0.38		
2002	Chuang et al.	1st	-1.85	Sulfate, OC, BC	*Chuang and Penner (1995)*
2002	Menon et al.	1st and 2nd	-1.55 ~ -4.36	Sulfate, OM	*Leaitch et al. (1996)*
		1st	-1.82		
2002	Lohmann and Lesins	1st and 2nd	-1.4	Sulfate, OC, BC	*Chuang and Penner (1995)*
2002	Kristjansson	1st and 2nd	-1.76	Sulfate, BC	CCN lookup table with fixed S
		1st	-1.3		
		2nd	-0.46		
2003	Peng and Lohmann	1st and 2nd	-1.2 ~-1.4	Sulfate, OC, BC	Modified from *Ghan et al. (1993)*
2003	Rostayn and Liu	1st	-0.90 ~ -1.39	Sulfate	*Boucher and Lohmann (1995)*
2004	Suzuki et al.	1st	-0.54	Sulfate, OC, BC	*Numaguti (1999)*

investigation of modeling uncertainty by varying the settings of GCM parameters whose values cannot be accurately determined from observations. They perturbed these parameters one at a time relative to the standard version of the GCM, creating a perturbed physics ensemble of 53 model versions each used to simulated climate. The likelihood-weighted PDF of climate sensitivity was produced by estimating the Climate Prediction Index (CPI) of the model ensemble. *Stainforth et al.* (2005) used a similar method to study the uncertainty in the estimation of climate sensitivity. They perturbed 6 parameters chosen to affect the representation of clouds and precipitation. Unlike the method by *Murphy et al.* (2004), these parameters were perturbed from their standard values simultaneously.

In the present study, we use 3-D meteorological fields together with a radiative transfer model to examine the spatially-resolved uncertainty in estimates of indirect forcing. The forcing of anthropogenic sulfate and carbonaceous aerosols is calculated, and the effect of natural aerosols species which act as cloud condensation nuclei is included in the simulation. We consider each uncertainty source in the calculation of aerosol indirect forcing, including those that arise from the specified or assumed aerosol properties, the specified aerosol-cloud droplet relationship, and the relation between the cloud droplet effective radius and volume mean radius. We only consider physically-based cloud nucleation parameterizations as opposed to empirically-based parameterizations, since only the former can be applied to all aerosols. Our aim is to determine what aspect of the indirect forcing calculation for the first indirect effect is the most uncertain and in which spatial regions the uncertainty is largest. The method of calculation and the sources of uncertainty are discussed in section 3.2. The results, including the calculated cloud effective radius and the forcing uncertainty, are presented in section 3.3. Section 3.4 presents a discussion and our conclusions.

3.2 Methodology

3.2.1 Experimental design

In this study, we use the model-averaged monthly mean aerosol mass concentrations developed from the IPCC aerosol model inter-comparison (*Penner et al.*, 2001a; *Zhang*, 2003). In addition to sulfate aerosols, we also include sea salt, dust, organic carbon (OC), and black carbon (BC). The aerosols are assumed to be internally mixed. The mass concentrations are converted to number concentration by an assumed log-normal size distribution. We vary the mean radius and standard deviation to consider the uncertainty related to this assumption. These number concentrations are used to calculate the cloud droplet number concentration using different cloud nucleation parameterizations. In addition, different options for specifying the in-cloud updraft velocity are used.

The effective radius of the cloud droplet is related to cloud droplet number concentration by $r_e = \beta r_v = \beta \left(\frac{3LWC}{4\pi \rho_w N_d} \right)^{\frac{1}{3}}$, where β is a coefficient which relates the cloud droplet effective radius (r_e) to the mean volume radius (r_v) (*Martin et al.*, 1994). This 3-D effective radius field is input to a radiative transfer model for the radiative calculation. The radiation transfer model is based on the shortwave radiative code developed by *Grant et al.* (1999). For warm clouds, the optical depth, single scattering albedo, and asymmetry factor are parameterized as a function of cloud effective radius. The ice cloud effective radius is assumed to be fixed at 40 μm. The cloud overlap scheme used is a maximum-random overlap scheme, i.e., continuous cloud layers are assumed to be maximally overlapped, while discontinuous cloud layers are randomly overlapped (*Feng et al.*, 2004; *Geleyn and Hollingsworth*, 1979). The meteorological data are the 2000 GEOS-3 data from NASA Data Assimilation Office (DAO).

To calculate the radiative forcing with anthropogenic aerosols, two sets of radiative calculations are made, one with pre-industrial (PI) aerosols and one with present day (PD) aerosols. The difference in the TOA net incoming flux between these two scenarios is the anthropogenic aerosol indirect forcing. In the radiative calculation, the aerosol concentrations and distributions are assumed at their present day values while allowing the present day and pre-industrial aerosols to only affect the calculation of the cloud droplet number concentration, to make sure that the direct aerosol radiative scattering/absorption is the same in the PI and PD. In this study, the cloud microphysics is calculated once every six hours, and the radiative flux is calculated once per hour. Since the meteorological fields are from an offline calculation, we only consider the first indirect effect. However, we include the change in the cloud single scattering albedo caused by treating the in-cloud presence of absorbing aerosols in one perturbation case.

3.2.2 Sources of uncertainty

A flowchart of the parameters needed to calculate the indirect aerosol forcing and the sources of uncertainties is presented in Figure 3.1. The sources of uncertainty include the aerosol and aerosol precursor emissions, the aerosol mass concentrations for a given source inventory calculated from a chemical transport model, the aerosol size distribution, the cloud nucleation parameterization, the method of determining the in-cloud updraft velocity, the relationship between effective radius and volume mean radius, the cloud liquid water content, the cloud fraction, and the change of cloud radiative properties associated with the presence of BC. In this study, we perturb each of these parameters and calculate the difference in the aerosol indirect forcing associated with each perturbation. For some parameters, the uncertainty in

the radiative forcing is calculated by simulating both the maximum and minimum cases. For other parameters, we only consider different options for treating the indirect effect. In the following, we give an introduction to the different sources of uncertainties.
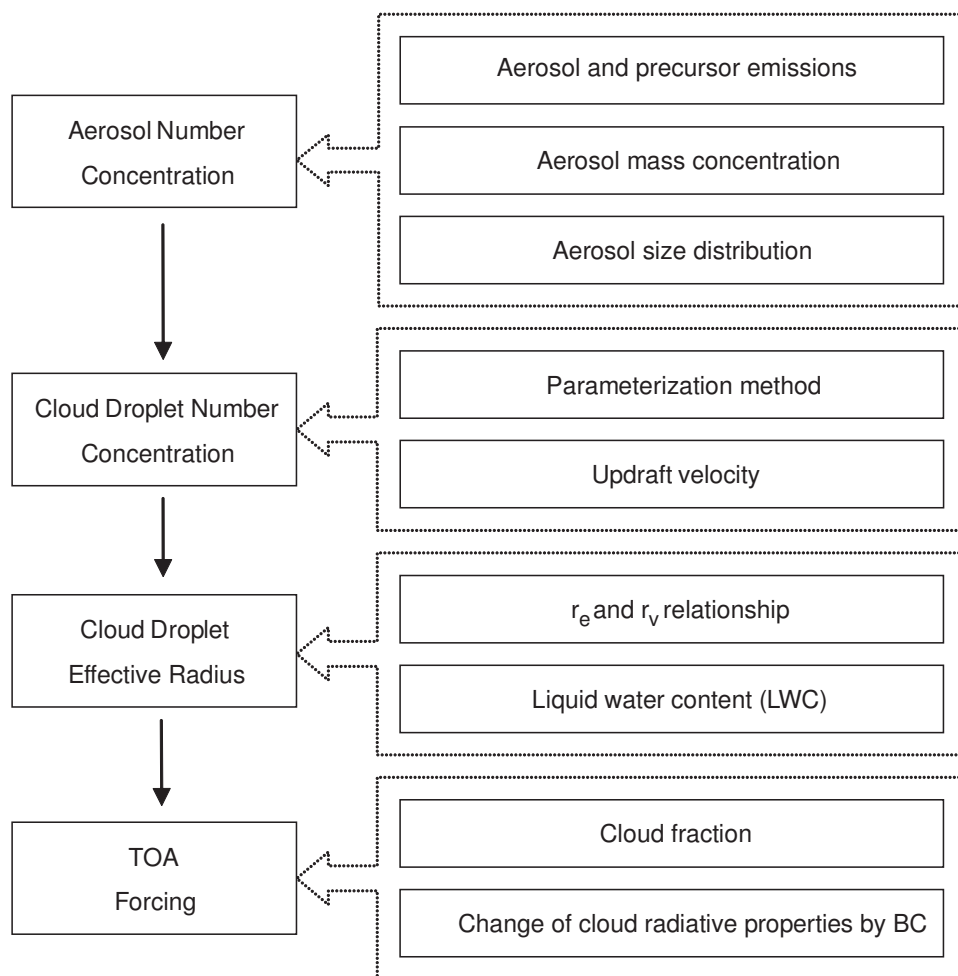
Figure 3.1: List of sources in the calculation of aerosol indirect forcing. The left part shows the main parameters in the aerosol effects on clouds and climate. The right part shows the sources of uncertainty.

The IPCC aerosol inter-comparison project which is used to estimate the uncertainty associated with the aerosol mass concentration (see next paragraph) is based on a fixed set of aerosol and aerosol precursor emissions. However, there are uncertainties related to the emission of the aerosols and their precursors. Here we adopt

the low and high values of the anthropogenic emissions from Table 5.2 and 5.3 in *Penner et al.* (2001a) (which reflect estimates reported in the literature) as a measure of the 1σ limit of the emissions uncertainty. Because the aerosol concentrations were almost linearly related to their emissions in the models used in the IPCC inter-comparison, we scaled the aerosol mass concentrations by the ratio of the maximum or minimum emissions to the mean emissions. The calculated forcing based on the aerosol mass after scaling and before scaling is used to estimate the variance due to the emissions of aerosols and aerosol precursors.

The estimate of the mean, maximum, and minimum global aerosol mass concentrations was based on the IPCC Aerosol Model Inter-comparison (*Penner et al.*, 2001a; *Zhang*, 2003). Eleven aerosol chemical transport models participated in this inter-comparison. These models from different contributors include GISS, GSFC, Hadley Center GCM, KNMI/TM3, LLNL/Umich CCM1/GRANTOUR, MPI/Dalhousie ECHAM, NCAR/Mozart, PNNL, UKMO/STOCHEM, ULAQ, and Umich version ECHAM/GRANTOUR (*Zhang*, 2003). The output aerosol species from these models included natural sulfate (nSO_4), anthropogenic sulfate (aSO_4), natural and anthropogenic organic carbon (OC), anthropogenic black carbon (BC), dust and sea salt. Natural BC was not specified in the IPCC Aerosol Inter-comparison but was estimated here from the anthropogenic BC and a monthly averaged scaling factor, which was derived from the GMI model aerosol simulations (*Liu and Penner*, 2005). In this study, the monthly mean aerosol concentrations approximately represented the year 2000. For the pre-industrial case, the total aerosol mass is the sum of natural sulfate, natural organic aerosols (POM), dust and sea salt. For present day case, the total aerosol mass concentration is the sum of all aerosols. To be consistent with the aerosol size used later, only sub-micron dust and sea salt are considered.

The reference case is calculated using the model-average aerosol mass concentration from those models whose concentrations were in reasonable agreement with observations (*Penner et al.*, 2001a). To calculate the uncertainty associated with the aerosol mass concentrations from different chemical transport models, the maximum and minimum aerosol concentrations from these models were used in the perturbation case.

To provide a uniform platform for different cloud nucleation parameterizations, a single mode log-normal size distribution for the aerosol was assumed. The reference mode radius and geometric standard deviation of both continental and marine aerosols were taken from the central values determined from a literature search (*Penner et al.*, 2001a). The uncertainties in the mode radius and geometric standard deviation are considered in the calculation of forcing uncertainty. These uncertainties are also based on the ranges of values in the literature as summarized in *Penner et al.* (2001a). The mode radius and 1σ ranges were 0.05 ± 0.04 μm (over land) and 0.095 ± 0.015 μm (over ocean). The geometric standard deviation ranges were 1.9 ± 0.3 (over land) and 1.5 ± 0.15 (over ocean). Since the effect of size distribution on the forcing is non-linear, we used both the maximum and minimum values of the mode radius and standard deviation in our tests. Except for one case (see below), the same values were used in our uncertainty analysis for both the present day and pre-industrial aerosols.

The above measurements actually summarize the size distribution of the present day aerosol. But there are large uncertainties associated with the size of the pre-industrial aerosols. The anthropogenic aerosol may form by condensation onto pre-existing aerosols, and therefore, would not change the aerosol number but would increase the aerosol size (*Chuang et al.*, 1997). If this assumption is correct, a

different choice with a smaller pre-industrial aerosol should be used to examine the uncertainty of the indirect forcing. For this case we assumed that the mean size and standard deviation of free troposphere aerosol (r=0.036 μm, σ_g=2.2) from *Penner et al.* (2001a) were the appropriate size distribution parameters of the pre-industrial continental aerosol.

Currently, there are two categories of approaches to relate the aerosol properties (concentration, size and composition) to the cloud microphysical properties (number concentration and effective radius). Some researchers used an empirical relationship between cloud droplet number and aerosol mass concentration (*Boucher and Lohmann*, 1995; *Roelofs et al.*, 1998; *Lohmann and Feichter*, 1997), or number concentration (*Jones et al.*, 1994; *Menon et al.*, 2002a; *Suzuki et al.*, 2004). These methods are based on observations and are easy to use in global forcing calculations, but they do not reflect the physical and chemical processes that occur during cloud nucleation, which depend on the size, chemical composition of the aerosol, as well as the updraft velocity. In addition, they are based on measurements at particular places and times, and so may be biased if they are used a global calculation or used to project future scenarios. Therefore in this study, only cloud nucleation parameterizations based on a mechanistic parameterization of nucleation are used. Three mechanistic parameterizations have been used to calculate the cloud droplet number concentration: *Chuang et al.* (1997) (hereafter CP); *Abdul-Razzak and Ghan* (2002) (hereafter AG3); and *Nenes and Seinfeld* (2003) (hereafter NS). The relationship between cloud droplet number and aerosol number from these different parameterizations has been tested and compared to detailed parcel model simulation results (See Figure 3.2). Based on the results, the AG3 parameterization is closest to the results of parcel model. So in this study, we chose the AG3 parameterization as

the method used in the reference case. And we examined the results from the other parameterizations in the perturbation cases.
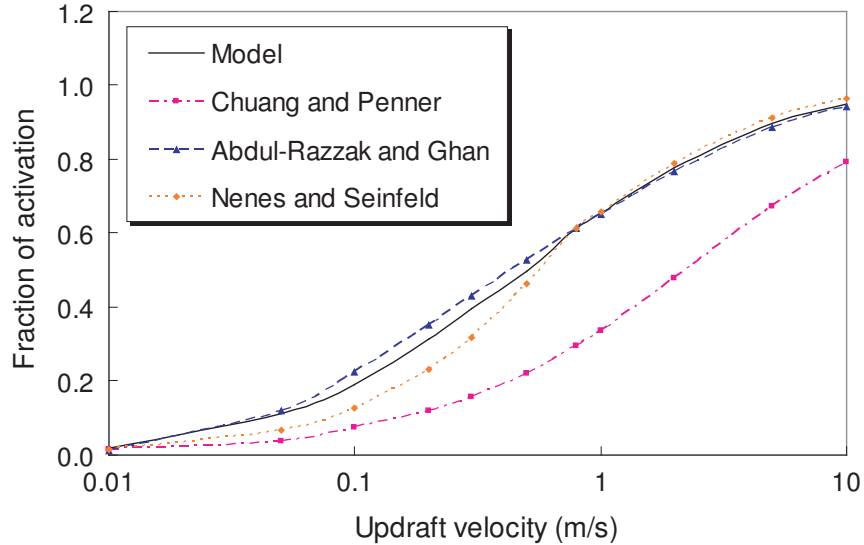
Figure 3.2: Comparison of N_d from the three parameterizations and the cloud nucleation parcel model. The fraction of activated aerosols (N_d/N_a) calculated from three mechanistic parameterizations has been compared to that from a size-resolved cloud nucleation parcel model (*Liu and Seidl*, 1998). In the comparison, the total aerosol number concentration is set to be 1000 cm^{-3}. The size distribution is assumed to be a single log-normal distribution with a mode radius of 0.05 μm and a standard deviation of 2. The aerosols are pure ammonium sulfate.

The large scale vertical velocity in a General Circulation Model (GCM) does not resolve sub-grid variations and it is these variations that determine cloud droplet nucleation (*Feingold and Heymsfield*, 1992). To estimate the in-cloud updraft velocity, two approaches are used. The first approach (hereafter PDF) uses a normal probability distribution with the GCM-predicted vertical velocity as the mean value and a prescribed standard deviation (*Chuang et al.*, 2002). *Chuang et al.* (1997) used a value of 50 cm/s for the standard deviation of the updraft for warm clouds based on measured updrafts in stratiform clouds (*Paluch and Lenschow*, 1992) and argued

that the sensitivity of indirect forcing to this value is small. Another method that has been used to estimate the amount of sub-grid variation of the updraft velocity is to use the GCM model-generated turbulent kinetic energy (TKE). By assuming that the sub-grid vertical velocity variability is dominated by the turbulent transports and by choosing the root-mean-square value of TKE as a measure of this, the in-cloud updraft velocity could be expressed as $w = \overline{w} + 0.7\sqrt{TKE}$, where $\overline{w}$ is the GCM-resolved large scale updraft velocity (*Lohmann et al.*, 1999a,b). Using a single updraft velocity for the entire grid cell is a simplification, since the updraft velocity varies over the grid cell (*Lohmann et al.*, 1999a). In this study, we use the PDF approach in the reference case and the TKE approach in the perturbation case.

As stated above, the effective radius is related to the volume mean radius (r_v) by the coefficient β. According to Martin et al. [1994], the value of β^{-3} is 0.67 ± 0.07 and 0.80 ± 0.07 over the land and ocean, respectively. In the reference case, a fixed coefficient β for equal to 1.12 over both land and ocean is used to account for the relationship between the effective radius and the volume mean radius. However, alterations in the linear relationship between r_e and r_v are expected in the presence of entrainment, precipitation, and ice particles (*Andronache et al.*, 1999). Recently, *Liu and Daum* (2002) showed that the dispersion of the cloud droplet spectrum is related to the cloud droplet number concentration. They argued that the effect of dispersion on the reflected radiation may substantially negate the effect due to increasing cloud droplet concentration. Based on their results, *Penner et al.* (2004) presented a parameterization of this coefficient as a function of cloud droplet number concentration: $\beta = 5.0 \times 10^{-4} \times N_d + 1.18$. Therefore we considered this option for expressing β in a perturbation case to examine the uncertainty associated with the calculation of r_e. *Rotstayn and Liu* (2003) examined three different relationships

between β and N_d, and estimated the sensitivity of the first aerosol indirect effect to these different expressions of dispersion term. In this study, we also examined the sensitivity of the indirect effect to the use of the relationships given in *Rotstayn and Liu* (2003).

If the droplet number concentration is fixed, the effective radius of cloud droplets is directly linked to the cloud liquid water content. Liquid water path (LWP) is the vertical integral of the cloud liquid water content (LWC). In the reference case, we used a parameterization that relates the LWP (*Hack*, 1998) and the cloud fraction (CF) (*Sundqvist et al.*, 1989) to the RH values from the DAO meteorological fields. To study the effect of LWP uncertainty, we compared the global mean LWP from the parameterization to different LWPs retrieved from satellites, including those from ISCCP, MODIS, SSM/I (see Table 3.2). Note there were two retrieval method and corresponding data for SSM/I satellite. Clearly there are large differences of CF and LWP values from the parameterization and from the satellite retrieval. There is large gap even between the measurement data from different satellite and from different retrieval methods. Based on these results, we scaled the 3-D LWC by the ratio of the maximum LWP value of the measurements and the model-generated LWP from the parameterization. We also calculated the ratio from the minimum satellite-measured values. These LWC fields after scaling were used to calculate the forcing uncertainty due to LWP uncertainty. In these two cases, we assumed the LWP difference is due only to the in-cloud LWC difference, i.e., we assumed the cloud fraction was the same as in the reference case.

The cloud fraction directly affects the solar radiation reaching the surface. As in the LWP uncertainty study, we compared the CF fraction from the parameterization to the cloud fraction retrieved from satellites and calculated the maximum and

72

Table 3.2: Comparison of annual average Cloud Liquid Water Path (LWP) (gm^{-2}) used in reference case from the parameterization and satellite measurements. MODIS data are for the year 2000. Other data are for the year 1997. The scale factors are calculated by dividing the value from satellite measurements by the value used in reference case.

	DAO all	ISCCP all	DAO warm	MODIS warm	DAO warm, ocean	SSM/I,weng warm, ocean	SSM/I,green warm, ocean
Jan	64.303	78.757	50.574	88.365	59.688	48.724	76.258
Feb	64.803	73.834	51.324	89.164	61.207	48.265	78.53
Mar	64.951	66.151	51.183	94.070	59.920	48.294	81.288
Apr	64.706	71.501	50.935	96.078	59.389	48.312	80.054
May	65.080	73.610	52.312	107.511	60.577	48.251	80.443
Jun	65.658	72.313	53.659	113.284	62.478	49.844	84.111
Jul	63.714	70.759	52.351	92.825	60.174	49.994	83.011
Aug	62.055	68.341	50.697	93.327	58.531	49.490	81.257
Sep	63.930	67.389	51.875	93.429	59.972	48.888	79.143
Oct	64.854	73.256	51.749	92.867	59.723	49.240	78.262
Nov	63.767	80.434	50.285	91.464	58.272	48.939	78.375
Dec	61.936	78.506	48.860	90.903	56.730	48.778	73.763
Annual mean	64.146	72.904	51.317	95.274	59.722	48.918	79.541
Scale factor		1.136		1.856		0.819	1.331

minimum ratio of CF to the parameterized value (see Table 3.3). Since the CF from parameterization is larger than the values from all satellites, only the CF parameterization scaled by the minimum ratio is used in the perturbation case. We also note that our radiative transfer scheme uses the maximum random overlap method described in *Feng et al.* (2004).

Light-absorbing aerosols such as black carbon (BC) can be activated as cloud droplets and their presence in cloud may reduce the single scattering albedo of cloud and change the radiation balance of the atmosphere. Most studies of indirect forcing assume that all of the BC aerosols are present as interstitial aerosols and this is also assumed in our reference case. In this study, we examined a perturbation case in which the effect of BC on the cloud optical properties in the present day scenario was considered. The modification of cloud droplet single scattering albedo was based on the parameterization developed by *Chuang et al.* (2002). Compared to reference case, only the modification of cloud single scattering albedo is considered, and the BC used to calculate aerosol scattering/absorption and cloud nucleation is the same as in the reference case.

3.2.3   Calculation of uncertainty

Table 3.4 summarizes the perturbation cases considered in this study. In the central or reference case, most of the variable parameters are set to the mean values, although for some parameters, we arbitrarily select one option to use in reference case: for in-cloud updraft velocity we select the PDF method; for the cloud nucleation parameterization, we select the AG3 method (which is closest to the parcel model simulation); for BC effect on cloud single scattering albedo, we assume it is not included in the reference case. In all the perturbation cases, only one parameter is

Table 3.3: Comparison of annual average Cloud Fraction (CF) used in reference case from the parameterization and satellite measurements. MODIS data are for the year 2000. Other data are for the year 1997. The scale factors are calculated by dividing the value used in reference case by the value from satellite measurements.

	DAO all	ISCCP all	MODIS all	SSM/I all	DAO low	ISCCP low	DAO warm	MODIS warm
Jan	0.852	0.672	0.630	0.467	0.570	0.271	0.565	0.535
Feb	0.845	0.663	0.641	0.475	0.568	0.261	0.564	0.534
Mar	0.851	0.660	0.614	0.460	0.570	0.258	0.571	0.514
Apr	0.860	0.659	0.595	0.454	0.566	0.259	0.581	0.503
May	0.874	0.657	0.582	0.466	0.577	0.269	0.599	0.502
Jun	0.869	0.647	0.579	0.477	0.585	0.268	0.612	0.495
Jul	0.862	0.648	0.607	0.500	0.580	0.278	0.603	0.522
Aug	0.858	0.647	0.612	0.487	0.565	0.283	0.587	0.516
Sep	0.859	0.645	0.611	0.470	0.573	0.273	0.590	0.516
Oct	0.864	0.664	0.632	0.478	0.580	0.273	0.586	0.524
Nov	0.867	0.657	0.628	0.458	0.570	0.261	0.577	0.523
Dec	0.857	0.673	0.635	0.462	0.562	0.269	0.564	0.533
Annual mean	0.86	0.658	0.614	0.471	0.572	0.269	0.583	0.518
Scale factor		0.765	0.713	0.548		0.470		0.888

changed, in order to calculate the uncertainty in the indirect forcing associated with each parameter.

3.3 Analysis of the uncertainty associated to different sources

3.3.1 Cloud droplet number and effective radius

Figure 3.3 shows the zonal mean annual average cloud droplet number concentration (N_d) from the PD scenario in the reference case. There are two regions with large values for N_d. The region in the northern hemisphere mid-latitudes is due to high aerosol and precursor emissions from industrialized regions, while the high concentration in the 50-60 degree region in the southern hemisphere is mainly due to high sea salt concentrations. N_d has its largest values below 900mb, and these decrease with an increase in altitude. In the layers in which low cloud occurs most frequently (800mb - 950mb), the zonal average N_d is between 50 and 250 cm^{-3}.
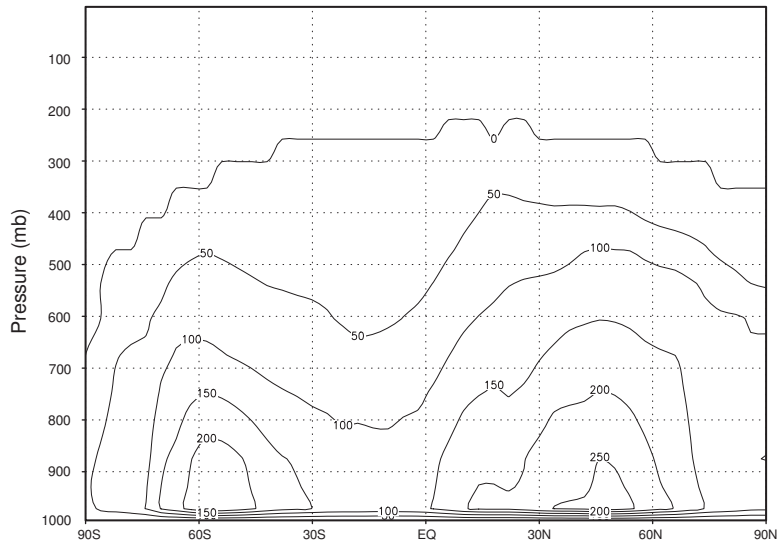
Figure 3.3: Zonal mean annual average cloud droplet number concentration (N_d) in the PD in the reference case. The unit for N_d is cm^{-3}.

Han et al. (1994) reported retrieved r_e for liquid-water clouds from ISCCP satellite data. MODIS satellite data have also been used to retrieve the cloud effective

Table 3.4: Name and description of the reference case and perturbation cases simulated in this study. In the perturbation cases, only parameters different from the reference case are listed.

Name	Description
REFERENCE	Aerosol and precursor emissions: the average emissions used in the 2001 IPCC model inter-comparison
	Aerosol mode radius: 0.05μm over land, 0.095μm over ocean
	Aerosol standard deviation: 1.9 over land, 1.5 over ocean
	Aerosol mass concentration: mean values from IPCC model inter-comparison
	In-cloud updraft velocity: Probability Distribution Function method
	Cloud nucleation parameterization: AG3 method
	BC effects on cloud single scattering albedo: Not included
	LWP: from parameterization based on DAO RH data
	CF: from parameterization based on DAO RH data
	Dispersion coefficient β: fixed single value = 1.12
MAX_EMI	Aerosol precursor emission: scaled to maximum emission
MIN_EMI	Aerosol precursor emission: scaled to minimum emission
MAX_R	Aerosol mode radius: 0.09μm over land, 0.11μm over ocean
MIN_R	Aerosol mode radius: 0.01μm over land, 0.08μm over ocean
MAX_SG	Aerosol standard deviation: 2.2 over land, 1.65 over ocean
MIN_SG	Aerosol standard deviation: 1.6 over land, 1.35 over ocean
DIST_PI	Natural aerosol size distribution: use the free troposphere aerosol size distribution
MAX_MA	Aerosol mass concentration: maximum values from the IPCC model inter-comparison
MIN_MA	Aerosol mass concentration: minimum values from the IPCC model inter-comparison
W_TKE	In-cloud updraft velocity: $\bar{w} + 0.7\sqrt{TKE}$
PARA_NS	Cloud nucleation parameterization: Nenes and Seinfeld method
PARA_CP	Cloud nucleation parameterization: Chuang and Penner method
BC_INC	BC effects on cloud single scattering albedo: Included
MAX_LWP	LWP: scale the parameterized LWP to maximum based on satellite measurements
MIN_LWP	LWP: scale the parameterized LWP to minimum based on satellite measurements
MIN_CF	CF: scale the parameterized CF to the minimum based on satellite measurements
β_FND	Dispersion coefficient β: the function of cloud droplet number (N_d) specified in Penner et al. (2004).
β_RLlow	Relationship between β and N_d: the LOWER simulation by Rotstayn and Liu (2003)
β_RLup	Relationship between β and N_d: the UPPER simulation by Rotstayn and Liu (2003)
β_RLmid	Relationship between β and N_d: the MIDDLE simulation by Rotstayn and Liu (2003)

radius (*King et al.*, 1997). We compare these data with the r_e from our simulations in Table 3.5. The simulated r_e does capture the spatial variations seen in the satellite data. The r_e over the SH oceans is 0.7 μm larger than that over the NH oceans, compared to 0.6 μm from ISCCP. The simulations also show a clear land-sea contrast, although the value of this difference is smaller than that derived from ISCCP and from MODIS. The simulated global mean r_e is also smaller than the retrieved data, which may be due to our reference case parameterization of the in-cloud liquid water content. This underestimate of r_e is also common to many present GCMs (*Quaas et al.*, 2004). In addition, the measured r_e refers only to the cloud-top value of r_e, whereas the model results in Table 3.5 refer to the LWC-weighted value of r_e above temperature zero. This can partially explain why the modeled effective radius is smaller than retrieved value.We also note that satellite determination of r_e is probably no more accurate than a few micrometers (*Han et al.*, 1994).

Figure 3.4a and 3.4b show the total anthropogenic and natural aerosol burden while Figure 3.4c shows the simulated change in the cloud droplet number concentration at 875mb between the PD scenario and the PI scenario. The global distribution of the aerosol indirect forcing resulting from these changes is presented in Figure 3.4d. These plots show similarities in their spatial distribution, and demonstrate a clear relationship between anthropogenic emissions and their effects on cloud droplet concentrations and radiative forcing. The largest anthropogenic aerosol and droplet concentration changes are located in Europe, East Asia, North America, the African savanna, and the South America rainforest region. The former three are mainly related to aerosol emissions from fossil fuel use, and the latter two are related to carbonaceous aerosol emissions from biomass burning. Note that the marine regions near these regions also have a large forcing, which is related to the small value of

Table 3.5: Cloud droplet effective radius from model simulation and from satellite measurements: ISCCP (*Han et al.*, 1994) and MODIS (*King et al.*, 1997).

	NH land	SH land	NH ocean	SH ocean
REFERENCE	5.12	6.00	6.68	7.50
MAX_EMI	4.97	5.81	6.56	7.42
MIN_EMI	5.24	6.10	6.76	7.55
MAX_R	6.84	8.61	7.49	8.52
MIN_R	14.31	8.71	5.96	6.56
MAX_SG	6.25	7.66	7.56	8.53
MIN_SG	5.00	5.14	6.01	6.71
DIST_PI	5.12	6.00	6.68	7.50
MAX_MA	4.53	5.04	5.40	5.92
MIN_MA	7.03	8.77	10.65	12.00
W_TKE	4.71	5.19	5.45	5.88
PARA_NS	5.32	6.05	6.78	7.56
PARA_CP	5.58	6.78	7.92	9.09
BC_INC	5.12	6.00	6.68	7.50
MAX_LWP	6.30	7.38	8.21	9.22
MIN_LWP	4.79	5.61	6.25	7.02
MIN_CF	5.12	6.00	6.68	7.50
β_FND	5.88	6.70	7.42	8.23
β_RLlow	5.34	6.11	6.77	7.52
β_RLup	6.86	7.62	8.28	9.00
β_RLmid	5.99	6.67	7.33	8.02
ISCCP	8.2	9	11.6	12
MODIS	7.2	8.3	10.9	10.5

the pre-industrial aerosol concentration in these areas (Figure 3.4b) and the small surface albedo over the ocean. The global mean value for the first indirect effect in the reference case is -1.30 Wm^{-2} which is within the range reported in literature, summarized by *Suzuki et al.* (2004) (i.e., -0.5 to -1.6 Wm^{-2}).

The change in the aerosol concentrations between the PD and PI cases causes a change in the cloud droplet number concentration. However, due to the spatial distribution of natural and anthropogenic aerosols, the change in the droplet concentration also varies with region. Figure 3.5a shows the change in the LWC-weighted in-cloud droplet concentrations over the SH ocean, SH land, NH ocean and NH land for different perturbation cases. A general characteristic is that the change of N_d over land is more than that over ocean, and it is larger in the NH than in the SH.

In the first indirect effect, aerosols change the radiative balance by modifying the cloud droplet effect radius (r_e). Therefore, we show the change in r_e after the addition of the anthropogenic aerosols in Figure 3.5b. In most cases, the present day global average r_e is about 0.5 μm smaller than the pre-industrial value. Moreover, the change is much larger over land ($\sim$0.8 μm) than over ocean ($\sim$0.25 μm), which is quite reasonable considering that there are larger anthropogenic aerosols over land. Over the ocean, the decrease in r_e in the northern hemisphere is clearly larger than that in the southern hemisphere in all cases. Over the land, however, there is no clear signature of the change between the southern hemisphere and the northern hemisphere for all cases.

3.3.2 TOA forcing

The zonal mean forcing from the simulations of the perturbation cases is shown on Figure 3.6. The perturbation cases have been divided into several groups to compare
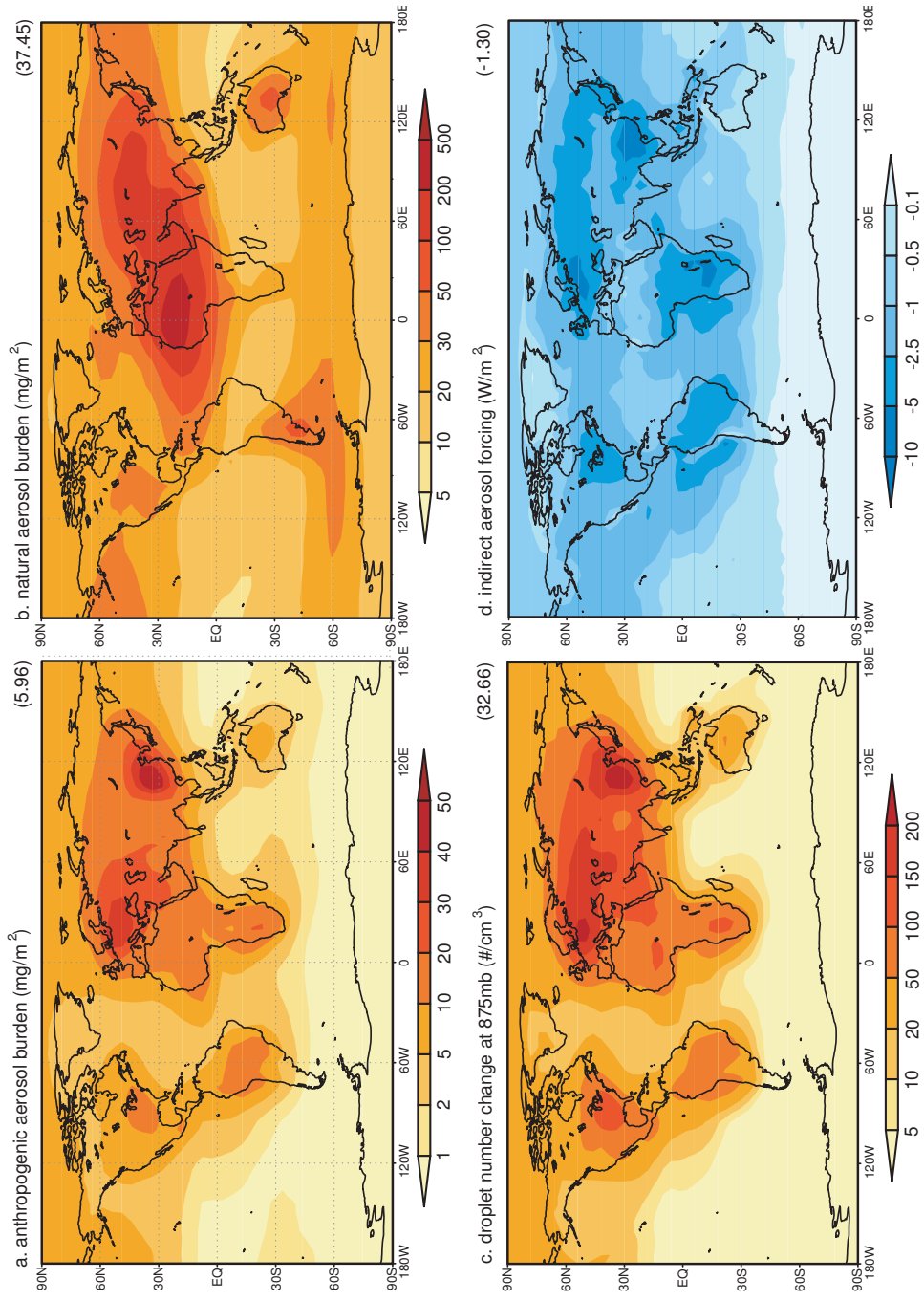
Figure 3.4: (a) Annual mean anthropogenic aerosol burden. (b) Annual mean natural aerosol burden. (c) Annual mean cloud droplet change at 875mb level from PI to PD. (d) Four-month (Jan, Apr, Jul, Oct) mean aerosol indirect forcing from the reference case. The numbers in the parentheses give the global mean values.
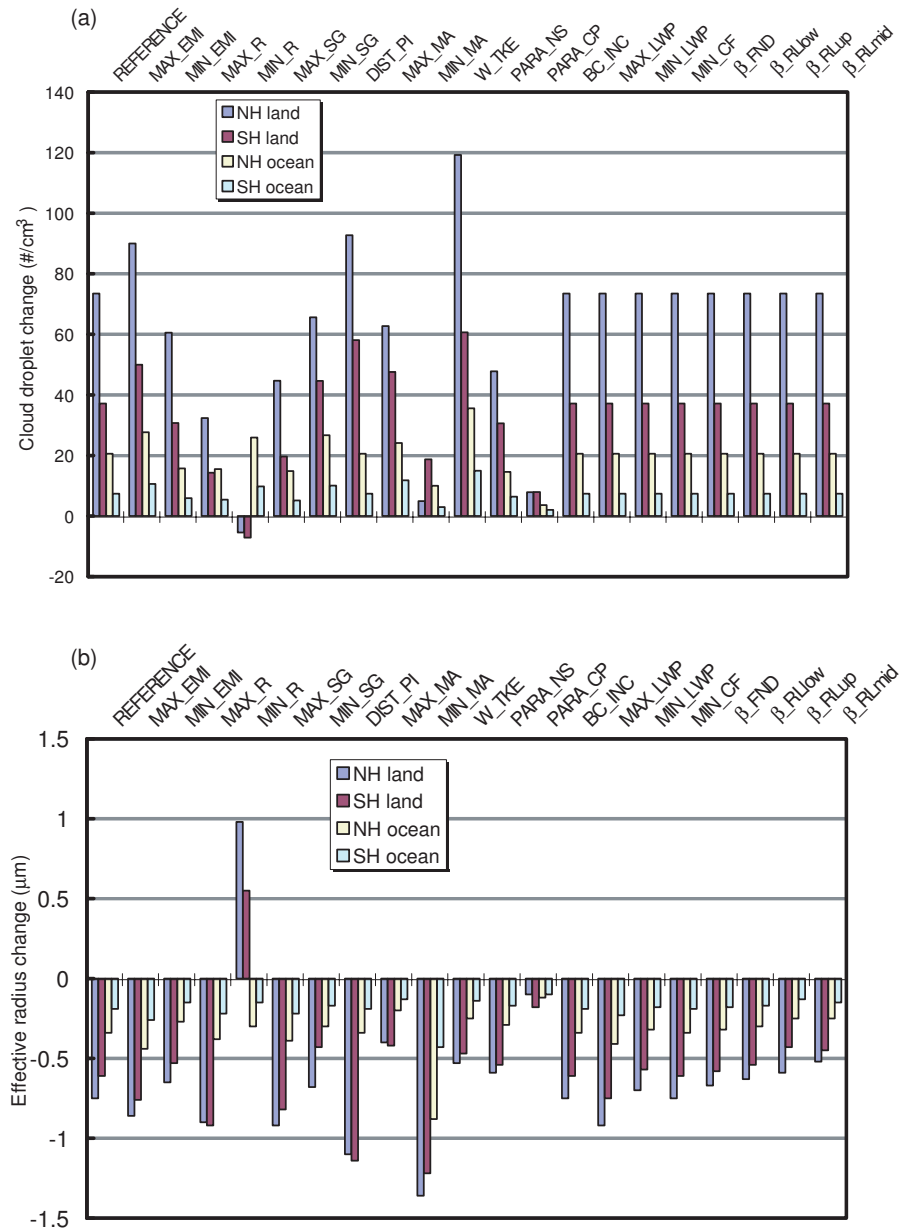
Figure 3.5: (a) Global mean cloud droplet number concentration change from PI to PD. (b) Global mean cloud effective radius change from PI to PD.

them to the results of the reference case. These groups are shown on different panels on Figure 3.6. Table 3.6 gives the forcing from each of the cases and Figure 3.6 shows the change in global average forcing from the reference case.

Table 3.6: Global average aerosol indirect forcing from different perturbation cases.

Case	Forcing(Wm^{-2})
REFERENCE	-1.30
MAX_EMI	-1.63
MIN_EMI	-1.06
MAX_R	-1.25
MIN_R	-0.45
MAX_SG	-1.30
MIN_SG	-1.24
DIST_PI	-1.60
MAX_MA	-0.94
MIN_MA	-2.16
W_TKE	-1.23
PARA_NS	-1.07
PARA_CP	-1.79
BC_INC	-1.29
MAX_LWP	-1.21
MIN_LWP	-1.30
MIN_CF	-0.63
β_FND	-1.07
β_RLlow	-1.10
β_RLup	-0.75
β_RLmid	-0.86

Figure 3.6a shows that the uncertainty associated with aerosol and aerosol precursor emissions is very large. This is because the range of anthropogenic emissions themselves is very large, e.g. the global SO_2 emission range is from 67 to 130 TgS/Yr (*Penner et al.*, 2001a). The MAX_EMI case the forcing (-1.63 Wm^{-2}) is larger than in the reference case (-1.30 Wm^{-2}) because the difference in aerosol concentration from the PI to PD increases since the PI aerosol concentrations remain constant.

Changes associated with changes in the aerosol concentration are shown in Figure
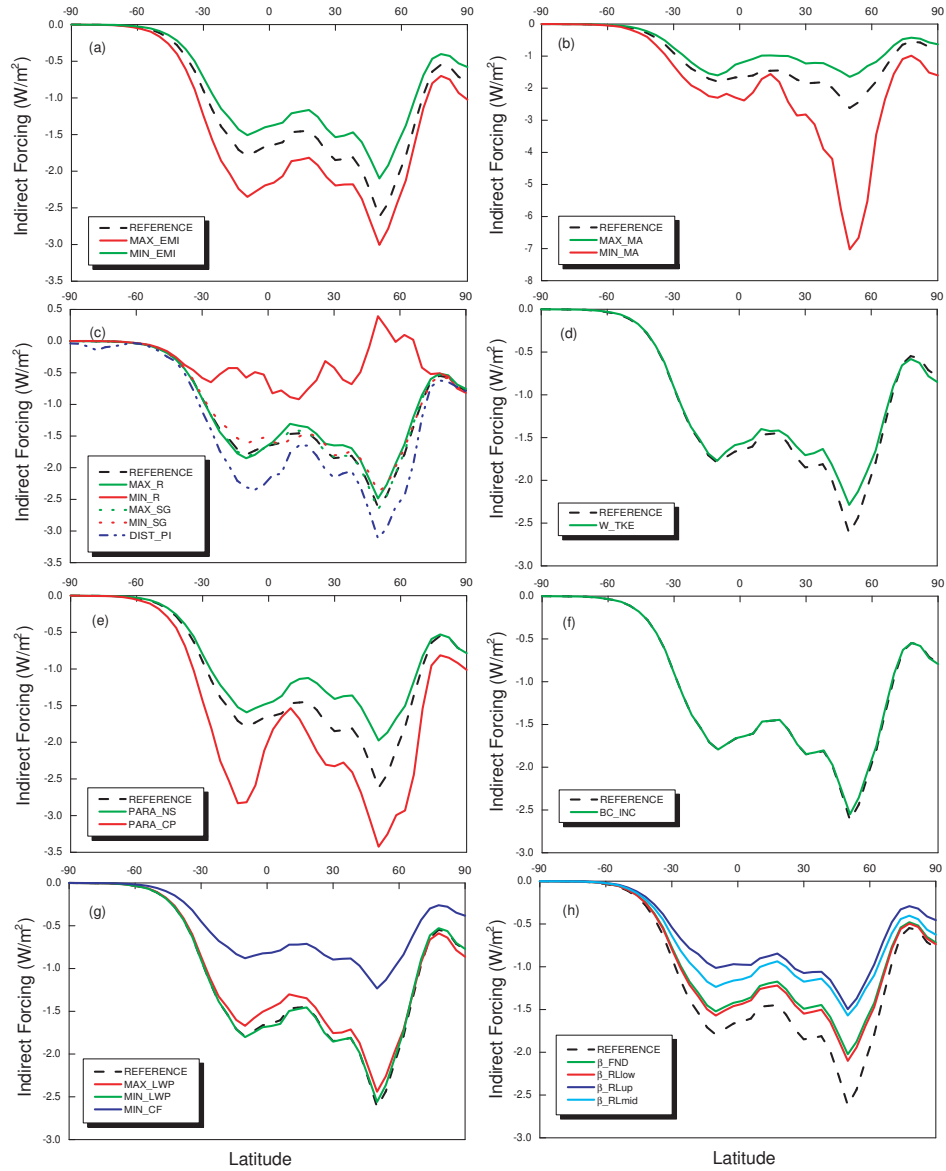
Figure 3.6: Zonal mean aerosol indirect forcing results from different cases in which we consider the uncertainty due to: (a) aerosol and aerosol precursor emission, (b) aerosol mass concentration from different chemical transport models, (c) aerosol size distribution, (d) updraft velocity, (e) cloud nucleation parameterization method, (f) inclusion of BC in clouds, (g) liquid water path and cloud fraction, (h) dispersion coefficient relating cloud droplet effective radius and volume mean radius.

3.6b. In the MAX_MA case, the maximum aerosol mass concentration in both the PD and PI cases from the model inter-comparison was used. Both the PI and PD aerosol number concentrations increase compared to those in the REFERENCE case. But since the relationship between the droplet number (N_d) and the aerosol number (N_a) is non-linear, N_d changes faster than Na when the value of N_a is smaller as in the PI case. Therefore, compared to the REFERENCE case, the N_d difference between PI and PD is smaller in the MAX_MA case. And the forcing in MAX_MA case is smaller (i.e. -0.94 Wm^{-2} compared to -1.30 Wm^{-2}). Similarly, due to the non-linear relationship between N_d and N_a, the N_d difference between PI and PD and the forcing in MIN_MA case are larger than those in the REFERENCE case (i.e. -2.16 Wm^{-2} compared to -1.30 Wm^{-2}).

The effect of changes in the aerosol size distribution is shown in Figure 3.6c. The change in the aerosol size distribution modifies the total aerosol number concentration calculated based on the fixed mass concentration. It also affects the fraction of aerosols that are activated to droplets because large aerosols activate more easily than smaller aerosols. Increasing the aerosol mode radius (MAX_R) reduces the total aerosol number concentration, thereby reducing the forcing (-1.25 Wm^{-2}). But the forcing change is small, and most of the change is in the northern hemisphere. Decreasing the mode radius (MIN_R) increases the total aerosol number. However, the indirect forcing calculated from the MIN_R case (-0.45 Wm^{-2}) is much smaller than that in the reference case (-1.30 Wm^{-2}). This is because in MIN_R case, the aerosol mode radius is very small, which causes extremely high aerosol number concentration (calculated from the fixed mass concentration and size distribution), especially over the continents. This high concentration can not exist in the real atmosphere for a long time because small aerosols with high number concentrations

coagulate very quickly and transform to the accumulation mode in a very short time. If we assume a uniform distribution of aerosols with $R_p = 0.001 \mu m$ and $N_0 = 1.6 \times 10^5 cm^{-3}$, we can calculate the coagulation rate by (*Seinfeld and Pandis*, 1997):

$$J_{col}(\#/s) = 8\pi R_p D N_0 \left(1 + \frac{2R_p}{\sqrt{\pi Dt}} \right) \qquad (3.1)$$
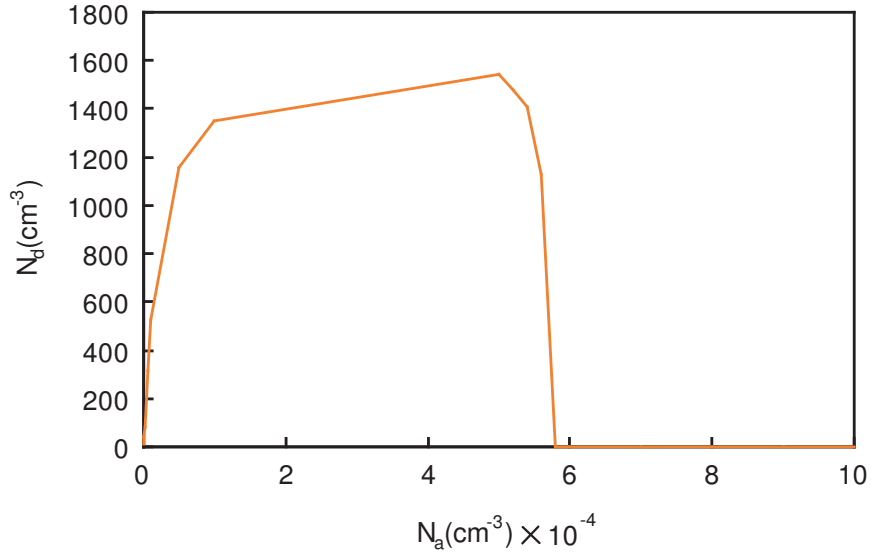
Figure 3.7: The parcel model results showing the decrease of N_d as N_a increases when N_a is very high. The cloud droplet number concentration can be simulated from a cloud nucleation parcel model. In the simulation, the updraft velocity is 50 cm/s. The size distribution is assumed to be a single log-normal distribution with a mode radius of 0.05 μm and a standard deviation of 2.

This leads us to calculate on average e-folding time for coagulation of 300s over the continents given the concentrations calculated for this case. If this high concentration did exist, the addition of more aerosols will decrease the number of nucleated cloud droplets due to their competition for water vapor. This can be seen from the parcel model simulation. Figure 3.7 shows that above a certain aerosol number concentration, the cloud droplet number decreases with N_a. Nevertheless, we do not

consider this case to be realistic, and therefore do not include it in our estimates of the most important uncertainty.

The MAX_SG curve and MIN_SG curve are very close to those in the REFER-ENCE case, which implies that the forcing is insensitive to the choice of σ if the same σ is used in both the PD and PI simulations. However, if a different size distribution is used in the PD and PI cases, the sensitivity of the indirect forcing is very high. When we use the free troposphere aerosol size distribution as the PI aerosol size distribution, the indirect forcing increases substantially (i.e., -1.60 Wm^{-2} compared to -1.30 Wm^{-2}), because the droplet number concentration in the PI case is decreased.

Changes in the forcing associated with the method of computing the updraft velocity are shown in Figure 3.6d. Compared to the PDF method of calculating updraft velocity (w), the forcing calculated using the TKE method for estimating w is smaller (i.e., -1.23 Wm^{-2} compared to -1.30 Wm^{-2}). By comparing the cloud droplet number concentration from the PI and PD cases, we find that when using the TKE method for w, the N_d is larger than that when using the PDF method in most regions. However, the combined effect of changing the method for calculating w on both the PI and PD droplet concentration causes the forcing calculated by using the TKE method to be smaller than that using the PDF method.

Figure 3.6e shows the effect of changing the method of parameterizating the relationship between N_a and N_d. The pattern of forcing obtained using the NS parameterization is very similar to that in the reference case (AG3 parameterization), though the forcing value (-1.07Wm^{-2}) is smaller when using the NS parameterization. The reason is that when the aerosol number is small, the NS parameterization produces more N_d than does the AG3 parameterization, and when the aerosol number is large, the NS parameterization produces less N_d (see Figure 3.2). The results

from the CP parameterization are very different. For most regions, the N_d and forc-ing value are larger than those in the reference case. The reason is that the N_d from low N_a is much smaller than that in the reference case (see Figure 3.2), while the N_d from high N_a is similar to that in the reference case. Because the CP parameteriza-tion assumes a change in the aerosol size distribution between the PD and PI cases, it incorporates some of the uncertainty associated with the change in PD size (i.e., the change in the forcing (-1.79 Wm^{-2}) is similar to the change in forcing associated with case DIST_PI, which was -1.60 Wm^{-2}). Both AG3 and NS parameterization are sectional resolved methods, so their patterns are more similar than those of the CP parameterization.

Figure 3.6f shows the effect of including the change in droplet single scattering albedo due to BC within the cloud. The forcing decreases after including the effect of BC within the clouds. The global mean difference in the forcing is +0.01 Wm^{-2}, which is smaller than the results reported by Chuang et al. (2002). This change is small compared to the other factors considered here, but in those regions with high BC concentration and high cloud fraction, the impact of this change is more important.

Figure 3.6g shows the effect of changing the LWP and CF. Changing the LWP will not change the number of cloud droplets but will change the effective radius in the cloud. A change in the LWC of the cloud (Δq) will lead to a change of $(\Delta q)^{1/3}$ in effective radius. However, since the relative change of effective radius is not too different in the PD and PI cases, the forcing differences are small (<0.1 Wm^{-2}). The change in the cloud fraction (CF) does not change N_d or r_e, but will change the reflected solar radiation. The forcing is very sensitive to CF. The minimum CF produces less than 1/2 the forcing of the reference case. We notice that the CF for

total clouds from the reference parameterization is higher than that in the satellite observations, but it is similar to the MODIS warm cloud fraction. Thus we believe that the estimated forcing of the REFERENCE case (-1.30 Wm^{-2}) is close to that which would be calculated with these higher observed CFs. It is important to note that the cloud fraction is a major source of uncertainty in the calculation of the aerosol indirect forcing. The forcing is decreased to -0.63 Wm^{-2} in this case.

Most GCM-based calculations of indirect forcing do not consider the effect of cloud drop dispersion. The relationship between the effective radius and the droplet number is often represented by a coefficient between volume mean radius and effective radius (*Martin et al.*, 1994). However, our results show that the change in the indirect forcing associated with changing from the fixed coefficient β to a β that is related to N_d is of some importance. The global mean change of indirect forcing after considering the dispersion effect using the method employed in *Penner et al.* (2004) is 0.23 Wm^{-2}, and the uncertainty due to the different representations of this dispersion effect in *Rotstayn and Liu* (2003) is 0.2∼0.4 Wm^{-2}. These results compare well with those reported by *Rotstayn and Liu* (2003) and *Peng and Lohmann* (2003).

To summarize the effect of different perturbations, we show the relative difference from different cases to the forcing from the reference case in Figure 3.8. This can be used to analyze the major sources of uncertainty in the estimation of aerosol indirect radiative forcing. From the plot, we can see the uncertainty associated with the aerosol mass concentration is very large, and can increase the forcing by almost 0.8 Wm^{-2}. The uncertainty associated with cloud fraction is next in importance, followed by the uncertainty associated with the treatment of dispersion of the cloud drops.

The aerosol and aerosol precursor emissions, aerosol mean radius, updraft ve-

locity, droplet parameterization method, and natural aerosol size also have some influence (0.2~0.6 Wm^{-2}) on the indirect forcing. The aerosol size standard deviation, BC effect on cloud albedo, and LWP have a relatively small effect on the simulated global average forcing.
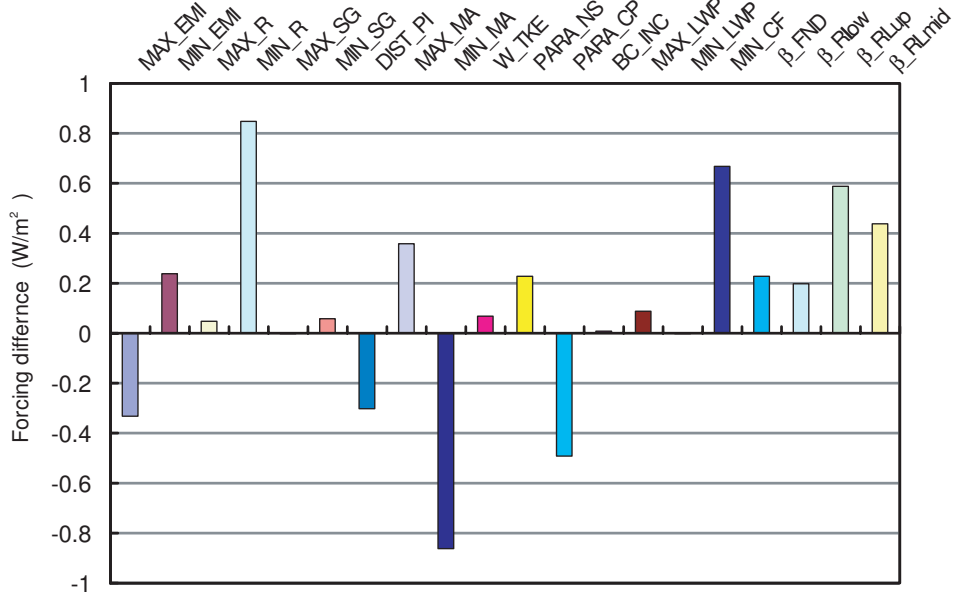
Figure 3.8: The global mean indirect forcing difference compared to REFERENCE case.

3.4   The global uncertainty calculation

3.4.1   Calculation method

By varying the above uncertainty sources, we can calculate the global aerosol indirect forcing for different cases, thereby estimating the 2-D distributions of the uncertainty. The uncertainty in the forcing can be estimated from

$$(F - F_0)^2 = \sum_i \left[\frac{\partial F}{\partial x_i}\right]^2 (\partial x_i)^2 + \sum_i \sum_j cov\,(x_i, x_j) \left[\frac{\partial F}{\partial x_i}\right] \left[\frac{\partial F}{\partial x_j}\right] \qquad (3.2)$$

where $(F - F_0)^2$ is the variance in the forcing, so $|F - F_0|$ is the uncertainty. x_i refers to the list of uncertain variables, and $(\partial x_i)^2$ is the variance in the variable x_i.

The function $cov(x_i, x_j)$ is the covariance of the variables in the argument. In our preliminary calculations of the spatial distribution of the uncertainty, the covariance between the pre-industrial forcing and present forcing is omitted (Penner et al., 2001).

In the calculation of uncertainty associated with aerosol and aerosol precursor emissions, aerosol mass, aerosol size standard deviation, cloud nucleation parameterization method, LWP, and the cloud drop dispersion coefficient β, we assume that the maximum difference between REFERENCE and other cases (e.g. MAXIMUM or MINIMUM) is a measure of the 1σ uncertainty associated with that source. For the uncertainty associated with the aerosol mode radius, only the results from the maximum mode radius are used since in the MIN_R case, there were unrealistically small aerosol sizes and large N_a. For all other cases, the difference between reference case and perturbation case is considered.

3.4.2 Result

Figure 3.9 shows that the largest values of absolute uncertainty occur in the same regions that have the highest indirect forcing. However, the largest relative values of the uncertainty are mostly over the ocean areas that are closest to continent regions with high aerosol indirect forcing. The global average relative uncertainty in aerosol indirect forcing is about 130%. This value is in reasonable agreement with that based on the range in GCM assessments (*Ramaswamy et al.*, 2001b) and with box model calculations (*Penner et al.*, 2001a).

Seasonal change of the global mean aerosol indirect forcing and the relative uncertainties is shown in Figure 3.10. Since most human activities occur in the Northern Hemisphere, the forcing value is largest on July, when the nucleation formation of sulfate aerosols is large. The global mean relative uncertainty is smallest in July

(a) Uncertainty of the indirect forcing (W/m^2) (1.82)

(b) Relative uncertainty of the indirect forcing (1.3)
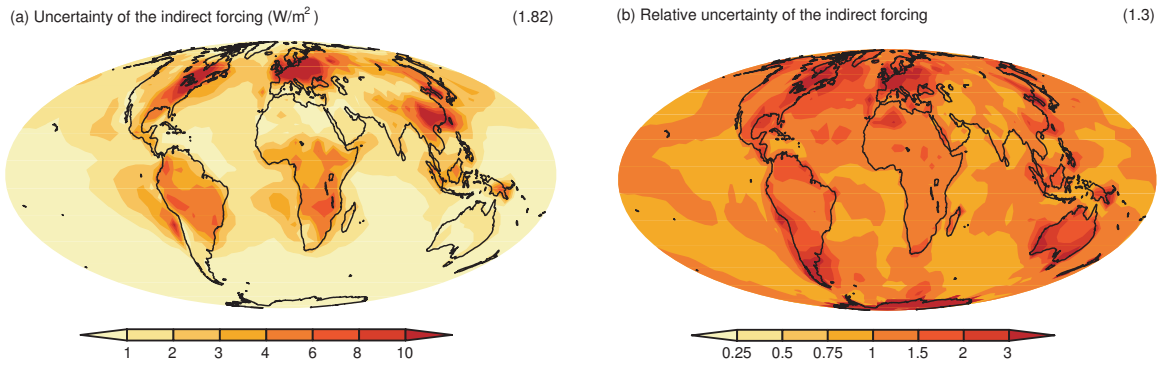
Figure 3.9: The global indirect forcing uncertainty. (a) Absolute uncertainty (Wm^{-2}). (b) Relative uncertainty. The numbers in the parentheses give the global mean values.
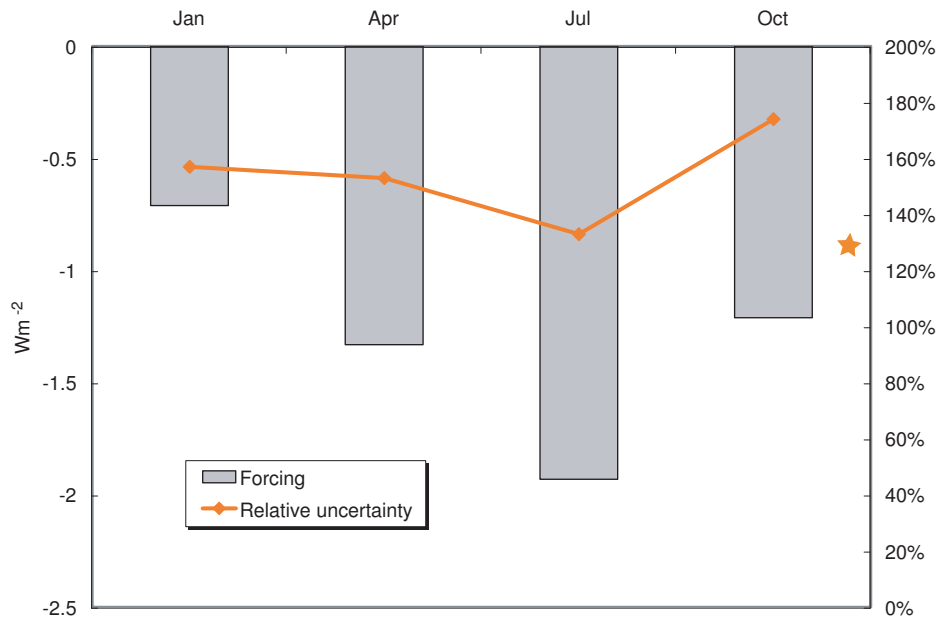
Figure 3.10: Seasonal variation of global aerosol indirect forcing (left axis) and the relative uncertainties (right axis). The star sign shows the relative uncertainty of the annual global mean forcing.

and largest in October. However, compared to the relative uncertainty for annual mean forcing (which is indicated as star sign in Figure 3.10), the uncertainty for each monthly mean forcing is larger.

Figure 3.11 shows how much each parameter contributes to the total uncertainty for the aerosol indirect forcing estimation. Consistent with the results shown in Figure 3.8, the largest contribution is from the uncertainties associated with aerosol mass concentration calculated by chemical transport models, and uncertainties associated with cloud fraction. These two account for about half of the total uncertainty. Other importance sources of uncertainty include aerosol and aerosol precursor emissions, representation of aerosol size distribution, representation of cloud droplet spectral dispersion effect, and cloud nucleation parameterization methods.
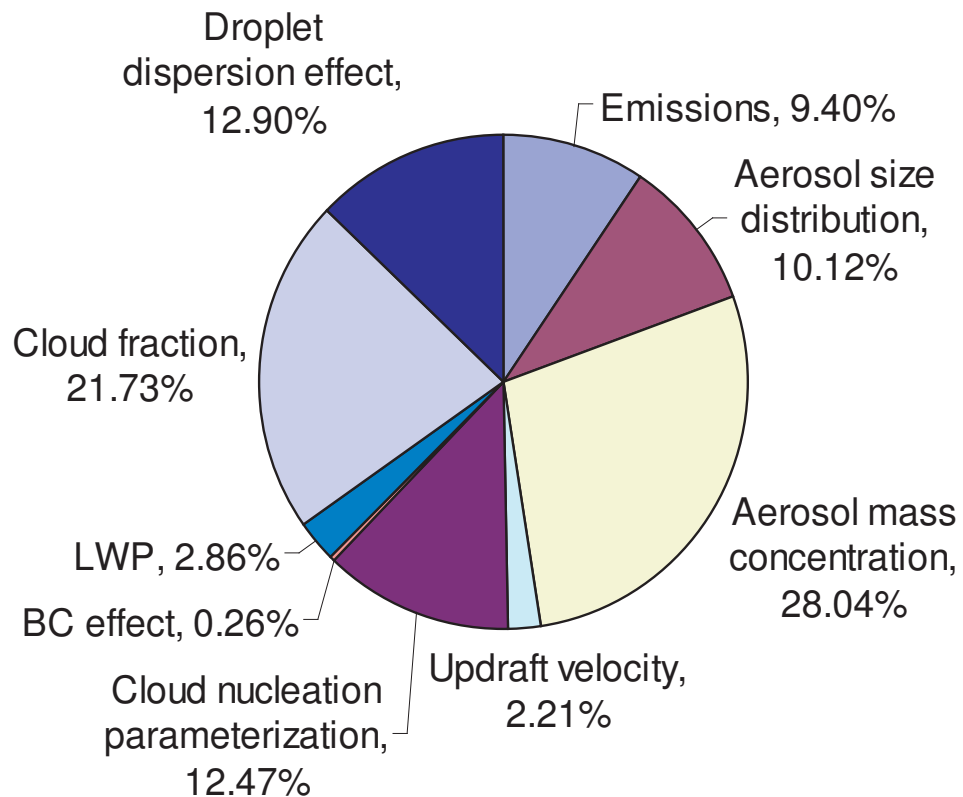
Figure 3.11: Fractions of contribution from each parameter to the total uncertainty.

3.4.3 Covariance discussion

In this study, we studied the uncertainty of calculated first aerosol indirect forcing associated with each variable. We did not calculate the global mean total variance of this forcing and did not consider the covariance term as shown in Equation 3.2. However, it is necessary to discuss the effect of this covariance term in the calculation of global mean variance.

First, in applying Equation 3.2 to calculate the uncertainty in one grid, the variations in different parameters may have correlations. A simple example is that when a high value of CF is used, there may be a more chance that a large LWP is used. Therefore in this case, if we omit the correlation term in Equation 3.2, we may underestimate the total uncertainty. Second, the forcing is the difference in TOW SW flux calculated by using the PD aerosols and the PI aerosols. There is a possible correlation between the PD aerosols and the PI aerosols. *Penner et al.* (2001a) found that the uncertainty was reduced when the covariance between the cloud albedo calculated for the present-day case and the pre-industrial case was taken into account. As in *Penner et al.* (2001a), the correlation with the spatial and temporal distribution may be estimated by calculating the correlation in the outgoing shortwave radiation for matched pairs of the change in N_d in the pre-industrial and present-day scenarios.

In calculating the global mean variance of aerosol indirect forcing, we also expect the correlations between the parameters used for different grids. In our current study, we changed parameters for different grids in the same way (e.g. in case MAXLWP, the maximum LWP is applied to every grid). In this way, we implicitly assumed that the parameters in different grids are fully correlated (correlation coefficient equals to 1), which may cause an overestimation of the global mean value of uncertainty.

3.5   Conclusions and discussion

In this paper we analyzed the uncertainties in the model calculation of aerosol forcing associated with the first indirect effect. We have used a radiation transfer model to study the role of each uncertainty source in the aerosol effect on clouds. The aerosol burden calculated by chemical transport models and the cloud fraction are found to be the most important sources of uncertainty. A 2-D distribution of the uncertainty in indirect forcing has been shown. The global mean value of the relative uncertainty is about 130%. The highest absolute uncertainty occurs in high anthropogenic aerosol emission regions, while the highest relative uncertainty occurs in coastal regions near these high anthropogenic aerosol emissions regions.

It appears from our simulation that the representation of the pre-industrial aerosol size distribution plays an important role in the calculation of anthropogenic aerosol forcing. A different selection of the pre-industrial aerosol size distribution causes a larger forcing because the cloud droplet number of the PI case decreases. This is consistent with the result by *Platnick and Twomey* (1994), which states that the cloud susceptibility (defined as the increase in albedo resulting from the addition of one cloud droplet per cubic centimeter for a constant cloud liquid water content) is larger when the droplet number is smaller. The uncertainty due to the pre-industrial aerosol mass concentration is also important.

We note that the uncertainty of the first indirect effect was based on the model and the criteria used in this study. If a different radiative transfer model was used, or if other choices of criteria such as model resolution, cloud overlap scheme, or the aerosol mixing scheme were selected, the estimated uncertainty would probably be different.

The off-line simulation in the present study could cause other uncertainties since we used the monthly average aerosol number concentration from the IPCC model inter-comparison study. A fully coupled GCM would give us a better estimation of the interactions of aerosols, clouds and radiation. In addition, the use of a GCM can take into account some of the cloud feedbacks due to the aerosol change (i.e. the second indirect effect), so it may be used to assess the second aerosol indirect forcing. Ongoing work is also concerned with assessing the uncertainty associated with these feedbacks.

CHAPTER IV

Indirect effect of nitric acid gas and nitrate aerosols on clouds and radiative flux

4.1 Nitric acid gas and nitrate aerosols in the atmosphere

Sulfate has long been considered to be the main component of the anthropogenic aerosols, and most studies of the indirect aerosol effect have concentrated on sulfate aerosols. This is probably true on global scale. But regionally, the mass fraction of nitrate can exceed that of sulfate, especially in some urban areas. The manmade nitrate has been found to be at least as important as sulfate in some regions of Europe (*ten Brink et al.*, 1996). Many nitrate salts have lower deliquescence relative humidity (DRH) than ammonium sulfate. Therefore, nitrate can modify the hygroscopic efficiency of aerosol particles, and change their optical properties and their ability to form cloud droplets. The gas phase presence of nitrate is the nitric acid gas (HNO_3), which is also able to modify the activation of aerosols (*Kulmala et al.*, 1993b). This change in cloud droplet number concentration can lead to a modification of the scattering of clouds and the radiative balance of the earth.

4.1.1 Nitrogen cycle in the troposphere

Nitrogen gas (N_2) is the most abundant nitrogen-containing substance, but it is extremely stable in both the troposphere and stratosphere. The important species are

more reactive nitrogen-containing compounds, including nitrous oxide (N_2O), nitric oxide (NO), nitrogen dioxide (NO_2), the nitrate radical (NO_3), dinitrogen pentoxide (N_2O_5), nitric acid (HNO_3) and ammonia (NH_3). In the aqueous phase, nitrogen is also present in the form of different ions, such as ammonium ion (NH_4^+), and nitrate ion (NO_3^-).

Figure 4.1 shows the nitrogen cycle in troposphere, excluding N_2. Since HNO_3 and N_2O_5 are oxidation products of NO_x ($NO+NO_2$) and are not emitted to the troposphere directly, the majority of the nitrate aerosols are secondary aerosols. Ozone (O_3) and hydroxyl radical (OH) are the two main oxidants. NO_x can be transformed to HNO_3 directly by OH, which is important in the day light. NO_x can also be oxidized by O_3 to form NO_3 and N_2O_5 first, and then HNO_3 through heterogeneous hydrolysis. This path is only important at night when the NO concentration is very low.

Nitrogen in the atmosphere comes from both natural sources and anthropogenic sources. Bacterial activity is the main natural source of N_2O. The significant natural source of NH_3 includes animal waste, vegetation and ocean source. Although most of the NO_x is from fossil-fuel combustion and biomass burning, there are some natural sources such as soil release and lightning production.

We are mainly concerned with the change of global climate due to human activities. Anthropogenic emissions have been increased rapidly since the industrial revolution. The major emissions of anthropogenic N_2O and NH_3 come from the cultivated soils and animal waste. But for NO_x, which is the main precursor of HNO_3 and nitrate aerosol, fossil-fuel combustion and biomass burning are the dominant emissions, particularly in urban areas.

The main gas phase precursors of HNO_3 and nitrate aerosols are N_2O through
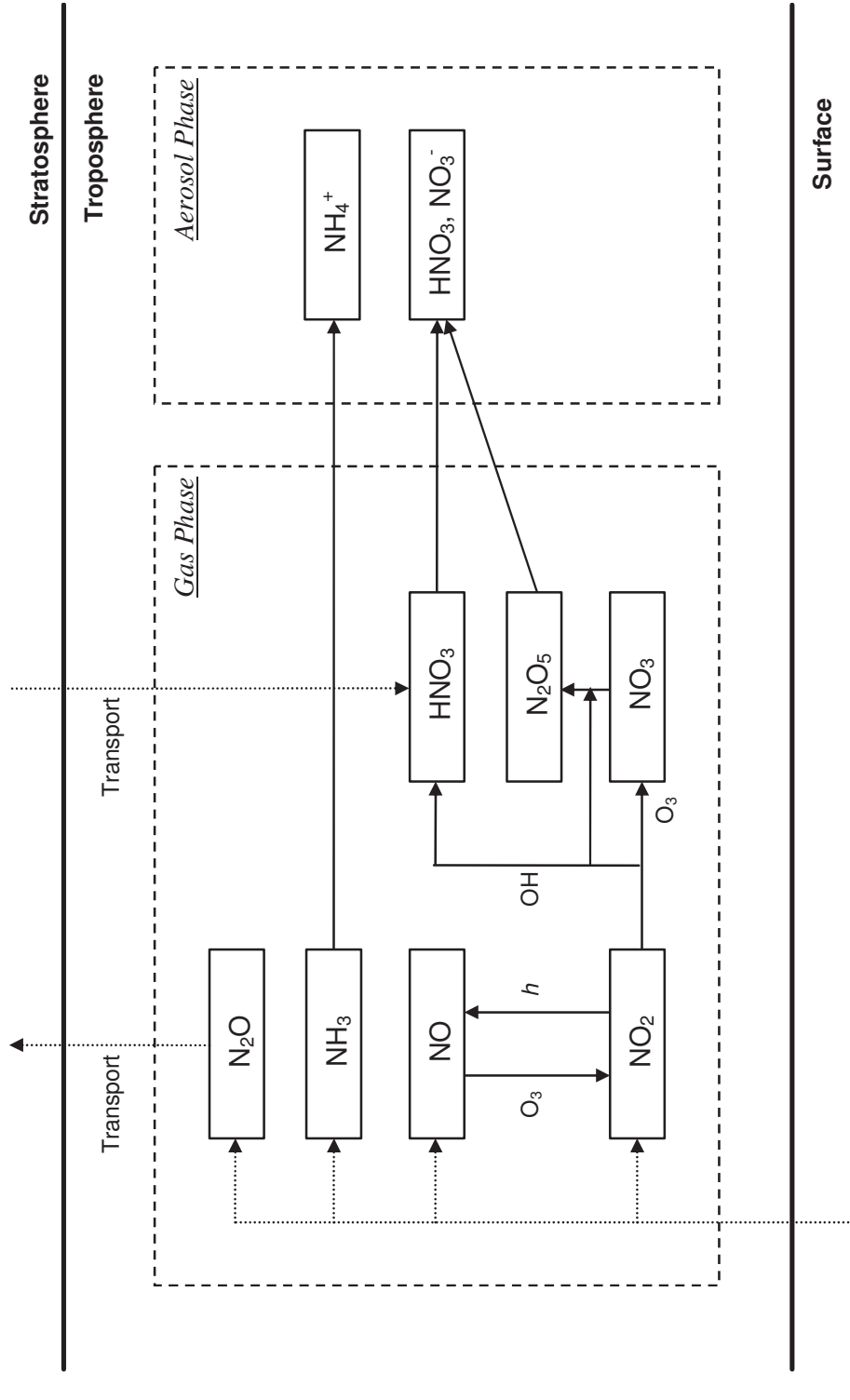
Figure 4.1: Nitrogen cycle in the troposphere. Species are shown in the solid boxes and the arrows denote the transformation between them.

the production of HNO_3 in the stratosphere, NO_x, and NH_3. Table 4.1 summarizes the global emissions of these precursors from natural and anthropogenic sources. Anthropogenic sources are dominant for NO_x and NH_3, while the main N_2O emissions come from natural sources. The total anthropogenic emission of nitrogen-contain compounds is about 90 Tg-N yr^{-1}.

Table 4.1: Global emissions of N_2O, NO_x and NH_3 from natural sources and anthropogenic sources (Tg-N yr^{-1}). Data are based on IPCC(2001).

	N_2O	NO_x	NH_3
Natural sources	9	10.6	10.7
Anthropogenic sources	6.9	40.8	42.8

HNO_3 is present in both the gas phase and aerosol (aqueous) phase. In the aqueous phase, it usually dissociates and combines with positive ions to form nitrate. Ammonium nitrate (NH_4NO_3) is a predominant form of the nitrate compounds.

Nitrate aerosols are removed from the atmosphere through dry deposition and wet deposition. Gas phase HNO_3 can be transformed back to NO_x by photolysis or by reaction with OH radicals.

4.1.2 Emission trend and the concentrations

With the application of control measures, emissions of sulfur gas and NO_x from fossil fuel burning have been reduced in many countries during recent decades. However, emissions of NO_x have decreased less than SO_2, probably due to the rapid growth of automobiles and better control technologies for sulfate pollution. Therefore, the relative importance of NO_x versus SO_2, and hence the relative importance of nitrate versus sulfate aerosols is increasing in most industrialized regions of Europe and North America. For instance, as shown in Figure 4.2, the emissions of NO_x and SO_2 in United States decreased 15% and 33% during 1983-2002, respectively.

The concentrations of NO_2 and SO_2 were reduced by 21% and 54% during the same period. The NO_x/SO_2 emission ratio globally was estimated to reach 0.58 at year 2100 (*Kulmala et al.*, 1995). Another modeling study of one future emission scenario showed that the global annual mean nitrate forcing could increase from -0.19 Wm^{-2} today to -1.28 Wm^{-2} at the year 2010, while sulfate forcing could decline from -0.95 Wm^{-2} to -0.85 Wm^{-2} (*Adams et al.*, 2001).

The increase of NO_x emissions affects the concentration of nitrate in the gas phase and in the aerosol particles. A typical value for the HNO_3 concentration in remote areas is 0.56 ppbv (*Kitto and Harrison*, 1992). While in polluted areas the concentrations are much higher (*Hoek et al.*, 1996). *Warneck* (1988) tabulated average values for gaseous HNO_3 from several measurements from remote marine to urban areas and at different seasons and altitudes: concentrations vary from 0.07 ppbv (in the marine boundary layer at 0-3 km height) to 4.4 ppbv (9 days average at Claremont, California). *Kitto and Harrison* (1992) reported that the highest measured HNO_3 concentration at southeast England during a hot summer day was 8 ppbv. Vertically, HNO_3 in the troposphere decreases very slowly with height (*Penner et al.*, 1991).

4.1.3 Equilibrium and mass transfer between gas and aqueous phase

The equilibrium state between the gas and aqueous phase can be explained by using the Henry's Law:

$$C_{aq} = H_A P_A \tag{4.1}$$

where C_{aq} is the aqueous phase concentration of substance A, P_A is the partial pressure of A in the gas phase, and H_A is the Henry's Law coefficient. For HNO_3 at 298K, the value of H_A is 2.1×10^5 M atm^{-1}. Since HNO_3 in the aqueous phase
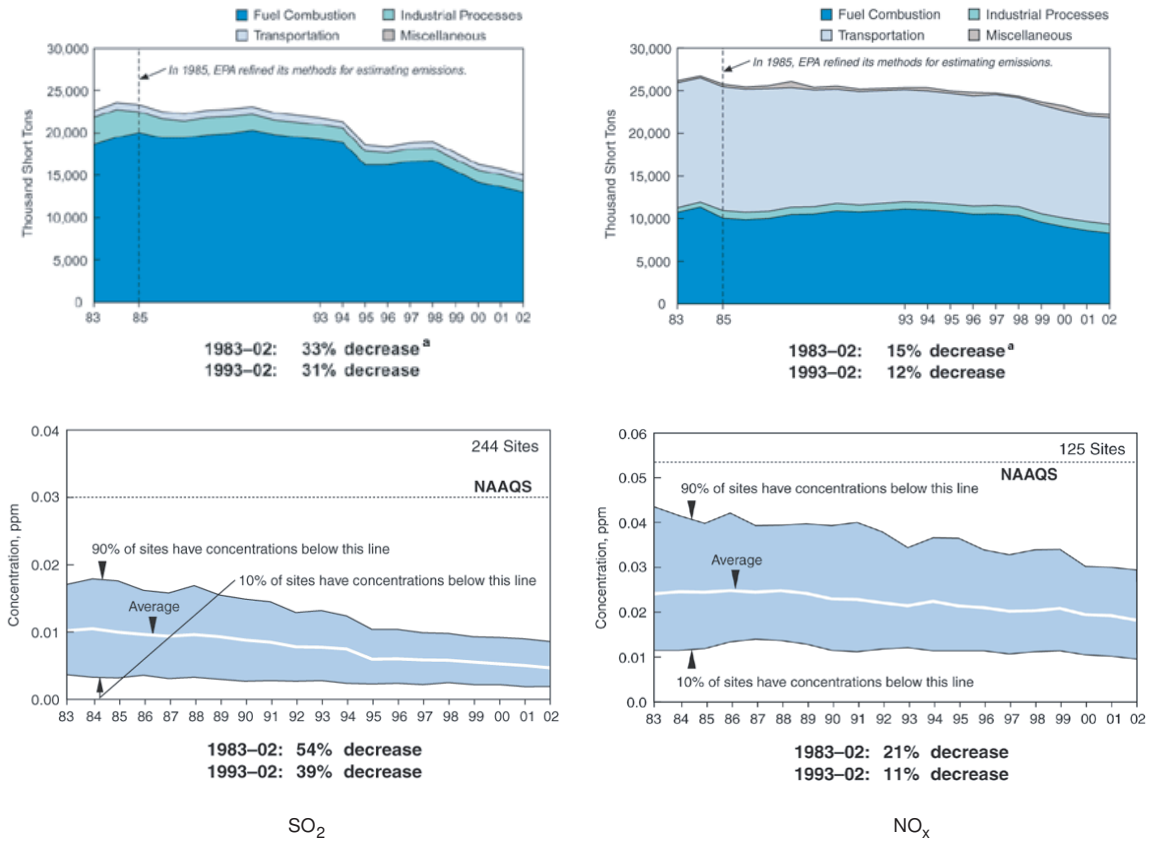
Figure 4.2: SO$_2$ (left) and NO$_x$ (right) emissions(upper) and surface concentrations (bottom) in United States during 1983-2002. Source: US EPA website: http://www.epa.gov.

dissociates quickly to nitrate, the effective Henry's Law constant defined as $H'_A = H_A \left(1 + \frac{K_{n1}}{[H^+]}\right)$ is much higher (3.2×10^9 M atm^{-1} when the PH=3), where K$_{n1}$ is the dissociation constant.

However, the time to establish this equilibrium depends on particle size distribution and ambient meteorological conditions (*Seinfeld and Pandis*, 1997). Particularly for large aerosol particles, the diffusion of semi-volatile gases is slow and these aerosols are not generally in equilibrium with their gas concentrations. Thus one must account for the mass transfer between the gas phase and the aqueous phase.

The mass transfer rate can be calculated from

$$R_{aq} = k_{mt} \left(P_A - \frac{C_{aq}}{H'_A} \right)$$ (4.2)

where k_{mt} is the mass transfer coefficient:

$$k_{mt} = \left[\frac{r^2 RT}{3D_A} + \frac{r\sqrt{2\pi M_A RT}}{3\alpha_A} \right]^{-1}$$ (4.3)

where r is the radius of particle, T is the temperature, D_A is the diffusivity of HNO_3 in the air, M_A is the molecular weight of HNO_3, and α_A is the accommodation coefficient of HNO_3. Note both gas-phase transport and interfacial mass transport are included in the above equation.

4.1.4 Nitrate effect on clouds and the motivation of this study

As shown in Chapter 2, the equilibrium vapor saturation ratio on an aerosol particle is affected by the dissolved solute in the aqueous phase (Raoult effect). HNO_3 is a very soluble gas and its presence in the aqueous phase could contribute soluble material to the particle and enhance the cloud droplet nucleation. The deposition of nitrate on non-soluble aerosols such as mineral dust could facilitate the water uptake and growth of these particles. In addition, HNO_3 gas can evaporate from one mode and deposit on another mode, causing the re-distribution of nitrate in different aerosol sizes.

The presence of HNO_3 gas and nitrate in the aerosol particles modifies the activation ability of the aerosols. The increased cloud droplets due to addition of nitrate scatter more solar radiation back to space, which cools the earth surface and counteracts the greenhouse effect. This indirect effect, together with the direct influence on the deliquescence relative humidity and refractive index of the aerosols, emphasizes the role of nitrate aerosols in climate studies.

Although sulfate aerosols have been traditionally considered the main contributor to the aerosol cooling effect, the manmade nitrate aerosols may exert a similar radiative forcing as sulfate regionally. Furthermore, nitrate aerosol may play an even more important role in the future. However, not much work has been done to quantify the nitrate aerosol scattering effect, or its indirect effect on clouds and climate. In this chapter, we will study the impact of nitrate on cloud nucleation, as well as its implication to global radiative balance. The results of changes in cloud droplet number concentration and radiative flux are compared to the aerosol indirect effect due to other aerosol species. We will also improve a parameterization method so that it can account for the effect of gas phase HNO_3 in the actual activation process.

4.2 Effect of nitrate concentration and distribution on CCN activation

4.2.1 Method overview

Six representative sites are used to study the nitrate effect on cloud nucleation and climate. The geographical locations of these sites are shown in Figure 4.3. All these sites are near the coastline, but they all represent polluted sites. The Europe site (EUR, 5W, 38N) and Eastern US (EUS, 77.5W, 38N) site are two typical sites with high sulfate pollution from fossil fuel emissions. The Northern Pacific (NPA, 122.5W, 36N) site is a marine site with the influence of nitrate pollution from California. The East Asia (EAS, 127.5E, 36N) site is often impacted by dust from the Gobi desert. The Central Africa (CAF, 7.5E, 4N) and Southern America (SAM, 52.5W, 28S) sites are two sites with high concentrations of carbonaceous compounds.

Aerosol mass concentrations were simulated by the UMICH/LLNL IMPACT model (*Feng*, 2005). In the IMPACT model running, sea salt aerosols and dust particles are carried in 4 size sections. The radii separating these sections are 0.63
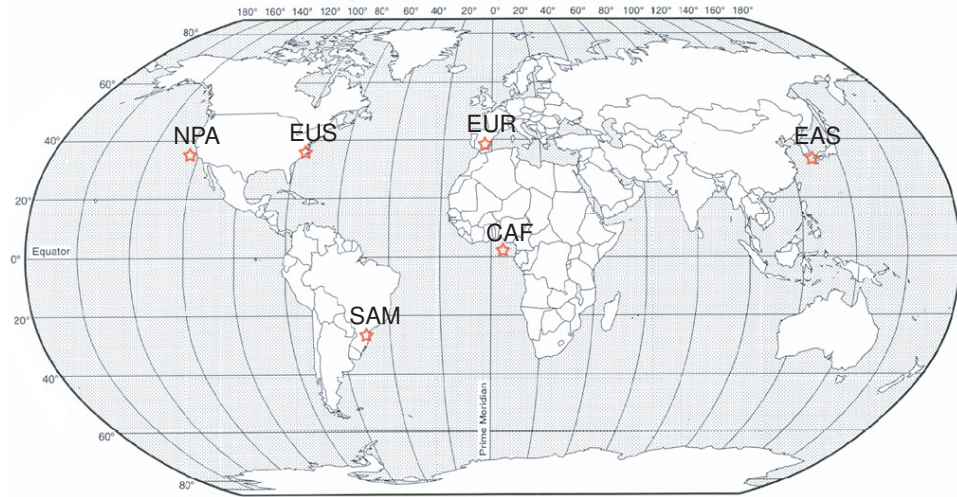
Figure 4.3: Geographical locations of the six sites considered in this study, including Europe site (EUR), Central Africa site (CAF), East Asia site (EAS), East USA site (EUS), Northern Pacific site (NPA), and Southern America site (SAM).

μm, 1.25 μm, and 2.5 μm. The first section represents the fine mode and the rest three are in the coarse mode. Sulfate aerosols are assumed to be only present in the first three sections. Carbonaceous particles (including OC and BC from fossil fuel burning and biomass burning) are assumed to be only in the first section.

We used this mass concentration and a size fitting method to construct the number size distribution of aerosols. With the aerosol composition and size distribution, the cloud nucleation parcel model introduced in Chapter 2 was used to simulate the cloud droplet number concentrations (N_d) in an uplifting air parcel. We will compare the droplet concentration N_d calculated by using different distributions for the nitrate in the gas phase and in the aqueous phase. These distributions were derived from the IMPACT simulation using different aerosol dynamical modules (*Feng*, 2005). We will also study the contribution of HNO_3 in the gas phase and in different sections of aerosol phase to cloud condensation nuclei (CCN) activation. The re-distribution of HNO_3 in different phases during the nucleation process will be investigated.

4.2.2 HNO$_3$ distributions in gas phase and aerosol phase

The distribution of HNO$_3$ in the gas phase and aerosol phase before the cloud nucleation was determined using several different methods implemented in the IM-PACT simulation. The simplest way is to use the equilibrium method (EQU). In the EQU method, the concentration of HNO$_3$ in the aqueous phase is related to the HNO$_3$ gas concentration by the modified Henry's Law coefficient. This method has been used in many previous studies (*Adams et al.*, 1999; *Jacobson*, 2001; *Chin et al.*, 2002). However, the time to establish the thermodynamic equilibrium between the gas and aqueous phase varies substantially depending on particle sizes and ambient meteorological conditions (*Meng and Seinfeld*, 1996; *Seinfeld and Pandis*, 1997). Therefore several other methods that can approximately account for the mass transfer process have been used.

The most accurate method for treating HNO$_3$ thermodynamics is to use a fully dynamic mass transfer calculation applied to each aerosol size bin (*Meng et al.*, 1998; *Jacobson*, 1997; *Pilinis et al.*, 2000). This dynamical method (DYN) is set as the reference method in our study. In this method, a set of the nonlinear time-dependent equations is solved simultaneously in each size bin i (i=1,2,3,...,n):

$$\frac{dC_\infty}{dt} = -\sum_{i=1}^{n} J_i \tag{4.4}$$

$$\frac{dC_i}{dt} = J_i \tag{4.5}$$

$$J_i = 4\pi D_g R_i N_i f\left(K_{n_i}, \alpha\right)\left(C_\infty - C_{i,eq}\eta_i\right) \tag{4.6}$$

where C_∞ is the ambient gas-phase HNO$_3$ concentration, C_i is the aqueous-phase

concentration in the size bin i, $C_{i,eq}$ is the gas-phase HNO_3 concentration at thermodynamic equilibrium in size bin i. J_i is the mass transfer rate in size bin i. D_g is the diffusivity of HNO_3, R_i is the radius of the particles in size bin i, N_i is the aerosol number concentration. f is a function of the Knudsen number (K_{n_i}) and accommodation coefficient (α). η_i is the Kelvin effect correction for size bin i.

Figure 4.4 gives the total aerosol number concentrations and mass concentrations in each section calculated by using the DYN method. Clearly, in all six sites, the number concentration in section 1 dominates, for both January and July. The summation of other three sections is less than 0.1% of the aerosol number in section 1. However, a large portion of the aerosol mass is in the coarse mode (section 2, 3, 4). This aerosol mass may compete for the water vapor with small particles, and thus may affect the total number of cloud droplets nucleated.

The soluble mass fraction in the aerosols will probably affect the effect of nitrate on the cloud nucleation. Therefore, in Figure 4.5, we list the fractions of soluble species in section 1 for all sites. The aerosol particles in regions with large fossil fuel burning, such as EUR, EUS, and NPA, are mainly soluble. In other sites, due to the inclusion of dust and insoluble carbonaceous species, the soluble fraction is lower.

Figure 4.6 shows the ratio of HNO_3 mass in each section to total HNO_3 mass calculated from the IMPACT simulations. The ratio of gas phase HNO_3 mass to total aerosol mass in section 1 is also shown. The fraction of nitrate in the coarse mode is small since most coarse mode aerosols originate from fragmentation of dust and outburst of sea salt. In the small mode (section 1), the nitrate accounts for a large portion in January.

Another alternative approach that is commonly adopted by gas-phase chemistry models is to use the first-order loss rate to account for the uptake of HNO_3 on
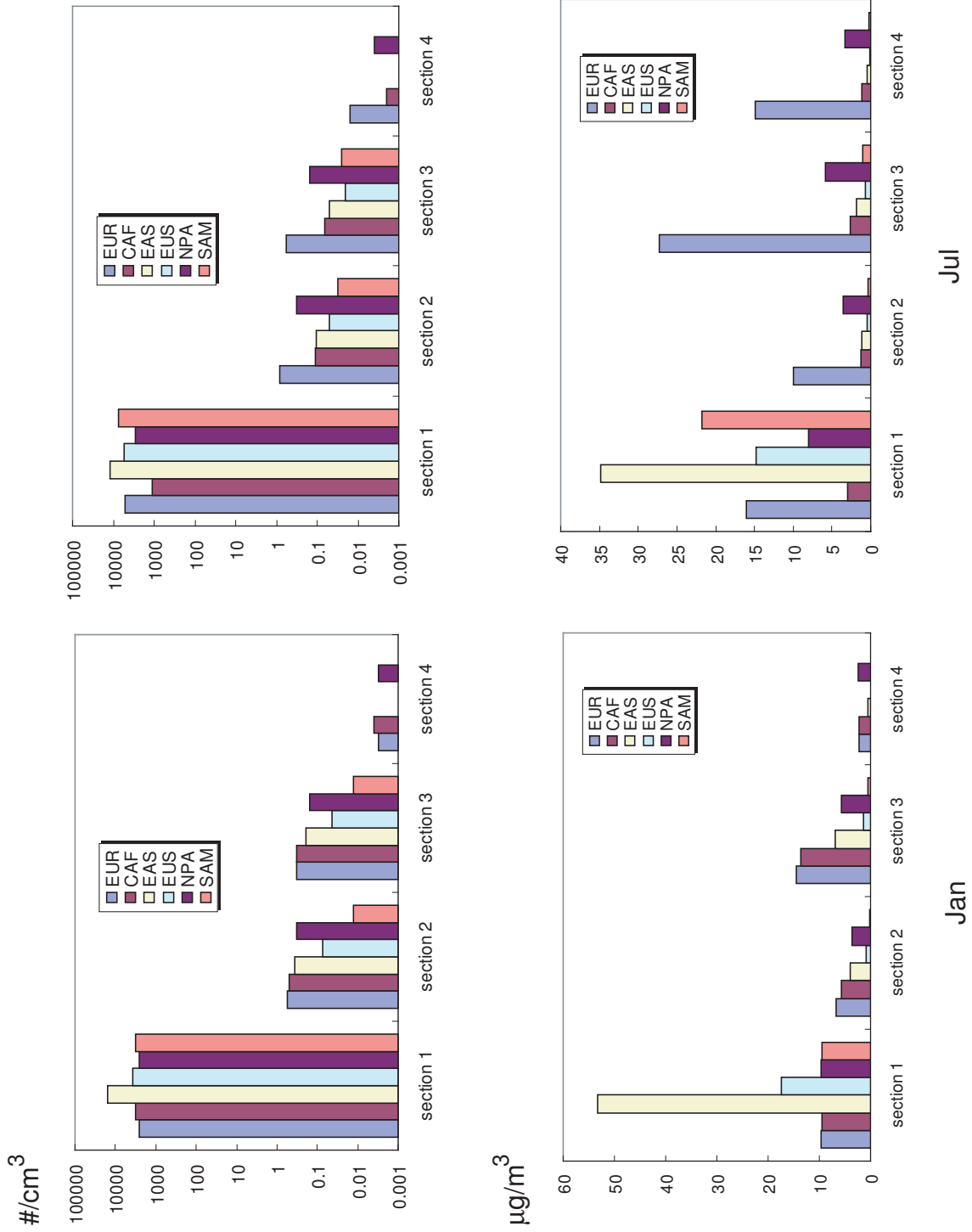
Figure 4.4: Monthly average number and mass concentrations from the IMPACT simulation with the DYN aerosol dynamical module for January and July.
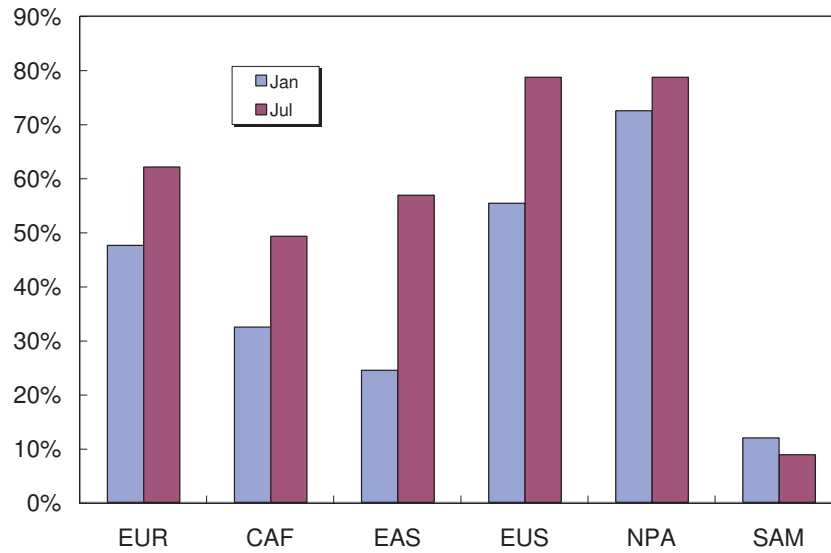
Figure 4.5: Soluble fractions of the aerosols in section 1 calculated from the IMPACT simulation with the DYN aerosol dynamical module at six sites.
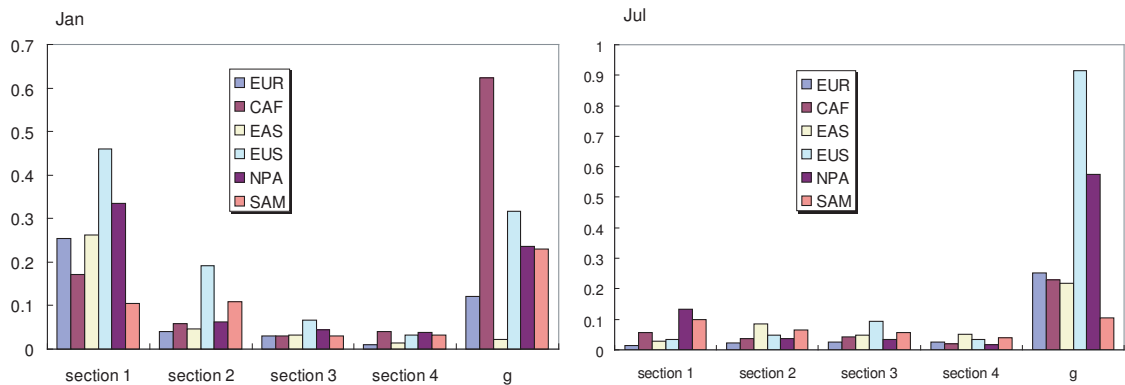
Figure 4.6: The ratio of HNO_3 mass in each section to total HNO_3 mass calculated from IMPACT simulations with DYN aerosol dynamical module. The ratio of gas phase HNO_3 mass to total aerosol mass in section 1 (denoted as g) is also shown (the unit of gas phase HNO_3 has been changed to mass concentration unit).

aerosol surfaces (*Dentener and Crutzen*, 1993; *Tie et al.*, 2003; *Bauer et al.*, 2004). This method is called the uptake method (UPT) in this study. In this method, the removal rate of gas phase HNO_3 is approximated by using a pseudo first-order rate coefficient k:

$$\frac{dC_\infty}{dt} = -\sum_{i=1}^{n} k_i C_\infty \qquad (4.7)$$

$$\frac{dC_i}{dt} = k_i C_\infty \qquad (4.8)$$

$$k_i = 4\pi D_g R_i N_i f\left(K_{n_i}, \nu\right) \qquad (4.9)$$

Compared to the DYN method, the accommodation coefficient α has been replaced by an uptake coefficient ν, which represents all the processes that affect the rate of gas uptake.

The hybrid method (HYB) combines the EQU method and the UPT method (*Liao et al.*, 2003, 2004). The uptake of nitrate by the sulfate and sea salt aerosols is predicted by a bulk-phase thermodynamic equilibrium model, while the uptake of nitrate by dust particles is predicted using the first-order loss rate method.

A Detailed description and comparison of the performance of these methods is shown in *Feng* (2005).

4.2.3   Aerosol number size distribution

The mass concentrations of different aerosol species in four sections as described above are from the IMPACT model run output. To study the aerosol effect on clouds, the number size distribution of the aerosols is constructed based on the

mass concentration in each section. The basic rules of the aerosol size distribution construction are shown below:

1. The total mass in each section calculated from the number size distribution should be the same as the input mass concentration.

2. The number distribution should be continuous at the edge of bins.

3. The number distribution should be always positive.

Two basic functions used in size fitting are $n(r) = \frac{dN}{dr}$, which represents the number size distribution, and $M = \frac{4}{3}\pi\rho \int n(r)r^3 dr$, which is used to calculate the total mass. Note in our calculation, the internal mixing of different aerosol species is assumed.

A log-normal number distribution with $r_g = 0.04$ μm and $\sigma = 1.75$ (*Penner et al.*, 2001a) is used for section 1. So the distribution can be represented by

$$n_1(r) = \frac{N_1}{(2\pi)^{1/2}r\ln\sigma}\exp\left(-\frac{(\ln r - \ln r_g)^2}{2\ln^2\sigma}\right) \tag{4.10}$$

And the total number in section 1 (N_1) can be calculated by

$$M_1 = \frac{4}{3}\pi\rho_1 N_1 \int \frac{1}{(2\pi)^{1/2}\ln\sigma}\exp\left(-\frac{(\ln r - \ln r_g)^2}{2\ln^2\sigma}\right)r^2 dr \tag{4.11}$$

The subscript 1 denotes the section 1.

To assure the continuous distribution between section 1 and section 2, we assume that $n_2(r_{2-1}) = n_1(r_{1-2})$, in which $n_1(r_{1-2})$ is the number concentration for the maximum radius in section 1, and $n_2(r_{2-1})$ is the number concentration for the minimum radius in section 2.

We use the following size distribution for section 2:

$$n_2(r) = \frac{1}{k(r - r_{2-1}) + 1/n_2(r_{2-1})} \tag{4.12}$$

$$M_2 = \frac{4}{3}\pi\rho_2 \int \frac{r^3}{k(r - r_{2-1}) + 1/n_2(r_{2-1})} dr \qquad (4.13)$$

The coefficient k is calculated by assuring that the total mass in this section derived from the distribution is same as that given in the input. This size distribution is better than the linear size distribution, because if a linear size distribution is used, to keep the total mass calculated in this section equal to that from the input, a negative value of $n_2(r)$ at the maximum radius in this section may have to be assumed, which violates rule 3 shown above.

A similar method is used to calculate the size distribution of aerosols in section 3 and section 4. After the above calculations, the aerosol number size distribution in all 4 sections is constructed. A sample size distribution is shown in Figure 4.7. Note that most of the aerosol numbers are in the first section.
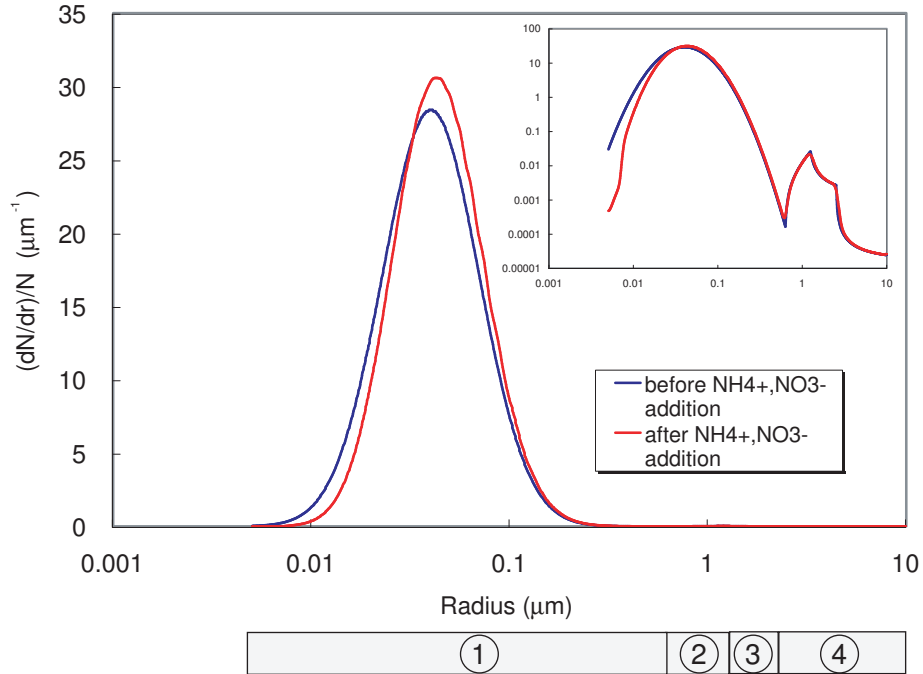
Figure 4.7: Sample size distribution before and after addition of NH_4^+ and NO_3^-. Logarithmic y axis is used in the embedded figure. The numbers in the circles show the range of four size sections used in IMPACT simulation.

The above size fitting applies to aerosol species other than NO_3^- and NH_3^+. NO_3^- and NH_3^+ form through the deposition of volatile gases. Therefore we assume the addition of them does not change the concentration of aerosols. They only modify the size and the chemical composition of the aerosols. Here we term the aerosol before addition of NO_3^- and NH_3^+ as pre-existing aerosols. The mass of NO_3^- and NH_3^+ from the IMPACT simulation is distributed to pre-existing aerosols according to their size distribution. For most aerosol particles, the Knudsen number, which is defined as the ratio of the mean free path of the fluid and the radius of the aerosol particle, is larger than 1. So we may assume the mass transfer is in the kinetic regime. Therefore, the new size distribution after addition of these deposited solutes can be calculated by assuming a surface area weighting addition:

$$dm_{ij} = \left(\frac{S_j}{\sum_{j=1}^{j_i} S_j} \right) m_i(NO_3^-, NH_4^+) \tag{4.14}$$

$$r'_{ij} = r_{ij} \times \left(\frac{m_{ij} + dm_{ij}}{m_{ij}} \right)^{1/3} \tag{4.15}$$

where i denotes the sections (i=1,2,3,4), and j denotes the size bins in each section. dm_{ij} is the deposited mass of HNO_3 and NH_3 in size bin j of section i. r'_{ij} is the new center radius for each size bin. A sample plot of new size distribution after NO_3^- and NH_4^+ is also shown in Figure 4.7.

4.2.4 Results and discussion

The IMPACT model simulations with different aerosol dynamical modules provide different aerosol concentrations and chemical compositions. The main difference between these simulations is in the distribution of nitrate in the aqueous phase and HNO_3 in the gas phase. Based on the aerosol data from the DYN, UPT, HYB and

EQU methods, we calculated the cloud droplet number concentrations (N_d) at the six sites (EUR, CAF, EAS, EUS, NPA, SAM) mentioned above. In the parcel model simulation, a constant updraft velocity 40 cm/s was assumed.

The results are shown in Figure 4.8. Both the January and July results are given. The EAS and EUS sites have a largest N_d in both months. The two sites where biomass burning is the main source of aerosol particles, CAF and SMA, have small N_d. And at the CAF site there is a very clear seasonal difference.

The N_d from the HYB method agrees quite well with that from the DYN method. However, the UPT and the EQU methods both underestimate N_d in all sites by 1% to 12% compared to the more accurate DYN method. The reason why the UPT and the EQU methods tend to underestimate N_d is that in these two methods, more nitrate is distributed to large particles due to their inability to represent the mass transfer process. Because of their low critical supersaturation, these large particles are easily activated even without the addition of nitrate. Therefore, the addition of nitrate does not affect the number of activated particles in these size bins. On the other hand, the nitrate distributed to the size range around $\sim$0.05 μm is smaller from the UPT and the EQU methods. Because this is the size dividing the activated and inactivated aerosols in most conditions, a smaller solution effect can cause smaller N_d calculated from the UPT and the EQU methods, compared to the DYN method.

The nitrate effect on N_d can be calculated by comparing the N_d simulated with and without the HNO_3 gas and nitrate aerosols. The baseline aerosols are given by using the DYN method. For comparison, we also calculate sulfate effect on N_d by removing the sulfate from the aerosol population. Figure 4.9 shows the change in the simulated cloud droplet number concentration due to the nitrate and anthropogenic sulfate. The change of N_d due to HNO_3 and nitrate is between 5% and 30%, de-
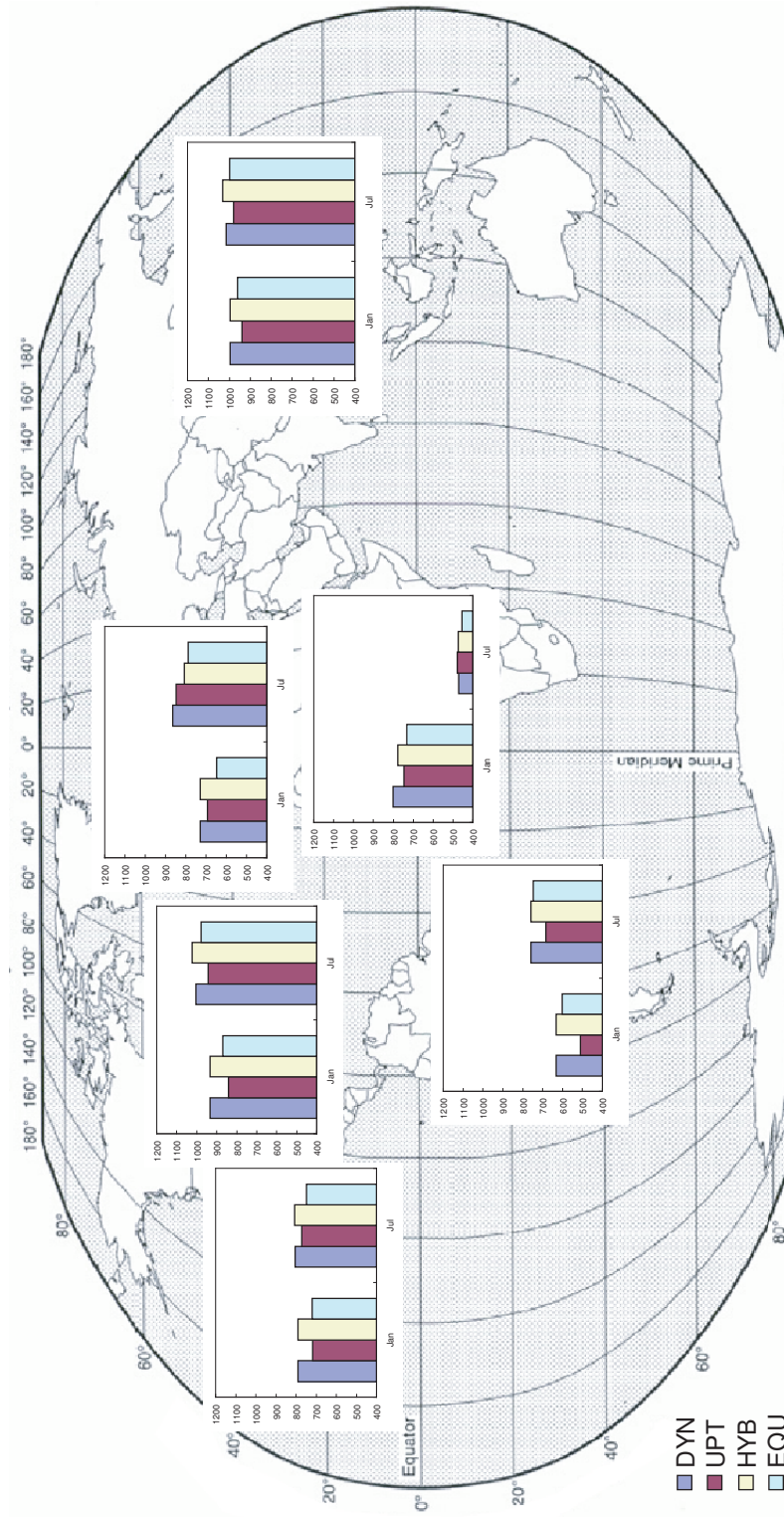
Figure 4.8: Cloud droplet number concentrations simulated by using different aerosol dynamical modules.

pending on the location and the season. The nitrate effect on clouds are comparable to that of anthropogenic sulfate in most sites in July. In January, the relative importance of nitrate is even larger. This simulation gives us an idea of how large the HNO_3 effect on clouds is, compared to the effect due anthropogenic sulfate.
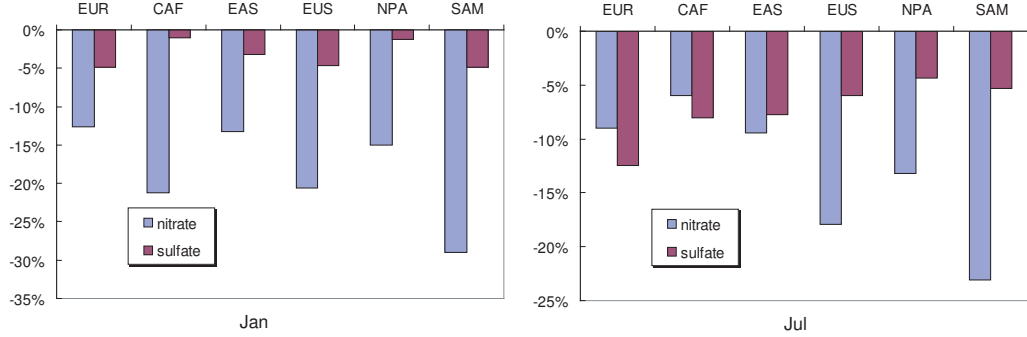
Figure 4.9: Percentage change of cloud droplet number concentrations by removing nitrate in the aerosol and HNO_3 in the air, and by removing anthropogenic sulfate.

In the above calculation, we combined the effect due to HNO_3 gas and the effect due to the presence of nitrate in the aerosol particles. To better demonstrate the HNO_3 effect on cloud droplet number concentration, we differentiate these two effects by adding the nitrate in the aerosol and the HNO_3 gas separately. The nitrate in the fine mode (section 1) and in the coarse mode (section 2,3,4) are also treated individually so that we can see which mode is more important in the nitrate effect on clouds. The results at EUR site are shown in Figure 4.10. We can see that both HNO_3 gas and nitrate in the fine mode contribute to the increase of N_d. The relative importance depends on the distribution of nitrate in gas phase and aqueous phase. In January, most nitrate is in the aerosol particles, so nitrate in the fine mode has a larger contribution than HNO_3 gas. The situation is reversed in July, when the HNO_3 gas concentration effect is more important. On both months, nitrate in the coarse mode has little effect. However, this does not mean that the nitrate in the

coarse mode has no effect in all scenarios. A test (not shown) showed that an increase of the nitrate in the coarse mode by 5 times lowers the maximum supersaturation and decreases N_d.
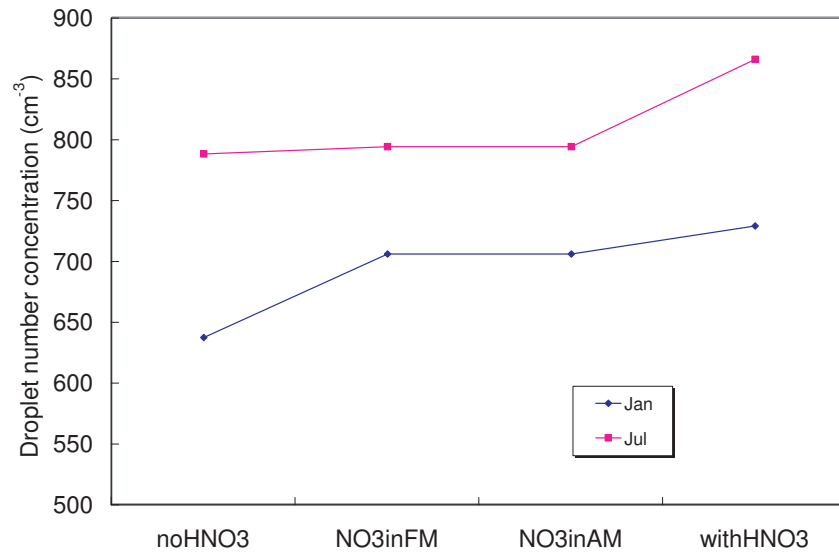
Figure 4.10: N_d calculated at EUR site by using the aerosols from IMPACT run with DYN dynamical module. 'noHNO3' means no gas or aerosol nitrate is included. 'NO3inFM' denotes the only nitrate is the NO_3^- in fine mode aerosols. 'NO3inAM' denotes NO_3^- is in both fine mode and coarse mode aerosols. 'withHNO3' means the gas phase HNO_3 is also included besides the NO_3^- in the aerosol particles.

Basically, two counteracting effects caused by HNO_3 and nitrate modify the simulation of cloud droplet number concentration. First, the addition of nitrate (a part is from the deposition of HNO_3 in the gas phase) increases the size and the solute concentration in the aerosol particles. This change affect both the Kelvin effect and the Raoult effect. The increase in size lowers the surface tension term in the Köhler curve and thereby decreases the equilibrium vapor saturation (Kelvin effect). The addition of dissolved molecules of solute in the aqueous phase also decreases the equilibrium vapor pressure according to Raoult effect. This effect is influenced by the fraction of soluble species in the pre-existing aerosols. When the pre-existing

aerosol is mainly non-soluble, the addition of nitrate can boost the water uptake ability, thereby increasing the cloud droplet nucleated. This is why the N_d change due to nitrate is so large at the SAM site as shown in Figure 4.9. The generally larger change in N_d change due to nitrate in January compared to July could also be mainly explained by this. In addition to the soluble fraction in pre-existing aerosols, the nitrate effect on N_d is also related to the total mass of nitrate and HNO_3. The second way that nitrate affects the cloud nucleation is through the modification of the maximum vapor pressure obtained during the uplifting of the parcel. When the number of aerosol particles is sufficiently large, the availability of water vapor could be a factor influencing the cloud nucleation. The addition of nitrate competes for water vapor with the pre-existing aerosol particles, therefore the maximum supersaturation obtained in the uplifting process is lower. The result of this effect is to decrease the number of aerosols activated, and may counteract the first effect.

The change in the distribution of HNO_3 in the gas phase and aqueous phase in the cloud nucleation processes can be explained by using Figure 4.11 and Figure 4.12. Figure 4.11 clearly shows that most gas phase HNO_3 is transformed to nitrate in the fine mode aerosols. Figure 4.12 shows the size-resolved aqueous phase NO_3^- concentration recorded in the parcel model simulation. From this plot, we can see that for the fine mode aerosol, the change of nitrate is different for small particles and big particles. For the particles large enough to be activated to form cloud droplets, more nitrate is added by the deposition of gas phase HNO_3 molecules, as a result of increase in surface area during the updraft. For small particles which are not activated in the updraft, the main flow of HNO_3 is from aqueous to gas phase, due to the small equilibrium HNO_3 vapor pressure for these aerosols.

The change of N_d due to the above two effects may be affected by other fac-
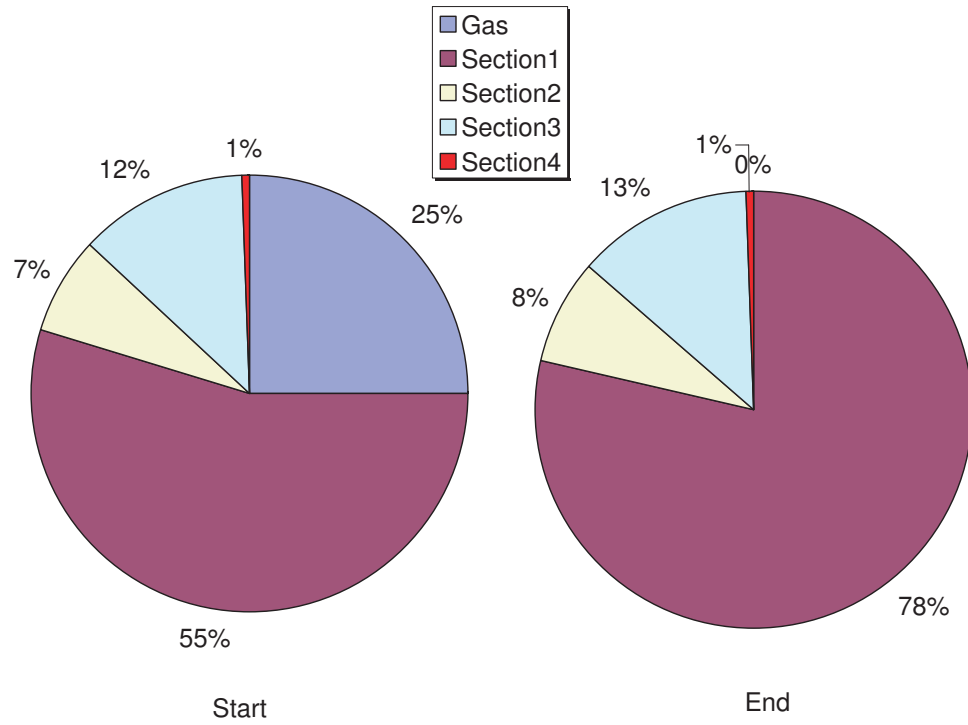
Figure 4.11: The fraction of nitrate in gas phase and in different sections of aerosol phase at the beginning and at the end of parcel model simulation.
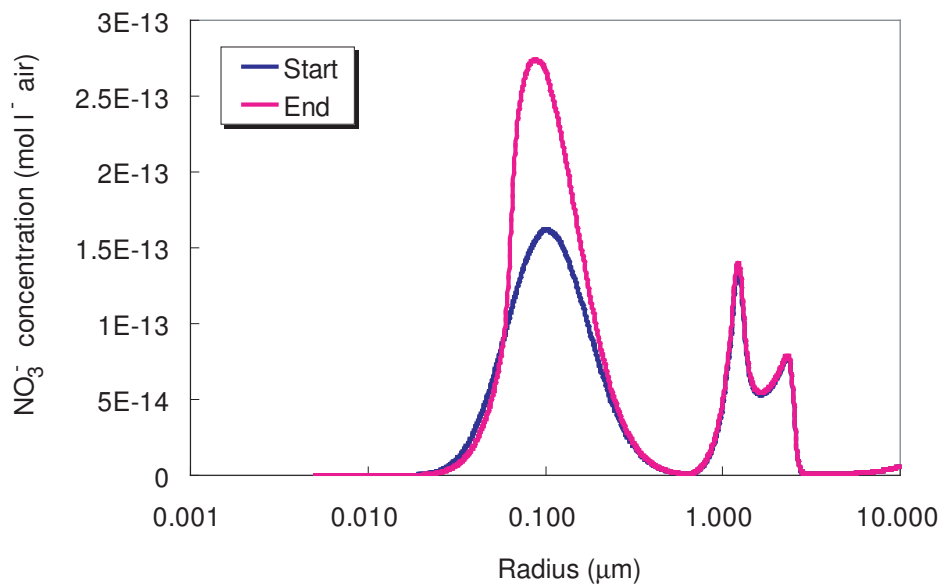
Figure 4.12: NO_3^- distribution in each size bin at the beginning and at the end of parcel model simulation.

tors. The pre-existing aerosol mass and the updraft velocity (w) can influence the availability of water vapor in the air parcel and decide whether the competition of water vapor between different aerosol particles is important. The temperature (T) is also important in determining the equilibrium and the mass transfer rate of HNO_3. The choice of equilibration relative humidity (ERH), which is the relative humidity at the start of parcel model simulation where the equilibrium state of water vapor is assumed, may also affect the number of droplets activated during a cloud model simulation (*Romakkaniemi et al.*, 2005). Therefore, in the following study, we did several sensitivity tests by modifying the total pre-existing aerosol mass, the updraft velocity, the temperature, the ERH value, together with the previously mentioned soluble fraction in aerosol particles, the nitrate and HNO_3 concentrations. These cases are based on the DYN aerosol results at the EUR site on January. The results are given in Figure 4.13.

The nitrate effect on N_d depends on the mass of pre-existing aerosol particles. We can see the change of N_d by adding nitrate is very large when the mass of the pre-existing aerosols is small. This is partly due to the non-linear relationship between N_a and N_d (N_d increases much faster when N_a is small), partly due to the small water vapor competition in this case. The increase of HNO_3 and NO_3^- concentrations obviously enhanced the cloud nucleation. As mentioned above, the nitrate effect is more distinct when the soluble fraction of pre-existing aerosol particles is smaller. Figure 4.13 shows that reducing the soluble fraction by one half almost doubles the nitrate effect. The temperature can change the adiabatic cooling rate and the nucleated CCN due to the non-linear equilibrium vapor saturation as a function of T. However, the change in T does not change the nitrate effect too much according to our simulation. Updraft velocity can change both the number of N_d and the nitrate
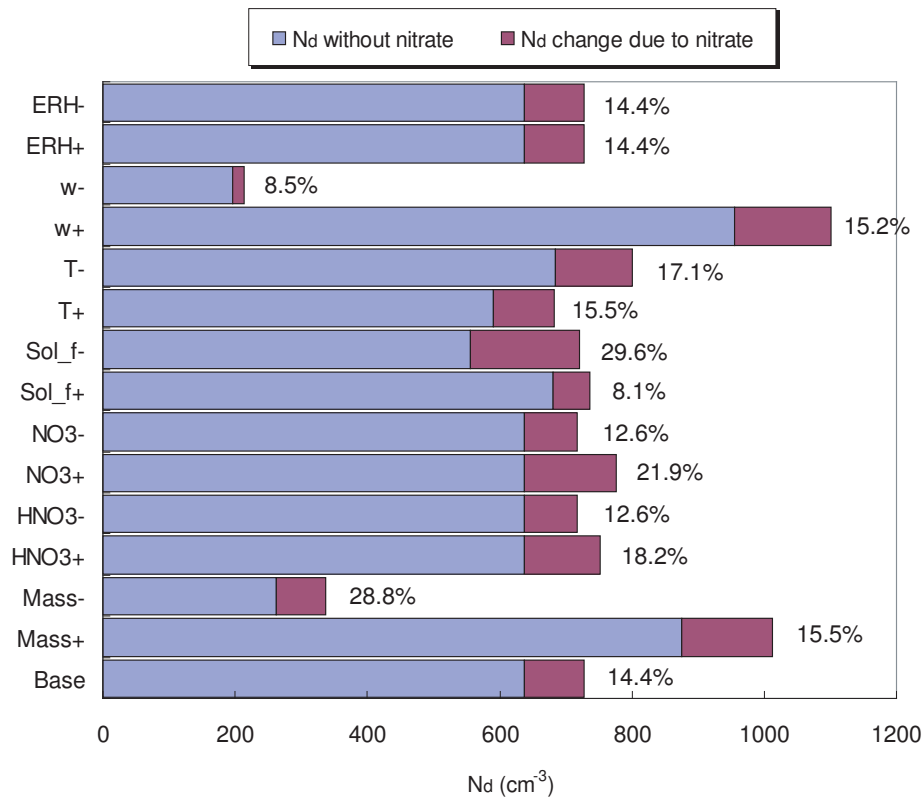
Figure 4.13: Sensitivity tests of different parameters on the change of cloud droplet number concentration due to inclusion of nitrate. The bars show the N_d values with or without nitrate. The numbers shown on the right of the bars are the percentage change of N_d from simulations without nitrate to with nitrate. In the base case, temperature is assumed to be 15 °C, and updraft velocity is assumed to be 40 cm/s. The ERH is set to 98%. In Mass+ and Mass- cases, the mass concentrations of all species other than NO_3^- are multiplied or divided by 10. In HNO3+ and HNO3- cases, the gas phase HNO_3 concentration is doubled or halved. In NO3+ and NO3- cases, the NO_3^- concentration is doubled or halved. In Sol_f+ and Sol_f- cases, the soluble fraction of pre-existing aerosols is doubled or halved. Temperature is set to be 25 °C and 5 °C for T+ and T- cases. Updraft velocity is set to be 70 cm/s and 10 cm/s for w+ and w- cases. ERH is set to be 99% and 97% in ERH+ and ERH- cases, respectively.

effect on N_d. When the updraft velocity is low, the change in N_d due to NO_3^- and HNO_3^- is smaller, probably because of the slowdown of HNO_3 vapor deposition on aerosol and cloud particles. The change in N_d is small when ERH changes from 97% to 99%.

4.3 Effect of nitrate on radiative flux

The radiative forcing of HNO_3 and nitrate aerosols on clouds was calculated by using the cloud droplet number concentration simulated above and a radiative transfer model. To calculate the forcing, two scenarios were used. In the first scenario, HNO_3 mixing ratio and nitrate mass in aerosol particles were obtained from the IMPACT simulation using the DYN thermodynamic aerosol module. In the second scenario, the HNO_3 mixing ratio and nitrate mass in aerosol particles are assumed to be zero. The difference in the top of atmosphere (TOA) short wave fluxes calculated for these two scenarios is the nitrate aerosol indirect forcing.

The nitrate aerosol indirect forcings simulated under different cloud conditions are shown in Figure 4.14. The uncertainties due to cloud fraction and cloud LWC are also indicated in the plot. In the base simulation, two cloud layers are assumed as in *Feng et al.* (2004). Clouds are placed between 2-3 km and 3-4 km. Column cloud fractions in these two layers are 0.5 and 0.5. The cloud liquid water content is 0.2 gm^{-3}. The error bars shown in the plots are obtained from the simulation tests, in which we change the cloud fraction and cloud LWC. We used a setting for cloud fractions of 0.1 and 0.2 (low cloud fraction case), and 0.7 and 0.9 (high cloud fraction case). We also used cloud LWC=1.2 gm^{-3} to examine the impact of a higher liquid content.

The forcing of nitrate is related to the N_d change due to the addition of NO_3^-
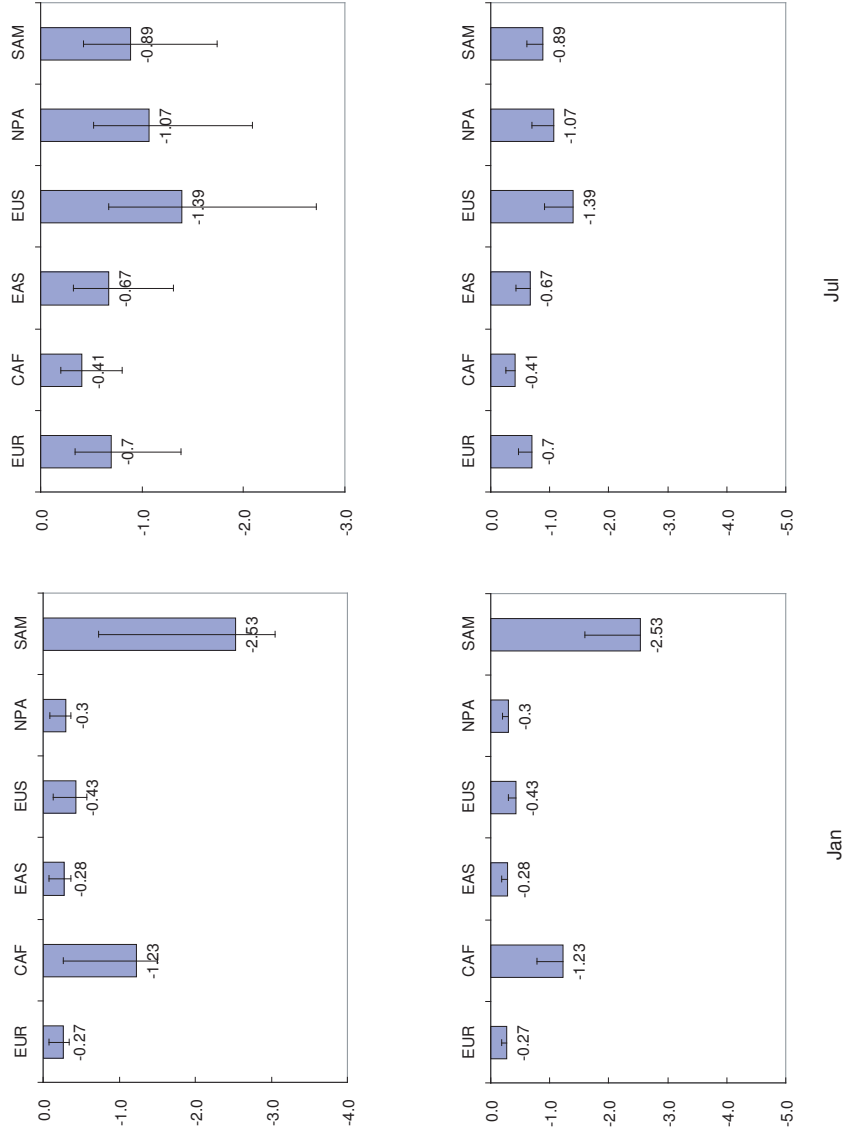
Figure 4.14: Nitrate forcing simulated by a radiative transfer model. Two cloud layers are assumed to be located between 2-3km and 3-4km, respectively. In the base case, the cloud fractions are 0.5 and 0.5. The cloud LWC is 0.2 gm^{-3}. The uncertainty bars for the top two graphs show the perturbation by changing the cloud fraction to 0.1 and 0.2, and 0.7 and 0.9. The uncertainty bars for the bottom two graphs show the perturbation by changing the cloud LWC to 1.2 gm^{-3}.

and HNO_3. Therefore, the relative magnitude of nitrate forcing for the different sites shown in Figure 4.14 is similar to the percentage change in N_d shown in Figure 4.9. However, the difference in solar incident radiation also affects the value of nitrate indirect forcing. For the sites in Northern Hemisphere (EUR, EAS, EUS, NPA), the forcing tends to be larger in July. For the SAM site which is in Southern Hemisphere, the forcing is much larger in January than in July, due to a combination effect of high nitrate in fine mode and high solar incident radiation. Although the CAF site is also in Northern Hemisphere, the much larger HNO_3 concentration in January makes the N_d change higher than July. This effect dominates the effect due to the difference in solar incident radiation, so the forcing is higher in January at the CAF site.

What we also can see from Figure 4.14 is the uncertainty of the calculated nitrate indirect forcing due to different choices of CF and LWC. The absolute value of this forcing is larger when the cloud fraction is larger and the LWC is smaller.

The forcings at the EUP site by simulations using different aerosol dynamical module methods are shown in Figure 4.15. The two month (January and July) average values are given. The uncertainties due to different options of CF and LWC are shown as the error bars. Similar to the results for the nitrate effect on N_d, the forcing value by using the HYB method is very close to that using the DYN method. The UPT method underestimates the forcing on average by about 30%.

The nitrate aerosol forcing calculated for January and July has been averaged and compared to the indirect forcing due to anthropogenic sulfate aerosols (see Figure 4.16). At these sites, the nitrate aerosol indirect forcing is comparable to that of anthropogenic sulfate. This large forcing indicates that in the future calculation of aerosol indirect effect, the effect of nitrate aerosols and HNO_3 gas can not be omitted.
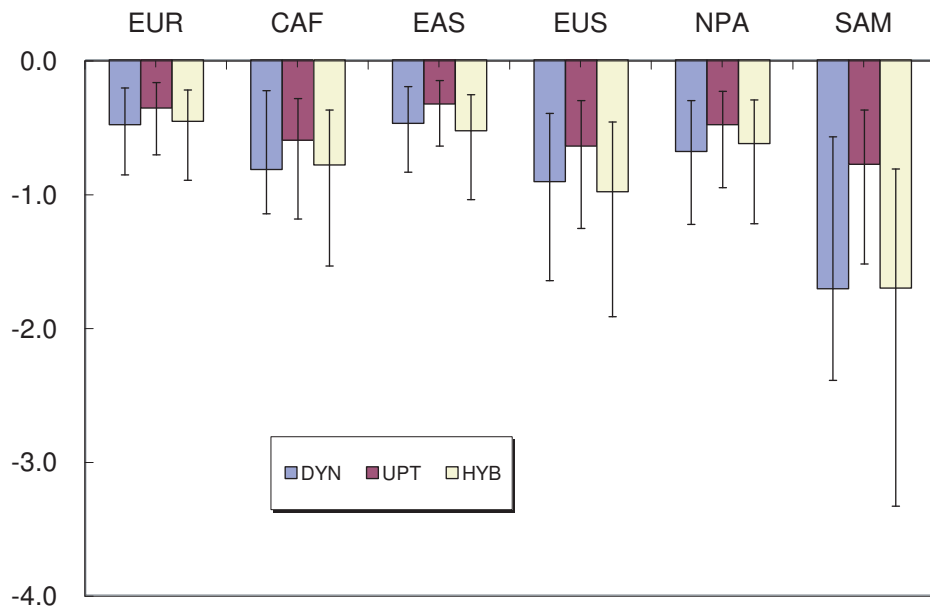
Figure 4.15: January and July average nitrate indirect forcing (Wm^{-2}) calculated by using different aerosol dynamical modules.
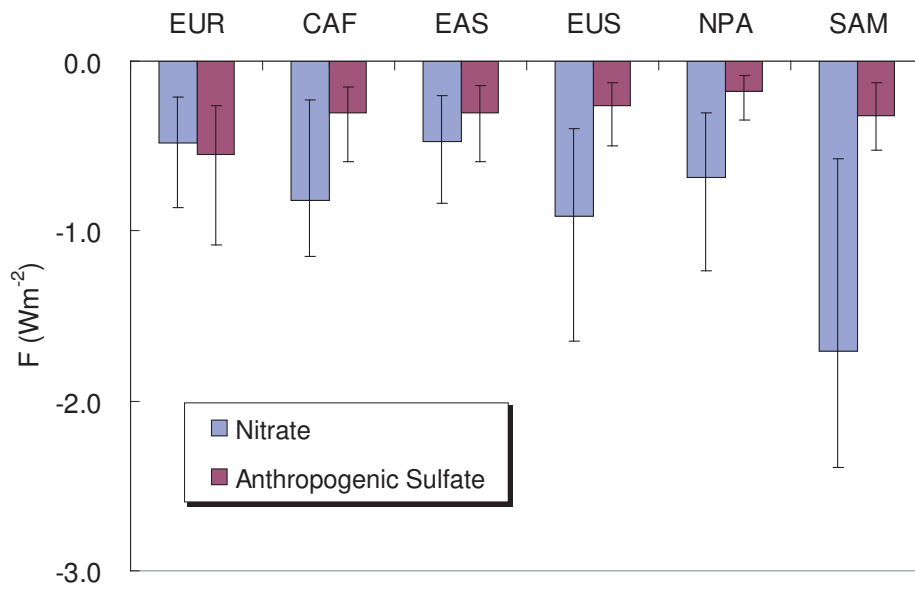
Figure 4.16: Simulated January and July average aerosol indirect forcing by nitrate and anthropogenic sulfate.

4.4 Cloud droplet number parameterization including nitrate effect

4.4.1 Introduction

To simulate the aerosol indirect effect, it is essential to relate the cloud droplet number concentration to the aerosol properties. The calculation of N_d can be obtained by detailed simulations such as the cloud parcel model simulation we used in the above study. However, applying these detailed simulations on the global scale is not realistic due to the large computation time needed. Therefore a parameterization is usually used, either an empirical method based on measurements, or a mechanistic method based on microphysics.

The empirical methods link the cloud droplet number concentration and aerosol properties based on surface measurements or chamber experiments. They do not represent any physical mechanisms in the nucleation process. Physically based parameterization methods use information of aerosol properties and the atmosphere to estimate the maximum supersaturation a rising parcel could obtain. They explicitly or implicitly assume the solute mass in a droplet is fixed as it grows in size. Therefore, the critical size can be calculated according to Köhler curve based on the aerosol size and composition at the cloud base.

However this is not often the case. When highly or weakly soluble gases are in the atmosphere, or weakly soluble substances are in the aerosol, the critical saturation ratio of water vapor can change during the updraft process (*Kulmala et al.*, 1997). *Kulmala et al.* (1993b) used numerical simulations to show that enhanced concentrations of atmospheric nitric acid vapor affect the cloud formation by increasing the number of cloud droplets. The study in our research also shows this effect.

Here we propose a parameterization method in which the effect of HNO_3 is con-

sidered. In this method, we distribute the gas phase HNO_3 into aerosol particles within some size range. Then a physically based cloud nucleation parameterization which represents the sectional aerosol size distribution is used to calculate the cloud droplet number concentration.

4.4.2 Substitution method

Figure 4.11 shows that at the time of activation, most HNO_3 molecules are deposited in section 1 in the aerosol phase. So variation of the gas-phase HNO_3 is generally controlled by equilibrium with the fine-mode particles.

As stated before, most of the mass transfer to the aerosol particle size is in the kinetic region. Therefore, we re-distribute the gas-phase HNO_3 to the fine mode aerosols by using the surface area weighting method. Figure 4.17 shows a comparison of simulated N_d before and after nitrate re-distribution by using an air parcel model. Both simulations are based on aerosols and HNO_3 gas from the IMPACT simulations with the DYN thermodynamic module. The only difference between them is that we re-distribute all the gas phase HNO_3 into the fine mode aerosols in one case. They show good agreement for most simulations. The relative bias defined as $RMS(N_{DYN}-N_{sub})/MEAN(N_{DYN})$ is less than 5%. And there is no systematic bias when the re-distribution of HNO_3 is used. This comparison provided the basis for using the re-distribution of HNO_3 in the aerosols to estimate N_d.

Since the detailed parcel model simulation on a global scale is impractical, we need to use a parameterization to relate cloud droplet number concentration to aerosol properties. The physically based cloud nucleation methods that use a sectional representation of aerosol population can treat any aerosol size distribution and chemical composition. Therefore, we chose two such parameterization methods, one by *Abdul-*
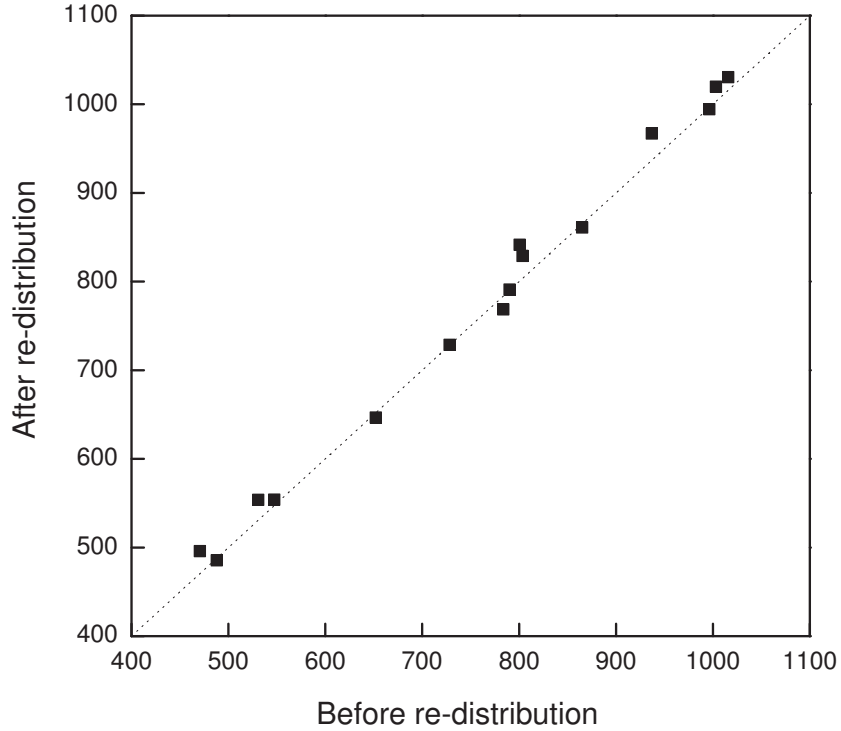
Figure 4.17: Comparison of N_d by a parcel model simulations before and after re-distributing HNO_3 to fine mode aerosols. The unit is cm^{-3}.

Razzak and Ghan (2002) (Later as AG3), and one by *Nenes and Seinfeld* (2003) (Later as NS), to calculate the cloud droplet number concentrations. According to the above theory, we distributed the gas phase HNO_3 to the aerosol particles by assuming all HNO_3 molecules are deposited on the first section (fine mode). We also assumed the mass added to each size bin in section 1 is calculated based on the fraction of surface area. We call this method as the 'substitution method'.

Tests have been done to show the performance of this parameterization. Figure 4.18 shows a comparison of N_d from the detailed parcel model simulation and from the substitution method. The results from the AG3 and NS parameterizations without considering the HNO_3 gas effect is also shown for comparison. For simplicity, we assume a single lognormal size distribution (r=0.05 μm, σ=1.9) for the aerosol

population. The pre-existing aerosols are pure ammonium sulfate. We varied three variables in the test: the aerosol number concentration, the updraft velocity, and the HNO_3 mixing ratio in the atmosphere. The results show that the substitution method can capture the increase of N_d due to the deposition of HNO_3. However, we can see the N_d from the AG3 parameterization is biased to larger values, particularly when the N_d values are high, While the N_d from the NS parameterization is biased to small values when the activation ratio is small. When the activation ratio is high, an overestimation is observed. This can not be explained by the difference of nitrate distribution in re-distribution method and in DYN method, since Figure 4.17 shows there is no clear systematic bias between them. We suppose this bias comes from the AG3 and NS parameterization methods themselves. According to Figure 3 in the paper by *Abdul-Razzak and Ghan* (2002), AG3 method tends to overestimate the N_d when the aerosol number is high. And the plots in *Nenes and Seinfeld* (2003) also show their method tends to underestimate the N_d, particularly in cases with high aerosol activation ratios.

4.5 Summary

In this chapter, we studied the aerosol indirect effect by an important aerosol component nitrate, and its counter part in the atmosphere, HNO_3. Different distribution methods of nitrate in the gas phase and aerosol phase were used to calculate the cloud droplet number concentration in different representative sites on the earth. Compared to the more accurate DYN method, the HYB method produces very similar N_d. The UPT and EQU methods tend to underestimate the cloud droplet number concentration. Both nitrate in the aqueous phase and HNO_3 in the gas phase have an effect on cloud nucleation. Most of the HNO_3 gas is re-distributed to the fine mode
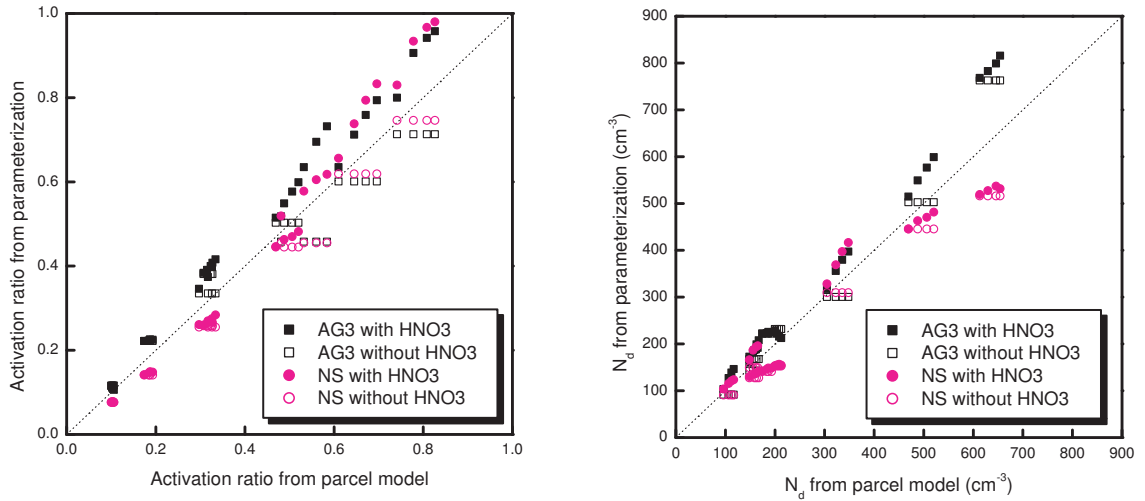
Figure 4.18: The comparison of simulated N_d from detailed parcel model and from the parameterization by assuming the gas phase HNO_3 is distributed to find mode aerosols according to surface area distribution. The N_d values from the parameterization without considering gas phase HNO_3 effect are also shown. Two physically based parameterizations (*Abdul-Razzak and Ghan* (2002) (AG3), *Nenes and Seinfeld* (2003) (NS)) are used.

aerosols in the uplifting process. The change of N_d due to nitrate and HNO_3 gas is affected by some properties of the aerosol particles and the atmosphere, including the soluble fraction of the pre-existing aerosol, the pre-existing aerosol concentration, the HNO_3 concentration in the atmosphere, the NO_3^- concentration in the aerosols, the updraft velocity, etc.

We also calculated the indirect radiative forcing due to the nitrate and HNO_3, and compared it to the anthropogenic sulfate indirect forcing. Different options of cloud fraction and cloud liquid water content were used. The nitrate aerosol indirect effect on the TOA radiative flux was found to be comparable to that by anthropogenic sulfate at these sites.

Based on the theory that most HNO_3 is transferred to fine mode aerosol particles, we re-distributed the HNO_3 to the aerosol phase according to the surface area dis-

tribution. Then, two parameterization methods (AG3 and NS) were used together with the new nitrate distribution to approximate the effect due to HNO_3 gas. A comparison of N_d from the parameterization and from the model was made and discussed. The substitution method is better in representing the HNO_3 effect than the original non-HNO3 method.

Other condensable species, such as HCl and NH_3, may have a similar effect on the CCN activation. There are very few studies to quantify the effects by HCl and NH_3 on clouds and climate. We hope to include them in a future study.

CHAPTER V

Influence of anthropogenic aerosols on cirrus clouds and global radiation

5.1 Introduction and motivation

5.1.1 Cirrus clouds and the nucleation mechanisms

The fraction of cirrus cloud cover is about 30% globally and more than 70% in the tropics (*Wylie and Menzel*, 1999). Cirrus clouds scatter shortwave solar radiation (SW) and absorb longwave terrestrial radiation (LW), thereby modifying the global radiative balance (*Liou*, 1986). Cirrus clouds may also modify the formation and the properties of aerosols in the upper troposphere. The formation of new particles is favored in this region (*Liu and Penner*, 2005) and these newly formed particles may grow to Cloud Condensation Nuclei (CCN) and impact the cloud formation (*Lee et al.*, 2003, 2004). Pre-existing aerosols can also be modified by heterogeneous reactions on ice crystals (*DeMott et al.*, 2003). In addition, cirrus clouds have an important role in precipitation initialization as well as influencing the ozone concentration in the upper troposphere and lower stratosphere (*Borrmann et al.*, 1996; *Kley et al.*, 1996).

Cirrus clouds are made of ice crystals. The creation of new ice phase from a metastable state occurs via germs of the new phase (*Vali*, 1996). The free energy

131

of a germ has to be overcome before it becomes stable. This phase transition can take place through either homogeneous nucleation or heterogeneous nucleation. Homogeneous nucleation is the spontaneous freezing of a supercooled droplet or haze particles at sufficiently low temperature and is the dominant nucleation mechanism in upper troposphere if the supersaturation with respect to ice is large (*Jensen and Toon*, 1994). Heterogeneous nucleation occurs when the foreign material is available for nuclei. This foreign material (called ice nuclei, IN) can be bacteria debris, or mineral dust, or soot particles. Heterogeneous nucleation could also be important because it occurs at lower supersaturation (*DeMott et al.*, 1998). IN such as soot particles coated with sulfuric acid requires a vapor saturation ratio with respect to ice $S_i \approx 1.3$ before freezing occurs (*Kärcher et al.*, 1998; *Mohler et al.*, 2005), compared to a requirement of $S_i \approx 1.4 - 1.7$ for homogeneous nucleation (*Koop et al.*, 2000). The INterhemisphere differences in Cirrus properties from Anthropogenic emissions (INCA) field measurements provided evidence for the existence of heterogeneous nucleation in mid-latitude cirrus clouds (*Haag et al.*, 2003). However, there are still open issues regarding the preferred mode of ice nucleation in cirrus clouds (*DeMott et al.*, 2003). No decisive data on this topic have been published.

For heterogeneous nucleation, several nucleation modes represent the different pathways in which the liquid phase or vapor phase is converted to ice phase (*Vali*, 1996). The deposition nucleation mode is the direct deposition of water vapor on the surface of IN. The condensation freezing mode occurs when an aerosol particle first serves as a CCN to form a drop, which then freezes at some time during the condensation stage. The immersion mode refers to the freezing of a haze drop in which the IN is immersed. This mode is common for those particles with insoluble core and soluble coating. The contact mode occurs when the IN comes into contact

with the supercooled drop and causes freezing. The condensation freezing mode and the contact mode may be dominant in mixed-phase clouds with the temperature between 0 and -37 ℃ (*Pruppacher and Klett*, 1997). However, in cirrus clouds, because the relative humidity rarely exceeds the water supersaturation to activate the CCN, the condensation freezing mode is not important. So we do not consider this mode here. The contact mode is also omitted in this study, since the collision and collection rate between IN and drops are low in the upper troposphere (*Young*, 1993).

5.1.2 Ice crystal number in cirrus clouds

A key but still poorly understood parameter in studying cirrus clouds is the ice crystal number concentration (N_i). Similar to the Twomey effect occurred in warm clouds, a change in N_i can modify the size of ice crystals, thereby changing the microphysical and radiative properties of cirrus clouds. *Gultepe et al.* (1998) showed that a 50% uncertainty in equivalent radius for ice crystals may cause a 10 Wm^{-2} change in net radiative cloud forcing. Better understanding and estimation of N_i are also important for a better understanding of the atmospheric moisture budget (*Fowler and Randall*, 1996), and for a better estimation of the greenhouse gas warming effect (*Senior and Mitchell*, 1993).

The value of N_i depends on microphysical, thermodynamical, and dynamical parameters as well as the characteristics of the aerosols which form the ice. The interactions between these factors are complex. Variations in the factors that drive the nucleation of ice and variations in the physical and chemical characteristics of aerosol particle populations lead to the formation of cirrus with different microphysical characteristics (*DeMott et al.*, 2003). Low temperature (T) and high relative humidity

with respect to ice (RH$_i$) are necessary conditions for ice formation. Aerosol particles can change N$_i$ in different ways, depending on the aerosol properties and the environment for cloud nucleation. Although sulfate has sometimes been observed to dominate the aerosol population (*Sheridan et al.*, 1994), insoluble species were found in a large proportion of aerosols on other occasions (*Chen et al.*, 1998; *Talbot et al.*, 1998; *Buseck and Posfai*, 1999). The main pathway for sulfate aerosols to affect the cirrus clouds is through homogenous freezing of sulfate haze particles. The presence of insoluble aerosols that act as IN can alter this pathway through heterogeneous nucleation.

The relationship between N$_i$ and the properties of aerosol particles is not very clear yet. Previous studies showed that the majority of particles found in the troposphere are not IN (*Sassen and Dodd*, 1988). However, *DeMott et al.* (1994) suggested that changing aerosol size and composition may have a large impact on cirrus formation and the crystal number concentration. And several measurements have demonstrated that N$_i$ can be modified by aerosols (*Ström and Ohlsson*, 1998; *Kristensson et al.*, 2000). Anthropogenic activities can change the concentrations and properties of aerosol particles in the upper troposphere and affect the crystal number concentrations in cirrus clouds. However, in most current GCMs, simple relationships between N$_i$ and temperature (T) or supersaturation (S$_i$) or both (*Fletcher*, 1962; *Meyers et al.*, 1992) are used. These relationships are derived from measurements at low altitudes or from chamber experiments in relatively warm temperatures (-2 $\sim$ -30 °C) (*Gultepe et al.*, 2001). So they may be not suitable for simulations of upper troposphere atmosphere, where the temperature and aerosol concentrations are much lower, and the vapor supersaturation could be much higher. In addition, these relationships do not include the ice number dependence on aerosol particles

and the competition between different ice nucleation modes. Therefore they can not be used to study the impact of anthropogenic aerosols on the climate through their alteration of cirrus clouds.

5.1.3 Aerosol effect on cirrus and climate

The radiative properties of cirrus clouds are very sensitive to the size, concentration, phase, and shape of the cirrus particles (*Stephens et al.*, 1990). These cloud properties could be affected by changes in aerosol particles acting as ice nuclei (IN). The role of anthropogenic aerosols on cirrus cloud properties is still an open question because the interactions between aerosols and cirrus clouds are complex and poorly known, and measurements of cirrus cloud properties are sporadic due to the lack of appropriate instruments, the low concentration and irregular shape of ice crystals, and the high altitude of occurrence. This dearth of measurements make it hard to fully validate results from models of cirrus formation and their interaction with aerosols.

Human activities can influence concentration of aerosol particles in the upper troposphere in several ways. For example, surface generated soluble and insoluble particles due to combustion processes could be transported to high altitude by cumulus convection. Soot particles from biomass burning and fossil fuel burning become more soluble when aging in the atmosphere (*Cachier et al.*, 1995; *Liousse et al.*, 1996; *Liu et al.*, 2005). Aircraft exhaust contains insoluble soot which becomes coated with the soluble sulfate in the exhaust plume(*Mohler et al.*, 2005). Global aviation has experienced rapid growth and the total aviation fuel use was projected to increase by 3% per year between 1990 and 2015 (*Penner et al.*, 1999). This changing of aerosol particles may affect the ice nucleation process and the ice crystal number. *Ström*

and Ohlsson (1998) observed that the crystal number density is enhanced about a factor two in cirrus clouds where the soot content exceeded 0.01 μg m^{-3} compared to cirrus with less soot. If the cloud water content remains constant, a two-fold increase in crystal number would translate into a reduction of the mean crystal size by about 20%. This reduction of crystal size will modify both the SW and LW radiative balance in the atmosphere, and may therefore change surface temperatures. *Kristensson et al.* (2000) observed that the effective crystal diameter decreased by 10-30% in cirrus clouds perturbed by aircraft. The radiative forcing due to increased cloudiness by increasing aviation-produced aerosols is believed to be small on a global scale, but could approach 1 Wm^{-2} regionally (*Fahey and Schumann*, 1999; *Boucher*, 1999). *Minnis et al.* (2004) estimated the maximum contrail radiative impact by assuming that the long-term trends in cirrus coverage are due entirely to air traffic in areas where humidity has been relatively constant over time. They estimated a radiative effect of between 0.006 and 0.025 Wm^{-2} over the US.

The effect of aerosols on cirrus clouds could be very different for different modes of nucleation. If homogenous freezing of solution droplets is the dominant formation path of cold cirrus, then the number of ice crystals formed is expected to depend on the updraft velocity, and is relatively insensitive to the number of aerosols or their composition (*Jensen and Toon*, 1994). This is because soluble particles are not the limiting factor that determine the number of cirrus ice crystals (*Haag and Kärcher*, 2004). When heterogeneous nucleation is dominant, an increase in IN can increase the concentration of ice crystals formed. A pronounced indirect aerosol effect on cirrus is also possible when two types of freezing aerosol particles compete during cloud formation. Adding efficient ice nuclei to liquid aerosol particles can lead to a marked suppression of RH$_i$ and thereby reducing ice crystal number densities if the number of

heterogeneous IN is less than the number of homogeneous IN. The magnitude of this effect depends on the updraft velocity, temperature, and the number and freezing properties of the ice nuclei (*Kärcher and Lohmann*, 2003).

The importance of heterogeneous IN on cirrus clouds is unknown. *Heymsfield and Miloshevich* (1993) and *Jensen and Toon* (1994) concluded that homogeneous nucleation of supercooled drops are responsible for the occurrence of ice, and that aerosol properties do not significantly affect cirrus cloud properties. However, *Rogers* (1994) and *DeMott et al.* (1994) argued that even a small number of heterogeneously nucleated ice crystals would lower the maximum relative humidity, so that the change in aerosol properties would have a large impact on cirrus formation. *Seifert et al.* (2004) observed a complex relationship between the number density of interstitial aerosol (N_{int}) and crystals (N_{cvi}), which were measured simultaneously by aircraft-carried instruments. For lower number densities N_{int} and N_{cvi} were positively correlated. But when N_{int} increased above about 100 to 200 cm^{-3}, the mean N_{cvi} decreased. Compared to warm clouds, the macro- and microphysical properties of cirrus clouds have a high degree of variability (*Mace et al.*, 1997) in horizontal, vertical, and temporal dimensions. GCM-produced RH$_i$ and updraft velocity (w) do not generally resolve small scale sub-grid variations and can not therefore be used for ice cloud nucleation directly. This limits our ability to model ice nucleation since the understanding of upper troposphere relative humidity and turbulence is still poor. Another difficulty originates from the irregular shape of ice crystals in clouds. This makes the representation of the ice crystal size spectrum and the calculation of effective radius for use in radiative codes difficult. The calculated aerosol effect on ice crystal radiative properties could be influenced by different assumptions about ice crystal shape and size distribution, and different definitions of ice cloud effective radius.

5.1.4 Motivation of this study

As stated above, human influences on aerosol particles could affect the number concentration and the size of ice crystals in cirrus clouds. And this will change the radiative balance by modifying the scattering of incoming solar radiation and the absorption of upwelling LW radiation emitted by the surface and lower atmosphere. However, due to the lack of measurements and the insufficient understanding of the detailed physical processes, not much effort has been done in characterizing the ice properties and simulating the anthropogenic aerosol effect on cirrus clouds and climate, particularly on the global scale. A parcel model or trajectory model (*Haag and Kärcher*, 2004) has been exploited for studying regional scale aerosol effects. However, in global modeling, the nucleation parameterization methods have to be used instead.

Recently, two physically-based ice nucleation parameterizations, which relate the ice crystal number concentration to the aerosol properties, have been developed (*Liu and Penner*, 2005; *Kärcher et al.*, 2006). In the following sections of this chapter, we use these two methods to simulate the ice crystal number concentration (N_i) and effective radius (r_e) in the global scale. We evaluate the changes of N_i and r_e due to the anthropogenic aerosols. We also use a radiative transfer model to study the radiative impacts of these aerosols on cirrus clouds and global climate. In Section 2, the simulation method, including the preparation of aerosol concentrations and the meteorological fields, the parameterization methods, and the calculation of radiative properties and radiative transfer, is presented. In section 3, the results of N_i and r_e from two parameterization methods and different meteorological fields are shown and compared. The detailed physics causing the patterns and the relative importance of different nucleation modes are discussed. In section 4, we calculate indirect effect on

cirrus clouds by anthropogenic sulfate, anthropogenic soot from surface sources, and aircraft generated soot particles. We also provide a discussion of the different factors affecting SW radiation and LW radiation. Sensitivity tests are made. Section 5 gives a summary of the whole chapter.

5.2 Simulation method and data preparation

5.2.1 Overview of the simulation method

The calculation of anthropogenic aerosol indirect forcing on cirrus clouds and global climate follows the method used in previous chapters. We perform a set of model simulations in which different emission scenarios of aerosols and aerosol precursors are used (See Table 5.1). The first simulation uses only the natural emissions of aerosol particles, which include natural emissions of sulfate, soot from surface sources, and dust particles. Particles from the emissions for anthropogenic sulfate, anthropogenic soot from surface sources, and soot from aircraft source are added in succession in different simulation cases. By using the aerosol concentrations simulated by a Chemical Transfer Model (CTM), we calculate the in-cloud N_i using ice nucleation parameterizations. The values of N_i are then used to derive the ice crystal effective radius and cloud radiative properties, and a two-stream radiative transfer model is used to calculate the difference in the top of the atmosphere (TOA) radiative flux for the different emission scenarios listed in Table 5.1. This provides a first-order measure of the indirect effect due to anthropogenic sulfate, anthropogenic soot from surface sources, and soot generated by aircraft. We concentrate our study on the first indirect effect only, so the subsequent effects of aerosols on the precipitation efficiency of ice clouds is ignored.

Two sets of global aerosol and meteorological data are used to provide the input

Table 5.1: Emission scenarios used in the simulations. Only those aerosol species affecting the formation of ice crystals are listed.

Scenario 1	Scenario 2	Scenario 3	Scenario 4
Natural sulfate	Natural sulfate	Natural sulfate	Natural sulfate
Natural soot	Natural soot	Natural soot	Natural soot
Dust	Dust	Dust	Dust
	Anthrop. sulfate	Anthrop. sulfate	Anthrop. sulfate
		Anthrop. soot	Anthrop. soot
		(surface sources)	(surface sources)
			Anthrop. soot
			(aircraft source)

for the ice nucleation parameterization. In the first set, the meteorological data are from the 1997 GEOS assimilation by NASA Data Assimilation Office (DAO) (*Pfaendtner et al.*, 1995). The cloud fraction (CF) (*Sundqvist et al.*, 1989) and cloud ice water content (IWC) (*Hack*, 1998) are from parameterization methods based on DAO data. The aerosol concentrations are based on simulations of the University of Michigan version of the LLNL Integrated Massively Parallel Atmospheric Chemical Transport model (IMPACT) (*Rotman et al.*, 2004; *Liu et al.*, 2005) in which the DAO meteorological data are used for input. Hereafter we call the simulation using this data set as the DAO simulation. In the second set, the aerosol and meteorological fields are from simulations of the CAM3 version of the Community Atmosphere Model (CAM) (*Collins et al.*, 2004), to which the IMPACT model is coupled. The simulation using this data set is called the CAM simulation. Both meteorological fields are provided every 6 hours.

The aerosol concentrations used in the radiative transfer calculations for direct scattering and absorption are assumed to be the same in all cases in order to exclude any effects from aerosol direct radiative forcing. Since we only concern the aerosol effects on cirrus clouds, we do not apply the parameterization in clouds with temper-

atures above -35 ℃. For the warm clouds, we assume a fixed effective radius based on *Han et al.* (1994): 11.8μm over ocean and 8.5μm over land.

In the calculation of N_i, two physically-based ice nucleation parameterization methods are used, which will be described in section 5.2.3. In using these parameterization methods, we consider three different types of aerosols and their corresponding ice cloud nucleation modes. Sulfate aerosols are highly soluble so we assume they form ice through homogeneous freezing after deliquescence. The major IN for immersion nucleation is assumed to be soot particles coated with soluble substances (*Mohler et al.*, 2005). Deposition nucleation is assumed to occur on dust aerosols. These species have have been revealed to be the major aerosol components in the upper troposphere and lower stratosphere (*Chen et al.*, 1998; *Cziczo et al.*, 2004).

5.2.2 Simulation of aerosol number concentrations

Monthly mean aerosol number concentrations are calculated by running the IMPACT model. In the DAO simulation, the DAO meteorological filed is input to IMPACT. In the CAM simulation, IMPACT is coupled with CAM so that CAM provides real time meteorological parameters for IMPACT.

In the IMPACT simulations of this study, the anthropogenic sulfur and anthropogenic soot from surface sources represent an emission scenario for the year 2000. The emissions of anthropogenic sulfur were derived based on *Smith et al.* (2001), with update and extension. Total amount of global anthropogenic sulfur emissions is 61.8 Tg-S per year. Volcanic sulfur emissions were based on *Andres and Kasgnoc* (1998) and the global value is 4.8 Tg-S per year. Marine DMS emissions are the average of the high end estimate and the low end estimate from *Kettle and Andreae* (2000), with global total value of 26.1 Tg-S per year. The total amount of natural

Organice carbon (OC) emissions is 14.4 Tg per year which was derived by assuming that 9% of the terpene emissions (*Guenther et al.*, 1995) were rapidly converted to OC. OC and soot emissions from fossil fuel and biomass burning were estimated by using *Ito and Penner* (2005) with some sdjustments. The total amount of BC from fossil fuel burning and biomass burning is 5.80 Tg per year and 4.71 Tg per year, respectively. Sea salt particles emissions were calculated by using an emission flux parameterization based on *Gong et al.* (1997). Sea salt particles are assumed to be injected into the lowest model layer only. Dust emissions were derived from the source regions defined in *Ginoux et al.* (2001) and the 10 meter wind speed. Dust particles are assumed to be uniformly injected in the boundary layer.

Mass concentrations from the IMPACT simulations and size distributions for different aerosol species are used to calculate the number concentrations. Sulfate particles and soot particles are assumed to have a single log-normal size distribution. The soot generated by aircraft is assumed to have a smaller mode radius than that of soot from surface source. Dust particles are assumed to have a 3-mode log-normal size distribution fitted from airborne observations in the free troposphere. To convert aerosol mass concentration to number concentration, particle densities for these species are assumed. Table 5.2 provides a summary of the aerosol size distributions and densities in upper troposphere.

Figure 5.1 shows the annual zonal mean and 200mb anthropogenic sulfate number concentrations from the DAO simulation and the CAM simulation. There is reasonable agreement in lower troposphere between these two runs. The largest concentrations are found at the surface of northern hemisphere mid-latitudes, where most anthropogenic sulfur from fossil fuel burning is emitted. There is clear inter-hemispheric difference of concentrations. In upper troposphere where ice clouds

Table 5.2: Number size distributions and densities of sulfate, soot and dust particles in upper troposphere.

Species	Density (g cm^{-3})	Size distribution	Source
Sulfate	1.7	r = 0.02 μm	*Lin et al.* (2002)
		$\sigma = 2.3$	
Soot (surface sources)	1.5	r = 0.07 μm	*Pueschel et al.* (1992)
		$\sigma = 1.5$	
Soot (aircraft source)	1.5	r = 0.023 μm	
		$\sigma = 1.5$	
Dust	2.6	$r_1 = 0.010$ μm	*de Reus et al.* (2000)
		$\sigma_1 = 2.3$	
		$f_1 = 0.152$	
		$r_2 = 0.045$ μm	
		$\sigma_2 = 1.6$	
		$f_2 = 0.727$	
		$r_3 = 0.275$ μm	
		$\sigma_3 = 2.5$	
		$f_3 = 0.121$	

occurs, the CAM simulation has more anthropogenic sulfate concentrations in mid- to high latitude. Typical values at these regions are 10~80 cm^{-3} for the DAO simulation and 20~200 cm^{-3} for the CAM simulation. In the upper troposphere on some tropical region, the anthropogenic sulfate concentrations, which is calculated from the difference of sulfate concentrations using PD emissions and PI emissions, is very low.

Similarly, we show the zonal mean and 200mb number concentrations of anthropogenic soot from surface sources in Figure 5.2. Better agreement between the DAO simulation and the CAM simulation is found. Even at the upper troposphere, there is small difference from these two simulations. High values are present in Central Africa and Southern America, where biomass burning is large. At 200mb, typical concentrations of anthropogenic soot from surface source are $0.5 \sim 10$ cm^{-3}.

Soot particles generated by aircraft are mostly emitted in the upper troposphere,
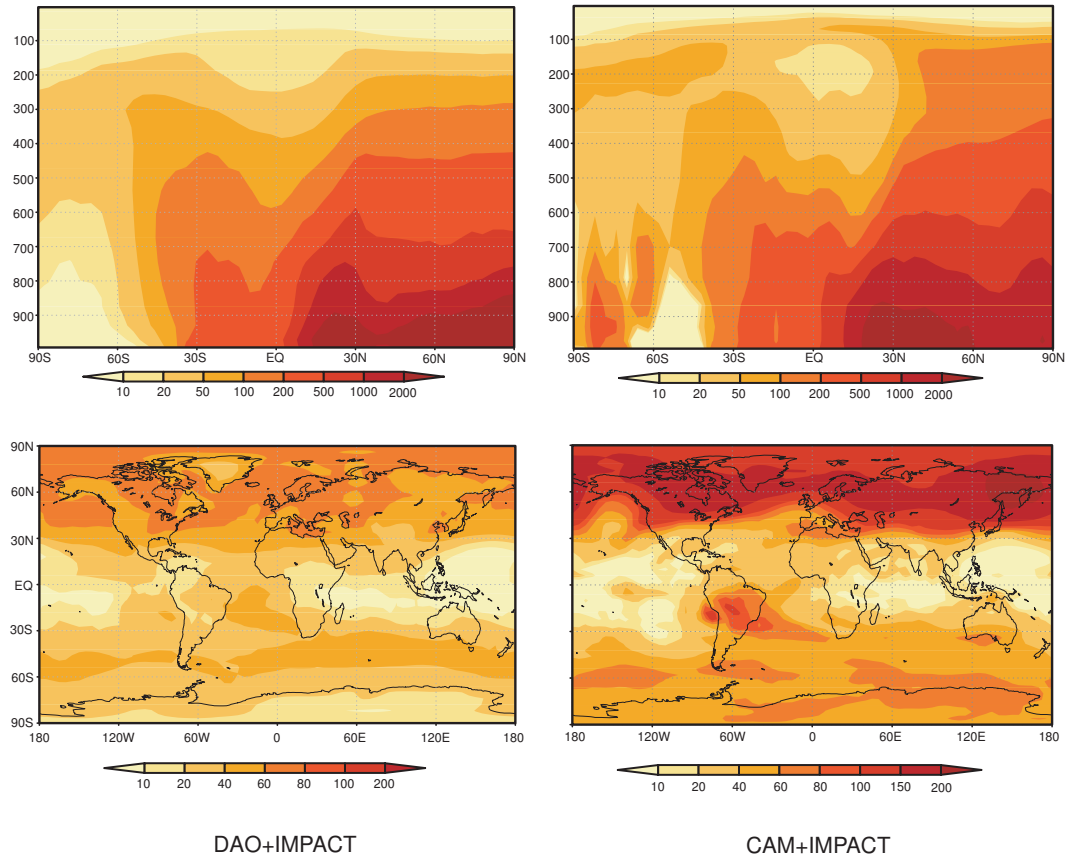
Figure 5.1: Zonal mean (upper) and ∼200mb (bottom) anthropogenic sulfate number concentrations (cm^{-3}) calculated from the DAO simulation and the CAM simulation.

although some of them could be emitted at the low altitudes during take-off and landing near the airports. So from Figure 5.3, we can see the largest values are between 200mb and 300mb, where the main aircraft flight levels are located. Their spatial variability is different from that of soot from surface sources. Most airplanes fly in the northern hemisphere mid-latitudes, therefore high values of aircraft soot can be found in this region, particularly between Europe and Northern America where most number of airlines are present. The lifetime of soot particles at high altitudes is long enough to survive the transport from mid-latitudes to the polar regions. The DAO simulation and the CAM simulation provide similar values and patterns of aircraft generated soot concentrations at high altitude. Typical values
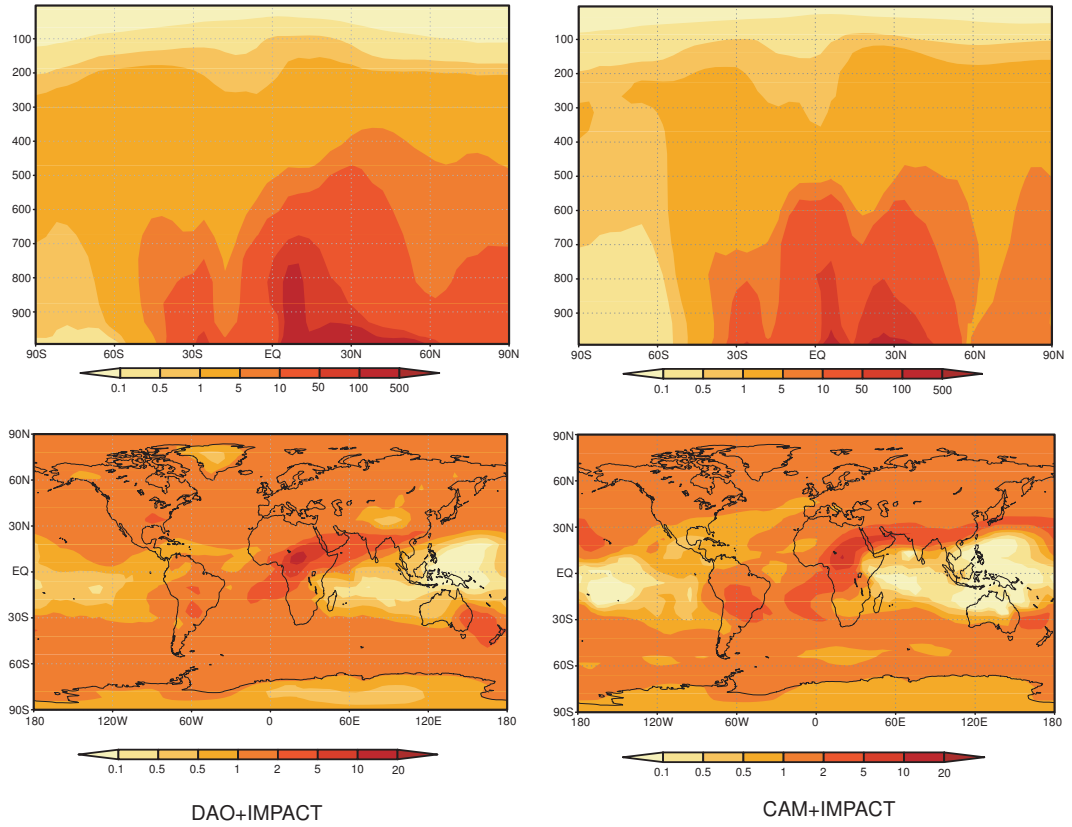
Figure 5.2: Zonal mean and ∼200mb number concentrations (cm^{-3}) of anthropogenic soot calculated from surface sources from the DAO simulation and the CAM simulation.

are $0.01 \sim 2$ cm^{-3} at 200mb.

At ∼200mb, the number concentrations of soot from surface sources are generally 10 times higher than that from aircraft sources in the SH. While in the NH, the aircraft generated soot could account for a very important fraction in the total soot. This result agrees well with that from *Hendricks et al.* (2004), which shows the aviation can cause large scale increase in the Upper-Troposphere Lowermost Stratosphere (UTLS) soot particle number concentration of more than 30% in regions highly frequent by aircraft.
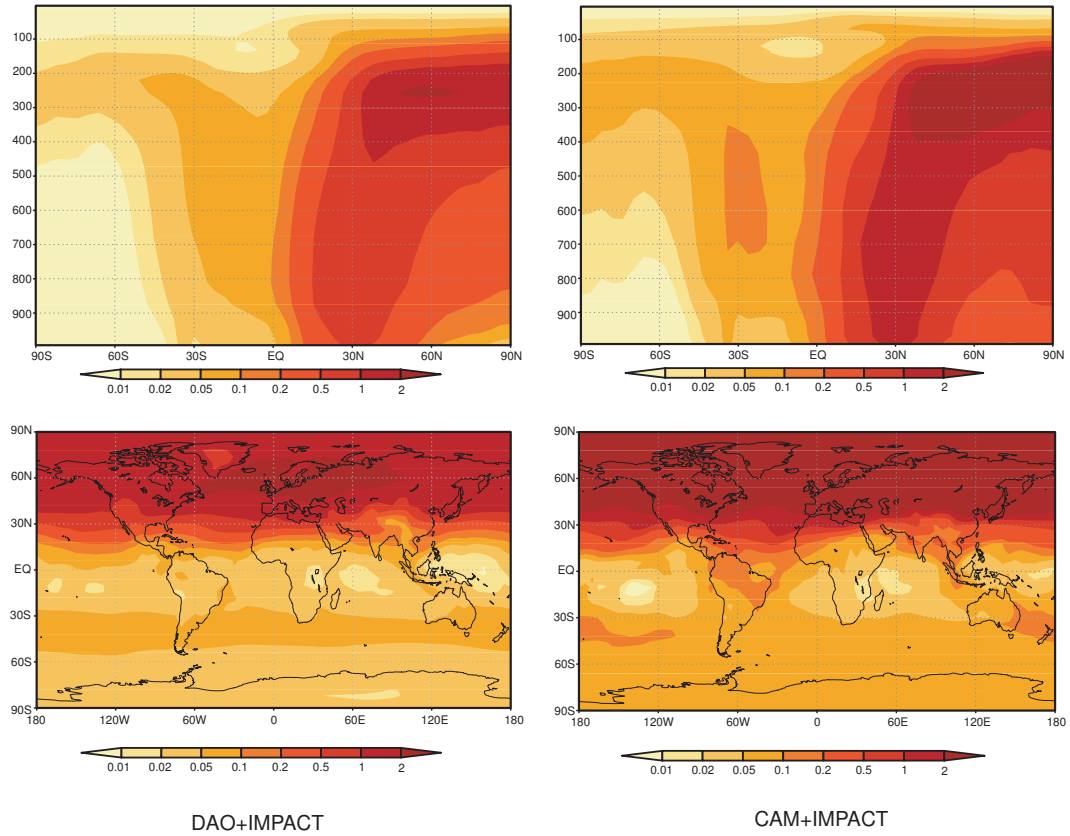
Figure 5.3: Zonal mean and 200mb number concentrations (cm^{-3}) of soot generated by aircraft calculated from the DAO simulation and the CAM simulation.

5.2.3 Parameterization methods

As stated above, calculations of the ice crystal numbers in the current GCMs are generally based on simple empirical equations which do not depend on aerosol properties. Therefore they are not suitable for estimating the effect of anthropogenic aerosols on cirrus clouds and climate. Recently two methods for treating ice nucleation which account for the effect of aerosols and for the competition between different nucleation modes have been published. Both of these two methods are based on physical theory. By using these parameterization methods, N_i can be related to aerosol and meteorological parameters.

Liu and Penner (2005) proposed an ice nucleation parameterization for a global model, based on detailed simulations of a cloud parcel model (*Lin et al.*, 2002) (Hereafter called the LP method). This method treats homogeneous nucleation and two modes of heterogeneous nucleation: deposition nucleation and immersion freezing mode. In this method, N_i is related to aerosol concentrations, and microphysical and dynamical parameters, based on the results of the parcel model simulations.

A transition regime between homogenous and heterogeneous nucleation is considered in this parameterization to account for the vapor competition between homogeneous nucleation and heterogeneous nucleation. RH_i is a necessary input in this parameterization method.

Kärcher et al. (2006) developed a parameterization scheme for ice initialization and initial growth in young cirrus clouds (Hereafter called the KL method). A prognostic supersaturation equation that accounts for the increase in supersaturation due to the adiabatically ascending parcel and the decrease in supersaturation due to vapor deposition on pre-existing ice particles is integrated using variable time steps. The number of nucleated ice crystals is tracked in the integration. This method also allows for multiple particle types and competition between different nucleation modes.

These two physically based ice cloud nucleation parameterization methods have been implemented in the global scale calculation in this study. In the DAO simulation, since the in-cloud variability of relative humidity is represented by a normal probability (which will be given in detail in a later section), we do not track the RH_i change as the KL method does. So for the DAO simulation, we only use the LP method to calculate N_i.

The CAM model only provides the large scale RH_i after saturation adjustment,

in which any supersaturation with respect to the ice above 100% is converted to ice water immediately after each time step. Therefore, no supersaturation is given in the CAM output. This RH_i field can not be used to predict N_i directly since most cirrus clouds form at high supersaturation. By assuming this RH_i is the out-of-cloud value, we may track the N_i and RH_i change of the air parcel by using the KL method. In another option, we record the maximum RH_i simulated in the KL method, and apply this relative humidity to the LP method to calculate N_i. The detailed consideration of the sub-grid variations of RH_i is described in the next section.

5.2.4 Meteorological field

The most important meteorological parameters that affect the calculation of N_i are the temperature (T) and the relative humidity respect to ice (RH_i). In addition, the cloud fraction (CF) and cloud ice water content (IWC) can affect the TOA radiative forcing in the radiative transfer modeling. As stated before, in the DAO simulation, these meteorological parameters are obtained from the DAO assimilation or parameterization methods based on the DAO data. In the CAM simulation, they were saved from the instantaneous fields of coupled CAM-IMPACT simulations.

Ice crystals may form as long as the temperature is colder than 0 ℃. However, when the temperature is above $\sim$37 ℃, mixing phase of water and ice could exist (*Rogers and Yau*, 1989). In this study, we only consider these clouds formed at a temperature of less than -37 ℃, i.e., pure ice clouds. As Figure 5.4 shows, these low temperatures occur only at polar regions or in the upper troposphere.

The 1997 DAO GEOS assimilation did not remove surplus water vapor over the saturation vapor pressure with respect to water, therefore the distribution of RH_i is biased high. Here we utilize the relative humidity in the upper troposphere derived
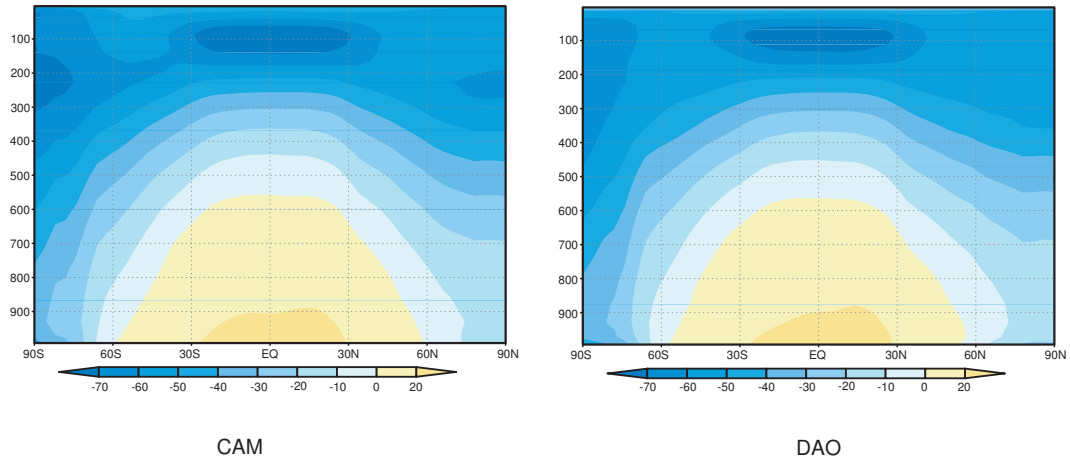
Figure 5.4: Annual zonal mean temperature (°C) calculated from the DAO simulation and the CAM simulation

from the MOZAIC (Measurement of OZone on Airbus In-service airCraft) data set (*Marenco et al.*, 1998; *Gierens et al.*, 1999) to adjust the large scale DAO RH_i. The occurrence fractions of RH_i in each 10% section in the flight route between 200mb and 300mb from MOZAIC measurements were calculated. Note since what we want is to adjust large scale DAO RH_i, we averaged the MOZAIC measured RH_i in each DAO grid. The derived histograms of the RH_i from MOZAIC data and DAO data are shown on Figure 5.5. These histograms show the fraction of supersaturation respect to ice from DAO data is much larger than that from MOZAIC. Based on MOZAIC RH_i distribution, we adjust the DAO RH_i in the following way. Starting from the highest RH_i, a fraction of the data in a particular RH_i section is modified so that it is moved to adjacent RH_i section. And this fraction is determined in such a way that after the modification, the occurrence percentage in this RH_i section is same as that in MOZAIC RH_i histogram. After the smallest RH_i section has been modified, the resulting DAO RH_i distribution after adjustment is very close to MOZAIC RH_i distribution (see Figure 5.5).

But even after the adjustment, the RH_i is only the grid average value and can
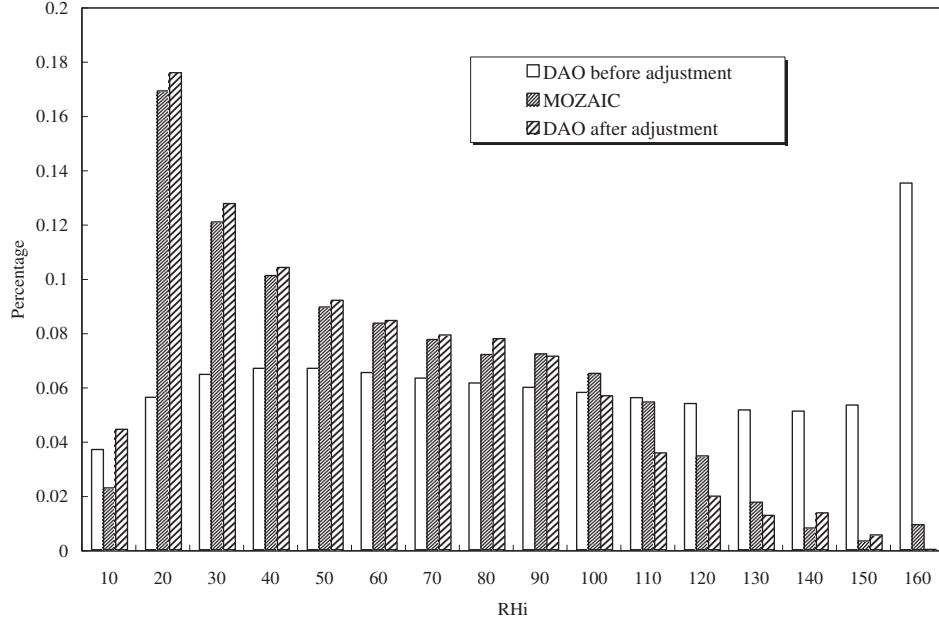
Figure 5.5: Grid average RH_i distribution between 200mb and 300mb calculated from the DAO simulation before and after the adjustment based on MOZAIC measurements.

not represent the sub-grid scale variation of RH_i. In the DAO simulation, the sub-grid variation is considered by using a normal probability distribution function in our parameterization of ice formation. The large scale RH_i obtained from the above adjustment is used as the mean value of the normal distribution in each grid. In order to calculate the standard deviation of this distribution, we extracted a set of measured values for each MOZAIC flight within each DAO grid. We then calculated the variance of RH_i from these sets. The annual global mean value of variance (7%) is used for all the grids. Note since only the in-cloud N_i values are used for radiative calculation, we assume a minimum RH_i (RH_{imin}) in the normal distribution. This RH_{imin} can be calculated by $\int_{RH_{i\min}}^{\infty} n(RH_i)dRH_i = CF$, in which $n(RH_i)$ is the distribution of RH_i and CF is the cloud fraction. We only calculate the N_i when $RH_i \geq RH_{i\min}$ is satisfied. This is explained in Figure 5.6. The shadowed region of $n(RH_i)$ is assumed to be the in-cloud $n(RH_i)$.
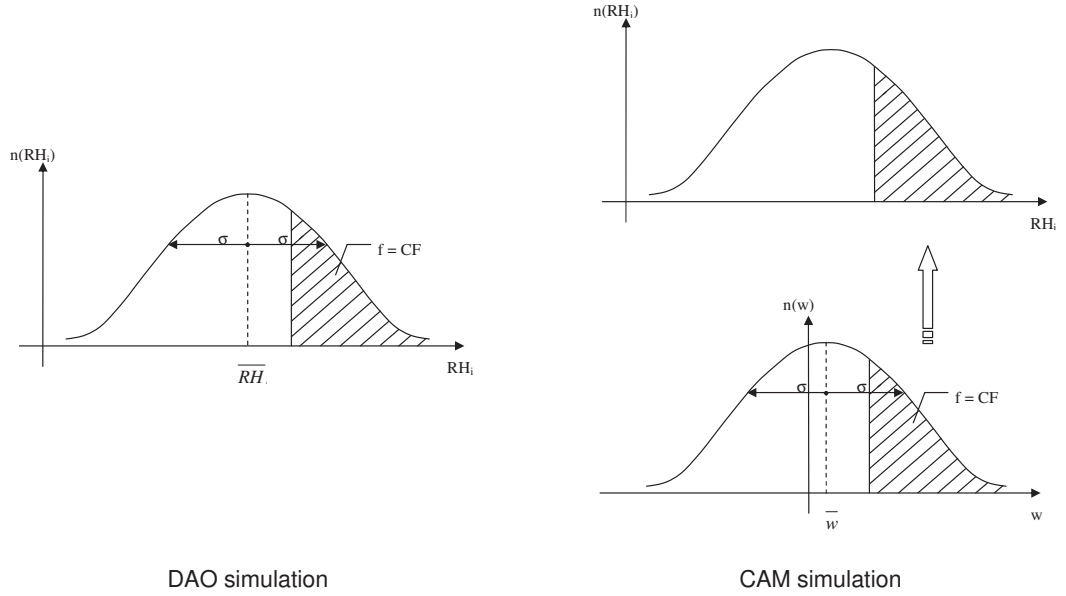
Figure 5.6: Treatments of in-cloud relative humidity variation in the DAO simulation and the CAM simulation. The shadowed region denotes the in-cloud fraction of RH_i or w.

In the CAM simulation, the output large scale RH_i is after the relative humidity adjustment in which the vapor above the supersaturation is converted to ice water. Therefore, for the grids where cirrus clouds are present, the values of large scale RH_i are all close to 100%. We assume this RH_i is the starting RH_i for an uplifting air parcel, and calculate the RH_i when nucleation commences by the method given in KL parameterization. We assume the sub-grid variance of RH_i is caused by the sub-grid variation of updraft velocity (w). The efficiency with which aerosol particles freeze has been shown to strongly link to the dynamical conditions prevailing during ice formation (*Kärcher and Lohmann*, 2003), since dynamical processes impact the temperature and cooling rate (*Lynch et al.*, 2002). *Kärcher and Lohmann* (2002) showed that changing the vertical wind speed from 0.1 to 1 m/s can increase the simulated ice crystal number density by two orders of magnitude. A model study of cirrus cloud showed that the maximum N_i in a lifting air parcel increases with

increasing updraft (*DeMott et al.*, 1994). However, the dynamical processes are still not fully understood (*Blyth and Latham*, 1993; *DeMott et al.*, 1994). Little correlation is found between cirrus occurrence and large-scale ascent (*Mace et al.*, 2001), but the meso-scale variance of updraft velocity could affect the formation of ice crystals. However, even in the most advanced state-of-the-art GCMs, they are not explicitly resolved (*Haag and Kärcher*, 2004; *Hoyle et al.*, 2005).

In the CAM simulation of this study, we use a normal probability distribution to represent the sub-grid scale variance of w (*Chuang et al.*, 2002). The large scale vertical velocity is taken as the mean value. The variance of w is assumed to be 0.33 m/s, which makes the mean value of w match that from INCA campaign (*Kärcher and Ström*, 2003). Similarly, we also set a minimum updraft velocity for each grid which can be calculated using the cloud fraction: $\int_{w_{\min}}^{\infty} n(w)dw = CF$. When the updraft velocity is larger than this minimum value, we assume the N_i calculated represents the in-cloud value.

Figure 5.7 presents the annual mean grid average RH_i between 200mb and 300mb from the DAO simulation, the CAM simulation and the MOZAIC measurements. Note the MOZAIC measurements are only available in the routes of major commercial airlines. Clearly after adjustment, the RH_i in the DAO simulation is much closer to MOZAIC RH_i. In the CAM simulation, since the direct output of RH_i from CAM simulation is only the RH_i in cloud free region, we need the in-cloud RH_i in order to calculate the grid average RH_i. We assume the maximum value of RH_i calculated for an uplifting air parcel based on the normal distribution of w represents the in-cloud RH_i. Then the grid average RH_i is calculated by

$$RH_i = RH_i(in-cloud) \times CF + RH_i(cloudfree) \times (1-CF)$$

The results are also shown in Figure 5.7. This RH_i from the CAM simulation has similar pattern as that from MOZAIC and the DAO simulation. But compared to the DAO simulation, the CAM simulation produces more higher RH_i values in tropical region, which is more resemble to the MOZAIC measurements.
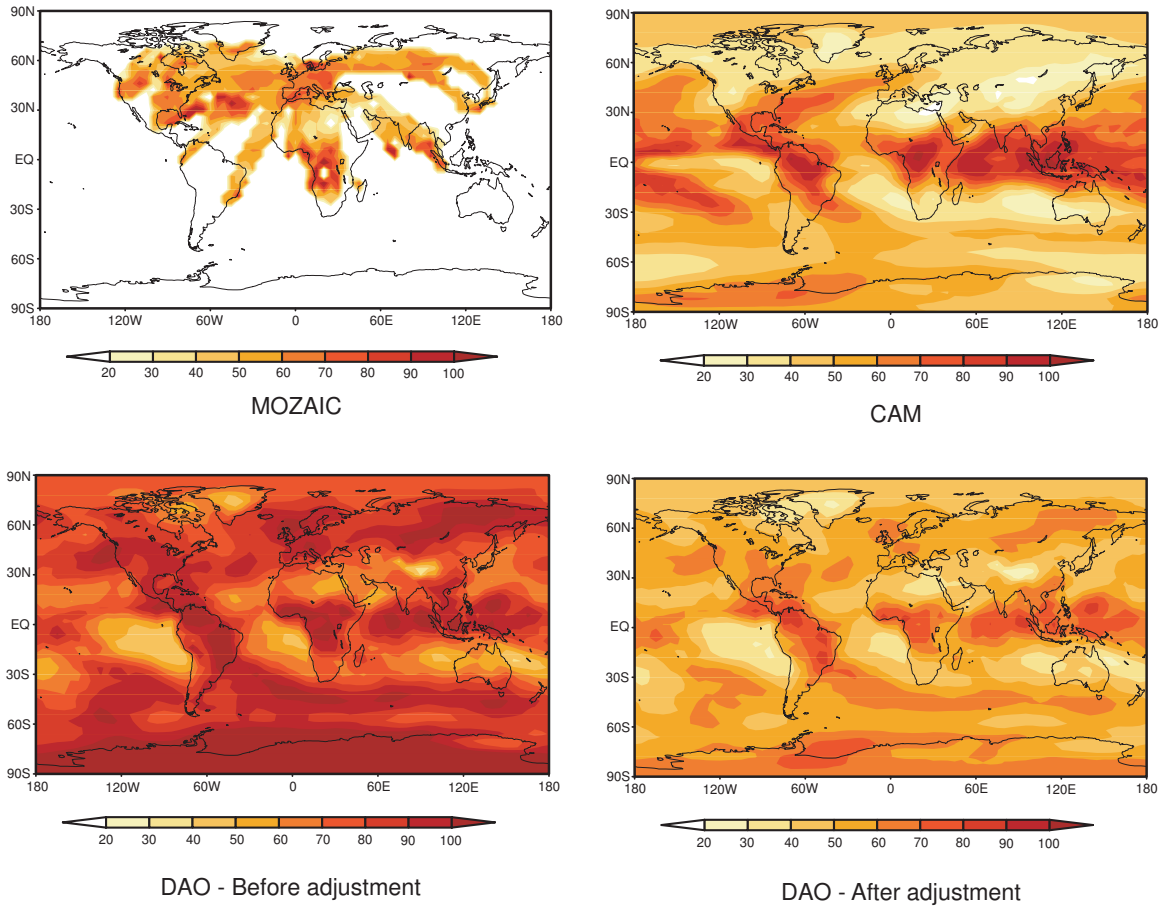
Figure 5.7: Annual mean large scale RH_i between 200 and 300mb before and after adjustment.

5.2.5 Calculation of ice crystal effective radius (r_e)

N_i affects the radiative properties of cirrus clouds through modifying the effective radius of the ice crystals. In warm clouds, the effective radius can be related to volume mean radius (r_v) by: $r_v^3 = kr_e^3$ (*Martin et al.*, 1994). For ice clouds, this relationship is more complex because most ice crystals are non-spherical particles. There

are different mathematical expressions for the size spectrum based on observations. The effective radius which is a measure for the mean size for use in optical depth calculations has been interpreted in various ways (*Wyser*, 1998). Most large-scale models do not take into account the varying size of ice particles, or only parameterize the effective radius as a function of IWC (*McFarlane et al.*, 1992) or temperature (*Ou and Liou*, 1995), or both (*Wyser*, 1998). In order to facilitate the simulation of the effects of aerosols on cloud optical properties, we assume there is a similar relationship between effective radius (r_e) and the equivalent sphere volume mean radius (r_v). Since r_v is a function of the ice crystal number, the r_e can be modified due to the change in aerosol particles.

In the derivation of k for crystals, all crystals were treated as hexagonal columns with length L and width D. The relationship between L and D is defined as (*Wyser*, 1998):

$$\frac{L}{D} = \begin{cases} 1, & L < 30\mu m, \\ 1 + 0.003(L - 30\mu m), & L \geq 30\mu m. \end{cases} \tag{5.1}$$

To estimate the k value, we assume the ice crystal spectrum is a combination of a Γ distribution for small particles up to 20μm and a power-law distribution for the larger particles (*Wyser*, 1998):

$$n(L) = A_M n_x(L) \tag{5.2}$$

where

$$n_x(L) = \begin{cases} L^\nu \exp(-\lambda L), & L \leq 20\mu m, \\ \alpha L^B, & L > 20\mu m, \end{cases} \tag{5.3}$$

α is chosen to make n(L) continuous at 20 μm. $\nu = 3, \lambda = 0.3\mu m^{-1}$.

B and A_M are calculated by

$$B = -2 + 10^{-3}(273 - T)^{1.5} \log_{10}\left(\frac{IWC}{IWC_0}\right) \tag{5.4}$$

and

$$A_M^{-1} = IWC^{-1} \int \rho(L)V(L)n_x(L)dL \tag{5.5}$$

in which IWC$_0$=50g/m^3, $V(L) = \frac{3\sqrt{3}}{8}D^2L$.

We calculated r$_e$ and r$_v$ using different sets of T and IWC by

$$r_e = \frac{1}{2}\frac{\int D^2Ln(L)dL}{\int (D^2L)^{2/3}n(L)dL} \tag{5.6}$$

and

$$r_v = \sqrt[3]{\frac{3IWC}{4\pi\rho_iN_i}} \tag{5.7}$$

where $N_i = \int A_Mn_x(L)dL$.

We calculate $k = r_v^3/r_e^3$ for different values of temperature and IWC. Then k value can be regressed as a function of T(K) and IWC(g/m^3):

$$k = \exp(a + b(T - 240) + c\ln(IWC)) \tag{5.8}$$

where

$$a = -3.15393$$

$$b = \begin{cases} -0.03387 & (T \leq 240K) \\ 0 & (T > 240K) \end{cases}$$

$$c = \begin{cases} -0.14738 & (IWC \leq 1g/m^3) \\ 0 & (IWC > 1g/m^3) \end{cases}$$

The k values from detailed calculation and from the parameterization are shown in Figure 5.8. The parameterization captures the main pattern of k from detailed calculation quite well in the given T and IWC range.
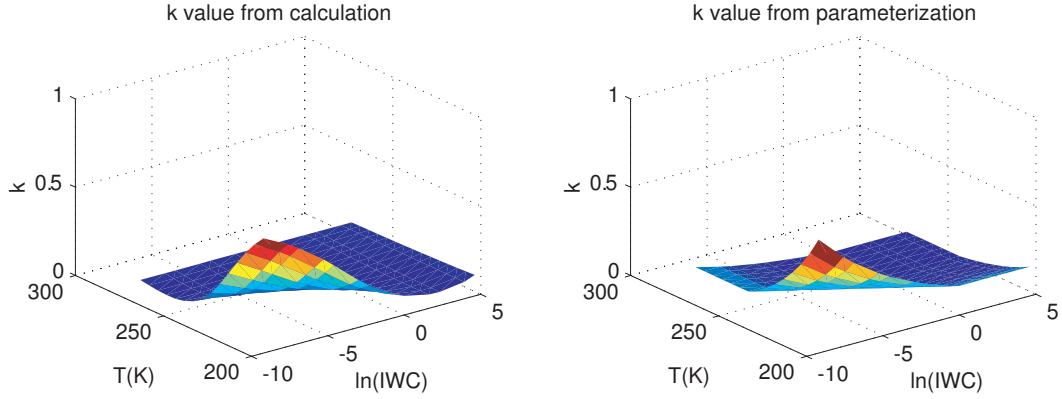
Figure 5.8: k from simulation and from parameterization. The unit for IWC is g/m^3.

5.2.6 Radiative transfer model

Both shortwave radiation and longwave radiation are calculated in this study. The shortwave code is based on *Grant et al.* (1999), and the longwave code is based on *Chou* (1990). In the shortwave radiation package, Raleigh scattering, absorption by ozone, water vapor and other absorptive gases, and aerosol and cloud scattering extinction are considered. For ice clouds, the optical depth, single scattering albedo, and asymmetry factor are parameterized as a function of ice cloud effective radius (*Ebert and Curry*, 1992). The longwave radiation package includes absorption by H_2O, CO_2, CH_4, CFC_s, as well as aerosol and clouds scattering extinction. The optical depth, single scattering albedo, and asymmetry factor at different wavelengths are also parameterized as a function of cloud effective radius (*Chou*, 1990). The cloud overlap scheme used is the maximum-random overlap scheme (*Feng et al.*, 2004), i.e., the continuous cloud layers are assumed to be maximally overlapped, while discontinuous cloud layers are randomly overlapped.

5.2.7 Summary of cases

In summary, we use two sets of aerosol and meteorological fields, which are called as the DAO simulation and the CAM simulation. For the DAO simulation, the

LP nucleation parameterization method is used. For the CAM simulation, the KL parameterization and LP parameterization methods are used for calculating N_i. In the CAM-LP simulation, we use RH_i sub-grid scale distribution derived from KL method.

Four aerosol emission scenarios are used for the forcing calculation. In the first scenario, only emissions for natural source aerosols, including natural sulfate, natural soot, and dust particles, are used in the IMPACT model to calculate aerosol number concentration and for N_i estimation. In the second scenario, we add the anthropogenic sulfate aerosols. So the difference of the TOA flux between these two simulations is a measure of the anthropogenic sulfate forcing. In the third scenario, emissions for anthropogenic soot particles surface sources are added in the simulation. In the fourth scenario, soot particles caused by aircraft emission are included. So difference between scenario 2 and 3, between scenario 3 and 4, give the indirect forcing due to the anthropogenic soot from surface source and aircraft source, respectively.

5.3   Simulation of N_i and r_e

5.3.1   Zonal mean and 200mb N_i and r_e

The number concentrations of in-cloud ice crystals directly affect the ice crystal size in our simulation. They also provide information on which nucleation modes are more important. In Figure 5.9, we show the zonal mean values of in-cloud N_i calculated in the DAO simulation, the CAM-KL simulation and the CAM-LP simulation for scenario 4, which represents the present day emissions. N_i at $\sim$200mb level is also shown. Note hereafter in this chapter all the results are 4-month (Jan, Apr, Jul, Oct) average values.
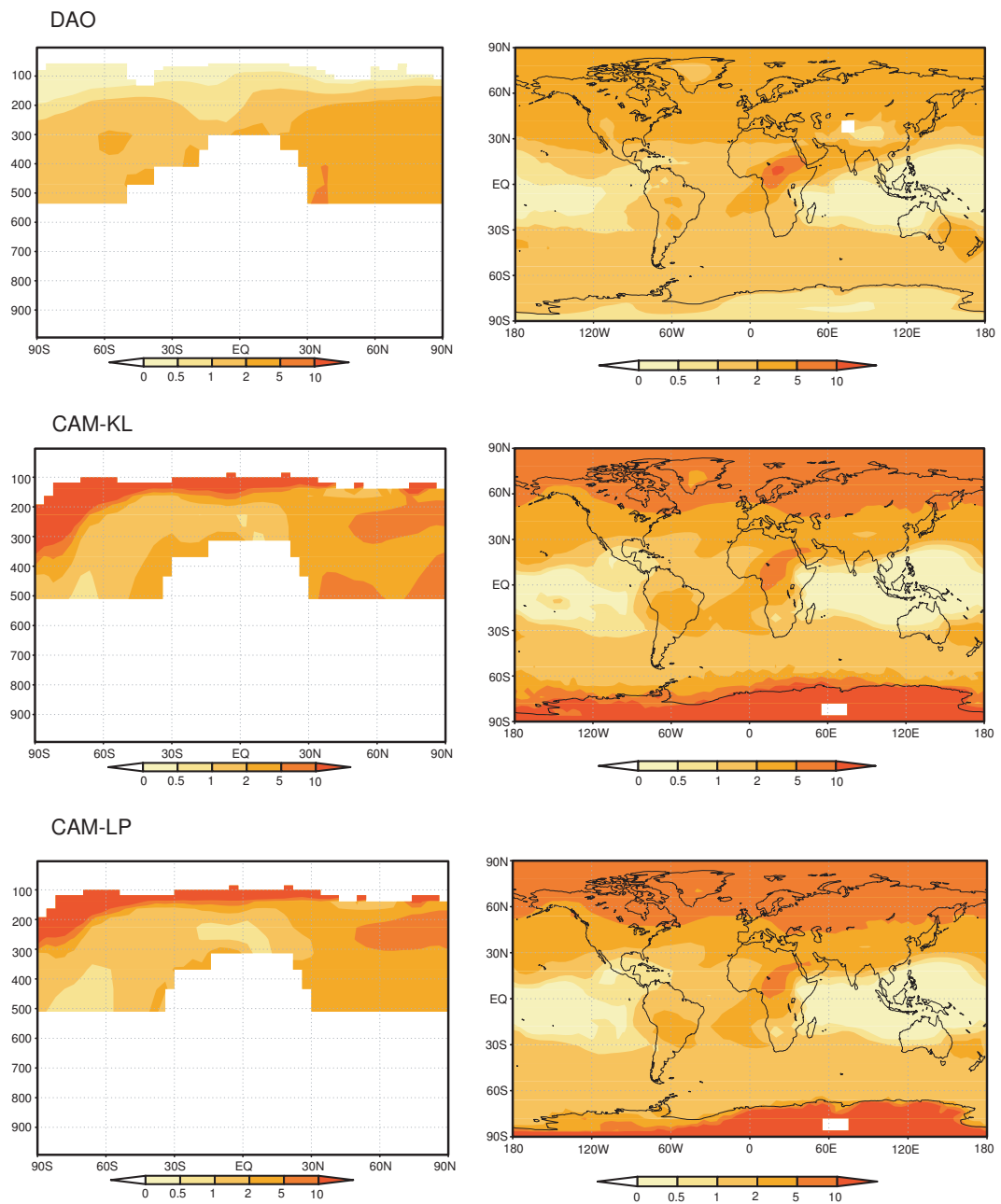
Figure 5.9: Zonal mean (left) and 200mb (right) in-cloud ice crystal number concentration cm^{-3} from three simulations.

Three simulations have similar N_i values below 200mb. Typical values at these regions are 0.5~5 cm^{-3}. Simulations show very clear difference of N_i between NH and SH mid-latitudes, indicating that human activities have already modified the properties of cirrus clouds at high altitude. N_i from the CAM-KL simulation and the CAM-LP simulation is very close, indicating the good agreement between the KL parameterization and the LP parameterization. At 200mb, N_i values from the CAM simulations are larger and could reach above 10 cm^{-3}. These large values of N_i can also be found in lower altitude at south polar region. However, we do not see these large values in the DAO simulation.

The zonal mean effective radius results are shown in Figure 5.10. Note that r_e is calculated by r_v and the coefficient k as given in Equation 5.8. The two CAM simulations have smaller r_e than the DAO simulation in the tropical region. Again, all the simulations show the difference between NH and SH, with larger r_e in SH. r_e does not only depends on N_i, but also affected by the IWC in clouds.
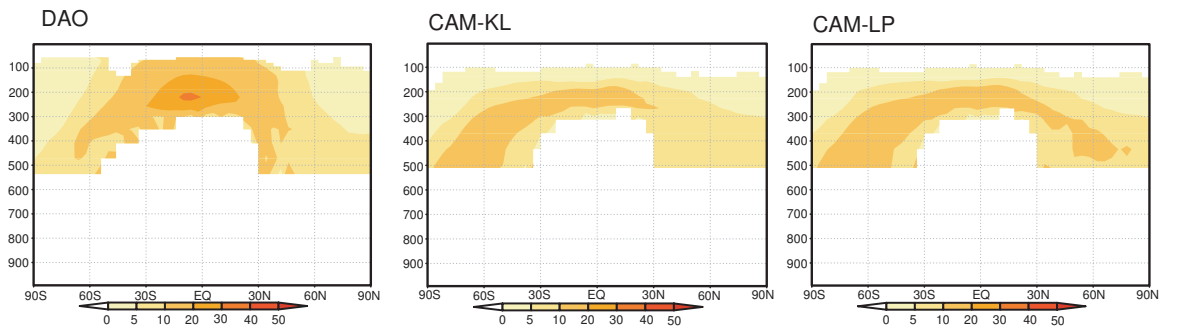
Figure 5.10: Zonal mean and 200mb in-cloud ice crystal effective radius from three simulations.

5.3.2   Fractions of different nucleation modes

To better understand the pattern of N_i shown above, it is necessary to learn the relative importance of different ice nucleation modes. Figure 5.11 shows the zonal

mean fraction of ice crystals formed though homogeneous nucleation, immersion nucleation and deposition nucleation from the three simulations. In the CAM simulations, homogeneous nucleation is important only at very high altitudes ($\sim$100mb) in tropics and at south polar region. These regions have lowest temperature and high RH_i. In addition, the heterogeneous IN concentration at this level is low. So the competition of water vapor by the heterogeneous nucleation is not important. Since homogeneous nucleation generally produces more N_i than heterogeneous nucleation, we can see high N_i values at this level (shown in Figure 5.9). In the DAO simulation, the homogeneous nucleation is not important for most regions. This is probably because the PDF RH_i used in this study does not resolve high values of RH_i very well. In most other regions, immersion freezing is the main nucleation mode. And with the increase of soot number concentration, the immersion nucleation fraction is more important at lower altitude. When the LP parameterization is used, deposition nucleation becomes more importance at low altitudes. Dust concentrations decrease with altitude very rapidly, therefore deposition nucleation on dust particles is very small above 200mb.

5.3.3 Probability distributions of N_i and r_e

By counting the number of occurrence, we can calculate the frequency distribution of different N_i and r_e values in cirrus clouds. Figure 5.12 presents such a frequency distribution of N_i and r_e for both pre-industrial (scenario 1) and present day (scenario 4). Compared to two CAM simulations, the DAO simulation has smallest N_i and corresponding largest r_e. The single mode distribution and the absence of large values of N_i indicates the lack of homogeneous nucleation in this run.

N_i distribution from the two CAM simulations has two modes. The small mode
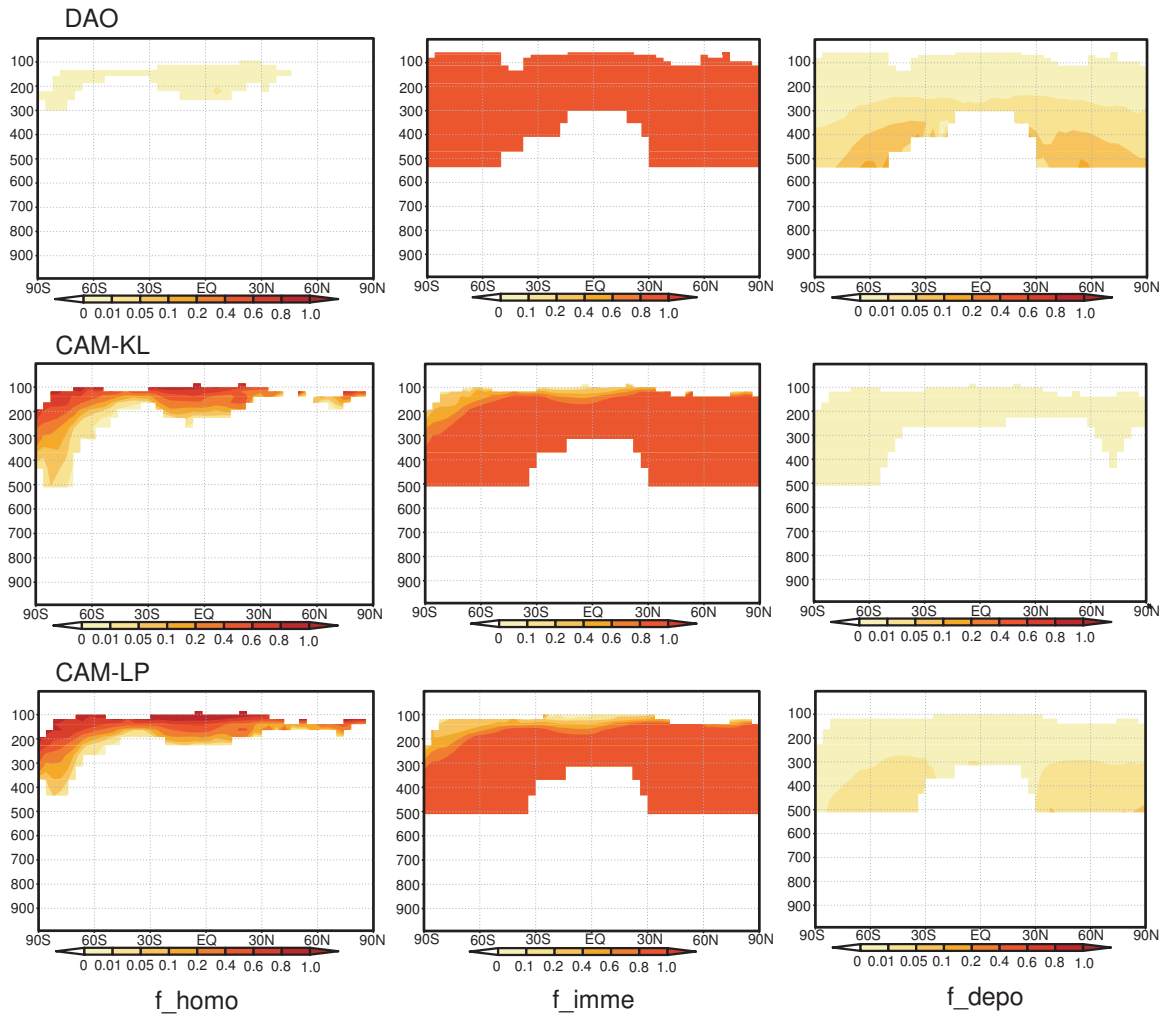
Figure 5.11: Zonal mean and high altitude (∼200mb) global view of fractions of homogeneous nucleation, immersion nucleation and deposition nucleation from three runs.

is associated with the heterogeneous nucleation while the large mode is associated with the homogeneous nucleation. The distribution of N_i has most values in the concentration range $0.1 \sim 10$ cm^{-3}. This range of N_i can be explained by the mesoscale variability of vertical air motion, because synoptic-scale updrafts affect low concentration regime (< 0.1 cm^{-3}) and convection mostly cause a maximum in high concentration regime (> 10 cm^{-3}) (*Kärcher and Ström*, 2003). The CAM-KL simulation and the CAM-LP simulation have similar distributions for both pre-industrial scenario and present day scenario, although the CAM-LP simulation has more large ice crystals.

A large portion of ice crystals has small size ($r < 20\mu m$) in the CAM simulations. This high number densities of small ice crystals has been observed in the INCA experiments (*Kärcher and Ström*, 2003). However, this is not observed in the DAO simulation, which may indicate the underestimation of high N_i values in this simulation.

By comparing the distributions for pre-industrial and present day, we can see the modification of N_i and r_e distributions by anthropogenic aerosols. The detailed discussion on this modification will be presented in section 5.4.4.

5.3.4 Comparison to measurements

The microphysical properties of cirrus clouds have been studied by using satellite (*Ou et al.*, 1998), ground-based remote sensing (*Intrieri et al.*, 1993; *Mace et al.*, 1998), and in-situ measurements (*Ovarlez et al.*, 2002; *Marenco et al.*, 1998). However, there are not many measurements available that have attempted to quantify the ice crystal number in the cirrus clouds. Even for the available measurements of N_i, they have been made with a variety of instruments for which the modes were not
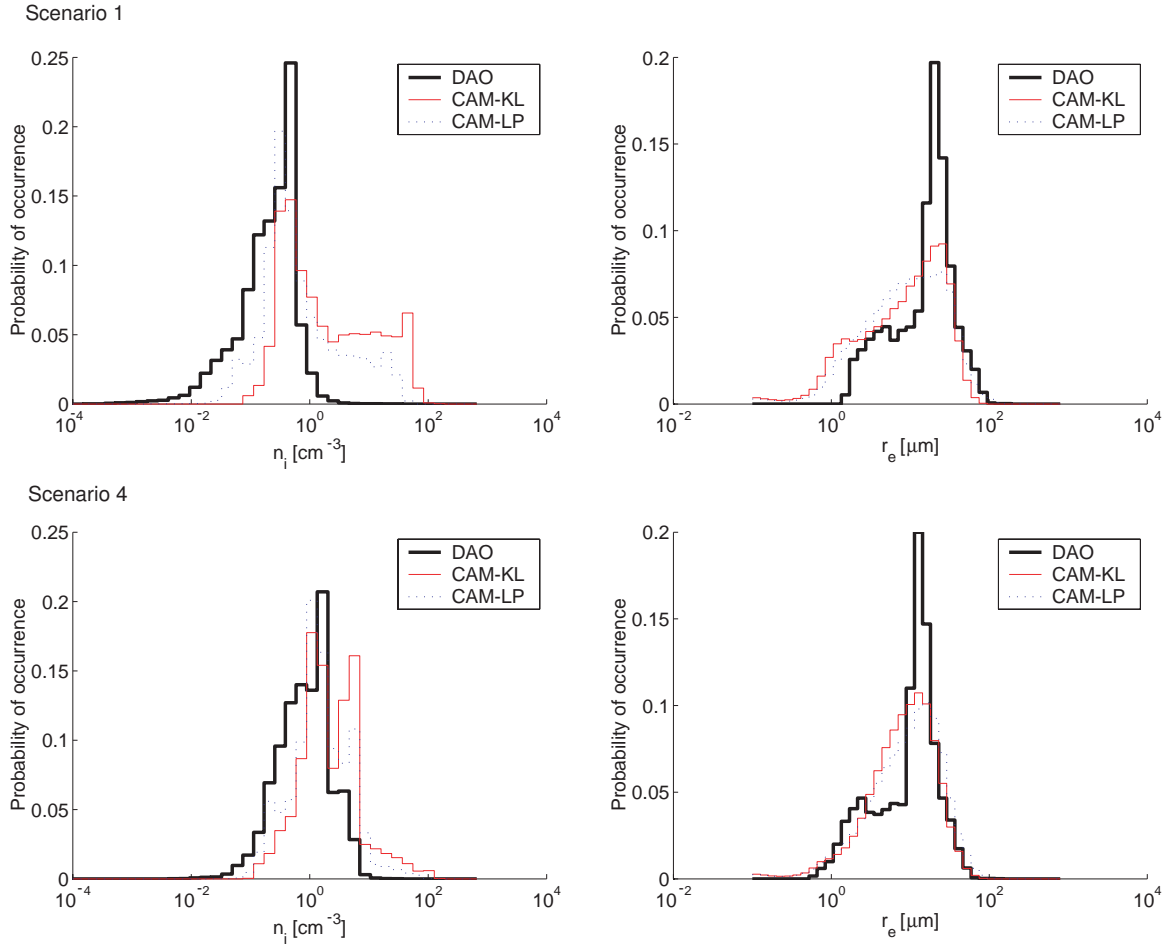
Figure 5.12: Normalized distribution of ice crystal number concentration and effective radius, calculated from DAO, CAM-KL, and CAM-LP simulations. Both PI (Scenario 1) and PD (Scenario 4) are shown.

always well defined, and the temporal and spatial scatter of observed values is large (*Meyers et al.*, 1992). *Dowling and Radke* (1990) summarized the microphysical data of cirrus from a wide number of projects before 1990. They found the crystal number densities ranging from 10^{-4} to 10^4/L, which were widely scattered.

In Table 5.3, we summarized measurements of ice crystal number concentration in cirrus clouds published since 1990. We also compared these numbers with the results from our three simulation simulations. We note this is only a rough comparison due to the difference in time and spatial resolution between the modeled and measured values.

N_i values from our three simulations are close, and they are well within the range of most measurements. In the two sites where INCA measurements were taken, our simulated N_i shows a clear difference between the NH site, where the air traffic and other human activities are dense, and the relatively clean SH site. And the mean values are close to that from INCA experiments. Comparison of simulated r_e to the measurements is more difficult. In Table 5.4, we summarized the in-situ measured values of r_e reported in recent years. The calculated values in our simulations are also shown for comparison. The r_e values from the simulations are smaller than the measured values, which could be due to several possible reasons. First, the underestimation of IWC or the overestimation of N_i in the model could cause smaller r_e. Second, the relationship between r_e and r_v is derived from assumed size distribution, which may not applicable to globe. Third, as we mentioned before, our calculation is tend to estimate the properties of ice crystals in the young cirrus clouds. During the aging of clouds, ice crystals could aggregate to larger particles, which could be detected in measurements but not represented in our simulations.

Table 5.3: Comparison of recent measurements of N_i to modeled N_i. The values in the parenthesis are mean values from measurements. N_i from simulations are monthly mean or annual mean values.

Reference	Experiment	Time	Place	N_i (Measure)	N_i (DAO)	N_i (CAM-KL)	N_i (CAM-LP)
Mizuno et al. (1994)		Jun, 1989	Tsukuba, Japan	(0.1)	2.0	2.0	1.9
Strom and Heintzenberg (1994)		Jan, 1992	Austrian Alps	0.05 ~ 5	4.2	3.4	3.3
Strom et al. (1997)		Mar, 1994	Southern Germany	0.01 ~ 15	4.3	3.9	3.6
Strom and Ohlsson (1998)	AERO-CONTRAIL	Oct, 1996	Southern Germany	0.5 ~ 10	3.4	3.5	3.6
Mace et al. (2001)	ARM	1-year,1997	SGP, Oklahoma	(0.1)	2.9	2.7	2.1
Choularton et al. (2002)	EMERALD	Sep, 2001	Southern Australia	(0.49)	1.3	1.4	1.3
Seifert et al. (2004)	INCA	Local autumn, 2000	Prestwick, Sotland Punta Arenas, Chile	2 ~ 10 1 ~ 3	3.8 1.6	2.6 1.4	3.4 1.4
Hoyle et al. (2005)	SUCCESS	Spring,1996	4 States, USA	0.1 ~ 10	2.8	2.6	2.4

Table 5.4: Comparison of recent measurements of r_e to modeled r_e. The values in the parenthesis are mean values from measurements. r_e from simulations are monthly mean or annual mean values.

Reference	Experiment	Time	Place	r_e (Measure)	r_e (DAO)	r_e (CAM-KL)	r_e (CAM-LP)
Kristensson et al. (2000)	AERO-CONTRAIL	Oct, 1996	Southern Germany	(30) (low soot) (25) (high soot)	8.5	8.2	8.1
Mace et al. (2001)	ARM	1-year, 1997	SGP, Oklahoma	(35)	10.3	13.5	15.9
Strom et al. (2002)	INCA	Local autumn 2000	Prestwick, Sotland	$16 \sim 47$ (30)	7.5	9.1	8.1
			Punta Arenas, Chile	$19 \sim 50$ (33)	11.8	12.0	12.0
Sassen et al. (2003)		Sep, 1997	Salt Lake City	(50)	10.5	7.7	8.4

5.3.5   Sensitivity tests

As we mentioned before, the RH_i is a key parameter that determines the nucleation modes and the value of N_i. The difference of N_i patterns obtained from the DAO simulation and the CAM simulations is probably due to different representations of sub-grid scale variations of RH_i. In the CAM simulations, this variance is caused by the sub-grid scale variance of updraft velocity w, which is denoted using a normal probability distribution. This variance was set to make the mean value of w is the same as that from the INCA observations. However, INCA observations were only made in two sites in mid-latitude of NH and SH at local autumn. The variance of w obtained from these measurements may not be able to represent the global distribution of w. In addition, the use of a normal probability distribution of w is only a simplification. In the following sensitivity test, we reduced the standard deviation of the normal distribution of w from 33 cm/s to 10 cm/s to see how this change of dynamics would change the N_i simulated. In the DAO simulation, the sub-grid variation of RH_i is directly represented by using a mean variance value based on the MOZAIC data. However, this uniformed value may underestimate the RH_i variation in some grids. So in a sensitivity test, we increase the value of this uniformed variance from 7% to 14% to evaluate the sensitivity of N_i to this parameter.

The zonal mean N_i from these sensitivity tests are shown in Figure 5.13. With the decrease of w variance, the occurance of large in-cloud RH_i values obtained from KL parameterization decreases. This decreasing in RH_i reduces the N_i formed by homogeneous nucleation and heterogenous nucleation. Due to the small RH_i, the occurrence of homogeneous nucleation is largely inhibited. Therefore, the large N_i values in high altitude and south pole region which can be seen in the base case CAM runs, are not available in the sensitivity test.

The increase of RH_i in the DAO simulation can increase N_i formed by immersion nucleation. Potentially, this increase of RH_i could also increase the fraction of homogeneous nucleation. But the large N_i values in high altitude and south polar region are still not seen in this sensitivity test.
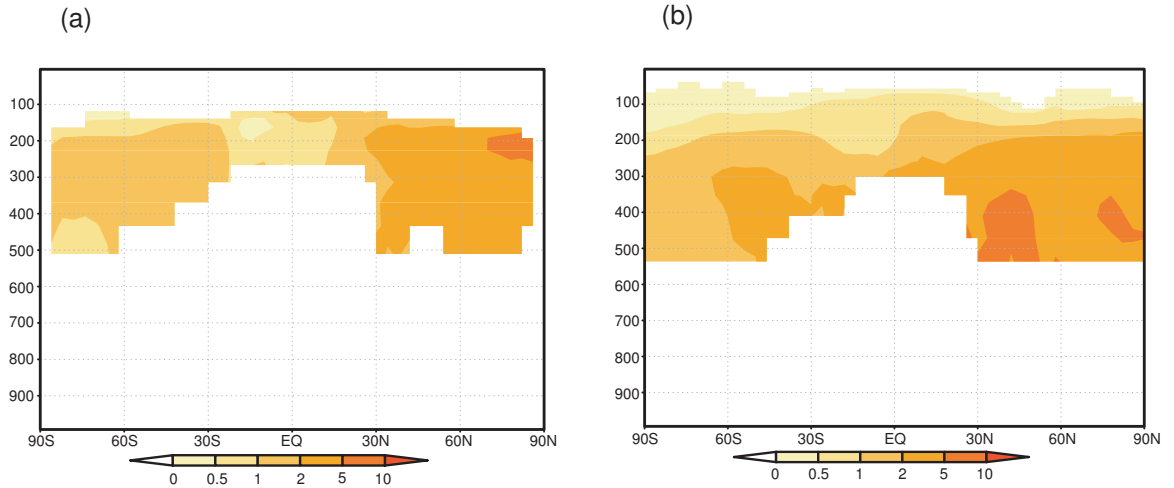
Figure 5.13: Zonal mean N_i calculated in the sensitivity test simulations. (a) Use standard deviation of w distribution = 0.1 cm/s instead of 0.33 cm/s used in the CAM-KL simulation. (b) Use the variance of RH_i = 14% instead of 7% used in the DAO simulation.

5.4 Effect of anthropogenic aerosols on cirrus clouds and radiative flux

5.4.1 Effect of anthropogenic sulfate

Figure 5.14 shows the zonal mean change in N_i due to addition of anthropogenic sulfate aerosols and the zonal mean TOA radiative flux change (i.e. the anthropogenic sulfate forcing) calculated from the DAO simulation and the CAM simulations using the KL parameterization and the LP parameterization. The global mean values of the forcing are listed in Table 5.5.

In the CAM simulations, large changes in N_i are found at high altitudes (higher than 200mb) and in polar regions. These regions have lowest temperature (see Fig-
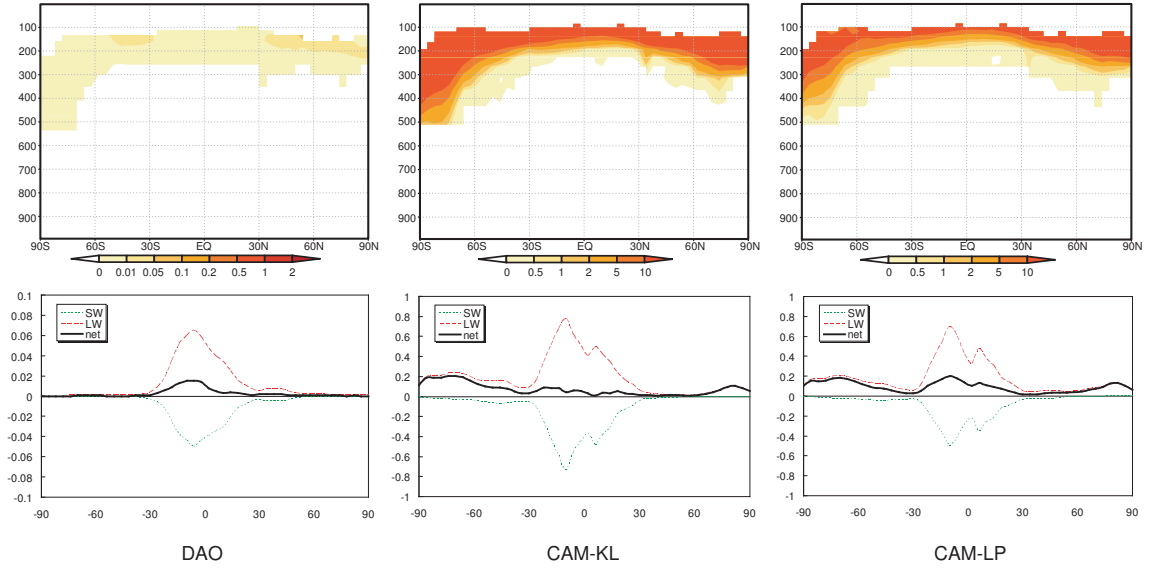
Figure 5.14: Anthropogenic sulfate effect on cirrus clouds and climate. Top two plots show the in-cloud ice crystal number change (cm^{-3}). Bottom two plots show the SW, LW and net forcing of anthropogenic sulfate (Wm^{-2}).

ure 5.4). The variance of w which is related to small-scale temperature fluctuations (*Hoyle et al.*, 2005) causes high values of RH_i in these regions. So in these regions homogeneous nucleation which requires RH_i greater than $\sim 160\%$ dominates. Although homogeneous nucleation is not very sensitive to the aerosol properties, the large change in sulfate number concentration does increase the number of ice crystals in these regions.

This change of N_i due to anthropogenic sulfate affects both the SW and LW radiation. Since in most regions, N_i increases when industrial emissions are added to the PI emissions, the TOA SW forcing is generally negative while the TOA LW forcing is positive. The largest forcing values, both SW and LW, are in the tropics. This is because the low temperature and high RH_i in these regions cause homogeneous nucleation to dominate in this region. Also, the cirrus cloud fraction is high in these regions and the solar incident radiation is high causing large changes in the SW flux by a small perturbation to N_i. The sensitivity of the LW flux to N_i is

also large due to the large difference between the cloud temperature and surface temperature. The net forcing is mainly determined by the LW forcing, due to the high altitude of cirrus occurrence. However in some tropical regions (not shown), the SW forcing dominates, probably due to the larger thickness of cirrus clouds there. The meteorological parameters are dominant in determining the forcing of anthropogenic sulfate, so that it is difficult to see correlation between the forcing and anthropogenic sulfate aerosol concentrations.

In the DAO simulation, high RH_i which is not large enough for homogeneous nucleation to occur in most regions. Therefore, the N_i change due to the addition of anthropogenic sulfate is small. The forcing has the similar pattern to that from two CAM simulations, i.e., large values are in the tropical region. However, the value of the forcing is much smaller.

Homogenous nucleation has been viewed as insensitive to aerosol concentration. Our simulations show that the global mean anthropogenic sulfate net forcing is less than 0.1 Wm^{-2}. The use of KL parameterization and LP parameterization in the CAM simulations produces similar forcing patterns and values. The difference of global mean forcing values from these two methods are within 50%.
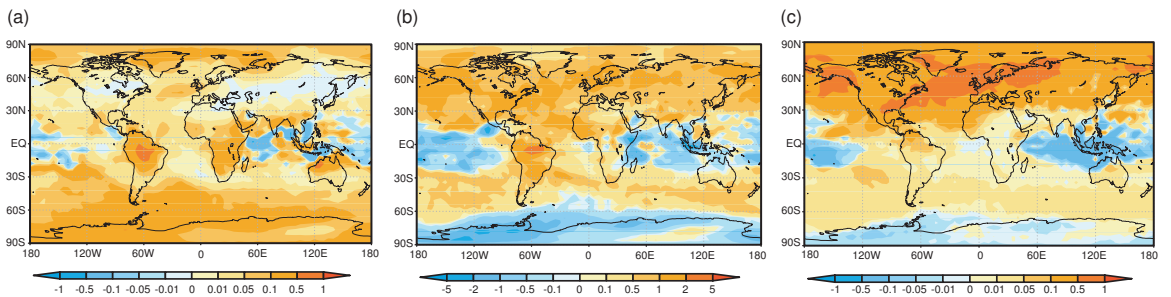
Figure 5.15: Four month (Jan, Apr, Jul, Oct) average TOA net forcing (Wm^{-2}) from (a) anthropogenic sulfate, (b) anthropogenic soot from surface sources, and (c) aircraft generated soot, calculated from the CAM-KL simulation.

5.4.2   Effect of anthropogenic soot from surface sources

Soot particles can act as heterogeneous IN and increase the N_i from immersion nucleation. They can also decrease the RH_i and thereby decrease the N_i from homogeneous nucleation (negative Twomey effect (*Haag and Kärcher*, 2004)). The relative importance of these two effects is largely affected by the available water vapor. As a result, our simulations show a different pattern of anthropogenic soot forcing (see Figure 5.15). We first discuss the effect of anthropogenic soot from surface sources.
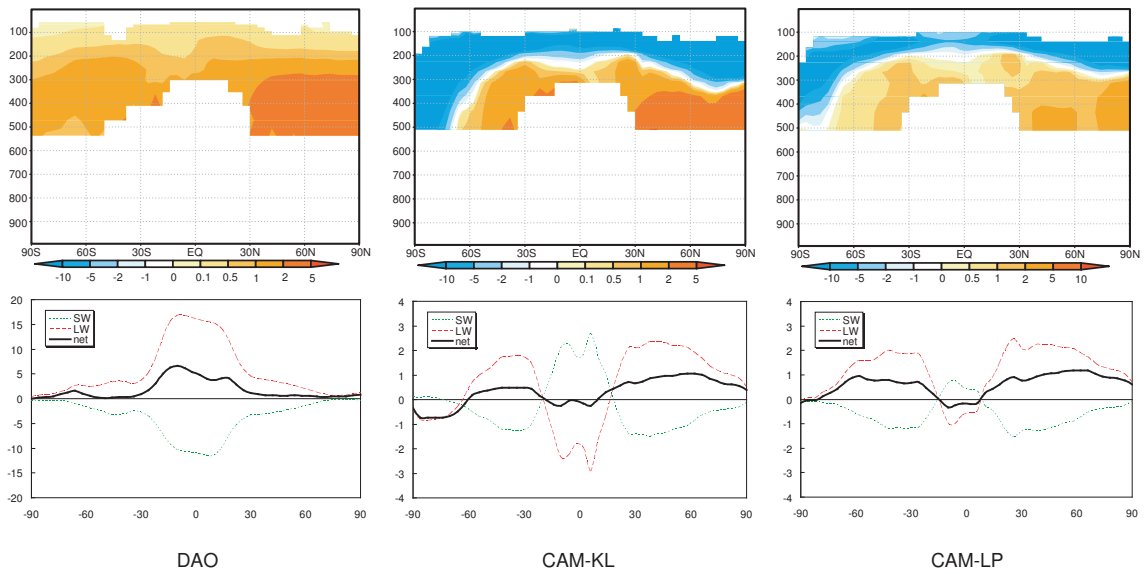
Figure 5.16: Effect of anthropogenic soot from surface sources on cirrus clouds and climate. Top two plots show the In-cloud N_i change (cm^{-3}). Bottom two plots show the SW, LW and net forcing of soot from surface sources (Wm^{-2}).

Homogeneous nucleations is important in the clouds that form between 100 and 250 mb and in polar regions. Heterogeneous nucleation dominates in the clouds that from between 250 and 500 mb. Therefore in the CAM simulations, as shown in Figure 5.16, adding anthropogenic soot from surface sources decrease the N_i in the high cirrus clouds, i.e., the negative Twomey effect dominates. While in low cirrus clouds, anthropogenic soot tends to increase the N_i, i.e., the positive effect dominates.

The patterns of both SW and LW forcing are influenced by the relative importance of these two effects. In most tropical regions and in the SH polar region, the decrease of N_i by the addition of heterogeneous IN is more important so that the SW forcing is positive and LW forcing is negative there. In other regions, heterogeneous nucleation is already dominant in the pre-industrial simulations so an increase of N_i occurs when soot aerosols are added. In these regions the SW forcing is negative and the LW forcing is positive. We also note the negative effect in the CAM-LP simulation is weaker than that in the CAM-KL simulation. Because LW forcing is dominant for cirrus clouds, the net forcing pattern is similar to that of the LW forcing, i.e., negative in tropical areas and SH polar region, and positive in other areas. The global mean net forcing is 0.335 Wm^{-2} for the CAM-KL simulation and 0.547 Wm^{-2} for the CAM-LP simulation. Moreover, the regional values (either positive or negative) are large enough to compare other anthropogenic forcings. The largest forcing values are in the NH mid-latitudes, where the anthropogenic soot concentrations from surface sources are high. This shows the spatial difference that human activities affect cirrus clouds and radiation.

In the DAO simulation, the increase of N_i from immersion nucleation by addition of anthropogenic surface source soot is dominant because the RH_i is low and the homogeneous nucleation is not important in most regions. This is true even for the high altitude region where the LW effect is large because of the low temperature. Due to the high cloud fraction and high solar incident radiation, the SW forcing shows clear latitudinal difference. Tropical region has largest SW forcing value. LW forcing is also largest in tropics, but this is mainly due to the high altitude and cold temperature of the cirrus clouds in this region. The combined effect is the dominance of LW warming effect in most area. Note since there is almost no 'negative Twomey

effect' in tropics, the forcing value from the DAO simulation is larger than those from the two CAM simulations.

5.4.3 Effect of aircraft generated soot

Aircraft emissions add more soot particles to atmosphere in the upper troposphere. These particles are coated with sulfuric acid and are very good heterogeneous IN. Model results by *Hendricks et al.* (2005) showed that the modifications induced by aircraft soot particles can change the annual mean zonal average N_i at northern mid-latitudes by 10% to 40%. Our global simulation shows that this effect is determined by the relative importance of nucleation modes and by the number concentration of aircraft generated soot.
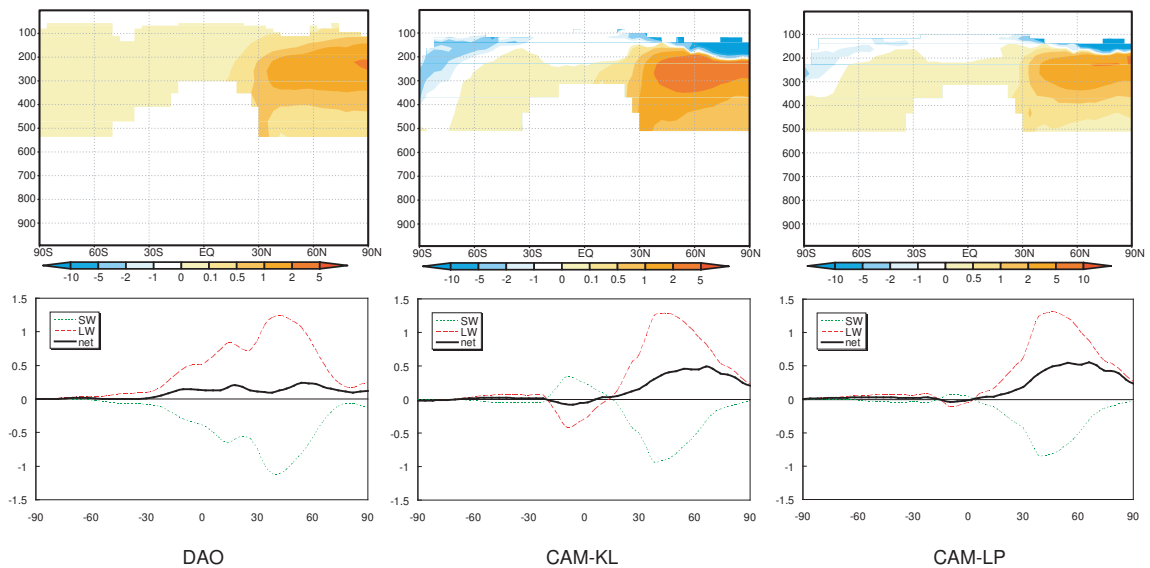
Figure 5.17: Effect of soot from aircraft on cirrus clouds and climate. Top two plots show the In-cloud N_i change (cm^{-3}). Bottom two plots show the SW, LW and net forcing of soot from aircraft (Wm^{-2}).

In addition to the large increases of N_i in the NH at mid- to high latitudes, the addition of soot from aircraft causes a decrease in N_i at high altitudes where homogeneous nucleation is important. However, this effect is much weaker compared

to that due to anthropogenic soot from surface sources. Figure 5.17 shows that there are large changes of N_i and large forcings are in the NH mid- and high latitudes, where aircraft emissions significantly increase the soot concentrations at high altitude. The global annual mean forcing is 0.100 Wm^{-2} (CAM-KL simulation) and 0.131 Wm^{-2} (CAM-LP simulation), which is smaller but comparable to the forcing due to the anthropogenic soot from surface sources.

Compared to the two CAM simulations, the change of N_i and the radiative forcing of aircraft generated soot from the DAO simulation are similar in high latitudinal regions. However, due to the dominance of heterogeneous nucleation, the increase of N_i by adding the aircraft soot is the main effect. So there is no negative forcing in tropics as in the CAM simulations. The global mean value of net forcing from the DAO simulation is 0.079 Wm^{-2}.

5.4.4   Discussion

Anthropogenic aerosols affect cirrus cloud properties and radiative balance differently depending on the aerosol species, nucleation modes for pre-existing clouds, and the concentration of anthropogenic aerosols. Figure 5.18 shows the N_i and r_e probability of occurrence calculated by using different parameterizations and different emission scenarios. This change in the spectral distribution gives us an idea on how different anthropogenic aerosol species modify the properties of cirrus clouds. In the DAO simulation, since homogeneous nucleation does not dominate, the increasing of sulfate due to human activities does not change the N_i and r_e distribution much. The addition of anthropogenic soot from surface sources obviously increases the occurrence of large N_i and and smaller r_e, so does the soot from aircraft emissions. For the soot from surface sources and from aircraft emissions, the former has

larger effect. In the CAM simulations, because homogeneous nucleation is important in some regions in the PI emission scenario, the addition of anthropogenic sulfate which act through homogeneous nucleation increases the nucleation of ice crystals in the large mode. However, this change does not affect the nucleation of ice crystals formed through heterogeneous nucleation, i.e., the small mode. The addition of soot particles has two effects. In regions in which homogeneous nucleation dominates, an increase in heterogeneous IN decreases the RH_i and inhibits the formation of ice crystals through homogeneous nucleation (negative effect). This can be seen in Figure 5.18 which shows that in scenario 3 the occurrence of particles in the large mode decreases. In the regions where the heterogeneous nucleation dominates, the increase in soot particles increases N_i (positive effect). So the small mode in the N_i distribution moves to larger N_i. The combination of these two effects narrows the N_i and r_e distributions.

Since the change of cirrus clouds and radiative properties due to anthropogenic emissions largely depends on which nucleation mode is dominant, the estimation of pre-industrial IN in the upper troposphere is very important. The transition from homogeneous to heterogeneous nucleation occurs over a narrow range of soot concentrations (*Gierens*, 2003), so that the IN calculated in the PI emissions determines the dominance of different nucleation modes, thereby affecting the effect of adding anthropogenic aerosols.

In summary, the global pattern of TOA forcing due to anthropogenic aerosols is a result of several factors, including the PI aerosols, anthropogenic aerosols, cloud dynamics (w), cloud microphysics (T, RH_i), cloud fraction (CF), solar incident radiation, etc. Each of them individually can not explain the whole pattern.
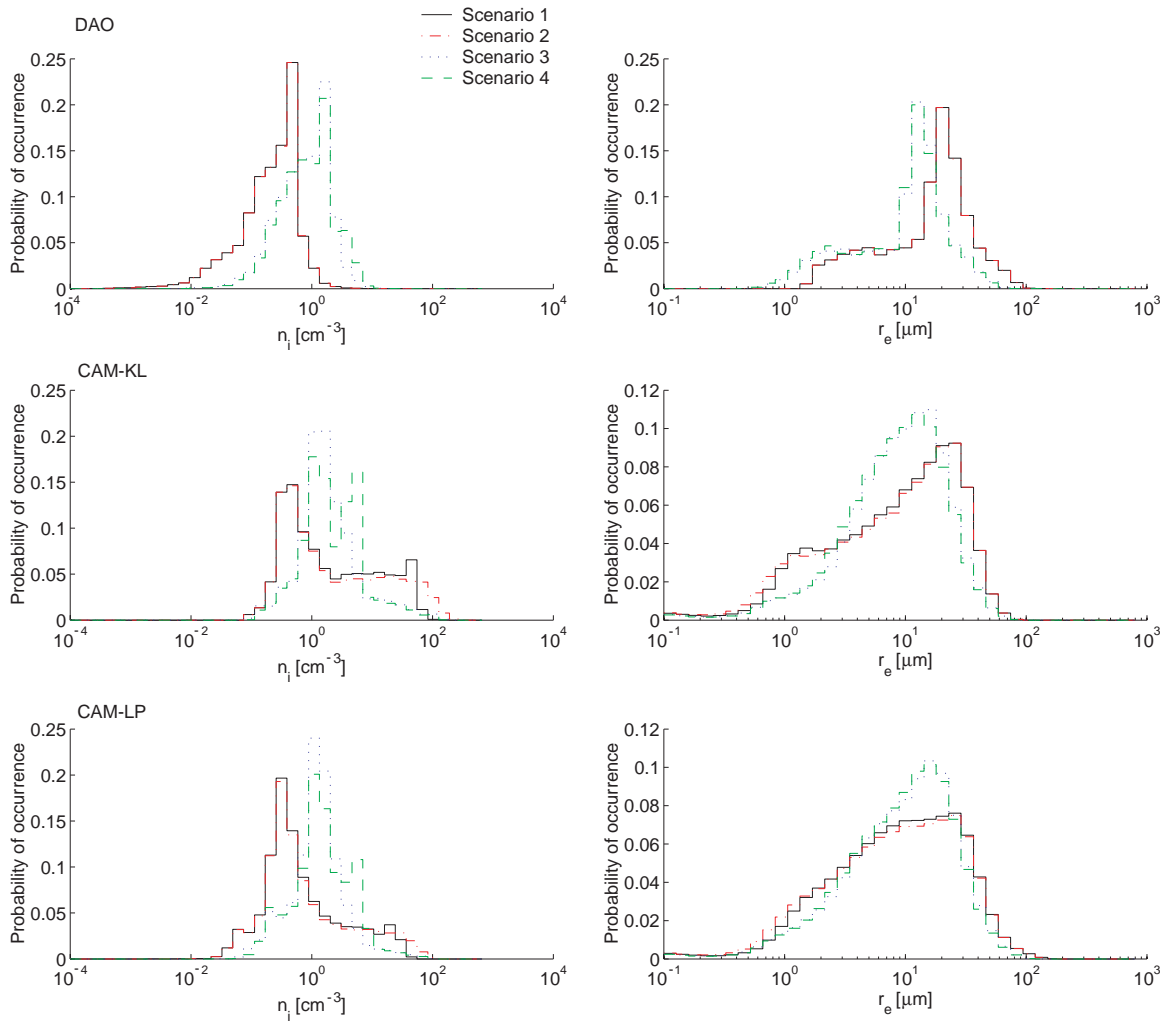
Figure 5.18: Change of normalized distribution of ice crystal number concentration and effective radius, calculated from DAO, CAM-KL, and CAM-LP simulations.

Table 5.5: Global mean TOA indirect radiative forcings by anthropogenic aerosols calculated in DAO, CAM-KL, and CAM-LP simulations. The unit of the forcing is Wm^{-2}.

		DAO	CAM-KL	CAM-LP
Anthropogenic	Net	0.004	0.055	0.087
sulfate forcing	SW	-0.014	-0.190	-0.129
	LW	0.018	0.245	0.216
Anthropogenic	Net	2.349	0.335	0.547
surface source	SW	-5.182	-0.111	-0.615
soot forcing	LW	7.531	0.445	1.163
Aircraft	Net	0.102	0.100	0.131
generated soot	SW	-0.405	-0.147	-0.194
forcing	LW	0.084	0.508	0.325

5.5 Summary and conclusion

In this chapter, we calculated the global scale ice crystal number concentrations N_i from the nucleation process. During the simulation, two sets of meteorological field, one from data assimilation (DAO), one from a GCM (CAM), are used together with a chemical transport model to estimate the number concentration of sulfate, soot from surface sources, aircraft generated soot and dust particles. We then used two ice nucleation parameterization methods (the KL method and the LP method) to calculate the in-cloud N_i.

Our N_i results from simulations agree well with the measurements. There are distinct difference of N_i between NH and SH mid-latitudes, indicating the anthropogenic effects on the high cirrus clouds. The two parameterization methods produced similar results of N_i and r_e. High values of N_i from the CAM simulation are found between 100mb and 200mb, as well as in the south polar region. These high N_i are mainly formed by the homogeneous nucleation. These high values of N_i are not found in the DAO simulation.

Our results show the immersion nucleation is the dominant mechanism to form ice crystals in most regions in upper troposphere. Homogeneous nucleation is important at very high altitude in tropics and at south polar region. Deposition nucleation is not important in the regions where cirrus clouds occur.

Our simulations also show that the results from the CAM simulations using two different parameterization methods are very close. Both methods are able to represent the competition between homogeneous nucleation and heterogeneous nucleation. Both methods demonstrate the positive indirect effect and the negative indirect effect.

The net TOA forcings are dominated by LW radiation changes in most regions and have positive global annual mean values. Therefore, the net climate effect of anthropogenic aerosols on cirrus clouds is to warm the surface. The sequence of the global annual mean TOA net forcing for three anthropogenic aerosol species is: F(anthropogenic soot from surface sources) > F(soot generated by aircraft) > F(anthropogenic sulfate).

The anthropogenic sulfate increases the N_i from homogeneous nucleation, thereby decreasing the r_e. In the regions where heterogeneous nucleation is dominant, the change of cloud radiative properties due to anthropogenic sulfate is small.

Anthropogenic soot particles have two effects on the icy crystal formation and climate. In the regions where heterogenous nucleation dominates, the increase of ice nuclei increase the ice crystals due to immersion nucleation (positive effect). On the other hand, in the region where homogeneous nucleation dominates, the increase of heterogeneous ice nuclei could limit the maximum supersaturation and prevent or inhibit the occurrence of homogeneous nucleation. Since homogeneous nucleation generally produces much larger numbers of ice crystals, this effect could decrease the

occurrence of large N_i values (negative effect). This negative Twomey effect occurs in some tropical regions and polar regions. The negative effect tends to remove the large mode in the N_i occurrence distribution, while the positive effects decreases the occurrence of small N_i values.

The forcing patterns are a result of the aerosols and meteorological parameters. The anthropogenic sulfate forcing is mainly determined by the temperature, cloud thickness, and solar incident radiation. The pattern of forcing has only a small correlation with anthropogenic sulfate aerosols. The forcing from anthropogenic soot (including that from surface sources and aircraft sources) also depend on the meteorological fields since they determine whether or not homogeneous nucleation or heterogeneous nucleation occurs. However, the pattern of forcing by anthropogenic soot is mostly determined by the aerosol changes and therefore is more similar to the anthropogenic aerosol pattern.

Our study was concentrated on the cirrus clouds. Some ice crystals may exist in the polar boundary layer. These clouds resemble cirrus in terms of physics but are not assigned to the category of cirrus. They often generate exceptional optical displays in the Arctic and Antarctic regions (*Tape*, 1994). Nevertheless, the ice crystal number concentrations in these low-altitude polar region clouds are still shown in the above plots. We also note that we only considered clouds with very low temperature (T<-37 ℃). In the polar regions, ice crystals often exist in warmer mixed-phase clouds. In these clouds, the condensation freezing nucleation and contact nucleation modes could be more important than in the cirrus clouds. The coexistence of the ice particles and liquid particles and possible ice enhancement mechanisms strengthen the complexity of the cloud properties and their impact on the radiation in mixed phase clouds. We do not include these clouds in the current study.

Some other factors may cause an overestimation or underestimation of N_i in our study. For example, the volume fraction of the sulfuric acid coating to the total aerosol volume concentration ranges from 21% to 81% (*Mohler et al.*, 2005). Therefore, some soot particles can act as deposition nuclei instead of immersion nuclei. However, the aging process and agglomeration of the soot particles are currently not well understood yet (*Hendricks et al.*, 2004). In addition, we only simulated the formation process of the ice crystals. A global model with a prognostic equation of N_i which includes the sinks of the ice crystals is needed to better characterize the N_i profile in the cirrus clouds. Furthermore, contrail-cirrus is another type of cirrus that forms by the rapid cooling of aircraft exhaust. When the relative humidity in the environmental atmosphere exceeds the ice supersaturation, contrail cirrus can be persistent and exhibit features that are similar to other cirrus. In this study, we only considered the influence of the soot generated by the aircraft on pristine cirrus.

CHAPTER VI

Conclusions and future work

6.1　Conclusions

The aerosol indirect effect (the modification of climate by anthropogenic aerosols through changing cloud properties) remains one of the most important uncertainties in the projection of the future climate. To understand the physical and chemical mechanisms behind this effect and to reduce the uncertainty in the estimation of the indirect forcing are essential for both scientists and policy makers.

The aerosol-cloud-climate system is a complex system. The roles of different aerosol species in modifying cloud properties are different. The aerosol effects on the climate also depend on the microphysical parameters, dynamical parameters and radiative parameters. The purpose of this research is to quantify the different indirect effects caused by anthropogenic aerosols and to provide a guideline for future measurements and simulations in the study of aerosol indirect effect.

In the first part of this work report, we provided an observational evidence of the change in radiative forcing due to the aerosol indirect effect. Our study is based on the observations of aerosol properties, cloud properties and surface fluxes at two sites which represent a polluted region (SGP) and a clean region (NSA). Stratiform clouds events that satisfy several criteria were selected. These criteria restricted our

study to the low altitude warm clouds and reduced the uncertainty by excluding the very thick (or very thin) clouds and the clouds occurring at a time when the solar incident radiation is very small. In order to calculate the aerosol number concentration at the cloud base, we screened the cloud events by selecting those in which the atmosphere below cloud base is well mixed. This criterion is satisfied by limiting the difference of water vapor mixing ratio at cloud base and at surface to within 15 %. Two methods were used to calculate the cloud optical depth of the cloud events we selected. In the first method, the surface measured downward SW flux was input to a parameterization method (*Dong et al.*, 1997) to derive the cloud optical depth. This parameterization requires that the surface SW fluxes calculated from a δ-2-stream radiative transfer model match the observed values. In the second method, the measured aerosol properties were input to a cloud nucleation parcel model to calculate the cloud droplet number concentration. The measured cloud liquid water path enables us to calculate the cloud optical depth from the cloud droplet number concentration.

We constructed a plot of the relationship between cloud optical depth and cloud liquid water path to separate the radiative effect due to aerosols and the effect due to cloud liquid water path. Both methods introduced above showed that the values of cloud optical depth at the SGP site for a given LWP are systematically larger than that at the NSA site. The agreement between these two methods indicates that aerosols can affect the cloud radiative properties and the surface radiative fluxes. The factors that could explain the scatter in the model simulation, including the entrainment, the drizzle formation, and the ice formation and splintering, were discussed. Sensitivity tests were also made to study the uncertainty associated with the model inputs, including the updraft velocity, aerosol composition, and nitric acid gas

concentration. All the above discussion and tests suggest that our main conclusions are not affected. We also used a radiative transfer model to show the difference in the aerosol properties at the two sites would affect the TAO outgoing radiative flux, a phenomenon could be seen from satellites.

To quantify how large this aerosol indirect effect would change the global climate, we used 3-D meteorological fields together with a radiative transfer model to calculate the global first indirect aerosol forcing. We also examined the spatially-resolved uncertainty in estimates of the first aerosol indirect forcing. The global mean forcing calculated in the reference case is -1.30 Wm^{-2}. Uncertainties in the indirect forcing associated with aerosol and aerosol precursor emissions, aerosol mass concentrations from different chemical transport models, aerosol size distributions, the cloud droplet parameterization, the representation of the in-cloud updraft velocity, the relationship between effective radius and volume mean radius, cloud liquid water content, cloud fraction, and the change in the cloud drop single scattering albedo due to the presence of black carbon were calculated. The aerosol burden calculated by chemical transport models and the cloud fraction were found to be the most important sources of uncertainty. Variations in these parameters cause an underestimation or overestimation of the indirect forcing compared to the base case by more than 0.6 Wm^{-2}. Uncertainties associated with aerosol and aerosol precursor emissions, uncertainties in the representation of the aerosol size distribution (including the representation of the pre-industrial size distribution), and uncertainties in the representation of cloud droplet spectral dispersion effect cause uncertainties in the global mean forcing of 0.2~0.6 Wm^{-2}. There are significant regional differences in the uncertainty associated with the first indirect forcing with the largest uncertainties in industrial regions (North America, Europe, East Asia) followed by those in the major biomass burning

regions.

Following the calculation of first aerosol indirect forcing, we considered two aerosol effects on clouds and climate that are not well known and not well represented in the current prevailing models.

First, we studied the aerosol indirect effect by an important aerosol component nitrate, and its counterpart in the atmosphere, HNO_3. Different treatments for the distribution of nitrate in aerosol (DYN, HYB, UPT, EQU) were used to calculate the cloud droplet number concentration for different representative sites. Compared to the more accurate DYN method, the HYB method produces very similar N_d. The UPT and EQU methods tend to underestimate the cloud droplet number concentration. Both nitrate in aqueous phase and HNO_3 in gas phase has effect on cloud nucleation. Most of the HNO_3 gas is re-distributed to the fine mode aerosols during cloud formation. The change of N_d due to nitrate and HNO_3 gas is affected by some properties of the aerosol particles and the atmosphere, including the soluble fraction of pre-existing aerosol, the pre-existing aerosol concentration, the HNO_3 concentration in the atmosphere, the NO_3^- concentration in the aerosols, and the updraft velocity. The indirect radiative forcings due to the nitrate and HNO_3 at several typical sites was calculated. Different options for treating the cloud fraction and cloud liquid water content were used. The nitrate aerosol indirect effect on TOA radiative flux was found to be comparable to that by anthropogenic sulfate in some sites. Based on the theory that most HNO_3 is transferred to fine mode aerosol particles, we use a substitution method to re-distribute the HNO_3 to the aerosol phase according to the surface area distribution. Then, two parameterization methods (AG3 and NS) were used together with the re-distributed HNO_3 as NO_3^- to approximate the effect due to HNO_3 gas. This substitution method is better in representing the HNO_3 effect

than the original no-HNO3 method.

Second, we investigated the effects of anthropogenic aerosols on cirrus clouds and global climate. For this simulation, two sets of meteorological field, one from data assimilation (DAO) and one from a GCM (CAM), were used together with a chemical transport model to estimate the number concentration of sulfate, dust, soot from surface sources, and soot generated by aircraft. Two newly developed ice nucleation parameterization methods (the KL method and LP method) were used to calculate the in-cloud N_i. Our N_i results from these simulations agree well with most measurements. There is a distinct difference in N_i between the NH and SH mid-latitudes, indicating that there are significant anthropogenic effects on high cirrus clouds. The two parameterization methods produced similar results of N_i and r_e when the same RH_i was used.

The indirect forcing due to anthropogenic aerosols was calculated using a radiative transfer model by considering different emission scenarios. Anthropogenic sulfate increases the N_i from homogeneous nucleation, thereby decreasing r_e. In the DAO simulation, since homogeneous nucleation is not dominant, this change is not very important. The effect of anthropogenic soot, including that from surface sources and aircraft sources, on N_i is largely affected by the competition between homogeneous nucleation and heterogeneous nucleation. Therefore anthropogenic soot has different effect on cirrus clouds in different regions. When homogeneous nucleation dominates, the addition of anthropogenic soot competes for the vapor and reduces the occurrence of homogeneous nucleation, thereby decreasing N_i. This negative Twomey effect occurs in some tropical regions and the south polar region in the CAM simulations. On the other hand, when heterogeneous nucleation is dominant, the addition of anthropogenic soot increases the N_i formed by immersion nucleation. This effect

occurs in most regions in the DAO simulation, and in the regions except some tropical areas and the south polar region in the CAM simulations.

The indirect radiative forcing of the anthropogenic aerosols on cirrus clouds is related to the N_i change, but it also depends on other parameters such as cloud fraction and cloud top temperature. The TOA net forcings are dominated by the LW radiation change in most regions and have positive global annual mean values. Therefore, the net climate effect of the anthropogenic aerosols on cirrus clouds is to warm the surface. The sequence of the global annual mean TOA net forcing for the three anthropogenic aerosol species is: F(anthropogenic soot from surface sources) > F(aircraft generated soot) > F(anthropogenic sulfate). The anthropogenic soot forcing in some tropical regions and the south polar region is negative, which is due to the negative Twomey effect.

6.2   Future work

For the topics covered in this study, we mainly used off-line calculations and assumed that the number concentrations of cloud droplets (N_d) or ice crystals (N_i) are only determined by the nucleation process. In the real atmosphere, they are governed by the equilibrium between the sources and the sinks. The above simplification does not take account of processes such as coagulation, advection, entrainment, detrainment, scavenging, etc. These processes could be included in an on-line GCM simulation with an explicit treatment of the (N_d) or (N_i). In addition, the use of an on-line simulation could allow us to track the change of the liquid water content or ice water content and simulate the second aerosol indirect effect.

As we continuously emphasized in previous chapters, the study of aerosol indirect effect is still in the developing stage. This is demonstrated by three aspects.

First, there are not enough measurements to provide reliable data and to validate simulations. Second, the mechanisms in the aerosol-cloud-climate system is not fully understood yet. Third, the method of simulation needs to be improved. Therefore, a lot of work is necessary before we can fully quantify this effect. I list several items among those in the following:

- Chemical effects on nucleation

  - Soluble gas effect

  - Partially soluble organics on solution effect

  - Surface active substances

- Physical effects on nucleation

  - Kinetic effect in cloud nucleation

  - Representation of in-cloud updraft velocity

- Characterization the aerosol and cloud properties

  - Aerosol concentration and size distribution

  - Cloud amount and cloud liquid water

  - Dispersion of cloud droplets

- Other radiative effects

  - Effects on ice clouds and mixed-phase clouds

  - BC burning effect

  - Convective clouds

Recently, the chemical effect on aerosol modulation of cloud microphysics has been addressed (*Nenes et al.*, 2002), specifically, the impact of soluble gases (such as HNO_3 and HCl) and carbonaceous aerosols (including partially soluble and surface active OC) on the activation of cloud condensation nuclei. *Kulmala et al.* (1993a) and *Laaksonen et al.* (1998) suggested that atmospheric HNO_3 could alter the activation and growth of CCN significantly. In this study, we investigated the effect of HNO_3 on the warm clouds and climate. However, the substitution parameterization method has not been applied in the global model and more measurements are needed to examine its performance. The effect of OC has been studied based on the experiments and parcel models (*Facchini et al.*, 1999; *Li et al.*, 1998). *Abdul-Razzak and Ghan* (2004) extended their parametric representation of aerosol activation by including two mechanisms for surface-active organic compounds that affect aerosol activation: lowering the surface tension and altering the bulk hygroscopicity of the particles. This provides an opportunity to study the organic aerosol effect on clouds and climate on the global scale, although further measurements are needed since the representation of surface tension in *Abdul-Razzak and Ghan* (2004) was based on experimental data considering only particular organic surfactants (*Facchini et al.*, 2001; *Li et al.*, 1998).

Current cloud parameterizations generally rely on the assumption that particles are at equilibrium with the ambient water vapor concentration until activated as cloud condensation nuclei. This was not always be appropriate for aerosol populations existing in the atmosphere. Several kinetic limitation processes can inhibit the formation of cloud droplets (*Chuang et al.*, 1997; *Nenes et al.*, 2001). *Nenes et al.* (2001) showed that the equilibrium assumption leads to an overprediction of N_d by less than 10% for marine aerosol and can exceed 40% for urban type aerosol. So future cloud nucleation parameterizations should be matched to simulations which

consider kinetic limitations.

Most current physically-based cloud parameterizations need to consideration of the sub-grid scale variation of the updraft velocity. As we stated in Chapter 3, two methods (TKE and PDF) are generally used. The TKE method uses a single value to represent the composite effect of the sub-grid variation, which is a simplification and causes large uncertainty. In addition, the calculation of the TKE may not account for the other factors that cause a sub-grid variation of the updraft velocity. In the PDF method, a probability distribution is assumed. However, the shape parameters of this distribution have not been well determined. More observations, particularly at high latitudes where cirrus clouds occur, are needed.

As we show in the uncertainty study of the first indirect effect, the characterization of aerosols and clouds contributes large uncertainties to the calculation of the aerosol indirect forcing. Therefore in the future, in order to reduce this uncertainty, we need to concentrate on the following: Increase the performance the Chemical Transport Models to provide more accurate aerosol field (This is also important for the simulation of aerosol effects on cirrus clouds); Develop better parameterizations of cloud fraction and cloud water content; Better represent the dispersion effect of the cloud spectra.

In current studies on aerosol indirect effect, more efforts have been spent on the Twomey effect and the Albrecht effect in stratiform clouds. However the aerosol-cloud-climate system is so complex that aerosols cloud affect clouds and climate through different mechanisms. We investigated the aerosol effect on cirrus clouds in Chapter V. But the uncertainty is still large and more measurements and theoretical developments are needed. The mixed phase clouds are more difficult to parameterize because the physical processes are not well known. This could be a very challenging

but a very interesting area in the study of aerosol-cloud relationships.

Due to its efficient absorption of solar radiation, black carbon (BC) could exert effects on clouds through different mechanisms (*Nenes et al.*, 2002; *Ackerman et al.*, 2000). The modification of extinction efficiency by BC has been calculated to be small (*Chen and Penner*, 2005). The dynamical response to BC heating and its effect on cloudiness reduction can be calculated by radiative transfer modules in GCMs. The heating due to BC absorption can also raise the droplet vapor pressure and inhibit the activation of CCN (*Conant et al.*, 2002). This effect is more complex. Based on some assumptions, *Conant et al.* (2002) extended Köhler theory by including the solar heating term due to BC absorption. This formula enables us to improve the current nucleation parameterizations used in global simulations.

BIBLIOGRAPHY

BIBLIOGRAPHY

Abdul-Razzak, H., and S. J. Ghan (2000), A parameterization of aerosol activation 2. multiple aerosol types, *Journal of Geophysical Research-Atmospheres*, *105*(D5), 6837–6844.

Abdul-Razzak, H., and S. J. Ghan (2002), A parameterization of aerosol activation - 3. sectional representation, *Journal of Geophysical Research-Atmospheres*, *107*(D3).

Abdul-Razzak, H., and S. J. Ghan (2004), Parameterization of the influence of organic surfactants on aerosol activation, *Journal of Geophysical Research-Atmospheres*, *109*(D3).

Abdul-Razzak, H., S. J. Ghan, and C. Rivera-Carpio (1998), A parameterization of aerosol activation - 1. single aerosol type, *Journal of Geophysical Research-Atmospheres*, *103*(D6), 6123–6131.

Ackerman, A. S., O. B. Toon, D. E. Stevens, A. J. Heymsfield, V. Ramanathan, and E. J. Welton (2000), Reduction of tropical cloudiness by soot, *Science*, *288*(5468), 1042–1047.

Adams, P. J., J. H. Seinfeld, and D. M. Koch (1999), Global concentrations of tropospheric sulfate, nitrate, and ammonium aerosol simulated in a general circulation model, *Journal of Geophysical Research-Atmospheres*, *104*(D11), 13,791–13,823.

Adams, P. J., J. H. Seinfeld, D. Koch, L. Mickley, and D. Jacob (2001), General circulation model assessment of direct radiative forcing by the sulfate-nitrate-ammonium-water inorganic aerosol system, *Journal of Geophysical Research-Atmospheres*, *106*(D1), 1097–1111.

Andres, R. J., and A. D. Kasgnoc (1998), A time-averaged inventory of sub-aerial volcanic sulfur emissions, *Journal of Geophysical Research-Atmospheres*, *103*(D19), 25,251–25,261.

Andronache, C., L. J. Donner, C. J. Seman, V. Ramaswamy, and R. S. Hemler (1999), Atmospheric sulfur and deep convective clouds in tropical pacific: A model study, *Journal of Geophysical Research-Atmospheres*, *104*(D4), 4005–4024.

Bauer, S. E., Y. Balkanski, M. Schulz, D. A. Hauglustaine, and F. Dentener (2004), Global modeling of heterogeneous chemistry on mineral aerosol surfaces: Influence on tropospheric ozone chemistry and comparison to observations, *Journal of Geophysical Research-Atmospheres*, *109*(D2), d02304.

Blyth, A. M., and J. Latham (1993), Development of ice and precipitation in new mexican summertime cumulus clouds, *Quarterly Journal of the Royal Meteorological Society*, *119*(509), 91–120, part A.

Borrmann, S., S. Solomon, J. E. Dye, and B. P. Luo (1996), The potential of cirrus clouds for heterogeneous chlorine activation, *Geophysical Research Letters*, *23*(16), 2133–2136.

Boucher, O. (1999), Air traffic may increase cirrus cloudiness, *Nature*, *397*(6714), 30–31.

Boucher, O., and U. Lohmann (1995), The sulfate-ccn-cloud albedo effect - a sensitivity study with 2 general-circulation models, *Tellus Series B-Chemical and Physical Meteorology*, *47*(3), 281–300.

Brenguier, J. L., H. Pawlowska, L. Schuller, R. Preusker, J. Fischer, and Y. Fouquart (2000), Radiative properties of boundary layer clouds: Droplet effective radius versus number concentration, *Journal of the Atmospheric Sciences*, *57*(6), 803–821.

Brenguier, J. L., H. Pawlowska, and L. Schuller (2003), Cloud microphysical and radiative properties for parameterization and satellite monitoring of the indirect effect of aerosol on climate, *Journal of Geophysical Research-Atmospheres*, *108*(D15), 8632.

Buseck, P. R., and M. Posfai (1999), Airborne minerals and related aerosol particles: Effects on climate and the environment, *Proceedings of the National Academy of Sciences of the United States of America*, *96*(7), 3372–3379.

Cachier, H., C. Liousse, P. Buatmenard, and A. Gaudichet (1995), Particulate content of savanna fire emissions, *Journal of Atmospheric Chemistry*, *22*(1-2), 123–148.

Chen, Y., and J. E. Penner (2005), Uncertainty analysis for estimates of the first indirect aerosol effect, *Atmospheric Chemistry and Physics*, *5*, 2935–2948.

Chen, Y. L., S. M. Kreidenweis, L. M. McInnes, D. C. Rogers, and P. J. DeMott (1998), Single particle analyses of ice nucleating aerosols in the upper troposphere and lower stratosphere, *Geophysical Research Letters*, *25*(9), 1391–1394.

Chin, M., P. Ginoux, S. Kinne, O. Torres, B. N. Holben, B. N. Duncan, R. V. Martin, J. A. Logan, A. Higurashi, and T. Nakajima (2002), Tropospheric

aerosol optical thickness from the gocart model and comparisons with satellite and sun photometer measurements, *Journal of the Atmospheric Sciences*, *59*(3), 461–483.

Chou, M. D. (1990), Parameterizations for the absorption of solar-radiation by o2 and co2 with application to climate studies, *Journal of Climate*, *3*(2), 209–217.

Chuang, C. C., and J. E. Penner (1995), Effects of anthropogenic sulfate on cloud drop nucleation and optical-properties, *Tellus Series B-Chemical and Physical Meteorology*, *47*(5), 566–577.

Chuang, C. C., J. E. Penner, J. M. Prospero, K. E. Grant, G. H. Rau, and K. Kawamoto (2002), Cloud susceptibility and the first aerosol indirect forcing: Sensitivity to black carbon and aerosol concentrations, *Journal of Geophysical Research-Atmospheres*, *107*(D21).

Chuang, P. Y., R. J. Charlson, and J. H. Seinfeld (1997), Kinetic limitations on droplet formation in clouds, *Nature*, *390*(6660), 594–596.

Coakley, J. A., R. L. Bernstein, and P. A. Durkee (1987), Effect of ship-stack effluents on cloud reflectivity, *Science*, *237*(4818), 1020–1022.

Cohard, J.-M., J.-P. Pinty, and B. C. (1998), Extending twomey's analytical estimate of nucleated cloud droplet concentrations from ccn spectra, *Journal of the Atmospheric Sciences*, *55*, 3348–3357.

Collins, W. D., P. J. Rasch, B. A. Boville, J. J. Hack, J. R. McCaa, D. L. Williamson, J. T. Kiehl, B. Briegleb, C. Bitz, S. J. Lin, M. Zhang, and Y. Dai (2004), Description of the ncar community atmosphere model (cam3.0), *Tech. Rep. NCAR/TN-464+STR*.

Conant, W. C., A. Nenes, and J. H. Seinfeld (2002), Black carbon radiative heating effects on cloud microphysics and implications for the aerosol indirect effect, 1. extended kohler theory, *Journal of Geophysical Research*, *107*(D21), 4604.

Cziczo, D. J., P. J. DeMott, S. D. Brooks, A. J. Prenni, D. S. Thomson, D. Baumgardner, J. C. Wilson, S. M. Kreidenweis, and D. M. Murphy (2004), Observations of organic species and atmospheric ice formation, *Geophysical Research Letters*, *31*(12).

de Reus, M., F. Dentener, A. Thomas, S. Borrmann, J. Ström, and J. Lelieveld (2000), Airborne observations of dust aerosol over the north atlantic ocean during ace 2: Indications for heterogeneous ozone destruction, *Journal of Geophysical Research-Atmospheres*, *105*(D12), 15,263–15,275.

DeMott, P. J., M. P. Meyers, and W. R. Cotton (1994), Parameterization and impact of ice initiation processes relevant to numerical-model simulations of cirrus clouds, *Journal of the Atmospheric Sciences*, *51*(1), 77–90.

DeMott, P. J., D. C. Rogers, and S. M. Kreidenweis (1997), The susceptibility of ice formation in upper tropospheric clouds to insoluble aerosol components, *Journal of Geophysical Research-Atmospheres*, *102*(D16), 19,575–19,584.

DeMott, P. J., D. C. Rogers, S. M. Kreidenweis, Y. L. Chen, C. H. Twohy, D. Baumgardner, A. J. Heymsfield, and K. R. Chan (1998), The role of heterogeneous freezing nucleation in upper tropospheric clouds: Inferences from success, *Geophysical Research Letters*, *25*(9), 1387–1390.

DeMott, P. J., D. J. Cziczo, A. J. Prenni, D. M. Murphy, S. M. Kreidenweis, D. S. Thomson, R. Borys, and D. C. Rogers (2003), Measurements of the concentration and composition of nuclei for cirrus formation, *Proceedings of the National Academy of Sciences of the United States of America*, *100*(25), 14,655–14,660.

Dentener, F. J., and P. J. Crutzen (1993), Reaction of n2o5 on tropospheric aerosols - impact on the global distributions of nox, o3, and oh, *Journal of Geophysical Research-Atmospheres*, *98*(D4), 7149–7163.

Dong, X. Q., and G. G. Mace (2003), Profiles of low-level stratus cloud microphysics deduced from ground-based measurements, *Journal of Atmospheric and Oceanic Technology*, *20*(1), 42–53.

Dong, X. Q., T. P. Ackerman, E. E. Clothiaux, P. Pilewskie, and Y. Han (1997), Microphysical and radiative properties of boundary layer stratiform clouds deduced from ground-based measurements, *Journal of Geophysical Research-Atmospheres*, *102*(D20), 23,829–23,843.

Dong, X. Q., G. G. Mace, P. Minnis, and D. F. Young (2001), Arctic stratus cloud properties and their effect on the surface radiation budget: Selected cases from fire ace, *Journal of Geophysical Research-Atmospheres*, *106*(D14), 15,297–15,312.

Dowling, D. R., and L. F. Radke (1990), A summary of the physical-properties of cirrus clouds, *Journal of Applied Meteorology*, *29*(9), 970–978.

Durkee, P. A., K. J. Noone, R. J. Ferek, D. W. Johnson, J. P. Taylor, T. J. Garrett, P. V. Hobbs, J. G. Hudson, C. S. Bretherton, G. Innis, G. M. Frick, W. A. Hoppel, C. D. O'Dowd, L. M. Russell, R. Gasparovic, K. E. Nielsen, S. A. Tessmer, E. Ostrom, S. R. Osborne, R. C. Flagan, J. H. Seinfeld, and H. Rand (2000), The impact of ship-produced aerosols on the microstructure and albedo of warm marine stratocumulus clouds: A test of mast hypotheses 1i and 1ii, *Journal of the Atmospheric Sciences*, *57*(16), 2554–2569.

Ebert, E. E., and J. A. Curry (1992), A parameterization of ice-cloud optical-properties for climate models, *Journal of Geophysical Research-Atmospheres*, *97*(D4), 3831–3836.

Facchini, M. C., M. Mircea, S. Fuzzi, and R. J. Charlson (1999), Cloud albedo enhancement by surface-active organic solutes in growing droplets, *Nature*, *401*(6750), 257–259.

Facchini, M. C., M. Mircea, S. Fuzzi, and R. J. Charlson (2001), Comments on "influence of soluble surfactant properties on the activation of aerosol particles containing inorganic solute", *Journal of the Atmospheric Sciences*, *58*(11), 1465–1467.

Fahey, D. W., and U. Schumann (1999), Aviation-produced aerosols and cloudiness, in *Aviation and the global atmosphere, A special report of IPCC (Intergovernmental Panel on Climate Change)*, edited by J. E. Penner, D. J. Griggs, and M. McFarland, pp. 65–120, Cambridge University, Cambridge.

Feingold, G., and A. J. Heymsfield (1992), Parameterizations of condensational growth of droplets for use in general-circulation models, *Journal of the Atmospheric Sciences*, *49*(23), 2325–2342.

Feng, Y. (2005), Global modeling of nitrate and ammonium aerosol: radiative effect and interaction with gas-phase chemistry and aerosols, Ph.D. thesis, Unviersity of Michigan.

Feng, Y., J. E. Penner, S. Sillman, and X. H. Liu (2004), Effects of cloud overlap in photochemical models, *Journal of Geophysical Research-Atmospheres*, *109*(D4), d04310.

Fletcher, N. H. (1962), Surface structure of water and ice, *Philosophical Magazine*, *7*(74), 255–.

Fowler, L. D., and D. A. Randall (1996), Liquid and ice cloud microphysics in the csu general circulation model .2. impact on cloudiness, the earth's radiation budget, and the general circulation of the atmosphere, *Journal of Climate*, *9*(3), 530–560.

Geleyn, J.-F., and A. Hollingsworth (1979), An economical analytical method for the computation of the interaction between scattering and line absorption of radiation, *Beitr. Phys. Atmos.*, *52*, 1–16.

Ghan, S., C. Chuang, and J. E. Penner (1993), A parameterization of cloud droplet nucleation, part i: single aerosol type, *Atmospheric Research*, *30*, 197–221.

Ghan, S., R. Easter, J. Hudson, and F. M. Breon (2001), Evaluation of aerosol indirect radiative forcing in mirage, *Journal of Geophysical Research-Atmospheres*, *106*(D6), 5317–5334.

Gierens, K. (2003), On the transition between heterogeneous and homogeneous freezing, *Atmospheric Chemistry and Physics*, *3*, 437–446.

Gierens, K., U. Schumann, M. Helten, H. Smit, and A. Marenco (1999), A distribution law for relative humidity in the upper troposphere and lower stratosphere derived from three years of mozaic measurements, *Annales Geophysicae-Atmospheres Hydrospheres and Space Sciences*, *17*(9), 1218–1226.

Ginoux, P., M. Chin, I. Tegen, J. M. Prospero, B. Holben, O. Dubovik, and S. J. Lin (2001), Sources and distributions of dust aerosols simulated with the gocart model, *Journal of Geophysical Research-Atmospheres*, *106*(D17), 20,255–20,273.

Glantz, P., and K. J. Noone (2000), A physically-based algorithm for estimating the relationship between aerosol mass and cloud droplet number, *Tellus Series B-Chemical and Physical Meteorology*, *52*(5), 1216–1231.

Gong, S. L., L. A. Barrie, and J. P. Blanchet (1997), Modeling sea-salt aerosols in the atmosphere .1. model development, *Journal of Geophysical Research-Atmospheres*, *102*(D3), 3805–3818.

Grant, K. E., C. C. Chuang, A. S. Grossman, and J. E. Penner (1999), Modeling the spectral optical properties of ammonium sulfate and biomass burning aerosols: parameterization of relative humidity effects and model results, *Atmospheric Environment*, *33*(17), 2603–2620.

Guenther, A., C. N. Hewitt, D. Erickson, R. Fall, C. Geron, T. Graedel, P. Harley, L. Klinger, M. Lerdau, W. A. McKay, T. Pierce, B. Scholes, R. Steinbrecher, R. Tallamraju, J. Taylor, and P. Zimmerman (1995), A global-model of natural volatile organic-compound emissions, *Journal of Geophysical Research-Atmospheres*, *100*(D5), 8873–8892.

Gultepe, I., G. A. Isaac, A. Korolev, S. G. Cober, and J. W. Strapp (1998), Effects of ice crystal shape on the radiative characteristics of low level ice clouds, in *Conference on cloud physics*, pp. 372–375, Everett, WA.

Gultepe, I., G. A. Isaac, and S. G. Cober (2001), Ice crystal number concentration versus temperature for climate studies, *International Journal of Climatology*, *21*(10), 1281.

Haag, W., and B. Kärcher (2004), The impact of aerosols and gravity waves on cirrus clouds at midlatitudes, *Journal of Geophysical Research-Atmospheres*, *109*(D12), d12202.

Haag, W., B. Kärcher, J. Ström, A. Minikin, U. Lohmann, J. Ovarlez, and A. Stohl (2003), Freezing thresholds and cirrus cloud formation mechanisms inferred from in situ measurements of relative humidity, *Atmospheric Chemistry and Physics*, *3*, 1791–1806.

Hack, J. J. (1998), Sensitivity of the simulated climate to a diagnostic formulation for cloud liquid water, *Journal of Climate*, *11*(7), 1497–1515.

Han, Q. Y., W. B. Rossow, and A. A. Lacis (1994), Near-global survey of effective droplet radii in liquid water clouds using isccp data, *Journal of Climate*, *7*(4), 465–497.

Han, Q. Y., W. B. Rossow, J. Chou, and R. M. Welch (1998), Global survey of the relationships of cloud albedo and liquid water path with droplet size using isccp, *Journal of Climate*, *11*(7), 1516–1528.

Han, Q. Y., W. B. Rossow, J. Zeng, and R. Welch (2002), Three different behaviors of liquid water path of water clouds in aerosol-cloud interactions, *Journal of the Atmospheric Sciences*, *59*(3), 726–735.

Hansen, J., M. Sato, and R. Ruedy (1997), Radiative forcing and climate response, *Journal of Geophysical Research-Atmospheres*, *102*(D6), 6831–6864.

Haywood, J., and O. Boucher (2000), Estimates of the direct and indirect radiative forcing due to tropospheric aerosols: A review, *Reviews of Geophysics*, *38*(4), 513–543.

Hendricks, J., B. Kärcher, A. Dopelheuer, J. Feichter, U. Lohmann, and D. Baumgardner (2004), Simulating the global atmospheric black carbon cycle: a revisit to the contribution of aircraft emissions, *Atmospheric Chemistry and Physics*, *4*, 2521–2541.

Hendricks, J., B. Kärcher, U. Lohmann, and M. Ponater (2005), Do aircraft black carbon emissions affect cirrus clouds on the global scale?, *Geophysical Research Letters*, *32*(12).

Heymsfield, A. J., and L. M. Miloshevich (1993), Homogeneous ice nucleation and supercooled liquid water in orographic wave clouds, *Journal of the Atmospheric Sciences*, *50*(15), 2335–2353.

Hobbs, P. V., T. J. Garrett, R. J. Ferek, S. R. Strader, D. A. Hegg, G. M. Frick, W. A. Hoppel, R. F. Gasparovic, L. M. Russell, D. W. Johnson, C. O'Dowd, P. A. Durkee, K. E. Nielsen, and G. Innis (2000), Emissions from ships with respect to their effects on clouds, *Journal of the Atmospheric Sciences*, *57*(16), 2570–2590.

Hoek, G., M. G. Mennen, G. A. Allen, P. Hofschreuder, and T. van der Meulen (1996), Concentrations of acidic air pollutants in the netherlands, *Atmospheric Environment*, *30*, 3141–3150.

Houghton, J. (2005), Global warming, *Reports on Progress in Physics*, *68*(6), 1343–1403.

Houghton, J. T., Y. Ding, D. J. Griggs, M. Noguer, P. J. van der Linden, X. Dai, K. Maskell, and C. A. Johnson (2001), *The scientific basis. Contribution of working group I to the Third Assessment Report of the Intergovernmental Panel on Climate Change*, Cambridge University Press, Cambridge, UK.

Hoyle, C. R., B. P. Luo, and T. Peter (2005), The origin of high ice crystal number densities in cirrus clouds, *Journal of the Atmospheric Sciences*, *62*(7), 2568–2579.

Intrieri, J. M., G. L. Stephens, W. L. Eberhard, and T. Uttal (1993), A method for determining cirrus cloud particle sizes using lidar and radar backscatter technique, *Journal of Applied Meteorology*, *32*(6), 1074–1082.

Ito, A., and J. E. Penner (2005), Historical emissions of carbonaceous aerosols from biomass and fossil fuel burning for the period 1870-2000, *Global Biogeochemical Cycles*, *19*(2), gB2028.

Iversen, T., A. Kirkevag, J. E. Kristjansson, and Seland (2001), Climate effects of sulphate and black carbon estimated in a global climate model, in *Air pollution modeling and its application*, vol. XIV, edited by Gryning and Schiermeier, pp. 335–342, Kluwer Academic/Plenum Publishers, New York.

Jacobson, M. Z. (1997), Numerical techniques to solve condensational and dissolutional growth equations when growth is coupled to reversible reactions, *Aerosol Science and Technology*, *27*(4), 491–498.

Jacobson, M. Z. (2001), Global direct radiative forcing due to multicomponent anthropogenic and natural aerosols, *Journal of Geophysical Research-Atmospheres*, *106*(D2), 1551–1568.

Jensen, E. J., and O. B. Toon (1994), Ice nucleation in the upper troposphere - sensitivity to aerosol number density, temperature, and cooling rate, *Geophysical Research Letters*, *21*(18), 2019–2022.

Jones, A., D. L. Roberts, and A. Slingo (1994), A climate model study of indirect radiative forcing by anthropogenic sulfate aerosols, *Nature*, *370*(6489), 450–453.

Jones, A., D. L. Roberts, M. J. Woodage, and C. E. Johnson (2001), Indirect sulphate aerosol forcing in a climate model with an interactive sulphur cycle, *Journal of Geophysical Research-Atmospheres*, *106*(D17), 20,293–20,310.

Joseph, J. H., W. J. Wiscombe, and J. A. Weinman (1976), Delta-eddington approximation for radiative flux-transfer, *Journal of the Atmospheric Sciences*, *33*(12), 2452–2459.

Kärcher, B., and U. Lohmann (2002), A parameterization of cirrus cloud formation: Homogeneous freezing of supercooled aerosols, *Journal of Geophysical Research-Atmospheres*, *107*(D1-D2).

Kärcher, B., and U. Lohmann (2003), A parameterization of cirrus cloud formation: Heterogeneous freezing, *Journal of Geophysical Research-Atmospheres*, *108*(D14).

Kärcher, B., and J. Ström (2003), The roles of dynamical variability and aerosols in cirrus cloud formation, *Atmospheric Chemistry and Physics*, *3*, 823–838.

Kärcher, B., R. Busen, A. Petzold, F. P. Schroder, U. Schumann, and E. J. Jensen (1998), Physicochemistry of aircraft-generated liquid aerosols, soot, and ice particles - 2. comparison with observations and sensitivity studies, *Journal of Geophysical Research-Atmospheres*, *103*(D14), 17,129–17,147.

Kärcher, B., J. Hendricks, and U. Lohmann (2006), Physically based parameterization of cirrus cloud formation for use in global atmospheric models, *Journal of Geophysical Research-Atmospheres*, *111*(D1), d01205.

Karl, T. R., and K. E. Trenberth (2003), Modern global climate change, *Science*, *302*(5651), 1719–1723.

Kaufman, Y. J., and R. S. Fraser (1997), The effect of smoke particles on clouds and climate forcing, *Science*, *277*(5332), 1636–1639.

Kettle, A. J., and M. O. Andreae (2000), Flux of dimethylsulfide from the oceans: A comparison of updated data seas and flux models, *Journal of Geophysical Research-Atmospheres*, *105*(D22), 26,793–26,808.

Kiehl, J. T., and K. E. Trenberth (1997), Earth's annual global mean energy budget, *Bulletin of the American Meteorological Society*, *78*(2), 197–208.

Kiehl, J. T., T. L. Schneider, P. J. Rasch, M. C. Barth, and J. Wong (2000), Radiative forcing due to sulfate aerosols from simulations with the national center for atmospheric research community climate model, version 3, *Journal of Geophysical Research-Atmospheres*, *105*(D1), 1441–1457.

King, M. D., S. C. Tsay, S. E. Platnick, M. K. Wang, and K. N. Liou (1997), Cloud retrieval algorithms for modis: optical thickness, effective particle radius, and thermodynamic phase, *Tech. Rep. ATBD-MOD-05*.

Kitto, A. M. N., and R. M. Harrison (1992), Nitrous and nitric-acid measurements at sites in south-east england, *Atmospheric Environment Part a-General Topics*, *26*(2), 235–241.

Kley, D., P. J. Crutzen, H. G. J. Smit, H. Vomel, S. J. Oltmans, H. Grassl, and V. Ramanathan (1996), Observations of near-zero ozone concentrations over the convective pacific: Effects on air chemistry, *Science*, *274*(5285), 230–233.

Koop, T., B. P. Luo, A. Tsias, and T. Peter (2000), Water activity as the determinant for homogeneous ice nucleation in aqueous solutions, *Nature*, *406*(6796), 611–614.

Kristensson, A., J. F. Gayet, J. Ström, and F. Auriol (2000), In situ observations of a reduction in effective crystal diameter in cirrus clouds near flight corridors, *Geophysical Research Letters*, *27*(5), 681–684.

Kristjansson, J. E. (2002), Studies of the aerosol indirect effect from sulfate and black carbon aerosols, *Journal of Geophysical Research-Atmospheres*, *107*(D15), 4246.

Kuang, Z. M., and Y. L. Yung (2000), Reflectivity variations off the peru coast: Evidence for indirect effect of anthropogenic sulfate aerosols on clouds, *Geophysical Research Letters*, *27*(16), 2501–2504.

Kulmala, M., A. Laaksonen, P. Korhonen, T. Vesala, and T. Ahonen (1993a), The effect of atmospheric nitric acid vapor on cloud condensation nucleus activation, *Journal of Geophysical Research*, *98*(D12), 22,949–22,958.

Kulmala, M., T. Vesala, and P. E. Wagner (1993b), An analytical expression for the rate of binary condensational particle growth, *Proceedings of the Royal Society of London Series a-Mathematical Physical and Engineering Sciences*, *441*(1913), 589–605.

Kulmala, M., P. Korhonen, A. Laaksonen, and T. Vesala (1995), Changes in cloud properties due to nox emissions, *Geophysical Research Letters*, *22*(3), 239–242.

Kulmala, M., A. Laaksonen, R. J. Charlson, and P. Korhonen (1997), Clouds without supersaturation, *Nature*, *388*(6640), 336–337.

Laaksonen, A., P. Korhonen, M. Kulmala, and R. J. Charlson (1998), Modification of the kuhler equation to include soluble trace gases and slightly soluble substances, *Journal of the Atmospheric Sciences*, *55*(5), 853–862.

Lawson, R. P., B. A. Baker, C. G. Schmitt, and T. L. Jensen (2001), An overview of microphysical properties of arctic clouds observed in may and july 1998 during fire ace, *Journal of Geophysical Research-Atmospheres*, *106*(D14), 14,989–15,014.

Leaitch, W. R., C. M. Banic, G. A. Isaac, M. D. Couture, P. S. K. Liu, I. Gultepe, S. M. Li, L. Kleinman, P. H. Daum, and J. I. MacPherson (1996), Physical and chemical observations in marine stratus during the 1993 north atlantic regional experiment: Factors controlling cloud droplet number concentrations, *Journal of Geophysical Research-Atmospheres*, *101*(D22), 29,123–29,135.

Lee, S. H., J. M. Reeves, J. C. Wilson, D. E. Hunton, A. A. Viggiano, T. M. Miller, J. O. Ballenthin, and L. R. Lait (2003), Particle formation by ion nucleation in the upper troposphere and lower stratosphere, *Science*, *301*(5641), 1886–1889.

Lee, S. H., J. C. Wilson, D. Baumgardner, R. L. Herman, E. M. Weinstock, B. G. LaFleur, G. Kok, B. Anderson, P. Lawson, B. Baker, A. Strawa, J. V. Pittman, J. M. Reeves, and T. P. Bui (2004), New particle formation observed in the tropical/subtropical cirrus clouds, *Journal of Geophysical Research-Atmospheres*, *109*(D20).

Li, Z. D., A. L. Williams, and M. J. Rood (1998), Influence of soluble surfactant properties on the activation of aerosol particles containing inorganic solute, *Journal of the Atmospheric Sciences*, *55*(10), 1859–1866.

Liao, H., P. J. Adams, S. H. Chung, J. H. Seinfeld, L. J. Mickley, and D. J. Jacob (2003), Interactions between tropospheric chemistry and aerosols in a unified general circulation model, *Journal of Geophysical Research-Atmospheres*, *108*(D1), 4001.

Liao, H., J. H. Seinfeld, P. J. Adams, and L. J. Mickley (2004), Global radiative forcing of coupled tropospheric ozone and aerosols in a unified general circulation model, *Journal of Geophysical Research-Atmospheres*, *109*(D16), d16207.

Liljegren, J. C., E. E. Clothiaux, G. G. Mace, S. Kato, and X. Q. Dong (2001), A new retrieval for cloud liquid water path using a ground-based microwave radiometer and measurements of cloud temperature, *Journal of Geophysical Research-Atmospheres*, *106*(D13), 14,485–14,500.

Lin, R. F., D. O. Starr, P. J. DeMott, R. Cotton, K. Sassen, E. Jensen, B. Kärcher, and X. H. Liu (2002), Cirrus parcel model comparison project. phase 1: The critical components to simulate cirrus initiation explicitly, *Journal of the Atmospheric Sciences*, *59*(15), 2305–2329.

Liou, K. N. (1986), Influence of cirrus clouds on weather and climate processes - a global perspective, *Monthly Weather Review*, *114*(6), 1167–1199.

Liousse, C., J. E. Penner, C. Chuang, J. J. Walton, H. Eddleman, and H. Cachier (1996), A global three-dimensional model study of carbonaceous aerosols, *Journal of Geophysical Research-Atmospheres*, *101*(D14), 19,411–19,432.

Liu, G. S., and J. A. Curry (1998), Remote sensing of ice water characteristics in tropical clouds using aircraft microwave measurements, *Journal of Applied Meteorology*, *37*(4), 337–355.

Liu, G. S., H. F. Shao, J. A. Coakley, J. A. Curry, J. A. Haggerty, and M. A. Tschudi (2003), Retrieval of cloud droplet size from visible and microwave radiometric measurements during indoex: Implication to aerosols' indirect radiative effect, *Journal of Geophysical Research-Atmospheres*, *108*(D1), 4006.

Liu, X. H., and J. E. Penner (2005), Ice nucleation parameterization for global models, *Meteorologische Zeitschrift*, *14*(4), 499–514.

Liu, X. H., and W. Seidl (1998), Modeling study of cloud droplet nucleation and in-cloud sulfate production during the sanitation of the atmosphere (sana) 2 campaign, *Journal of Geophysical Research-Atmospheres*, *103*(D13), 16,145–16,158.

Liu, X. H., and M. K. Wang (1996), A parameterization of the efficiency of nucleation scavenging of aerosol particles and some related physicochemical factors, *Atmospheric Environment*, *30*(13), 2335–2341.

Liu, X. H., J. E. Penner, and M. Herzog (2005), Global modeling of aerosol dynamics: Model description, evaluation, and interactions between sulfate and nonsulfate aerosols, *Journal of Geophysical Research-Atmospheres*, *110*(D18).

Liu, Y. G., and P. H. Daum (2002), Anthropogenica erosols - indirect warming effect from dispersion forcing, *Nature*, *419*(6907), 580–581.

Lohmann, U., and J. Feichter (1997), Impact of sulfate aerosols on albedo and lifetime of clouds: A sensitivity study with the echam4 gcm, *Journal of Geophysical Research-Atmospheres*, *102*(D12), 13,685–13,700.

Lohmann, U., and J. Feichter (2005), Global indirect aerosol effects: a review, *Atmospheric Chemistry and Physics*, *5*, 715–737.

Lohmann, U., J. Feichter, C. C. Chuang, and J. E. Penner (1999a), Prediction of the number of cloud droplets in the echam gcm, *Journal of Geophysical Research-Atmospheres*, *104*(D8), 9169–9198.

Lohmann, U., N. McFarlane, L. Levkov, K. Abdella, and F. Albers (1999b), Comparing different cloud schemes of a single column model by using mesoscale forcing and nudging technique, *Journal of Climate*, *12*(2), 438–461.

Lohmann, U., J. Feichter, J. Penner, and R. Leaitch (2000), Indirect effect of sulfate and carbonaceous aerosols: A mechanistic treatment, *Journal of Geophysical Research-Atmospheres*, *105*(D10), 12,193–12,206.

Lynch, D. K., K. Sassen, D. O. Starr, and G. Stevens (2002), *Cirrus*, Oxford Univeristy Press, New York.

Mace, G. G., T. P. Ackerman, E. E. Clothiaux, and B. A. Albrecht (1997), A study of composite citrus morphology using data from a 94-ghz radar and

correlations with temperature and large-scale vertical motion, *Journal of Geophysical Research-Atmospheres*, *102*(D12), 13,581–13,593.

Mace, G. G., T. P. Ackerman, P. Minnis, and D. F. Young (1998), Cirrus layer microphysical properties derived from surface-based millimeter radar and infrared interferometer data, *Journal of Geophysical Research-Atmospheres*, *103*(D18), 23,207–23,216.

Mace, G. G., E. E. Clothiaux, and T. P. Ackerman (2001), The composite characteristics of cirrus clouds: Bulk properties revealed by one year of continuous cloud radar data, *Journal of Climate*, *14*(10), 2185–2203.

Marenco, A., V. Thouret, P. Nedelec, H. Smit, M. Helten, D. Kley, F. Kärcher, P. Simon, K. Law, J. Pyle, G. Poschmann, R. Von Wrede, C. Hume, and T. Cook (1998), Measurement of ozone and water vapor by airbus in-service aircraft: The mozaic airborne program, an overview, *Journal of Geophysical Research-Atmospheres*, *103*(D19), 25,631–25,642.

Martin, G. M., D. W. Johnson, and A. Spice (1994), The measurement and parameterization of effective radius of droplets in warm stratocumulus clouds, *Journal of the Atmospheric Sciences*, *51*(13), 1823–1842.

McFarlane, N., G. J. Boer, J. P. Blanchet, and M. Lazare (1992), The canadian climate center second generation model and its equilibrium climate, *Journal of Climate*, *5*, 1013–1044.

Meng, Z. Y., and J. H. Seinfeld (1996), Time scales to achieve atmospheric gas-aerosol equilibrium for volatile species, *Atmospheric Environment*, *30*(16), 2889–2900.

Meng, Z. Y., D. Dabdub, and J. H. Seinfeld (1998), Size-resolved and chemically resolved model of atmospheric aerosol dynamics, *Journal of Geophysical Research-Atmospheres*, *103*(D3), 3419–3435.

Menon, S. (2004), Current uncertainties inassessing aerosol effects on climate, *Annual Review of Environment and Resources*, *29*, 1–30.

Menon, S., A. D. Del Genio, D. Koch, and G. Tselioudis (2002a), Gcm simulations of the aerosol indirect effect: Sensitivity to cloud parameterization and aerosol burden, *Journal of the Atmospheric Sciences*, *59*(3), 692–713.

Menon, S., J. Hansen, L. Nazarenko, and Y. F. Luo (2002b), Climate effects of black carbon aerosols in china and india, *Science*, *297*(5590), 2250–2253.

Meyers, M. P., P. J. Demott, and W. R. Cotton (1992), New primary ice-nucleation parameterizations in an explicit cloud model, *Journal of Applied Meteorology*, *31*(7), 708–721.

Minnis, P., J. K. Ayers, R. Palikonda, and D. Phan (2004), Contrails, cirrus trends, and climate, *Journal of Climate*, *17*(8), 1671–1685.

Mohler, O. M., S. Buttner, C. Linke, M. Schnaiter, H. Saathoff, O. Stetzer, R. Wagner, M. Kramer, A. Mangold, V. Ebert, and U. Schurath (2005), Effect of sulfuric acid coating on heterogeneous ice nucleation by soot aerosol particles, *Journal of Geophysical Research-Atmospheres*, *110*(D11).

Murphy, J. M., D. M. H. Sexton, D. N. Barnett, G. S. Jones, M. J. Webb, and M. Collins (2004), Quantification of modelling uncertainties in a large ensemble of climate change simulations, *Nature*, *430*(7001), 768–772.

Nakajima, T., A. Higurashi, K. Kawamoto, and J. E. Penner (2001), A possible correlation between satellite-derived cloud and aerosol microphysical parameters, *Geophysical Research Letters*, *28*(7), 1171–1174.

Nenes, A., and J. H. Seinfeld (2003), Parameterization of cloud droplet formation in global climate models, *Journal of Geophysical Research-Atmospheres*, *108*(D14).

Nenes, A., S. Ghan, H. Abdul-Razzak, P. Y. Chuang, and J. H. Seinfeld (2001), Kinetic limitations on cloud droplet formation and impact on cloud albedo, *Tellus Series B-Chemical and Physical Meteorology*, *53*(2), 133–149.

Nenes, A., W. C. Conant, and J. H. Seinfeld (2002), Black carbon radiative heating effects on cloud microphysics and implications for the aerosol indirect effect - 2. cloud microphysics, *Journal of Geophysical Research-Atmospheres*, *107*(D21).

Noone, K. J., D. W. Johnson, J. P. Taylor, R. J. Ferek, T. Garrett, P. V. Hobbs, P. A. Durkee, K. Nielsen, E. Ostrom, C. O'Dowd, M. H. Smith, L. M. Russell, R. C. Flagan, J. H. Seinfeld, L. De Bock, R. E. Van Grieken, J. G. Hudson, I. Brooks, R. F. Gasparovic, and R. A. Pockalny (2000), A case study of ship track formation in a polluted marine boundary layer, *Journal of the Atmospheric Sciences*, *57*(16), 2748–2764.

Numaguti, A. (1999), Origin and recycling processes of precipitating water over the eurasian continent: Experiments using an atmospheric general circulation model, *Journal of Geophysical Research-Atmospheres*, *104*(D2), 1957–1972.

Ou, S. C., and K. N. Liou (1995), Ice microphysics and climatic temperature perturbations, *Atmospheric Research*, *35*, 127–138.

Ou, S. C., K. N. Liou, and T. R. Caudell (1998), Remote sounding of multilayer cirrus cloud systems using avhrr data collected during fire-ii-ifo, *Journal of Applied Meteorology*, *37*(3), 241–254.

Ovarlez, J., J. F. Gayet, K. Gierens, J. Ström, H. Ovarlez, F. Auriol, R. Busen, and U. Schumann (2002), Water vapour measurements inside cirrus clouds in northern and southern hemispheres during inca, *Geophysical Research Letters*, *29*(16), 1813.

Paluch, I. R., and D. H. Lenschow (1992), Measurements of aitken nuclei and cloud condensation nuclei in the marine atmosphere and their relation to the dms-cloud-climate hypothesis - comment, *Journal of Geophysical Research-Atmospheres*, *97*(D7), 7657–7658.

Peng, Y. R., and U. Lohmann (2003), Sensitivity study of the spectral dispersion of the cloud droplet size distribution on the indirect aerosol effect, *Geophysical Research Letters*, *30*(10).

Penner, J. E. (2004), Climate change - the cloud conundrum, *Nature*, *432*(7020), 962–963.

Penner, J. E., C. S. Atherton, J. Dignon, S. J. Ghan, J. J. Walton, and S. Hameed (1991), Tropospheric nitrogen - a 3-dimensional study of sources, distributions, and deposition, *Journal of Geophysical Research-Atmospheres*, *96*(D1), 959–990.

Penner, J. E., R. J. Charlson, J. M. Hales, N. S. Laulainen, R. Leifer, T. Novakov, J. Ogren, L. F. Radke, S. E. Schwartz, and L. Travis (1994), Quantifying and minimizing uncertainty of climate forcing by anthropogenic aerosols, *Bulletin of the American Meteorological Society*, *75*(3), 375–400.

Penner, J. E., I. P. on Climate Change. Working Group I., and I. P. on Climate Change. Working Group III. (1999), *Aviation and the global atmosphere : a special report of IPCC Working Groups I and III in collaboration with the Scientific Assessment Panel to the Montreal Protocol on Substances that Deplete the Ozone Layer*, Cambridge University Press, Cambridge.

Penner, J. E., M. O. Andreae, H. Annegarn, L. Barrie, J. Feichter, D. Hegg, R. Jayaraman, R. Leaitch, D. M. Murphy, J. Nganga, and G. Pitari (2001a), Aerosols, their direct and indirect effects, in *Report to Intergovernmental Panel on Climate Change from the Scientific Assessment Working Group (WGI)*, edited by T. Houghton, Y. Ding, D. J. Griggs, M. Noguer, P. J. van der Linden, X. Dai, K. Maskell, and C. Johnson, Cambridge Unversity Press.

Penner, J. E., D. Hegg, and R. Leaitch (2001b), Unraveling the role of aerosols in climate change, *Environmental Science and Technology*, *35*(15), 332A–340A.

Penner, J. E., X. Q. Dong, and Y. Chen (2004), Observational evidence of a change in radiative forcing due to the indirect aerosol effect, *Nature*, *427*(6971), 231–234.

Pfaendtner, J., S. Bloom, D. Lamich, M. Seablom, M. Sienkiewicz, J. Stobie, and A. da Silva (1995), Documentation of the goddard earth observating system (geos) data assimilation system - version 1, *Tech. Rep. 104606*, Goddard Space Flight Center.

Pilinis, C., K. P. Capaldo, A. Nenes, and S. N. Pandis (2000), Madm - a new multicomponent aerosol dynamics model, *Aerosol Science and Technology*, *32*(5), 482–502.

Platnick, S. E., and S. Twomey (1994), Determining the susceptibility of cloud albedo to changes in droplet concentration with the advanced very high resolution radiometer, *Journal of Applied Meteorology*, *33*, 334–347.

Pruppacher, H. R., and J. D. Klett (1997), *Microphysics of clouds and precipitation*, Kluwer Academic Publishers.

Pueschel, R. F., G. V. Ferry, K. G. Snetsinger, J. Goodman, J. E. Dye, D. Baumgardner, and B. W. Gandrud (1992), A case of type-i polar stratospheric cloud formation by heterogeneous nucleation, *Journal of Geophysical Research-Atmospheres*, *97*(D8), 8105–8114.

Quaas, J., O. Boucher, and F. M. Breon (2004), Aerosol indirect effects in polder satellite data and the laboratoire de meteorologie dynamiquezoom (lmdz) general circulation model, *Journal of Geophysical Research-Atmospheres*, *109*(D8), d08205.

Quinn, P. K., T. L. Miller, T. S. Bates, J. A. Ogren, E. Andrews, and G. E. Shaw (2002), A 3-year record of simultaneously measured aerosol chemical and optical properties at barrow, alaska, *Journal of Geophysical Research-Atmospheres*, *107*(D11), 4130.

Radke, L. F., J. A. Coakley, and M. D. King (1989), Direct and remote-sensing observations of the effects of ships on clouds, *Science*, *246*(4934), 1146–1149.

Ramanathan, V., R. D. Cess, E. F. Harrison, P. Minnis, B. R. Barkstrom, E. Ahmad, and D. Hartmann (1989), Cloud-radiative forcing and climate - results from the earth radiation budget experiment, *Science*, *243*(4887), 57–63.

Ramaswamy, V., O. Boucher, J. Haigh, D. Hauglustaine, J. Haywood, G. Myhre, T. Nakajima, G. Y. Shi, and S. Solomon (2001a), Chapter 6. radiative forcing of climate change, in *IPCC WGI Third Assessment Report*, Cambridge University Press, Cambridge, UK.

Ramaswamy, V., M. L. Chanin, J. Angell, J. Barnett, D. Gaffen, M. Gelman, P. Keckhut, Y. Koshelkov, K. Labitzke, J. J. R. Lin, A. O'Neill, J. Nash, W. Randel, R. Rood, K. Shine, M. Shiotani, and R. Swinbank (2001b), Stratospheric temperature trends: Observations and model simulations, *Reviews of Geophysics*, *39*(1), 71–122.

Rangno, A. L., and P. V. Hobbs (2001), Ice particles in stratiform clouds in the arctic and possible mechanisms for the production of high ice concentrations, *Journal of Geophysical Research-Atmospheres*, *106*(D14), 15,065–15,075.

Roelofs, G. J., J. Lelieveld, and L. Ganzeveld (1998), Simulation of global sulfate distribution and the influence on effective cloud drop radii with a coupled photochemistry sulfur cycle model, *Tellus Series B-Chemical and Physical Meteorology*, *50*(3), 224–242.

Rogers, D. C. (1994), Detecting ice nuclei with a continuous-flow diffusion chamber - some exploratory tests of instrument response, *Journal of Atmospheric and Oceanic Technology*, *11*(4), 1042–1047, part 1.

Rogers, R. R., and M. K. Yau (1989), *A short course in cloud physics*, Butterworth-Heinemann.

Romakkaniemi, S., H. Kokkola, and A. Laaksonen (2005), Soluble trace gas effect on cloud condensation nuclei activation: Influence of initial equilibration on cloud model results, *Journal of Geophysical Research-Atmospheres*, *110*(D15), d15202.

Rosenfeld, D., and G. Feingold (2003), Explanation of discrepancies among satellite observations of the aerosol indirect effects, *Geophysical Research Letters*, *30*(14), 1776.

Rosenfeld, D., and W. L. Woodley (2000), Deep convective clouds with sustained supercooled liquid water down to-37.5 degrees c, *Nature*, *405*(6785), 440–442.

Rotman, D. A., C. S. Atherton, D. J. Bergmann, P. J. Cameron-Smith, C. C. Chuang, P. S. Connell, J. E. Dignon, A. Franz, K. E. Grant, D. E. Kinnison, C. R. Molenkamp, D. D. Proctor, and J. R. Tannahill (2004), Impact, the llnl 3-d global atmospheric chemical transport model for the combined troposphere and stratosphere: Model description and analysis of ozone and other trace gases, *Journal of Geophysical Research-Atmospheres*, *109*(D4).

Rotstayn, L. D., and Y. G. Liu (2003), Sensitivity of the first indirect aerosol effect to an increase of cloud droplet spectral dispersion with droplet number concentration, *Journal of Climate*, *16*(21), 3476–3481.

Rotstayn, L. D., and J. E. Penner (2001), Indirect aerosol forcing, quasi forcing, and climate response, *Journal of Climate*, *14*(13), 2960–2975.

Sassen, K., and G. C. Dodd (1988), Homogeneous nucleation rate for highly supercooled cirrus cloud droplets, *Journal of the Atmospheric Sciences*, *45*(8), 1357–1369.

Schwartz, S. E., and A. Slingo (1996), Enhanced shortwave cloud radiative forcing due to anthropogenic aerosols, in *Clouds, Chemistry and Climate*, edited by P. J. Crutzen and V. Ramanathan, NATO ASI, pp. 191–236, Springer-Verlag, Berlin.

Schwartz, S. E., Harshvardhan, and C. M. Benkovitz (2002), Influence of anthropogenic aerosol on cloud optical depth and albedo shown by satellite measurements and chemical transport modeling, *Proceedings of the National Academy of Sciences of the United States of America*, *99*(4), 1784–1789.

Seifert, M., J. Ström, R. Krejci, A. Minikin, A. Petzold, J. F. Gayet, H. Schlager, H. Ziereis, U. Schumann, and J. Ovarlez (2004), Aerosol-cirrus interactions: a number based phenomenon at all?, *Atmospheric Chemistry and Physics*, *4*, 293–305.

Seinfeld, J. H., and S. N. Pandis (1997), *Atmospheric chemistry and physics*, John Wiley & Sons, INC.

Senior, C. A., and J. F. B. Mitchell (1993), Carbon-dioxide and climate - the impact of cloud parameterization, *Journal of Climate*, *6*(3), 393–418.

Sheridan, P. J., C. A. Brock, and J. C. Wilson (1994), Aerosol-particles in the upper troposphere and lower stratosphere - elemental composition and morphology of individual particles in northern midlatitudes, *Geophysical Research Letters*, *21*(23), 2587–2590.

Sheridan, P. J., D. J. Delene, and J. A. Ogren (2001), Four years of continuous surface aerosol measurements from the department of energy's atmospheric radiation measurement program southern great plains cloud and radiation testbed site, *Journal of Geophysical Research-Atmospheres*, *106*(D18), 20,735–20,747.

Smith, S. J., H. Pitcher, and T. M. L. Wigley (2001), Global and regional anthropogenic sulfur dioxide emissions, *Global and Planetary Change*, *29*(1-2), 99–119.

Stainforth, D. A., T. Aina, C. Christensen, M. Collins, N. Faull, D. J. Frame, J. A. Kettleborough, S. Knight, A. Martin, J. M. Murphy, C. Piani, D. Sexton, L. A. Smith, R. A. Spicer, A. J. Thorpe, and M. R. Allen (2005), Uncertainty in predictions of the climate response to rising levels of greenhouse gases, *Nature*, *433*(7024), 403–406.

Stephens, G. L., S. C. Tsay, P. W. Stackhouse, and P. J. Flatau (1990), The relevance of the microphysical and radiative properties of cirrus clouds to climate and climatic feedback, *Journal of the Atmospheric Sciences*, *47*(14), 1742–1753.

Stoffel, T. (2004), Ground radiation (gndrad) hand book, *Tech. Rep. ARM TR-027.*

Ström, J., and S. Ohlsson (1998), In situ measurements of enhanced crystal number densities in cirrus clouds caused by aircraft exhaust, *Journal of Geophysical Research-Atmospheres*, *103*(D10), 11,355–11,361.

Sundqvist, H., E. Berge, and J. E. Kristjansson (1989), Condensation and cloud parameterization studies with a mesoscale numerical weather prediction model, *Monthly Weather Review*, *117*(8), 1641–1657.

Suzuki, K., T. Nakajima, A. Numaguti, T. Takemura, K. Kawamoto, and A. Higurashi (2004), A study of the aerosol effect on a cloud field with simultaneous use of gcm modeling and satellite observation, *Journal of the Atmospheric Sciences*, *61*(2), 179–194.

Talbot, R. W., J. E. Dibb, and M. B. Loomis (1998), Influence of vertical transport on free tropospheric aerosols over the central usa in springtime, *Geophysical Research Letters*, *25*(9), 1367–1370.

Tape, W. (1994), Atmospheric halos, American Geophysical Union.

ten Brink, H. M., J. P. Veefkind, A. Waijers-Ijpelaan, and J. C. van der Hage (1996), Aerosol light-scattering in the netherlands, *Atmospheric Environment*, *30*, 4251–4261.

Tie, X. X., L. Emmons, L. Horowitz, G. Brasseur, B. Ridley, E. Atlas, C. Stround, P. Hess, A. Klonecki, S. Madronich, R. Talbot, and J. Dibb (2003), Effect of sulfate aerosol on tropospheric nox and ozone budgets: Model simulations and topse evidence, *Journal of Geophysical Research-Atmospheres*, *108*(D4), 8364.

Twohy, C. H., J. G. Hudson, S. S. Yum, J. R. Anderson, S. K. Durlak, and D. Baumgardner (2001), Characteristics of cloud-nucleating aerosols in the indian ocean region, *Journal of Geophysical Research-Atmospheres*, *106*(D22), 28,699–28,710.

Twomey, S., and P. Squires (1959), The influence of cloud nucleus population on the microstructure and stability of convective clouds, *Tellus*, *11*(4), 408–411.

Twomey, S. A. (1977), Pollution and cloud albedo, *Transactions-American Geophysical Union*, *58*(8), 797–797.

Vali, G. (1996), Ice nucleation - a review, in *Nucleation and atmospheric aerosols 1996*, edited by M. Kulmala and P. E. Wagner, pp. 271–279, Pergamon.

Warneck, P. (1988), *Chemistry of the natural atmosphere*, Academic, New York.

Wetzel, M. A., and L. L. Stowe (1999), Satellite-observed patterns in stratus microphysics, aerosol optical thickness, and shortwave radiative forcing, *Journal of Geophysical Research-Atmospheres*, *104*(D24), 31,287–31,299.

Whitby, K. T., and B. K. Cantrell (1976), Fine particles, in *International Conference on Environmental Sensing and Assessment*, Institute of Electrical and Electronic Engineers, Las Vegas, NV.

Wylie, D. P., and W. P. Menzel (1999), Eight years of high cloud statistics using hirs, *Journal of Climate*, *12*(1), 170–184.

Wyser, K. (1998), The effective radius in large-scale models: impact of aerosols and coalescence, *Atmospheric Research*, *49*(3), 213–234.

Young, K. C. (1993), *Microphysical processes in clouds*, Oxford Univeristy Press, Oxford.

Yum, S. S., J. G. Hudson, and Y. H. Xie (1998), Comparisons of cloud microphysics with cloud condensation nuclei spectra over the summertime southern ocean, *Journal of Geophysical Research-Atmospheres*, *103*(D13), 16,625–16,636.

Zhang, Y. (2003), A study of soot and smoke aerosols and improved biomass smoke emissions using the toms ai, Ph.D. thesis, University of Michigan.

ABSTRACT

AEROSOL INDIRECT EFFECTS ON CLOUDS AND GLOBAL CLIMATE

by

Yang Chen

Chair: Joyce E. Penner

The aerosol indirect effect remains one of the most important uncertainties in the projection of future climate. Here we first provided an observational evidence of the change in radiative forcing due to the aerosol indirect effect. Based on the observations of aerosol and cloud properties, we used a cloud parcel model to estimate the cloud optical depth at a polluted site and a clean site. We also determined the cloud optical depth required to fit the surface measured downward SW fluxes. Results from both methods show that the cloud optical depth is larger at the polluted site given a value of cloud liquid water path. From this good agreement we concluded that the aerosol indirect effect has a significant influence on the radiative fluxes.

Then, we used 3-D meteorological fields together with a radiative transfer model to calculate the global first aerosol indirect forcing. We also examined the spatially-resolved uncertainty in estimates of this forcing by perturbing the values of each parameter in the calculation. The global mean forcing calculated in the reference

case is -1.30 Wm^{-2}, and the global mean relative uncertainty is 130%. The aerosol burden calculated by chemical transport models and the cloud fraction were found to be the most important sources of uncertainty.

We also studied the aerosol indirect effect by nitrate and nitric acid gas. The indirect effect of nitrate on TOA radiative flux was found to be comparable to that by anthropogenic sulfate in some places. A substitution method that accounts for the gas phase nitric acid effect on CCN activation was developed and added to the cloud nucleation parameterization.

Anthropogenic aerosols may also change the formation of ice crystals in cirrus clouds, which has effects on both the SW and LW radiative balance of the earth. The indirect forcing due to anthropogenic aerosols was calculated by a radiative transfer model using aerosols from different emissions. The results show that anthropogenic aerosols may have two effects on cirrus clouds: increase in the ice number concentration (N_i) by increasing the ice nuclei concentration, or decrease N_i by lowering the maximum supersaturation.